**The Dissertation Committee for William Victor Taylor Certifies that this is the approved version of the following Dissertation:**

# Exploring the Interaction of Antimony Ligands with Late 3*d* Transition Metals: Enhancements in Metal Deposition, Magnetism and Luminescence through Heavy Atom Ligation

**Committee:**

Michael J. Rose, Supervisor

Simon M. Humphrey

Richard A. Jones

Sean T. Roberts

Xiaoqin Li

# Exploring the Interaction of Antimony Ligands with Late 3*d* Transition Metals: Enhancements in Metal Deposition, Magnetism and Luminescence through Heavy Atom Ligation

**by**

**William Victor Taylor**

**Dissertation**

Presented to the Faculty of the Graduate School of

The University of Texas at Austin

in Partial Fulfillment

of the Requirements

for the Degree of

**Doctor of Philosophy**

**The University of Texas at Austin**

**May 2019**

# Dedication

To my family: Thank you for all your love and support over the years. You kept me grounded and reminded me what was important through all of this. I love you all.

## Acknowledgements

Mike: You taught me so much about chemistry and were a truly excellent role model. Thank you for all of your guidance and support.

My friends: Thanks for all the fun times and distractions necessary to get through grad school. I'm going to miss our hang outs and game sessions.

The Rose group: Thanks for all the fantastic conversations—especially the ones that burned through sub-group time. I couldn't have asked for a better group of co-workers and friends, good luck in all of your endeavors.

# Abstract

Exploring the Interaction of Antimony Ligands with Late 3*d* Transition Metals: Enhancements in Metal Deposition, Magnetism and Luminescence through Heavy Atom Ligation

William Victor Taylor, Ph. D.

The University of Texas at Austin, 2019

Supervisor: Michael J. Rose

Antimony has been known to civilizations for thousands of years, and its role in cosmetics, metallurgy and alchemy helped shape the course of history. However, as a useful ligand in metal complex syntheses, organoantimony compounds have been largely ignored. This work explores the ligand syntheses and capabilities of both monodentate and polydentate antimony compounds towards higher valent ($M^{II/I}$) late row 3*d* transition metals, namely nickel(II), copper(I), and cobalt(II). A large library of homo- and heteroleptic antimony ligands with general structure $SbR_3$ (R = Me, Ph, $^{i}$Pr, Cy, $^{t}$Bu) were synthesized and characterized, and their successful complexation to metal halides afforded several novel complexes and crystal structures. Slight modifications to the steric and electronic properties of the antimony ligands were shown to drastically affect the coordination number, geometry, and pertinent reactivities and properties of the final metal-antimony complexes. More specifically, synthesized nickel-antimony complexes performed electroless deposition of a Cu/Ni alloy onto the surface of a Cu|Si substrate. It was determined that the electronic properties of the ligands had a direct effect on surface purity, as the strongest σ-donating ligands were able to more readily scavenge impurities

from the deposition solution. Among copper-antimony complexes, the steric size of the ligand dictated the formation of dimers (small ligands), or cuboids (large ligands), which displayed NIR thermoluminescent properties. A thorough investigation of the structure-luminescence correlation in these complexes revealed that short Cu-Cu bonds (ligand $\%V_{bur}$ ~ 27.0 %) inside the cuboid core and high complex symmetry (cubic) held co-responsibility for red-shifting emission wavelengths. Paramagnetic cobalt-antimony complexes were synthesized, and these complexes showed a significant increase in the extent of axial zero-field-splitting (*D*) versus analogous phosphine compounds, which has been attributed to an increase of spin-orbit-coupling on the metal center originating from the ligands. The translational spin-orbit-coupling donated to a 3*d* metal center from heavy donor ligands could help improve C-H activation catalytic activity in these new complexes via a higher probability of spin-crossover transitions and a stabilization of transition state energies. Although the cobalt-antimony complexes displayed signs of increased reactivity towards traditional C-H activation substrates, the results were preliminary and overall inconclusive.

# Table of Contents

# List of Tables

# List of Figures

# List of Schemes

# Chapter 1: The Role of Antimony in the Pursuit of Novel C-H Activation Catalysts: An Elemental and Synthetic History of Antimony Ligands, Metal Complexes, and Alchemy

## 1.1 The History of Antimony: From Makeup to Weaponry

The history of antimony is a rich vein as it has been known to civilizations dating back to the ancient era. One of the first uses of antimony was as an eye makeup for women who lived around the southeastern Mediterranean coastline.[1] Stibnite – the most common naturally occurring source of antimony with formula $Sb_2S_3$ – is a soft and brittle stone with a deep black color when crushed. As an eye makeup, it afforded the staring protruding appearance characteristic of Egyptian portraits, as can be seen in Figure 1.1. (*Disclaimer Image credit: Egyptian death mask from the 18$^{th}$ dynasty. Louvre, Paris. This image is licensed under the Creative Commons Attribution-Share Alike 2.0 France license, https://creativecommons.org/licenses/by-sa/2.0/fr/deed.en*)

**Figure 1.1** Portrayal of dark Egyptian eye makeup made using stibnite.

Stibnite is even referenced in the Bible on numerous occasions. In the Douay version of the Bible, a passage from IV Kings reads, "And Jehu came into Jezrahel: But Jezabel hearing of his coming in, painted her face in stibic stone…" (IV Kings 9, 30). Later on, the prophets Jeremiah and Ezekiel both condemn the practice, with Jeremiah stating, "Though thou deckest thee with ornaments of gold, and paintest thy eyes with stibick-stone, thou shalt dress thyself out in vain…" (Jer. 4, 30). Although the two soothsayers likely were merely chastising excessive vanity or prostitution, their words may have had the unintended consequence of preventing antimony poisoning. The "stibic(k) stone" is almost assuredly stibnite, with even further confirmation coming from the modern Spanish translation that reads: "aunque te pintes los ojos con *antimonio*" where we see the Latin etymological term "antimony" appear. Indeed, even pious and obedient Job named his youngest daughter Cornustibij, which translates to "horn of antimony", perhaps a reference to her beautiful eyes.[2]

Antimony quickly found its way into Roman society as Roman conquest expanded beyond Asia Minor and the Nile river valley. The early Italians were less interested in stibnite as a cosmetic item and more interested in its medicinal and metallurgical purposes.[3] However, the ignorant characterization practices employed by Roman physicians at the time caused them to believe they had synthesized lead when stibnite was heated. However, the likely product from this reaction of Sb metal and heat is antimony trioxide, $Sb_2O_3$. The famous naturalist Pliny the Elder wrote: "But the main thing of all is to observe such a degree of nicety in heating it, as not to let it become lead".[4] Roman doctors were interested in the healing properties of antimony, and antimony was used as a laxative, an emetic, and to treat depression.[5] These medicinal beliefs continued for centuries, and even practiced on

distinguished clientele. Some scholars believe Mozart died from being given antimony to treat his depression, although Mozart's death is highly mythologized and shrouded in mystery.[5] Although their smelting and pharmaceutical techniques were crude, the Romans were one of the first civilizations to probe antimony for its chemical properties. These practices, along with the quest for alchemical glory, continued past the fall of Rome and into the Middle Ages.

Science in the Medieval era was infamously plagued by the practice of alchemy, where budding chemists and philosophers sought impossible truths such as the creation of an elixir of life or the conversion of base metals into something much more valuable. In fact, antimony was held in high regard to medieval alchemists as they believed natural antimony to be the most suitable raw material for the transmutation of metals to gold.[6] When copper is alloyed with a small percentage of Sb, the resulting metal shares several similar characteristics of gold; however astute medieval alchemists (including Saint Albert the Great) knew the alloy to be false as it did not withstand the test of fire.[7] Antimony is one of only a handful of modern-day elements to have its own alchemical symbol – a circle with a cross affixed to the top, seen in Figure 1.2. This could have been derived from the belief that antimony symbolized "womanly features".[8] Antimony was also often referred to pictorially as a wolf or a lion because of the observation that antimony would "devour" other metals in the fire.[8] Some other elements with alchemical symbols include sulfur (a triangle with a cross affixed to the bottom) and silver (a moon in the early waxing stage).[9]

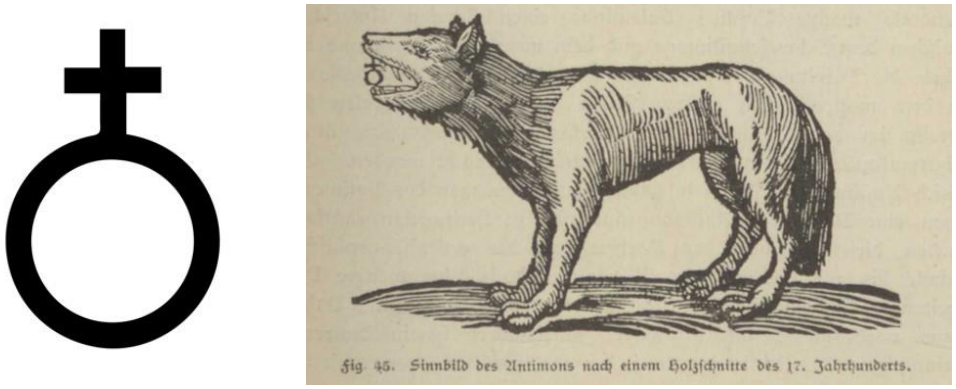


**Figure 1.2** Alchemical symbols of antimony.

Although their ventures were ultimately unsuccessful, medieval alchemists did uncover a fair amount of knowledge about antimony as an alloying agent, and they published that information in various texts. One of the earliest works is *De re metallica* written by Georgius Agricola in the 16th century.[10] Agricola proclaimed antimony could be smelted with tin to produce a compound known as "bookseller's alloy". This alloy was used for type settings in early printing presses and is thought to have been instrumental in Johannes Gutenberg's revolutionizing machine. In the early 17th century, a now-famous book was published: *Triumphal Chariot of Antimony*.[11] This monographical work extols both the "virtues" and "venoms" of antimony as well as some practical usages for the metal – perhaps most interesting is its role in giving church bells a more pleasant-sounding ring. At the time, *Triumphal Chariot of Antimony* was claimed to be written by a 15th century Benedictine monk, Basil Valentine. However, most historians agree the writing is too modern for that time period and the manuscript is instead attributed to Johann Thölde, a German saltworks operator.[1] Ultimately, the most comprehensive historical text about antimony belongs to Nicolas Lémery and his *Treatise on Antimony*, dated 1707.[12] The *Treatise* included names, diversities, origins, and medical virtues of antimony to go along

with precise procedures for extraction, purification, and reactivity towards other metals. His detailed study of one element led to praises from Bernard Le Bovier de Fontenelle: "One might learn from this example that the study of a single mixture is almost limitless and that each in particular might have its own chemist."[13] In his biographical sketch of Lémery, author Paul-Antoine Cap detailed the massive furnaces, instruments, glassware, and reactions that dotted his laboratory and proclaimed him, "(a) modest scholar who devoted his life, in good faith and unreservedly, to the search for truth."[14] Although Lémery is best known today for his work in acid-base theory and for his (at the time very popular) textbook *Cours de Chymie*, he reasonably could be considered to be the father of modern antimony research. He helped bring the element out of the alchemical dark ages and into the research spotlight.

Over the next two centuries, antimony was used primarily as a component in bearing metal or in Brittania metal – an alloy consisting of tin, antimony, and copper which was used for all manners of household items including teapots, mugs, and candlesticks.[1] Antimony metal also served a useful role as a lead hardening agent and improved lead plates and lead bullets used in World Wars I and II; it is still useful in that capacity today.[15] The most ubiquitous application of antimony in the present day is as a flame retardant (as the post "flame trial" product, $Sb_2O_3$) but it also has value in catalysis, batteries, and pigments.[16]

The beginning of small molecule antimony synthesis dates back to early 20$^{th}$ century Germany, with pioneers Partheil (mercurial antimonides into antimony alkyl-alcohols), Kaufmann (pentavalent antimony species), and Gruttner (trialkyl- and mixed alkylarylstibines) leading the way.[17–19] Organometallic stibine chemistry has roots starting in the 1920s but was not studied in detail until Breunig in the 1970s and 80s.[20,21] More

recently, there has been increased interest in the semiconductor and materials capabilities of antimony. Antimony has been known to humanity for millennia, and research into this intriguing element has been undertaken since B.C.E. Although not the most inherently useful material, it has played an important role in several different capacities for a multitude of civilizations and continues to be a worthwhile research avenue to explore in the modern day.

### 1.2 General Properties of Antimony

When first looking at antimony, it must be wondered, why would anyone work with this element? It is difficult to synthesize, difficult to form metal complexes with, toxic, and has both weak Sb-C bond and Sb-Metal bonds. Although all of those statements are at least partially true, there are many beneficial features of antimony that make it an appealing elemental building block. First, although both the organic and inorganic syntheses with antimony are technically challenging, there are literature precedents that prove antimony can be an effective donor atom in both mono- and multidentate ligand schemes. Additionally, there is a clear gap in knowledge with antimony-metal complexes. Simply put, there exist very few antimony-metal complexes synthesized with either alkyl-based antimony ligands or high valent metal centers. Thus, there is a large mine of untapped research for any type of scientific direction – and any new ligand or metal complex is likely a publication worthy achievement; the applications are important additions but do not necessarily need to be the main feature of the manuscript.

When designing new projects revolving around antimony ligands or metal complexes, it is important to keep in mind some of the core properties of antimony. For one, antimony is a heavy element, especially when compared to analogous nitrogen or

phosphine-based ligands. This heaviness affords it a major beneficial property: a high spin-orbit-coupling (SOC) constant.[22] Spin-orbit-coupling will be discussed in more detail later on, but SOC has many benefits including altered magnetic properties (both with and without a magnetic field) and increasing the rate of intersystem crossing to access triplet states in excited species. On a similar note, heavy atoms can impart the "heavy atom effect" in luminescent materials, which red-shifts the emission wavelength of those compounds compared with analogous compounds synthesized with lighter elements.[23,24] Even in its +3-oxidation state, it can behave as an excellent Lewis acid, having shown to readily accept anions (especially $F^-$) from solution even in nanomolar concentrations.[25] However, these antimony ligands were diagnosed as non-innocent, implying the oxidation state ($Sb^{III}$ or $Sb^{V}$) was not able to be absolutely determined. It has this advantage over bismuth, as bismuth will not willingly access the Bi(V) oxidation state.[26]

Each of these properties make antimony unique, and each property will be explored throughout this dissertation. However, the core property that enticed us to work with antimony in the first place was, in fact, its high spin-orbit-coupling constant. This fascinating relativistic effect could play a major role in designing new catalytic systems synthesized with earth abundant and inexpensive starting materials as the chemical industry slowly transitions away from rare elements for critical global processes.

## 1.3 Antimony Ligand Syntheses

### 1.3.1 Monodentate Antimony Ligands

Modern antimony research focuses on organoantimony manipulations to synthesize ligands suitable for metalations with transition metals. Triphenylstibine, $SbPh_3$, is a commercially available ligand that appears very similar to triphenylphosphine, $PPh_3$. $PPh_3$

is ubiquitously used in organometallic research and can bind to most transition metals in various oxidation states.[27] However, its antimony counterpart is a much weaker ligand due to the diffuse orbitals on Sb and the electron withdrawing nature of the phenyl ligands that remove electron density from an already disadvantaged antimony donor atom.[28] These effects led to the corresponding poor ligand capabilities of $SbPh_3$, and as such it was relegated to the organometallic sidelines; further research into the properties of antimony ligands were halted. Fortunately, chemists discovered other organoantimony compounds could be synthesized with different R groups, paving the way for antimony-based ligands that could successfully bind to transition metals. Some early examples include $Ru(CO)_4(SbMe_3)$ from Einstein and Pomeroy and a di-rhodium complex with a bridging $Sb^iPr_3$ ligand from Werner.[29,30] Electron donating (or at least non-electron withdrawing) substituents, such as alkyl groups, push a larger extent of electron density onto the antimony donor atom, which in turn allows for increased donicity for ligation onto transition metals – even higher valent and harder 3*d* transition metals. What follows is a general history on antimony ligand syntheses as well as crucial guidelines to follow when attempting to synthesize both mono- and polydentate antimony compounds.

Simple $SbR_3$ molecules (R = Me, Et, Pr, Bu, Cy, etc.) are readily synthesized through the use of Grignard reagents in combination with commercially available (Alfa Aesar or Sigma-Aldrich) antimony trihalides, $SbX_3$.[31] $SbCl_3$ was used almost exclusively in this thesis, as it is the more inexpensive and ubiquitous antimony starting material compared to $SbBr_3$ (3x more expensive) or $SbI_3$ (not commonly sold) while still performing perfectly fine in the desired reactions. The Grignard reagent can originate from either commercial sources or can be freshly synthesized (see experimental section of Chapter 2 for more detailed information on this process). Excess Grignard in combination with

refluxing conditions results in a successful reaction with most R-groups. There are several key details that must be followed during the reaction. Diethyl ether is the preferred solvent as it dissolves both the starting materials and the desired product, while the $MgX_2$ byproduct is insoluble in $Et_2O$, and $Et_2O$ is immiscible with water. The use of THF is reasonable, however the water wash must be replaced with a brine wash to avoid THF/water miscibility. The aqueous wash serves another critical purpose as it quenches excess Grignard and eliminates any unreacted $SbCl_x$ moieties (such as a $Sb^iPr_2Cl$ byproduct). It cleaves the Sb-Cl bond and dissolves the resulting product (likely an antimony alkyl-alcohol adduct, $Sb(R)_2(OH)$, but never confirmed in this work). The homoleptic $SbR_3$ product is nearly always pure and can be used without further purification. The only exceptions are ligands with very bulky substituents (e.g. R = $^t$Bu). These require a distillation to purify, and the distillations are often difficult due to the high boiling point of the bulky ligands. This reliable and (relatively) straightforward reaction is vital for any future antimony chemist and should be the first reaction that any new student masters before proceeding with their research.

Another useful tool in the arsenal of any antimony chemist is the synthesis of heteroleptic antimony ligands with the general form $SbPh_xR_{3-x}$. [19] With the addition of one or two phenyl groups, one can alter the steric and electronic properties on a more precise scale versus the complete change of the R group. The synthesis of these ligands is essentially the same as in the homoleptic ligands – via Grignard chemistry. However, the antimony starting material must be either $SbPhCl_2$ or $SbPh_2Cl$; these compounds are not commercially available but can be synthesized through a solventless comproportionation reaction.[32] For example, to synthesize $SbPhCl_2$, two equivalents of neat $SbCl_3$ is added to one equivalent of neat $SbPh_3$. These reactions are stirred for a few hours to yield a green

oil, which can be used as generated or further purified if desired. The ideal purified product is the crystallized form, which can be achieved through a concentrated pentane solution in the freezer, or through the classic crystallization seeding technique. After the Grignard reaction, the resulting heteroleptic ligand must be further purified. The impurities from the reaction are the result of low-energy-barrier R-group scrambling during the synthesis, a common issue in organoantimony synthetic chemistry.[33] For example, if $Sb^{i}Pr_2Ph$ were the target compound, the impurities in the crude product would include $Sb^{i}PrPh_2$ and $Sb^{i}Pr_3$. Fortunately, these products can be purified via fractional distillation. This is best achieved with a short path distillation apparatus, ice cold water in the condenser, and constant use of a heat gun to keep the short path distillation head hot enough – otherwise, the product will cool before reaching the condenser and return to the reaction flask. The general rule of thumb with antimony fractional distillations is that the presence of phenyl groups significantly increases the boiling points of the ligands; ligands with phenyl groups distill at a hotter temperature than all-alkyl ligands, and each additional phenyl group raises the boiling point by ~ 50 °C. Distillations are very challenging when working with bulky R-groups (e.g. $^{t}$Bu, Cy) or in the case of ligands with multiple Sb atoms. For these cases, a Kugelrohr is a very useful instrument. The Kugelrohr uses a hot air bath instead of an oil bath used in traditional distillations. This allows for more even heating of the crude mixture as well as the ability to heat to higher temperatures than an oil bath can safely reach (up to ~200 °C). Unfortunately, when a Kugelrohr does not work, there is not much else that can separate out antimony ligands from crude reaction mixtures. The products cannot be separated through column chromatography as they are air sensitive and likely sensitive to both acidic silica and basic alumina gels. Solubility separation is an option but may be untenable due to product structural similarity and solubility. Crystallization of the desired

product could be possible depending on the substituent (R = $^{i}$Pr, Cy, Bu; i.e. bulky ligands), but most alkyl-antimony compounds are liquids or oils and are thus not isolable via crystallization.

Another useful antimony compound that can serve as a precursor to syntheses is the five-coordinate species $SbR_3X_2$. As a ligand, this molecule is of little use because the coordinating lone pair is occupied by the additional halogen atoms. However, this product can theoretically be reduced to Sb(III) by removal of RX, yielding $SbR_2X$.[34] From there, another R' group can replace the halide via Grignard chemistry, or this intermediate can be a valuable starting material for a multidentate antimony ligand.

### 1.3.2 Multidentate Antimony Ligands

Multidentate antimony ligands are appealing for their increased bonding affinity due to the chelate effect, as well as the unique geometries attainable upon complexation to metal centers.[35–37] However, the synthesis of these multidentate ligands is much more difficult than monodentate ligands, as attaching two or more antimony centers to one organic scaffold runs into several issues. A common synthetic strategy is to utilize the Sb atom as a nucleophile and attempt to displace a leaving group. The generation of $SbR_2Na$ (R = Me, Ph) from the reaction of $SbR_2Ph$ with sodium metal in liquid ammonia is feasible, and this method has proven effective for several research groups.[38,39] Indeed, the rare tridentate Sb ligand, $MeC(CH_2SbPh_2)_3$ was synthesized in this manner, using the tribrominated $MeC(CH_2Br)_3$ as the organic scaffold. These reactions are often low yielding due to the tendency of the $SbR_2Na$ adduct to dimerize, yielding a $Sb_2R_4$ biproduct.[39] These dimers are yellow products, and a yellow color in the reaction mixture is often evidence for the formation of dimers. The methyl dimer is low-boiling and can be distilled off

(Kugelrohr recommended), but the phenyl dimer is too bulky for a typical distillation – solvent separation is the recommended approach. Consequently, multidentate antimony compounds are often very difficult to purify, and, coupled with low yields, render the overall synthesis very laborious, and possibly frustrating.[40,41] One root cause of the difficulty stems from common nucleophiles and synthetic reagents RLi or RMgX that can break weak carbon-antimony bonds.[42,43] This causes issues when multi-step syntheses are required to make multidentate Sb ligands.

Other routes in multidentate antimony synthesis are the use of Grignard reagents, lithium reagents, or heteroatoms to stabilize the reaction. Grignard chemistry is possible, but the overall synthesis of a multidentate ligand using this approach requires a stepwise addition of antimony centers. As Sb-C bonds are quite weak, the presence of a strong reactant such as activated magnesium or lithium can cleave that bond.[44,45] Lithium metal can replace sodium in the previously mentioned nucleophile reactions, but similar issues apply to Li-based reactions.[46] RLi reagents, however, ($^{n}$BuLi, $^{t}$BuLi) offer a more promising route.[35,47] The lithiation of an aryl halide followed by the addition of $SbR_2X$ allows antimony to behave as an electrophile. Levason et. al. concluded that reactions in which Sb behaves as an electrophile are nearly four times higher yielding than reactions in which antimony is the nucleophile (~20% vs ~80%).[38,45,48] As with the Grignard reactions, however, RLi reagents can cleave susceptible Sb-C bonds; careful considerations are advised. Reid et. al. reported great success using $^{n}$BuLi to synthesize bidentate antimony compounds, and a thorough understanding of their research is required reading for this field.[35,36,38,46,49–54] Heteroatoms (N, S, P, etc.) have become popular recently to stabilize the reaction intermediates (and final products) during multidentate antimony syntheses.[36,53] These can serve as useful tools, but for this project are undesirable as we are looking for

the effects of solely antimony or bismuth on transition metal centers. The presence of a heteroatom could lead to questions on the effect antimony has in the metal complex. However, a cleverly designed system or a synthetic analogue for comparison could lend for an easier synthesis and very interesting results on the magnetic, catalytic, and spectroscopic properties of the final metallated complex.

### 1.4 Antimony-Metal Complexes

Antimony-metal compounds are possible to synthesize, however the successful synthesis hinges on the identity of the antimony ligand. Triphenylantimony is the only ligand that is commercially available and is typically the first choice for chemists looking to investigate organometallic antimony chemistry. However, triphenylantimony is a poor ligand, as the phenyl groups are electron withdrawing, which removes electron density on the Sb center that is already plagued by soft diffuse orbitals.[49,55] Additionally, heavy pnictogen donors suffer from higher *s* character in the lone pair, which has less directional properties and is less available for binding. Thus, $SbPh_3$ can readily bind to 4*d*/5*d* metals or low valent 3*d* metals due to soft-soft interactions and the increased basicity on the metal center.[56,57] However, this project is interested in working with higher valent (I/II/III) 3*d* metals, which renders triphenylantimony generally not useful. By manipulating the electronic effects of the antimony center through the inclusion of more electron donating ligands (i.e. alkyl-based Sb ligands), we have uniformly demonstrated that the antimony ligands then can bind to higher-valent later-row 3*d* transition metals. Additionally, the use of bidentate ligands can greatly increase the binding strength of the antimony ligand via the chelate effect. The following paragraphs will 1) give a brief synopsis of existing 3*d* transition metal complexes with both monodentate and polydentate antimony ligands, 2)

inform the reader of existing complexes with alkyl-based Sb ligands, and 3) provide useful advice for the successful syntheses of antimony metal complexes.

### 1.4.1 Monodentate Sb-Metal complexes

Many metal-antimony complexes exist with metal carbonyls and they range across the *d*-block (M = Mo, W, Mn, Fe, Ru, Re, Ni etc.).[28,42,49] This is due to the low valency on the metal center as well as the π-backbonding from the CO ligands that makes the metal center more basic and willing to accept antimony ligands, even the weak $SbPh_3$.[58] Among specifically the 3*d* metals, there are a few structures from group 3-5 transition metals, however more structures exist with metals from groups 6-8.[56,59] Mostly, they consist of a low valent metal center ($M^0$, M = Cr, Mn) and are complexed with $SbPh_3$ or $SbMe_3$ (which is also quite weak, air sensitive, pyrophoric, and toxic). Iron-antimony complexes do exist, however they also contain an electron-rich iron center ($Fe^{0/2-}$) in both monometallic and cluster forms.[60,61] It is noted that many more complexes exist with both Ru and Os metal centers (as follows with most other transition metal groups).[62–64]

Cobalt presents a more intriguing case as some higher valent Co-Sb complexes exist ($Co^{II/III}$) in addition to the previously mentioned cobalt carbonyl compounds.[65] The synthetically most interesting compounds are tetrahedral $Co(I)_3(SbPh_3)$ and trigonal bipyramidal $Co(I)_3(SbPh_3)_2$.[66,67] Co(II) species have also been prepared, yet no halide bound X-Co-Sb complexes are found in the CCDC. Although there are several reports of low valent nickel antimony dimers and clusters, very few (three) nickel(II) antimony complexes exist with associated crystal structures.[38,68,69] More information on these compounds can be found in Chapter 2. Among previously published compounds, copper-antimony complexes using monodentate ligands are monomeric or dimeric compounds.[70,71]

Each of these compounds were synthesized with triphenylantimony or a slight variation (Sb(para-fluorophenyl)$_3$) and started with a Cu(I) precursor. Lastly, there are no non-cluster Zn-Sb metal complexes synthesized with monodentate antimony ligands.[72]

### 1.4.2 Multidentate Sb-Metal complexes

Among multidentate antimony ligands, bidentate ligands are more common, due to their more facile syntheses. Consequently, there are more multidentate $L_{Sb}$-3*d* transition metal complexes with bidentate ligands than tri- or polydentate Sb ligands, of which there are very few.[36,73] Multidentate antimony ligands are more preferential due to the aforementioned chelate effect affording increased binding affinity to higher valent metals, an increase in covalency between the metal and ligand, and overall stability in the complex when it comes to post-synthetic reactivity or modulations.

Although multidentate ligands should allow for increased binding to higher valent metals, most 3*d* transition metal complexes with such ligands still consist of low valent metal centers, mostly metal carbonyls. Indeed, multidentate Sb ligands have been complexed with metal carbonyls of Cr, Mn, Fe, Co, and Ni.[73–76] Additionally, Cu(I) complexes with multidentate antimony ligands have been published in the literature, in both monomeric and dimeric forms.[50,77] There are very few high valent 3*d* metals complexed with a multidentate Sb ligand. One group of complexes was synthesized with Co(III) and had the general form $[CoX_2\{o\text{-}C_6H_4(SbR_2)_2]^+$ (R = Me, Ph).[50] Additionally, two bidentate ligands, *o*-$C_6H_4(CH_2SbR_2)_2$ (R = Me, Ph), were metallated with $NiI_2$ to give the resulting trigonal bipyramidal complex.[50]

Very few tridentate antimony ligands have been synthesized, with the two most notable compounds being the tripodal compound, $Me(CH_2SbPh_2)_3$, and the heteroatomic

compound, $N(CH_2\text{-}2\text{-}C_6H_4SbMe_2)_3$.[36,73] Although interesting ligands, both were merely complexed with relatively common metals, including metal carbonyls (M = Cr, Mo, W, Mn, Fe) and Cu(I) salts. However, these ligands may still have been restricted to soft metals, as the authors of the $Me(CH_2SbPh_2)_3$ manuscript did report the unsuccessful complexation of their ligand with Co(II) and Ni(II) ions.[73]

### 1.5 Metal Complexes with Alkyl-Based Sb Ligands

As previously mentioned, and described above, most existing metal complexes with antimony ligands (whether mono- or multidentate) revolve around the $SbPh_x$ donor adduct, which substantially lowers binding strength and affinity towards higher valent metal centers.[49,78] A concerted effort towards alkyl-based antimony ligands could ameliorate those weaknesses and thus an investigation of the previously synthesized metal complexes with alkyl-based antimony ligands is valuable.

The vast majority of alkyl-based Sb ligands that form complexes with 3*d* transition metals are methyl based, either $SbMe_3$ or $SbMe_2Ph$.[53,79–81] This is likely due to the ease of synthesis when compared to bulkier alkyl R-groups, however metal complexes do also exist with $Sb^iPr_3$ and $Sb^tBu_3$.[82–84] No monodentate heteroleptic ligands (other than $SbMe_2Ph$) have been complexed with 3*d* transition metals. Although it would be expected that alkyl-based ligands would have a greater affinity for higher valent metals, the only two reported alkyl based Sb-3d metal complexes at a higher oxidation state (II/III) are the two previously mentioned, $[CoX_2\{o\text{-}C_6H_4(SbMe_2)_2\}]^+$ and $[NiI\{o\text{-}C_6H_4(CH_2SbMe_2)_2\}]^+$.[50,65] Each other 3*d* metal complex synthesized with $SbR_x$ ligands (R = alkyl) consists of low valent metals, mostly carbonyl compounds of Fe, Cr, Co, or Ni.[85,86] The only possible explanation for the lack of higher valent compounds in the literature is the presumed belief

held by previous researchers that antimony cannot bind to higher valent metals, due to the softness and diffuse orbitals of the ligands. However, the work in this dissertation has proven antimony will bind to higher valent "hard" metals, and this dissertation will show that is not only possible, but quite facile to engineer a ligand design that facilitates antimony ligation to all types of electron deficient 3*d* transition metals.

In summary, very few 3*d* metal-antimony complexes synthesized with higher valent (I-III) metal centers or non-$SbPh_3$ based ligands are reported in the literature. Thus, there is a rich vein of chemistry to be investigated on both the metal and ligand fronts. If antimony ligands were to become more ubiquitous in industries (such as catalysis or materials synthesis), it is important to delve into their properties and reactivity with an entire row of transition metals.

### 1.6 C-H Activation Catalysts and Spin-Orbit-Coupling

One of the most important and challenging reactions in modern chemistry is carbon-hydrogen activation. Current C-H activation catalysts that are employed in both industrial and academic settings consist of heavy transition metals, such as platinum, iridium, or osmium.[87–89] Although these catalysts are quite effective, they are composed of materials that are expensive and scarce.[90] Scarcity of precious resources is a major problem and one of higher concern than price for most chemical industries. China, who owns nearly 90% of the world's rare metals deposits, estimates its platinum deposits will be fully mined in 15 years and its indium mines in 10 years.[91,92] Metal costs and scarcity are also issues where large-scale C-H activation reactions are performed. For example, in the pharmaceutical or chemical feed-stocks industries, catalysts synthesized with less expensive starting materials could drive down costs. There also exist critical industrial

problems that could be solved by large-scale C-H activation catalysis. Methane flares plague the petroleum industry, costing companies nearly 100 billion dollars per year in lost profits.[93] Additionally, both methane and $CO_2$ are potent greenhouse gases that could be mitigated if these flares were decreased or eliminated.[94] It may not be economically viable for petroleum companies to invest billions of dollars into expensive C-H activation catalysts to curb methane flares (via in situ conversion to methanol), but catalysts that cost several orders of magnitude less (and that are more plentiful) could be quite appealing.

In order to design new C-H activation catalysts with less expensive and rare elements, it is important to identify the core properties of said catalysts that make them so effective. First, the heavier 4*d*/5*d* metals can access a wide range of stable oxidation states – critical for performing catalytic steps such as oxidative addition or group transfer.[95,96] Second, they have a "soft nature" (from hard/soft theory), due to their diffuse *d*-orbitals and high *d*-electron count.[97] This allows the catalyst to form stronger covalent bonds with substrates as well as enabling π back donation to occur. Lastly, heavy elements possess a large extent of spin-orbit-coupling, which has not been well studied for its role in catalysis. Theoretical investigations into this phenomenon have revealed that it can play a major part in enhancing catalysis, especially C-H activation catalysis.[98] In one particularly pertinent report, the isostructural complexes of general structure M(Cp)(CO) (M = Co, Rh, Ir) were both experimentally and theoretically investigated for their C-H activation capabilities. It was found that while the rhodium and iridium complexes were quite proficient in the C-H bond activation of methane, the cobalt version of the complex was entirely inert.[99–101] A theoretical investigation of the cobalt complex revealed a critical reason for its failure to perform catalysis: the triplet ground state of the starting complex.[102] The methane inserted complex is a singlet state, which requires a spin-orbit-induced spin-crossing for the C-H

activation reaction to occur.[103,104] As the cobalt complex lacks an appreciable amount of spin-orbit-coupling, that spin-crossing is highly unfavorable, especially when compared to the large amount of energy required to access that crossing point – again due to the triplet-singlet misalignment.[102,105] Thus, if the cobalt were to attain a larger degree of spin-orbit-coupling at the metal center, perhaps the spin-crossing step would be more favorable, and a reaction would occur.

Spin-orbit-coupling (SOC) is a relativistic effect most often observed among luminescent or magnetic complexes. SOC arises from the interaction of a particle's spin angular momentum (S) with its orbital angular momentum (L), leading to a final total angular momentum, J.[106] It can also be thought of as the co-influence that both the spin and orbital angular momenta induced magnetic dipoles have on each other.[107] From a mathematical approach, the total SOC in a system is proportional to L·S, where $L = \sum_i l_i$ and $S = \sum_i s_i$ ($i$ = # of unpaired electrons).[106] SOC is mostly important (large) when dealing with heavier elements, as the larger the nuclear charge on the nucleus, the stronger the orbital angular momentum on said nucleus couples with the magnetic fields generated by the spins of the electrons surrounding the nucleus. As SOC scales with increasing atomic number, most elements have a denoted spin-orbit-coupling constant that can range from relatively small values (~500 $cm^{-1}$, $Fe^{2+}$) to quite large (~5000 $cm^{-1}$, $Os^{2+}$).[108]

SOC has consequences in multiple areas of chemistry, including magnetochemistry, luminescence, and orbital splitting energies.[109–111] Spin-orbit-coupling can increase the magnetic properties of complexes due to altering the spin Hamiltonian and the classic L and S quantum numbers involved.[112] Additionally, high SOC can enhance the magnetic anisotropy in the molecule, which is an important parameter for the field of single-molecule-magnets (SMMs).[113] SOC will also increase the probability of spin

crossover (i.e. singlet > triplet transfer), as well as improve triplet state lifetimes, in excited states (depending on the ground state structure).[114] Consequently, SOC is an important factor in luminescence chemistry and can red-shift emission wavelengths via the heavy atom effect.[115] Spin-orbit-coupling can also lift the degeneracy of frontier orbitals when unpaired electrons are present.

When $J \neq L$, J assumes a half-integer value, and in those systems, the rotation necessary to complete the identity operation is doubled from $2\pi$ (in systems without unpaired electrons, u.p.e., and when J is an integer value) to the non-physical operation of $4\pi$.[116] This doubling operation has a similar effect on the number of symmetry elements present in the character table for a given point group – it doubles the number of elements and increases the number of irreducible representations present; this yields a new "double group". The effect of the doubling operator on the irreducible representations of the original group is the origin of the lifted orbital energy degeneracy in d-orbital splitting. The original irreducible representations are "doubled" by the doubling operator, leading to multiple-fold degeneracy that is not typically observed in d-orbital splittings with minimal SOC. For example, consider the case of an octahedral $d^1$ system. The two assumed ground and excited states are labelled as $^2T_g$ (three-fold degenerate) and $^2E_g$ (two-fold degenerate), respectively. When the doubling operator is applied, those degeneracies are each doubled: a four-fold degeneracy from $^2E$ and a six-fold degeneracy from $^2T$ are expected. The four-fold degeneracy is denoted as $^2G$, while the six-fold degeneracy is further lifted by SOC to yield a two-fold ($^2E$) and a four-fold ($^2G$) state. In systems with a large degree of SOC, this final splitting can be increased to quite substantial values. The biggest difference between energy splitting diagrams of a complex with low SOC versus one with high SOC is primarily the increased splitting of the J-states. These highly split J-states are more

delineated and discrete than their lesser split counterparts. When the J-states are too close to each other (i.e. in the low-SOC complex), they both can be easily thermally populated, which renders the splitting fairly meaningless, and the initial ground state assignment of $^2$T should be used. However, if the splitting is large and the $^2$G and $^2$E states are discrete, then these states can supplant the initial ground state assignment of $^2$T. The effect of this denomination will be further described in the following chapter. A summary diagram of these phenomena can be seen in Figure 1.3.

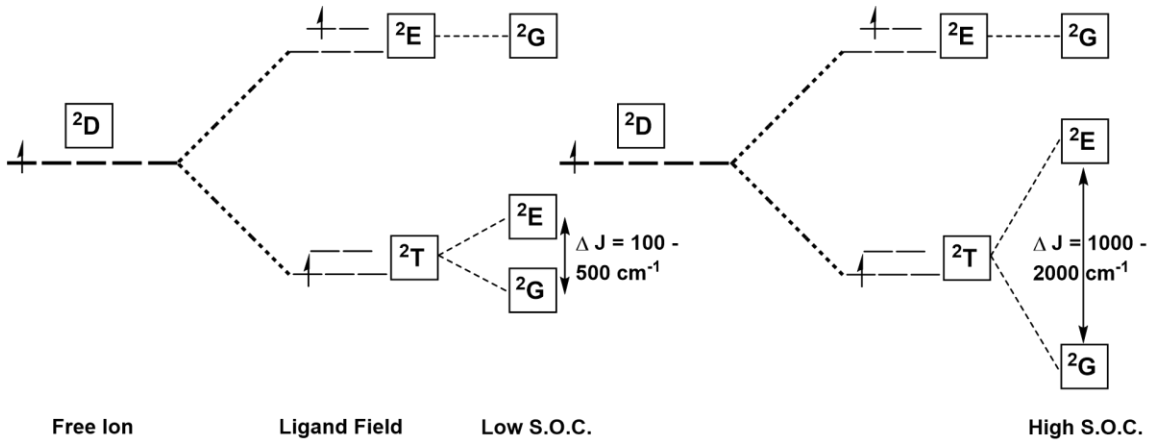


**Figure 1.3** Effect of spin-orbit-coupling on the ground and excited state degenerate orbitals of a hypothetical octahedral $d^1$ system.

Returning to catalytic systems, a large degree of SOC could enhance the catalytic potential due to the mixing of ground and excited states that are caused by the doubling operator. Once the orbital degeneracies are lifted and split by the double group, the ground and excited states could begin to have the same symmetry labels. This could remove spin-forbidden reactions that thwart catalysis.[117,118] Similarly, the increased splitting of orbital energies in systems with high SOC could encourage more mixing between the ground and

excited states. This mixing enhances the probability of ground to excited state communication which could lead to increased reactivity and lowered activation energy barriers.[119]

In conclusion, there does appear to be a connection between SOC and C-H activation, and an investigation to experimentally probe this connection is worthwhile. If a paramagnetic 3*d* metal complex could obtain a higher degree of spin-orbit-coupling than typical for that metal, perhaps it would show an improvement in C-H activation reactivity.

### 1.7 Translational Spin-Orbit-Coupling through Heavy Atom Ligation

It is possible to increase the amount of SOC at a metal center through a phenomenon known as translational spin-orbit-coupling.[120,121] Translational SOC involves either the direct bonding or simple nearby placement of heavy atoms to a metal. The metal will then accrue some of the spin-orbit-coupling character from those heavy atoms and consequently display a larger extent and effectiveness of SOC when compared to analogous complexes synthesized using lighter atoms. Translational SOC was first theorized by Mabbs and Collison,[122] who proposed the following equation to determine the overall SOC in an octahedral system:

$$\sum_{a.e.}\sum_{a.a.}\xi(n,l)L\cdot S=\sum_{a.e.}\xi(n,d)L\cdot S+\sum_{a.e.}\sum_{i=1}^{6}\xi(n,l)(i)L(i)\cdot S(i)$$

*a.e. = all electrons, a.a. = all atoms; i = 1-6 for 6 ligands in $O_h$*

From the equation, each atom in the molecule contributes towards the total SOC in a system. It was also concluded that in order for ligand contributions to be significant, the metal-ligand bond must be highly covalent.[122] Although theoretically translational SOC

should be possible, it has also experimentally been shown that heavy atoms do alter the magnetic properties of complexes. Cotton was one of the first to comment on this phenomenon, as he observed a higher magnetic moment for $[CoI_4]^{2-}$ ($\mu_{eff}$ = 4.8 BM) versus $[CoCl_4]^{2-}$ ($\mu_{eff}$ = 4.6 BM) and proposed it could be due to the spin-orbit-coupling effects of the different halides.[123] More recently, Long and Dunbar independently reported an increased amount of axial zero-field-splitting in cobalt(II) complexes ligated with heavy chalcogenides and pnictogens (but only extending their series to Se and As, respectively; the latter likely due to synthetic difficulties with Sb).[124,125] Both contributed these findings to the spin-orbit-coupling in the heavy atoms, as the axial zero-field-splitting is closely related to spin-orbit-coupling through the crystal-field Hamiltonian.[112]

The connection of spin-orbit-coupling to the axial zero-field-splitting and both of their relationships to the crystal-field Hamiltonian must be elaborated further. First, zero-field-splitting (ZFS) is defined as the lifting of degenerate energy levels with the presence of at least one unpaired election, but without the presence of a magnetic field. It is akin to the Zeeman effect, but the Zeeman effect is applicable only with the presence of a magnetic field. Several factors can contribute to ZFS in a complex, but the two main factors are distortion away from ideal geometry (e.g. Jahn-Teller effect) and spin-orbit-coupling.[106] Figure 1.4 is a pictorial description of ZFS, editorialized from Molecular Magnetism by Kahn, showing that both contributions to ZFS are communal and additive.[106] There have been many separate instances of authors contributing an increase in the axial magnetic anisotropy, *D*, to the enhanced spin-orbit-coupling in the system, whether through the addition of a heavy metal (e.g. Mo), or via their ligand donor atoms.[125,126]

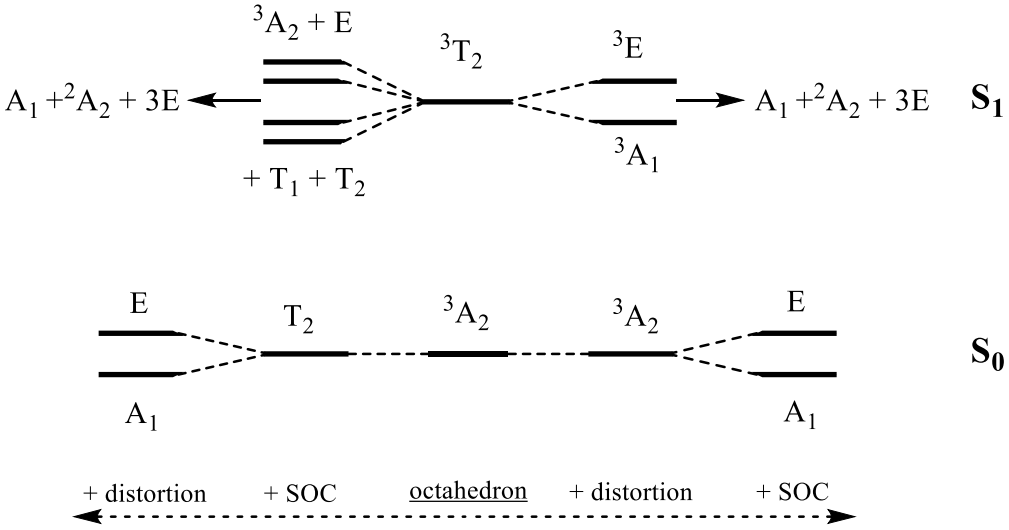


**Figure 1.4** Description of the effects of geometric distortion and spin-orbit-coupling on overall zero-field-splitting of the ground and first excited spin triplet state. In this example, the complex is a Ni(II) ion in a trigonally distorted octahedral surrounding.

Other authors corroborate Kahn's assertion that SOC and ZFS are connected. In Methods of Molecular Quantum Mechanics, Magnasco seeks to mathematically derive the origin of ZFS when he writes, "In fact, it is a challenge to understand the physical origin of the ZFSs in transition metal complexes. If one starts from spin-free wave functions and introduces relativistic effects up to second order, the ZFS consists of two contributions: a) the direct electron-electron spin-spin coupling (SSC) and b) the spin-orbit coupling to second order in perturbation theory … ZFS of transition metal complexes are usually dominated by the second-order SOC term."[127] Experimentally, ZFS has also been correlated with SOC and an increase in one begets an increase in the other. *For reference: zero-field-splitting is often broken up into two pertinent parameters: axial ZFS and transversal ZFS. The axial zero-field-splitting is denoted as D, while the transversal ZFS is denoted as E.* In a 2013 report, Long writes, "The magnitude of *D* is determined by two

factors: it is inversely proportional to the energy separation between the electronic ground state and the anisotropic excited states contributing to *D*, and it is proportional to the square of the effective spin-orbit coupling constant, ζ, for the spin center."[124] These claims are echoed by other authors studying similar magnetic systems.[128,129] From both a theoretical and an experimental viewpoint, one can definitively state that axial ZFS correlates to SOC.

The best way to quantify axial ZFS is by utilizing the close relation between the zero-field-splitting Hamiltonian of EPR and the crystal-field-splitting (CFS) Hamiltonian that is a core part of the full spin Hamiltonian used to fit magnetic susceptibility data.[112] For a full in-depth tutorial on the spin Hamiltonian, solving it, and the math behind everything, it is *highly recommended* to visit http://www.nfchilton.com/phi.html and download the tutorial file at the bottom of the page. A brief summary of this tutorial that affords a method to quantify *D* from susceptibility data can be seen in Chapter 4.

Thus, following the theoretical and experimental background research, a series of guidelines can be proposed that should be followed to maximize the extent of translational SOC – the NIC guidelines:

**N** = number of heavy atoms ligated

**I** = identity of the heavy atoms

**C** = covalency between the heavy donor atoms and the metal center

Following these guidelines, the goal of this project is to synthesize metal complexes with multiple ligands originating from heavy donor atoms. To increase the covalency of the metal-ligand bond, the ligands can be modulated with σ-donating or π-accepting substituents, or multidentate ligands can be used to invoke the chelate effect. Once the complexes are synthesized, they would be tested for their magnetic properties and C-H activation capabilities; however, it is notable that any appreciable amount of SOC

translated to the metal center would be an interesting result. This, in principle, can be deduced through SQUID, EPR, and XPS measurements. In order minimize catalyst cost and to work with more earth-abundant materials, we will use 3*d* metals as opposed to 4*d*/5*d* transition metals, which already have a large degree of SOC and have been shown to be effective C-H activation catalysts.[88,108] A graphical summary of the proposed complex and its relation to the canonical C-H activation catalyst can be seen in Figure 1.5.

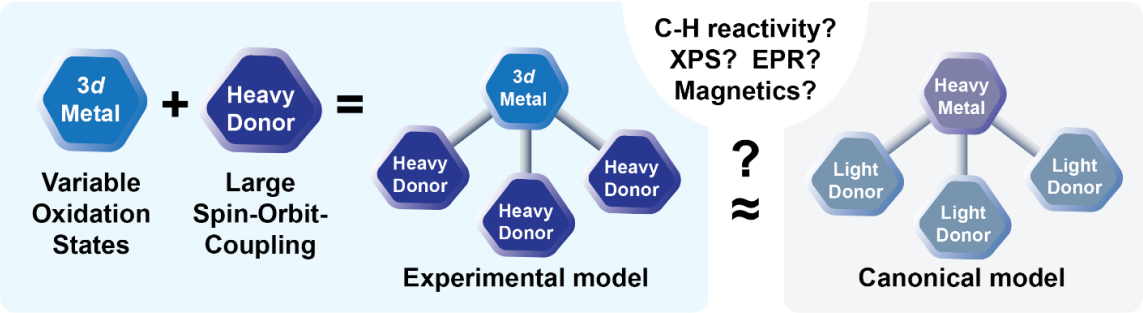


**Figure 1.5** Graphical Summary of a proposed experimental model complex compared to the canonical complex used in C-H activation catalysis.

### 1.8 Antimony Ligands towards Translational SOC and Other Avenues Worth Exploring for Sb-Metal Complexes

In this project, the heavy donor ligands that we've selected are oragnoantimony ligands. As mentioned previously, antimony has a large amount of spin-orbit-coupling, with an elemental SOC constant ($\xi$) of nearly 5000 $cm^{-1}$.[22] This value is comparable to late 5*d* transition metal such as Pt (~5400 $cm^{-1}$) or Ir (~4400 $cm^{-1}$).[130] Additionally, as discussed previously, antimony is an acceptable ligand towards 3*d* metals as there is evidence of both mono- and multidentate antimony ligands being successfully synthesized and metallated with 3*d* transition metals. Although most antimony-metal complexes in the literature are

low valent, there are still some complexes with higher valent metal centers, especially among the late 3*d* transition metals (Co, Ni) which are more intriguing as C-H activation catalysts. Additionally, the manipulation of antimony ligands to add electron density by exchanging phenyl groups for alkyl groups could increase the metal binding affinity of newly synthesized antimony ligands. With a healthy, but not oversaturated, amount of synthetic background material, we can design both mono- and multidentate antimony ligands that can successfully ligate to late open-shell 3*d* transition metals for enhanced translational spin-orbit-coupling. These complexes will hopefully serve as an effective C-H activation catalyst synthesized with inexpensive and ubiquitous materials.

Although the goal of this research is to synthesize a paramagnetic metal complex with enhanced spin-orbit-coupling for a potential C-H activation catalyst, antimony-metal complexes can have other useful applications due to the diverse chemical properties of antimony. As mentioned in previous sections, antimony is an excellent Lewis acid and can readily abstract even weakly coordinating anions from solution. Additionally, metal complexes with antimony are intriguing for their luminescent properties due to the 'heavy atom effect' which can red-shift emission wavelengths and lengthen triplet lifetimes. Finally, the weakly coordinated Sb-M bonds can be leveraged if the correct experiment is designed – namely metal complex decomposition and subsequent deposition onto desirable substrates. As antimony ligands and corresponding 3*d* metal complexes have not been well studied in general, any newly synthesized compound is worth investigating further, especially if analogous compounds with lighter pnictogens (and their properties) have already been reported.

## 1.9 REFERENCES


(1) Weeks, M. E.; Leicester, H. M. Antimony. In *Discovery of the Elements*; Journal of Chemical Education: Easton, PA, 1968; pp 95–103.

(2) Cheyne, T. K.; Black, J. S. Kerenhappuch. *Encyclopaedia Biblica*; Macmillan Co., 1902; p 2659.

(3) Jagnaux, R. *Histoire de La Chimie*, 2nd ed.; Baudry et Cie: Paris, 1891.

(4) Bostock, J.; Riley, H. T. *The Natural History of Pliny*; Geo. Bell and Sons: London, 1856.

(5) Krebs, R. E. *The History and Use of Our Earth's Chemical Elements*; Greenwood Press: Westport, CT, 1998.

(6) Dufrenoy, M. L.; Dufrenoy, J. The Significance of Antimony in The History of Chemistry. *J. Chem. Educ.* **1950**, *27*, 595–597.

(7) Berthelot, M. Sur Quelques Alliages Connus Au Moyen-Age. *Ann. Chem. Phys.* **1893**, *30*, 286.

(8) Winderlich, R. History of the Chemical Sign Language. *J. Chem. Educ.* **1953**, *30*, 58–62.

(9) Holmyard, E. J. *Alchemy*; Courier Corportation: Chelmsford, MA, 1990.

(10) Agricola, G. *De Re Metallica*; Hoover, H. C., Hoover, L. H., Eds.; Dover Publications: New York, 1950.

(11) Valentine, B.; Tholde, J. *Triumphal Chariot of Antimony*; Kirkringus, T., 1678.

(12) Lemery, N. *Traite de l'antimonie*; Paris, 1707.

(13) de Fontanelle, B. L. B. Eloge de M. Nicolas Lemery. In *Historie de l'Academie Royale des Sciences de Paris*; Paris, 1715; pp 73–81.

(14) Cap, P.-A. *Nicolas Lemery, Chimiste*; Imprimerie et Fonderie de Fain: Paris, 1839.

(15) Butterman, W. C.; Carlin, J. F. *Antimony Commodity Profile, U.S. Geological Survey*; 2004.

(16) Carapella, S. .; Hampel, C. Antimony. *The Encyclopedia of the Chemical Elements*; Reinhold Book Corporation, 1968; pp 22–25.

(17) Partheil, A.; Mannheim, E. Mercury Antimonide and Stibonium Compounds. *Arch. Pharm. (Weinheim).* **1900**, *238*, 166–184.

(18) Wieber, M. *Sb Organoantimony Compounds*; Mirbach, M., Ed.; Springer Science and Business Media: Berlin, Germany.

(19) Gruttner, G.; Wiernik, M. Organic Antimony Compounds. II. Preparation of Mixed Alkylarylstibines. *Berichte der Dtsch. Chem. Gesselschaft* **1915**, *48*, 1759–1764.

(20) Breunig, H. J.; Rösler, R. Organoantimony Compounds with Element—element Bonds. *Coord. Chem. Rev.* **1997**, *163*, 33–53.

(21) Breunig, H. J.; Rösler, R. New Developments in the Chemistry of Organoantimony and -Bismuth Rings. *Chem. Soc. Rev.* **2000**, *29*, 403–410.

(22) Dunn, T. M. Spin-Orbit-Coupling in the First and Second Transition Series. *Trans. Faraday Soc.* **1961**, *48*, 1441–1444.

(23) Koziar, J. C.; Cowan, D. O. Photochemical Heavy-Atom Effects. *Acc. Chem. Res.* **1978**, *11*, 334–341.

(24) *IUPAC. Comendium of Chemical Technology, 2nd Ed. (the "Gold Book").*; McNaught, A. D., Wilkinson, A., Eds.; Blackwell Scientific Publications: Oxford, 1997.

(25) Jones, J. S.; Wade, C. R.; Gabbaï, F. P. Guilty on Two Counts: Stepwise Coordination of Two Fluoride Anions to the Antimony Atom of a Noninnocent Stibine Ligand. *Organometallics* **2015**, *34*, 2647–2654.

(26) Dittes, U.; Vogel, E.; Keppler, B. K. Overview on Bismuth(III) and Bismuth(V) Complexes with Activity against Helicobacter Pylori. *Coord. Chem. Rev.* **1997**, *163*, 345–364.

(27) Wilkinson, G.; Stephenson, T. A.; Hallman, P. S. Tetrakis(Triphenylphosphine)Dichlororuthenium(II) and Tris(Triphenylphosphine)Dichlororuthenium(II). In *Inorganic Syntheses*; McGraw-Hill: New York, NY, 1970; pp 237–240.

(28) Champness, N. R.; Levason, W. Coordination Chemistry of Stibine and Bismuthine Ligands. *Coord. Chem. Rev.* **1994**, *133*, 115–217.

(29) Schwab, P.; Mahr, N.; Wolf, J.; Werner, H. Trialkylstibanes as Bridging Ligands: Synthesis and Structure of the Dinuclear Complexes $[Rh_2Cl_2(\mu\text{-}Sb^iPr_3)(\mu\text{-}CR_2)_2]$. *Angew. Chemie Int. Ed. English* **1994**, *33*, 97–99.

(30) Martin, L. R.; Einstein, F. W. B.; Pomeroy, R. K. Axial-Equatorial Isomerism in the Complexes $M(CO)_4(L)$ (M = Fe, Ru, Os; L = Group 15 Ligand). Crystal Structures of Ax-$Ru(CO)_4(AsPh_3)$, Ax-$Ru(CO)_4(SbMe_3)$, and Eq-$Os(CO)_4(SbPh_3)$. *Inorg. Chem.* **1985**, *24*, 2777–2785.

(31) Breunig, H. J.; Kanig, W. Preparation and Spectroscopic Studies of Methyl and Isopropyl Halides. *Phosphorus Sulfur Relat. Elem.* **1982**, *12*, 149–159.

(32) Wieber, M.; Wirth, D.; Fetzer, I. New Synthesis Methods for Organohalostibines. *Z. Anorg. Allg. Chem.* **1983**, *505*, 134–137.

(33) Wieber, M.; Gmelin, L. *Organoantimony Compounds Pt 1*, 8th ed.; Springer-Verlag: New York, 1981.

(34) Balzs, G.; Balzs, L.; Breunig, H. J.; Lork, E. Syntheses and Structures of $Me_3Sb^+CH_2COO^- \cdot H_2O$, the Monohydrate of the Antimony Analogue of Betaine, and Related Compounds. *Appl. Organomet. Chem.* **2002**, *16*, 155–159.

(35) Jura, M.; Levason, W.; Reid, G.; Webster, M. Preparation and Properties of Cyclic and Open-Chain Sb/N-Donor Ligands. *J. Chem. Soc. Dalt. Trans.* **2009**, No. 37, 7811–7819.

(36) Benjamin, S. L.; Levason, W.; Reid, G. Synthesis and Reactions of a Hybrid Tristibine Ligand. *Organometallics* **2013**, *32*, 2760–2767.

(37) Schwarzenbach, G. Der Chelateffekt. *Helv. Chim. Acta* **1952**, *35*, 2344–2359.

(38) Levason, W.; Matthews, M. L.; Reid, G.; Webster, M. Synthesis and Properties of New Ditertiary Stibines Based upon *o*-, *m*- or *p*-Xylyl and *m*- or *p*-Phenylene Backbones and Their Complexes with Tungsten, Iron and Nickel Carbonyls. *J. Chem. Soc. Dalt. Trans.* **2004**, *4*, 51–58.

(39) Shewchuk, E.; Wild, S. B. Organostibines as Ligands. Synthesis of Dimethyl(Alpha-Picolyl)Stibine, Dimethyl(8-Quinolyl)Stibine, and (R;S)-Methylphenyl(8-Quinolyl)Stibine and Some Transition Metal Derivatives. *J. Organomet. Chem.* **1981**, *210*, 181–191.

(40) Champness, N. R.; Levason, W. Coordination Chemistry of Stibine and Bismuthine Ligands. *Coord. Chem. Rev.* **1994**, *133*, 115–217.

(41) Shewchuk, E.; Wild, S. B. Synthesis of *o*-Phenylenebis(Dimethylstibine) and Some Derivatives of Divalent Nickel, Palladium, and Platinum and of Zerovalent Chromium, Molybdenum, and Tungsten. *J. Organomet. Chem.* **1977**, *128*, 115–129.

(42) Levason, W.; McAuliffe, C. A. Coordination Chemistry of Organostibines. *Acc. Chem. Res.* **1978**, *11*, 363–368.

(43) Meinema, H. A.; Martens, H. F.; Noltes, J. G. Investigations on Organoantimony Compounds: XV. The Synthesis of Heterocyclic Antimony Compounds via Thermolysis of α,ω-Bis(Dimethylstibino)Alkanes. A New Route to the Synthesis of 1-Methylstibacycloalkanes. *J. Organomet. Chem.* **1976**, *110*, 183–193.

(44) Levason, W.; McAuliffe, C. A.; Murray, S. G. Bidentate Group VB Chelates: XVI. The Preparation of *o*-Phenylenebis(Diphenylstibine) and Attempts to Prepare Cis- and Trans-1,2-Bis(Diphenylstibino)Ethylene. *J. Organomet. Chem.* **1975**, *88*, 171–174.

(45) Levason, W.; Smith, K. G.; McAuliffe, C. A.; McCullough, F. P.; Sedgwick, R. D.; Murray, S. G. Synthesis and Properties of Group 5B Ligand Analogues of *o*-Phenylenebis(Dimethylarsine), *o*-$C_6H_4(EMe_2)(E'Me_2)$ Where E, E′= P, N, As, or Sb. *J. Chem. Soc. Dalt. Trans.* **1979**, No. 11, 1718–1724.

(46) Jura, M.; Levason, W.; Reid, G.; Webster, M. Preparation and Properties of Sterically Demanding and Chiral Distibine Ligands. *J. Chem. Soc. Dalt. Trans.* **2008**, 5774–5782.

(47) *The Chemistry of Arsenic, Antimony, and Bismuth Compounds*; Patai, S., Ed.; John Wiley & Sons, Ltd: New York, 1994.

(48) Levason, W.; McAuliffe, C. A. *Phosphine, Arsine, and Stibine Complexes of the Transition Elements*; Elsevier: New York, 1979.

(49) Levason, W.; Reid, G. Developments in the Coordination Chemistry of Stibine Ligands. *Coord. Chem. Rev.* **2006**, *250*, 2565–2594.

(50) Levason, W.; Matthews, M. L.; Reid, G.; Webster, M. Synthesis and Characterisation of Transition Metal Halide Complexes of the Xylyl-Distibine, 1, 2-Bis(Dimethylstibanylmethyl) Benzene. *Dalt. Trans.* **2004**, 554–561.

(51) Benjamin, S. L.; Reid, G. Neutral Organoantimony(III) and Organobismuth(III) Ligands as Acceptors in Transition Metal Complexes - Role of Substituents and Co-Ligands. *Coord. Chem. Rev.* **2015**, *297–298*, 168–180.

(52) Benjamin, S. L.; Levason, W.; Reid, G.; Warr, R. P. Halostibines $SbMeX_2$ and $SbMe_2X$: Lewis Acids or Lewis Bases? *Organometallics* **2012**, *31*, 1025–1034.

(53) Benjamin, S. L.; Levason, W.; Reid, G.; Rogers, M. C. Hybrid Dibismuthines and Distibines as Ligands towards Transition Metal Carbonyls. *Dalt. Trans.* **2011**, *40*, 6565–6574.

(54) Brown, M. D.; Levason, W.; Reid, G.; Webster, M. Preparation, Properties and Structures of the First Series of Organometallic Pt(II) and Pt(IV) Complexes with Stibine Co-Ligands. *J. Chem. Soc. Dalt. Trans.* **2006**, *60*, 16671667–16741674.

(55) Orpen, A. G.; Connelly, N. G. Structural Systematics: The Role of P-A σ* Orbitals in Metal-Phosphorus π-Bonding in Redox-Related Pairs of $M\text{-}PA_3$ Complexes (A = R, Ar, OR; R = Alkyl). *Organometallics* **1990**, *9*, 1206–1210.

(56) Holmes, N. J.; Levason, W.; Webster, M. Triphenylstibine Substituted Manganese and Rhenium Carbonyls: Synthesis and Multinuclear NMR Spectroscopic Studies. X-Ray Crystal Structures of Ax-$[Mn_2(CO)_9(SbPh_3)]$, $[Mn(CO)_5(SbPh_3)][CF_3SO_3]$ and Fac-$[Re(CO)_3Cl(SbPh_3)_2]$. *J. Organomet. Chem.* **1998**, *568*, 213–223.

(57) Otto, S.; Roodt, A. Equilibrium, Solid State Behavior and Reactions of Four and Five Co-Ordinate Carbonyl Stibine Complexes of Rhodium. Crystal Structures of Trans-$[Rh(Cl)(CO)(SbPh_3)_2]$, Trans-$[Rh(Cl)(CO)(SbPh_3)_3]$ and Trans-$[Rh(I)_2(CH_3)(CO)(SbPh_3)_2]$. *Inorganica Chim. Acta* **2002**, *331*, 199–207.

(58) Bistoni, G.; Rampino, S.; Scafuri, N.; Ciancaleoni, G.; Zuccaccia, D.; Belpassi, L.; Tarantelli, F. How π Back-Donation Quantitatively Controls the CO Stretching

Response in Classical and Non-Classical Metal Carbonyl Complexes. *Chem. Sci.* **2016**, *7*, 1174–1184.

(59) Ishiguro, A.; Takahashi, M.; Takeda, M. $^{121}$Sb, $^{57}$Fe and $^{127}$I Mössbauer Spectroscopic Study on Antimony-Transition Metal Bond in Metal Carbonyl Derivatives of Tertiary Stibines. *J. Organomet. Chem.* **2000**, *611*, 558–565.

(60) Rheingold, A. L.; Fountain, M. E. Tetracarbonyl(Tri-Tert-Butylstibine)Iron, [$Fe(CO)_4${$Sb(C_4H_9)_3$}]. *Acta Crystallogr. Sect. C* **1985**, *41*, 1162–1164.

(61) Konchenko, S. N.; Virovets, A. V; Apenina, S. A.; Tkachev, S. V. Synthesis and Structure of the Cubane Type [$Fe_2Sb(CO)_5(H_5$-$C_5H_5)]_4$ Cluster. *Inorg. Chem. Commun.* **1999**, *2*, 555–557.

(62) Deng, M.; Leong, W. K. Novel Higher Nuclearity Osmium–antimony Clusters by Alkene- or Diene-Assisted Cluster Condensation. *J. Chem. Soc. Dalt. Trans.* **2002**, No. 6, 1020–1023.

(63) Li, Y.-Z.; Ganguly, R.; Leong, W. K.; Liu, Y. Synthesis and Reactivity of Ruthenium–Antimony Carbonyl Clusters. *Eur. J. Inorg. Chem.* **2015**, *2015*, 3861–3872.

(64) Becker, E.; Rüba, E.; Mereiter, K.; Schmid, R.; Kirchner, K. Facile Rearrangement of Metallacyclopentatrienes to Butadienyl Carbenes by a 1,2-Hydrogen Shift. *Organometallics* **2001**, *20*, 3851–3853.

(65) Jewiss, H. C.; Levason, W.; Spicer, M. D.; Webster, M. Coordination Chemistry of Higher Oxidation States. 25. Synthesis and Properties (Including Cobalt-59 NMR Spectra) of Cobalt(III) Complexes of Ligands Containing Two Tertiary Stibine Groups. Crystal Structure of Trans-[Co{*o*-$C_6H_4(SbMe_2)_2$}$_2Cl_2]_2$[$CoCl_4$]. *Inorg. Chem.* **1987**, *26*, 2102–2106.

(66) Godfrey, S. M.; Lane, H. P.; McAuliffe, C. A.; Pritchard, R. G. Inorganic Grignard Analogues. Reaction of Cobalt Powder with Triorganodiiodophosphorus Compounds to Form [$PR_3I$][$Co(PR_3)I_3$]. Crystal Structure of [$PPh_3I$][$Co(PPh_3)I_3$], and Isolation of the Novel Complexes [$PPh_3I$][$Co(PPh_3)IBr_2$] and [$SbPh_3I$][$Co(SbPh_3)I_3$]. *J. Chem. Soc. Dalt. Trans.* **1993**, No. 10, 1599–1604.

(67) Godfrey, S. M.; McAuliffe, C. A.; Pritchard, R. G. Extreme Symbiosis: The Facile One-Step Synthesis of the Paramagnetic Cobalt(III) Complex of Triphenylantimony, $CoI_3(SbPh_3)_2$, from the Reaction of Triphenylantimonydiiodine with Unactivated Coarse Grain Cobalt Metal Powder. *J. Chem. Soc. Chem. Commun.* **1994**, No. 1, 45–46.

(68) Jiménez-Tenorio, M.; Carmen Puerta, M.; Salcedo, I.; Valerga, P.; De Los Ríos, I.; Mereiter, K. Oligomerization of Styrenes Mediated by Cationic Allyl Nickel Complexes Containing Triphenylstibine or Triphenylarsine. *J. Chem. Soc. Dalt. Trans.* **2009**,10, 1842–1852.

(69) Jones, J. S.; Wade, C. R.; Gabbaï, F. P. Redox and Anion Exchange Chemistry of a Stibine-Nickel Complex: Writing the L-, X-, Z-Ligand Alphabet with a Single Element. *Angew. Chemie - Int. Ed.* **2014**, *53*, 8876–8879.

(70) Tsiatouras, V.; Banti, C. N.; Grześkiewicz, A. M.; Rossos, G.; Kourkoumelis, N.; Kubicki, M.; Hadjikakou, S. K. Structural, Photolysis and Biological Studies of Novel Mixed Metal Cu(I)-Sb(III) Mixed Ligand Complexes. *J. Photochem. Photobiol. B Biol.* **2016**, *163*, 261–268.

(71) Bowmaker, G. A.; Effendy; Hart, R. D.; Kildea, J. D.; White, A. H. Lewis-Base Adducts of Group 11 Metal(I) Compounds. LXXIII Synthesis, Spectroscopy and Structural Systematics of New 1 : 1 "Cubane" Tetramers of Copper(I) and Silver(I) Halides with Triphenylarsine. *Aust. J. Chem.* **1997**, *50*, 653–670.

(72) Thomas, F.; Schulz, S.; Nieger, M. Synthesis of Thermolabile Zinc–Pentel Compounds under Kinetically Controlled Reaction Conditions. *Angew. Chemie Int. Ed.* **2005**, *44*, 5668–5670.

(73) Chiffey, A. F.; Evans, J.; Levason, W.; Webster, M. Synthesis and Properties of the Transition Metal Complexes of a Tritertiary Stibine, 1,1,1-Tris((Diphenylstibino)Methyl)Ethane. Structure of Fac-$[Mo(CO)_3\{MeC(CH_2SbPh_2)_3\}]$. *Organometallics* **1996**, *15*, 1280–1283.

(74) Pope, S. J. A.; Reid, G. Phosphine, Arsine and Stibine Complexes of Manganese(I) Carbonyl Halides: Synthesis, Multinuclear NMR Spectroscopic Studies, Redox Properties and Crystal Structures. *J. Chem. Soc. Dalt. Trans.* **1999**, 1615–1621.

(75) Breunig, H. J.; Jönsson, M.; Rösler, R.; Lork, E. Tetracarbonylchrom-Komplexe Mit $Me_2SbESbMe_2$ (E=O, S) Und $MeSb(SSbMe_2)_2$ Als Liganden. *Zeitschrift für Anorg. und Allg. Chemie* **1999**, *625*, 2120–2124.

(76) Brown, M. D.; Levason, W.; Reid, G.; Webster, M. Preparation and Coordinating Properties of $\{CH_2(o\text{-}C_6H_4CH_2SbMe_2)\}_2$, a Novel Wide-Angle Cis-Chelating Distibine. *Dalt. Trans.* **2006**, No. 47, 5648–5654.

(77) Ke, I.-S.; Gabbaï, F. P. $Cu_3(M_2\text{-}Cl)_3$ and $Ag_3(M_2\text{-}Cl)_3$ Complexes Supported by Tetradentate Trisphosphino-Stibine and -Bismuthine Ligands: Structural Evidence for Triply Bridging Heavy Pnictines. *Aust. J. Chem.* **2013**, *66*, 1281–1287.

(78) Tolman, C. A. Electron Donor-Acceptor Properties of Phosphorus Ligands. Substituent Additivity. *J. Am. Chem. Soc.* **1970**, *92*, 2953–2956.

(79) Chan, K. H.; Leong, W. K.; Mak, K. H. G. Thermolysis of the Osmium−Antimony Clusters $Os_3(CO)_{11}(SbMe_2Ar)$: Higher Nuclearity Clusters and Arrested Ortho Metalation. *Organometallics* **2006**, *25*, 250–259.

(80) Miyamoto, T. K. Synthesis of Water-Soluble Platinum(II) Complexes Stabilized with Trimethylstibane. Stibane Transfer in Aqueous Solution. *Chem. Lett.* **1994**, *23*, 2031–2032.

(81) Hering, C.; Lehmann, M.; Schulz, A.; Villinger, A. Chlorine/Methyl Exchange Reactions in Silylated Aminostibanes: A New Route To Stibinostibonium Cations. *Inorg. Chem.* **2012**, *51*, 8212–8224.

(82) Schulz, S.; Kuczkowski, A.; Nieger, M. First Structural Characterization of Completely Alkyl-Substituted Al–Sb Lewis Acid–base Adducts. *J. Organomet. Chem.* **2000**, *604*, 202–207.

(83) Phadnis, P. P.; Jain, V. K.; Varghese, B. Preparation and Characterization of Tris(Iso-Propyl)Stibine Complexes of Palladium and Platinum. *Appl. Organomet. Chem.* **2002**, *16*, 61–64.

(84) Boddhula, R.; Ghosh, A.; Wölper, C.; Mobin, S. M.; Giri, S.; Chatterjee, S. Synthesis and Structure of Open and Closed Type Iron Telluride – Stibine Cluster Compounds. *J. Organomet. Chem.* **2017**, *851*, 22–29.

(85) Genge, A. R. J.; Holmes, N. J.; Levason, W.; Webster, M. Complexes of Distibinomethane Ligands: 3. Manganese and Rhenium Carbonyl Complexes. *Polyhedron* **1999**, *18*, 2673–2677.

(86) Lorenz, I.-P.; Rudolph, S.; Piotrowski, H.; Polborn, K. Reactions of $K_2[Fe(CO)_3(PPh_3)]$: Reductive Sb−Sb Coupling with $Ph_2SbCl$ To Form Trans-$[Fe(CO)_3(PPh_3)(Sb_2Ph_4)]$ and Salt Metathesis with $Me_3SbCl_2$ To Yield Trans-$[Fe(CO)_3(PPh_3)(SbMe_3)]$. *Eur. J. Inorg. Chem.* **2005**, *2005*, 82–85.

(87) Young, K. J. H.; Oxgaard, J.; Ess, D. H.; Meier, S. K.; Stewart, T.; Goddard William A., I. I. I.; Periana, R. A. Experimental Realization of Catalytic $CH_4$ Hydroxylation Predicted for an Iridium NNC Pincer Complex, Demonstrating Thermal, Protic, and Oxidant Stability. *Chem. Commun.* **2009**, *22*, 3270–3272.

(88) Gross, C. L.; Girolami, G. S. Metal−Alkane Complexes. Rapid Exchange of Hydrogen Atoms between Hydride and Methyl Ligands in $[(C_5Me_5)Os(Dmpm)(CH_3)H^+]$. *J. Am. Chem. Soc.* **1998**, *120*, 6605–6606.

(89) Periana, R. A.; Taube, D. J.; Gamble, S.; Taube, H.; Satoh, T.; Fujii, H. Platinum Catalysts for the High-Yield Oxidation of Methane to a Methanol Derivative. *Science.* **1998**, *280*, 560 LP-564.

(90) https://minerals.usgs.gov/minerals/pubs/commodity/.

(91) https://www.mining-technology.com/features/featuremined-into-extinction-is-the-world-running-out-of-critical-minerals-5776166/.

(92) Than, K.; Brown, G. Critical Minerals Scarcity Could Threaten Renewable Energy Future. *School of Eath, Energy, and Environmental Sciences*. 2018.

(93) Elvidge, C. D.; Ziskin, D.; Baugh, K. E.; Tuttle, B. T.; Ghosh, T.; Pack, D. W.; Erwin, E. H.; Zhizhin, M. A Fifteen Year Record of Global Natural Flaring Derived From Satellite Data. *Energies* **2009**, *2*, 595–622.

(94) Karacan, C. O.; Ruiz, F. A.; Cote, M.; Phipps, S. Coal Mine Methane: A Review of Capture and Utilizaiton Practices with Benefits to Mining Safety and to Greenhouse Gas Emission. *Intl. J. Coal Geol* **2011**, *86*, 121–156.

(95) Labinger, J. A. Platinum-Catalyzed C–H Functionalization. *Chem. Rev.* **2017**, *117*, 8483–8496.

(96) Crabtree, R. H.; Lei, A. Introduction: CH Activation. *Chem. Rev.* **2017**, *117*, 8481–8482.

(97) Bernskoetter, W. H.; Hanson, S. K.; Buzak, S. K.; Davis, Z.; White, P. S.; Swartz, R.; Goldberg, K. I.; Brookhart, M. Investigations of Iridium-Mediated C-H Cleavage: Characterization of a 16-Electron Iridium(III) Methyl Hydride Complex. *J. Am. Chem. Soc.* **2009**, *131*, 8603–8613.

(98) Khudyakov, I. V.; Serebrennikov, Y. A.; Turro, N. J. Spin-Orbit Coupling in Free-Radical Reactions: On the Way to Heavy Elements. *Chem. Rev.* **1993**, *93*, 537–570.

(99) Jones, W. D.; Feher, F. J. Mechanism of Arene Carbon-Hydrogen Bond Activation by $[C_5(CH_3)_5]Rh[P(CH_3)_3](H)(C_6H_5)$. Evidence for Arene Precoordination. *J. Am. Chem. Soc.* **1982**, *104*, 4240–4242.

(100) Janowicz, A. H.; Bergman, R. G. Activation of Carbon-Hydrogen Bonds in Saturated Hydrocarbons on Photolysis of $(\eta_5\text{-}C_5Me_5)(PMe_3)IrH_2$. Relative Rates of Reaction of the Intermediate with Different Types of Carbon-Hydrogen Bonds and Functionalization of the Metal-Bound Alkyl Groups. *J. Am. Chem. Soc.* **1983**, *105*, 3929–3939.

(101) Bengali, A. A.; Bergman, R. G.; Moore, C. B. Evidence for the Formation of Free 16-Electron Species Rather than Solvate Complexes in the Ultraviolet Irradiation of $CpCo(CO)_2$ in Liquefied Noble Gas Solvents. *J. Am. Chem. Soc.* **1995**, *117*, 3879–3880.

(102) Siegbahn, P. E. M. Comparison of the C-H Activation of Methane by $M(C_5H_5)(CO)$ for M = Cobalt, Rhodium, and Iridium. *J. Am. Chem. Soc.* **1996**, *118*, 1487–1496.

(103) Blomberg, M. R. A.; Siegbahn, P. E. M.; Svensson, M. Mechanisms for the Reactions between Methane and the Neutral Transition Metal Atoms from Yttrium to Palladium. *J. Am. Chem. Soc.* **1992**, *114*, 6095–6102.

(104) Siegbahn, P. E. M.; Blomberg, M. R. A. Halide Ligand Effects on the Oxidative Addition Reaction of Methane and Hydrogen to Second Row Transition Metal Complexes. *Organometallics* **1994**, *13*, 354–363.

(105) Siegbahn, P. E. M. Oxidative Addition of Methane to Rhodium(I) and Ruthenium(II) Complexes of Particular Interest. *Organometallics* **1994**, *13*, 2833–2842.

(106) Kahn, O. *Molecular Magnetism*; VCH Publishers, Inc: New York, 1993.

(107) Figgis, B. N. *Introduction to Ligand Fields*; John Wiley & Sons, Ltd: New York, 1966.

(108) Koseki, S.; Matsunaga, N.; Asada, T.; Schmidt, M. W.; Gordon, M. S. Spin–Orbit Coupling Constants in Atoms and Ions of Transition Elements: Comparison of Effective Core Potentials, Model Core Potentials, and All-Electron Methods. *J. Phys. Chem. A* **2019**, *123*, 2325–2339.

(109) He, L.; Bester, G.; Zunger, A. Singlet-Triplet Splitting, Correlation, and Entanglement of Two Electrons in Quantum Dot Molecules. *Phys. Rev. B - Condens. Matter Mater. Phys.* **2005**, *72*, 1–12.

(110) Stepanenko, D.; Rudner, M.; Halperin, B. I.; Loss, D. Singlet-Triplet Splitting in Double Quantum Dots Due to Spin-Orbit and Hyperfine Interactions. *Phys. Rev. B - Condens. Matter Mater. Phys.* **2012**, *85*, 7.

(111) Ishizuka, H.; Balents, L. Magnetism in S=1/2 Double Perovskites with Strong Spin-Orbit Interactions. *Phys. Rev. B* **2014**, *90*, 184422.

(112) Chilton, N. F.; Anderson, R. P.; Turner, L. D.; Soncini, A.; Murray, K. S. PHI: A Powerful New Program for the Analysis of Anisotropic Monomeric and Exchange-Coupled Polynuclear *d*- and *f*-Block Complexes. *J. Comput. Chem.* **2013**, *34*, 1164–1175.

(113) Layfield, R. A. Organometallic Single-Molecule Magnets. *Organometallics* **2014**, *33*, 1084–1099.

(114) Lv, L.; Wang, X.; Zhu, Y.; Liu, X.; Wang, Y. Theoretical Study of Spin-Orbit Coupling and Intersystem Crossing in the Two-State Reaction between $Nb(NH_2)_3$ and $N_2O$. *Sci. China Chem.* **2012**, *55*, 158–166.

(115) Rose, M. J.; Mascharak, P. K. Photosensitization of Ruthenium Nitrosyls to Red Light with an Isoelectronic Series of Heavy-Atom Chromophores: Experimental and Density Functional Theory Studies on the Effects of O-, S- And Se-Substituted Coordinated Dyes. *Inorg. Chem.* **2009**, *48*, 6904–6917.

(116) Dresselhaus, M. *Group Theory: Applications to the Physics of Condensed Matter*; Springer-Verlag: Berlin, 2008.

(117) Landis, C. R.; Morales, C. M.; Stahl, S. S. Insights into the Spin-Forbidden Reaction between $L_2Pd^0$ and Molecular Oxygen. *J. Am. Chem. Soc.* **2004**, *126*, 16302–16303.

(118) Matsunaga, N.; Koseki, S. Modeling of Spin-Forbidden Reactions. *Reviews in Computational Chemistry*. John Wiley and Sons: New York, 2004.

(119) Gorin, D. J.; Toste, F. D. Relativistic Effects in Homogeneous Gold Catalysis. *Nature* **2007**, *446*, 395.

(120) Ye, S.; Neese, F. How Do Heavier Halide Ligands Affect the Signs and Magnitudes of the Zero-Field Splittings in Halogenonickel(II) Scorpionate Complexes? A Theoretical Investigation Coupled to Ligand-Field Analysis. *J. Chem. Theory Comput.* **2012**, *8*, 2344–2351.

(121) Chen, J.-J.; Du, M.-L. Investigation of the Zero-Field Splitting and g-Values of $d^8$ Ions in Trigonal Compounds $CsMgX_3:Ni^{2+}$ (X = Cl, Br, I). *Phys. B Condens. Matter* **1996**, *228*, 409–413.

(122) Mabbs, F. E.; Collison, D. *Electron Paramagnetic Resonance of the d Transition Metal Series*; Elsevier: Amsterdam, 1992.

(123) Holm, R. H.; Cotton, F. A. Magnetic Investigations of Spin-Free Cobaltous Complexes: 1. Tetrahalo Cobalt(II) Ions. *J. Chem. Phys.* **1959**, *31*, 788–792.

(124) Zadrozny, J. M.; Telser, J.; Long, J. R. Slow Magnetic Relaxation in the Tetrahedral Cobalt(II) Complexes $[Co(EPh)_4]^{2-}$ (E = O, S, Se). *Polyhedron* **2013**, *64*, 209–217.

(125) Saber, M. R.; Dunbar, K. R. Ligands Effects on the Magnetic Anisotropy of Tetrahedral Cobalt Complexes. *Chem. Commun.* **2014**, *50*, 12266–12269.

(126) Shores, M. P.; Sokol, J. J.; Long, J. R. Nickel(II)-Molybdenum(III)-Cyanide Clusters: Synthesis and Magnetic Behavior of Species Incorporating $[(Me_3tacn)Mo(CN)_3]$. *J. Am. Chem. Soc.* **2002**, *124*, 2279–2292.

(127) Magnasco, V. *Methods of Molecular Quantum Mechanics*; John Wiley & Sons, Ltd: Chichester, 2009.

(128) Coste, S. C.; Vlaisavljevich, B.; Freedman, D. E. Magnetic Anisotropy from Main-Group Elements: Halides versus Group 14 Elements. *Inorg. Chem.* **2017**, *56*, 8195–8202.

(129) Karunadasa, H. I.; Arquero, K. D.; Berben, L. A.; Long, J. R. Enhancing the Magnetic Anisotropy of Cyano-Ligated Chromium(II) and Chromium(III) Complexes via Heavy Halide Ligand Effects. *Inorg. Chem.* **2010**, *49*, 4738–4740.

(130) Vijayakumar, M.; Gopinathan, M. S. Spin-Orbit Coupling Constants of Transition Metal Atoms and Ions in Density Functional Theory. *J. Mol. Struct. THEOCHEM* **1996**, *361*, 15–19.

# Chapter 2: Syntheses, Structures and Characterization of Nickel(II) Stibines: Steric and Electronic Rationale for Metal Deposition[1]

## 2.0 PROLOGUE

This chapter details the synthesis of some of our first monodentate antimony ligands as well as some of our first metal-antimony complexes. Although none of the nickel complexes synthesized in this chapter were paramagnetic, we still gained value in synthesizing and characterizing the complexes. Early on, we had very little understanding of how antimony ligands behaved towards and interacted with high valent 3*d* metal ions. Per the intro, there was not a lot of synthetic information in the literature regarding techniques or methodology regarding ligand or Sb-metal complex syntheses, so we had to uncover it ourselves. As there was little reported information about the electronic absorbance, steric, and electronic parameters of antimony complexes, let alone Ni-Sb complexes, we wanted to publish those results as they were. However, to put it bluntly, publishers did not believe our results had enough impact, and requested us to find some practical use for these complexes, rather than just reporting on synthesis and characterization. Thus, we turned to metal deposition reactions, as we had observed significant decomposition when these compounds were heated. The metal deposition results were incredibly serendipitous, but they did corroborate with previous reports extolling the Lewis acid properties of antimony. This research was initially meant as a synthetic guideline for the generation of metal-antimony complexes derived from 3*d*-

[1] Portions of this chapter were published in:
Taylor, W.V., Xie, Z-L., Cool, N.I., Shubert, S.A., Rose, M.J. *Inorg. Chem.*, **2018**, *57*, 10364-10374.
My contributions include the syntheses, structures, and characterization of all nickel-antimony complexes, as well as the metal deposition experiments and EDX/SEM characterization and analyses. Mike Rose and I wrote > 99 % of the published manuscript together.

metal(II) starting materials, but it evolved into a project that explored the interaction of molecular and materials chemistry.

## 2.1 INTRODUCTION

Nickel phosphine compounds have been studied for their catalytic properties for decades and they are associated with a variety of catalytic reactions such as hydrogen production,[131] hydrocyanation[132] and oligomerization.[133] In an effort to better comprehend and optimize catalysis, phosphine ligands and their corresponding organic substituents have been studied for both steric and electronic effects.[134,135] Concerning heavier phosphorus group (Group V) ligands, there have been studies on the relative steric and electronic effects in stand-alone antimony molecules,[136,137] but there are few extensive studies regarding the steric, electronic, magnetic and spectroscopic properties of antimony-nickel (or other 3*d* metal) complexes.[38,138,139] Such studies would provide a foundation of understanding for the design and synthesis of functional antimony-based complexes. Indeed, antimony ligands have proven to be effective donors to metal centers under certain conditions,[51,140] and productive catalysts that utilize antimony ligands have already been reported.[141–144]

Although a plethora of nickel-phosphine complexes have been synthesized, there are very few reported nickel-antimony complexes, and even fewer (three) nickel(II) antimony complexes with associated crystal structures. They are as follows: elegant work by Levason and Reid in the early 2000s showcased the first example of a nickel(II) halide stibine complex that was structurally characterized, namely [Ni(I){1,2-$C_6H_4(CH_2SbMe_2)_2\}_2$]($ClO_4$).[50] An allyl nickel(II) bromide complex containing triphenylstibine was synthesized in 2009 by Mereiter for use in the oligomerization of

styrenes.[68] In 2014, Gabbaï published several intriguing nickel(II) structures stabilized with tripodal antimony-phosphorus ligands (SbP3), which showcased the diverse functionality of antimony to behave as an L-, X-, or Z-type ligand.[69] Relatedly, there are reports of several nickel antimony dimeric structures[145,146] and clusters.[147–150] One likely reason for the general lack of nickel(II)-antimony compounds is the prevalent use of commercially available triphenylantimony as a ligand.[46] Antimony is a weak σ-donor compared with phosphorus or arsenic, and phenyl groups further weaken the donor strength due to their electron withdrawing nature.[49] However, we deemed it plausible that electron donating groups, such as alkyl substituents, would increase the σ-donating capability of antimony,[151] thus affording novel metal complexes that are otherwise inaccessible with triphenylantimony or related aryl ligands. Thus, a fundamental study on electron donating alkyl substituents on a series of antimony-nickel complexes would be beneficial to transition metal chemists presently working (or who might consider working) with stibines, and this would be a valuable contribution to the primary literature.

In addition to studying the electronic effects of antimony ligands, it is equally critical to examine the effects of sterics in stibine-metal complexes. Most five coordinate nickel-stibine complexes (mostly $Ni^0$ complexes) exhibit a geometric preference towards trigonal bipyramidal;[38,69] among the few four-coordinate nickel-stibine complexes in the literature, only one is square planar.[152] Thus, no systematic study to date has been performed to examine how the sterics and electronics of the ligand substituents affect the final geometries of the metal complexes. In contrast, extensive studies of varying phosphine ligands on nickel complexes has resulted in many successful instances of catalytic function and improvement.[153–155] Additionally, the Tolman electronic parameter has long been used to determine the donor strength of ligands. However, no such study has

been compiled for tertiary antimony ligands.[78] It is thus important to conduct a thorough analysis of possible ligands that could be utilized for future applications.

From initial observations of decomposition of our complexes when heated, we became interested to investigate deposition properties of our metallated compounds. Deposition of thin films – whether singular metals or alloys – is critical in the industries of semiconductor fabrication and electronic materials. Typical deposition methods (physical, thermal, or chemical vapor) are inefficient and/or expensive due to their non-specificity to the substrate and energy-intensive procedures (high temperature, vacuum, etc.). Electrodeposition is a promising avenue that can be more reagent-efficient than others, but the field is dominated by deposition from aqueous media, which leads to undesired oxidation of the substrate or deposition of mixtures of metals and metal oxides.[156,157] Similarly, the utility of electrodeposition is eliminated when the target substrate is not electrically conductive (like bulk silicon), or parts of the substrate are not in direct electrical contact.[158] Deposition under milder conditions from organic solvents could be valuable and reveal more information on the utility and reactivity of antimony-based metal complexes.

Herein, we report the synthesis, characterization and structural elucidation of a series of nickel iodide complexes derived from homoleptic and heteroleptic $SbR_3$ (R = $^{i}$Pr, Me, Ph) ligands. DFT was used to calculate the Tolman donor strength for each antimony ligand in the series. Additionally, the compounds were tested for the deposition of nickel metal onto silicon-copper wafers. This work lays fundamental groundwork regarding the steric and electronic effects of antimony ligands with late 3*d* metal ions and can hopefully serve as a blueprint for the future design of antimony-3*d* metal coordination complexes.

## 2.2 EXPERIMENTAL

### 2.2.1 Reagents and General Procedures

All reactions were conducted under a dry dinitrogen atmosphere with a Schlenk line (ligand syntheses) or under a dry argon atmosphere in a drybox (metalations). Dry solvents were HPLC-grade and purified over alumina using a Pure Process Technology solvent purification system. Deuterated solvents were purchased from Cambridge Isotope Laboratories and used without further purification; the standard freeze–pump–thaw technique was used to degas deuterated solvents as necessary. The starting materials trichloroantimony and triphenylantimony were purchased from Strem Chemicals and used without further purification. Magnesium turnings (Acros), iodine crystals (Acros), 2-chloropropane (Sigma Aldrich), nickel iodide (Strem Chemicals), fluorobenzene (Oakwood Chemical), and CO gas (Praxair) were purchased and used as received.

### 2.2.2 Ligand Syntheses

#### *2.2.2.1 Safety Precaution.*

Alkyl-substituted antimony ligands are volatile, air-sensitive and can be pyrophoric: they must be handled with caution under completely inert atmosphere. The corresponding metal complexes are also highly air-sensitive and often pyrophoric and must be handled with similar care.

On the toxicity of organoantimony ligands, antimony is not known to be as toxic and carcinogenic as arsenic ligands. However, antimony is still a class 2 carcinogen, which means it “may or possibly could be carcinogenic”. Essentially, it is unclear the exact effects that antimony – and especially organoantimony – compounds have on the human body. It

must be cautioned that every antimony compound must never leave a fume hood, unless it is sealed away from yourself and other people (e.g. in a Schlenk flask or pressure vessel). All glassware that organoantimony compounds touch should be thoroughly rinsed with acetone, water, THF, and acid. At this point, 99 % of the antimony reagent has been washed away or decomposed. Antimony waste should be handled in its own separate waste container – do not put antimony waste with other waste. Store antimony waste inside a hood – do not transport antimony waste outside of a hood to dispose of it in another carboy. These precautions extend to any antimony-metal complex as well as free antimony ligand.

The volatility of antimony ligands is another reason they are so dangerous. Antimony ligands are readily volatile, especially if they are exposed to oxygen. The first thing vaporized antimony ligands look for is water. The nearest source of water if a person is nearby an exposed antimony ligand is their mouth. Antimony ligands will plate on the back of the tongue – likely forming antimony oxide $Sb_2O_3$. This is a highly disgusting and dangerous event. Brushing the tongue and the rest of the teeth/mouth for several minutes will remove the taste and hopefully the chemical. As a personal anecdote, I was tested for antimony poisoning and it was found I was within the acceptable healthy limit but at the very edge of the limit. It is recommended to get periodically tested for antimony exposure (a lipid blood test) if one is working on this project.

To conclude, only handle antimony ligands and metal complexes inside a working fume hood or inside a sealed and properly working glovebox (when our glovebox had holes in the gloves, you could sometimes taste the antimony ligands – make sure that does not happen). Clean all glassware and waste carefully as dictated above. I have never directly felt any signs or symptoms of acute antimony poisoning, but it may cause cancers down the road (I pray not, but it is important to be open about this stuff). These paragraphs may

be the most important in this whole thesis – *safety is of the utmost importance when working with antimony compounds*.

#### *2.2.2.2 Triisopropylantimony ($Sb^iPr_3$)*

Magnesium turnings (2.46 g, 101.25 mmol) were activated with iodine (0.01 g, 0.04 mmol) and heated for 30 minutes under vacuum. Dry $Et_2O$ (125 mL) was added to the flask and 1,2-dibromoethane (0.22 g, 1.16 mmol) was subsequently added. Next, 2-chloropropane (5.88 g, 75 mmol) was added to the flask at 0 °C and the reaction was stirred overnight. The solution was filtered and antimony trichloride (3.42 g, 15 mmol) was added to the flask at 0 °C. The solution was refluxed for 3 h and then quenched with degassed water (70 mL). Under completely inert atmosphere, the organic layer was separated and dried over sodium sulfate and filtered. The solvent was removed *in vacuo* at 0 °C to afford the product as a colorless oil (3.31 g). Yield: 88% yield. $^1$H NMR ($CDCl_3$): δ 1.31 (d, $J$ = 7.3 Hz, 18H, -C$H_3$), 1.85 (hept, $J$ = 7.3 Hz, 3H, -C$H$). $^{13}$C NMR ($CDCl_3$): δ = 17.0, 22.5.

It is important to note that all the Grignard reagents used in these syntheses were freshly-generated and used immediately after preparation. During our initial ligand syntheses, we had difficulties with purchased Grignard reagents and only were successful with the reactions when using fresh Grignard. However, upon further experience with the reactions, we discovered the industry-prepared Grignard reagents to be sufficient. These pre-made reagents can save some time, but it is recommended to use freshly-prepared Grignard reagents if a reaction is unsuccessful with the pre-prepared version.

#### *2.2.2.3 Diisopropylphenylantimony ($Sb^iPr_2Ph$)*

Trichloroantimony (5.64 g, 24.7 mmol) and triphenylantimony (4.36 g, 12.4 mmol) were stirred together solvent-free for 3 h to afford dichlorophenylantimony (10 g, 37.06 mmol) in quantitative yield. Separately, the isopropylmagnesiumchloride Grignard solution was generated in situ in the same manner as above with magnesium turnings (2.70 g, 111 mmol) and 2-chloropropane (7.27 g, 92.6 mmol). The $SbCl_2Ph$ was then dissolved in $Et_2O$ (90 mL) and added dropwise to the filtered Grignard solution, and the reaction was refluxed for 3 hours. The solution was then quenched with degassed water (50 mL). Under completely inert atmosphere, the organic layer was separated and dried over sodium sulfate and then filtered. The solvent was removed *in vacuo* to afford a colorless oil. A fractional distillation was performed, which first distilled trace amounts of $Sb^iPr_3$ (75 °C, 0.01 mm Hg), followed by the desired product (120 °C, 0.01 mm Hg) as a colorless oil (4.7 g, 16.48 mmol). Yield: 45%. $^1$H NMR ($CDCl_3$): δ 1.32 (d, *J* = 7.2 Hz, 6H, -C*H*$_3$), 1.22 (d, *J* = 7.3 Hz, 6H, -C*H*$_3$), 2.08 (hept, *J* = 7.4 Hz, 2H, -C*H*), 7.51 (mult 2H, aromatic C*H*), 7.32 (mult 3H, aromatic C*H*). $^{13}$C NMR ($CDCl_3$): δ = 20.1, 21.9, 22.1, 128.3, 128.5, 136.5, 136.6.

It is important to note that the $SbPhCl_2$ was prepared and immediately carried over to the next reaction without purification. This material can be additionally purified via crystallization by two methods. One, the oil can be placed into a freezer (- 20 °C or colder) and left to crystallize over several days. Two, the classic "seeding" technique is viable with this material. A small crystalline chunk of $SbPhCl_2$ can be placed into the oil, then the mixture can be gently placed in a freezer (- 20 °C) and left to crystallize over a few days. Crystallizing the $SbPhCl_2$ helps remove unwanted $SbPh_2Cl$, which forms in a small amount during the conproportionation reaction. This leads to more facile distillations and higher yields for all future ligand syntheses.

#### *2.2.2.4 Dimethylphenylantimony ($SbMe_2Ph$)*

The methylmagnesiumiodide Grignard solution was generated in situ in the same manner as above with magnesium turnings (4.08 g, 168 mmol) and iodomethane (19.7 g, 139 mmol). Trichloroantimony (8.45 g, 37.1 mmol) and triphenylantimony (6.55 g, 18.5 mmol) were stirred together (no solvent) for 3 hours to afford dichlorophenylantimony (15.0 g, 55.6 mmol) in quantitative yield. The $SbCl_2Ph$ was dissolved in $Et_2O$ (125 mL) and added dropwise to the filtered Grignard solution, and the reaction was refluxed for 3 hours. The solution was then quenched with degassed water (70 mL). Under completely inert atmosphere, the organic layer was separated, dried over sodium sulfate and filtered. The solvent was removed *in vacuo* to produce a slightly yellow oil. A distillation was performed to afford the desired product (50 °C, 0.01 mm Hg) as a colorless oil (8.9 g). Yield: 70%. $^1$H NMR ($CDCl_3$): δ 0.98 (s 6H, -C*H*$_3$), 7.55 (mult 2H, aromatic C*H*), 7.32 (mult 3H, aromatic C*H*). $^{13}$C NMR ($CDCl_3$): δ = -1.24, 128.3, 128.6, 135.0, 137.5.

#### *2.2.2.5 Diphenylmethylantimony ($SbPh_2Me$)*

Methylmagnesiumiodide Grignard solution was generated in situ in the same manner as above with magnesium turnings (0.77 g, 32 mmol) and iodomethane (3.80 g, 26.9 mmol). Trichloroantimony (1.13 g, 5.33 mmol) and triphenylantimony (3.76 g, 10.7 mmol) were stirred together solvent-free for 3 h to afford diphenylchloroantimony (5.0 g, 16 mmol) in quantitative yield. The $SbPh_2Cl$ was dissolved in $Et_2O$ (75 mL) and added dropwise to the filtered Grignard solution, and the reaction was refluxed for 3 h. The yellow solution was then quenched with degassed water (50 mL). Under completely inert atmosphere, the organic layer was separated and dried over sodium sulfate and then filtered. The solvent was removed *in vacuo* to produce a slightly yellow oil. A fractional

distillation was performed, which first distilled $SbMe_2Ph$ (50 °C, 0.01 mmHg), followed by the desired product (80 °C, 0.01 mmHg) as a colorless oil (2.0 g, 6.9 mmol). Yield: 43%. $^1$H NMR ($CDCl_3$): δ 1.20 (s 3H, -C*H*$_3$), 7.50 (mult 4H, aromatic C*H*), 7.30 (mult 6H, aromatic C*H*). $^{13}$C NMR ($CDCl_3$): δ = 0.62, 128.5, 128.8, 135.6, 138.1.

In a similar manner to diphenylchloroantimony, $SbPh_2Cl$ can be purified through crystallization. In addition to the seeding method and the freezer method, $SbPh_2Cl$ can be dissolved in minimal diethyl ether then placed into a -20 °C freezer and crystallize out after a few days.

### 2.2.3 Synthesis of the Metal Complexes

#### *2.2.3.1 $Ni(I)_2(Sb^iPr_3)_2$ (1)*

Nickel iodide (0.62 g, 2.0 mmol) was added to $Sb^iPr_3$ (1.0 g, 4.0 mmol) in fluorobenzene at –20 °C under an inert argon atmosphere. The reaction was allowed to warm to room temperature and stirred overnight. The violet solution was filtered through Celite, and the solvent was removed *in vacuo* to afford a violet solid (0.80 g). Yield: 34%. The solid was redissolved in pentane and placed in a freezer at –20 °C. This yielded violet crystals suitable for X-ray diffraction. IR spectrum ($cm^{-1}$) 2929m, 2847s, 1450m, 1379w, 1361m, 1193s, 1144s, 1085w, 987m, 866w, 499s. $^1$H NMR ($CDCl_3$): δ 1.69 (d, *J* = 6.5 Hz, 18H, -C*H*$_3$), 2.92 (mult 3H, -C*H*). $^{13}$C NMR ($CDCl_3$): δ = 22.4, 28.6.

#### *2.2.3.2 $Ni(I)_2(Sb^iPr_2Ph)_2$ (2)*

Nickel iodide (0.27 g, 0.86 mmol) was added to $Sb^iPr_2Ph$ (0.50 g, 1.8 mmol) in fluorobenzene at –20 °C under an inert argon atmosphere. The reaction was allowed to warm to room temperature and stirred overnight. The violet solution was filtered through

Celite, and the solvent was removed *in vacuo* to yield a violet oil. The violet oil was redissolved in pentane and placed in a freezer at –20 °C. This yielded violet crystals suitable for X-ray diffraction (0.15 g). Yield: 19%. IR spectrum ($cm^{-1}$): 2948m, 2845s, 1572w, 1452m, 1423m, 1378w, 1358w, 1193m, 1143m, 988s, 867w, 720s, 688s, 499s, 448s. $^{1}$H NMR ($CDCl_3$): δ 1.57 (d 12H, -C*H*$_3$), 2.89 (mult 2H, -C*H*), 7.30-7.60 (mult 5H, aromatic C*H*). $^{13}$C NMR ($CDCl_3$): δ = 21.6, 22.2, 22.5, 129.7 (br, 2 resonances), 139.2 (br, 2 resonances).

#### *2.2.3.3 $Ni(I)_2(SbMe_2Ph)_3$ (3)*

Nickel iodide (0.34 g, 1.1 mmol) was added to $SbMe_2Ph$ (1.0 g, 3.2 mmol) in fluorobenzene at –20 °C under an inert argon atmosphere. The reaction was allowed to warm to room temperature and stirred overnight. The violet solution was filtered through Celite, and the solvent was removed *in vacuo*. The violet oil was redissolved in pentane and placed in a freezer at –20 °C. This afforded violet crystals suitable for X-ray diffraction (0.25 g). Yield: 23%. $^{1}$H NMR ($CDCl_3$): δ 1.34 (s 6H, -C*H*$_3$), 7.57 (mult 2H, aromatic C*H*), 7.32 (mult 3H, aromatic C*H*). $^{13}$C NMR ($CDCl_3$): δ = 1.28, 128.8, 129.4, 134.8, 135.5.

#### *2.2.3.4 $Ni(I)_2(SbMePh_2)_3$ (4)*

Nickel iodide (0.11 g, 0.34 mmol) was added to $SbMePh_2$ (0.30 g, 1.0 mmol) in fluorobenzene at –20 °C under an inert argon atmosphere. The reaction was allowed to warm to room temperature and stirred overnight. The violet solution was filtered through Celite, and the solvent was removed *in vacuo*. The purple oil was redissolved in pentane and placed in a freezer at –20 °C. This yielded purple crystals suitable for X-ray diffraction

(0.04 g). Yield: 30%. $^{1}$H NMR ($CDCl_3$): δ 1.23 (s 3H, -C*H*$_3$), 7.33 (mult 4H, aromatic C*H*), 7.07 (mult 6H, aromatic C*H*). $^{13}$C NMR ($CDCl_3$): δ = 3.47, 128.8, 129.5, 135.8, 136.5.

#### *2.2.3.5 $Ni(I)_2(Sb^iPr_3)_2CO$ (5)*

$Ni(I)_2(Sb^iPr_3)_2$ (0.10 g, 0.12 mmol) was dissolved in $Et_2O$ in a Schlenk tube. The headspace was filled with CO gas and the tube was then sealed and allowed to stir for 3 h. The solvent was removed *in vacuo* yielding a violet solid (0.06 g). Yield: 60%. The solid was redissolved in pentane inside an argon glovebox and placed in a freezer at –20 °C, which yielded crystals suitable for X-ray diffraction. IR spectrum ($cm^{-1}$): 2931m, 2848m, 1963s, 1447m, 1379w, 1360w, 1194s, 1143s, 1082w, 989m, 917w, 866w, 498m, 445w. $^{1}$H NMR ($CDCl_3$): δ 1.59 (d 18H, -C*H*$_3$), 2.87 (mult 3H, -C*H*). $^{13}$C NMR ($CDCl_3$): δ = 22.7, 27.0, 190.0.

#### *2.2.3.6 $Ni(I)_2(Sb^iPr_2Ph)_2CO$ (6)*

$NiI_2(Sb^iPr_2Ph)_2$ (0.05 g, 0.06 mmol) was dissolved in $Et_2O$ in a Schlenk tube. The headspace was filled with CO gas and the tube was then sealed and allowed to stir for 3 hours. The solvent was removed *in vacuo* yielding a violet oil (0.02 g). Yield: 40%. IR spectrum ($cm^{-1}$): 2962m, 2847m, 1990s, 1932s, 1584m, 1476m, 1454m, 1425m, 1244m, 1145m, 1063w, 994w, 726s, 692s, 451w. $^{1}$H NMR ($CDCl_3$): δ 1.62 (d, 6H, -C*H*$_3$), 1.45 (d, 6H, -C*H*$_3$), 3.55 (hept, 2H, -C*H*), 7.75 (mult, 2H, aromatic C*H*), 7.39 (mult, 3H, aromatic C*H*). $^{13}$C NMR ($CDCl_3$): δ = 21.8, 22.1, 22.3, 128.9, 130.7, 136.4, 197.8.

#### *2.2.3.7 $Ni(I)_2(SbPh_3)_2$*

Nickel iodide (0.22 g, 0.71 mmol) was added to $SbPh_3$ (0.50 g, 1.4 mmol) in $Et_2O$ at –20 °C under an inert argon atmosphere. The reaction was allowed to warm to room temperature and stirred overnight. No color change occurred. The clear, colorless solution was filtered through Celite, and the solvent was removed *in vacuo* to yield a white solid, which was determined to be unreacted starting material, $SbPh_3$. This reaction was also attempted in dichloromethane, toluene, and fluorobenzene, however, no reaction was observed in each case.

#### *2.2.3.8 $[Ni(I)_3(Sb^iPr_3)][NBu_4]$*

Tetrabutlyammonium iodide ($NBu_4I$, 0.044 g, 0.25 mmol) was added to a solution of $Ni(I)_2(Sb^iPr_3)_2$ (0.1 g, 0.24 mmol) in 15 mL fluorobenzene at -20 °C. The reaction was allowed to warm to room temperature and stirred for two hours. After two hours, the reaction was still purple, so ~30 mg of additional $NBu_4I$ was added and an immediate color change to red-brown was observed. The reaction was allowed to stir for another hour, then the solvent was removed in vacuo to yield a red/brown solid. The material was washed with pentane four times until the pentane washes were colorless (they are purple before they are colorless). The red-brown solid was crystallized via vapor diffusion of pentane into a solution of the product in fluorobenzene at -20 °C.

### 2.2.4 General Metal-Deposition Procedure

Copper-coated silicon wafers (100 nm PVD Cu on 1 μm Si substrate) were provided by Lam Research and used as the deposition substrates for these experiments. The wafers were cut into a 1 cm × 1 cm square and were washed with acetone prior to deposition. The metal complex (0.08 g, 0.09 mmol) was dissolved in 15 mL of

fluorobenzene and placed in a pressure vessel with the Si|Cu wafer. The solution was heated to 80 °C until the violet color of the solution had fully disappeared (2-4 days), although it appeared the color was mostly gone after 1 day. The colorless solution was removed, along with a non-adherent black precipitate. The wafer was washed with fluorobenzene and pentane, then removed from the glovebox for analysis.

### 2.2.5 Physical Measurements

The $^{1}H$ measurements were obtained using a 400 MHz Varian spectrometer and the $^{13}C$ NMR measurements were obtained using a 500 MHz Bruker AVANCE III NMR (supported by NSF grant 1 S10 OD021508-01); $CDCl_3$ was referenced to 7.26 ppm and 77.2 ppm for $^{1}H$ and $^{13}C$ spectra, respectively. Infrared spectra were measured under air-free conditions in the glovebox on a Bruker Alpha Fourier transform infrared (FTIR) spectrometer equipped with a diamond ATR crystal. UV/vis spectra were measured under air-free conditions using an Agilent Technologies Cary 60 UV/vis spectrometer. All UV/vis measurements were performed in dry pentane using an air-free cuvette. SEM images and EDX spectra were collected on a FEI Quanta 650 ESEM equipped with a Bruker EDX system. Powder XRD were collected using a Rigaku R-Axis Spider diffractometer operating with CuKα raduation (λ = 1.5418 Å). Data was collected in the range of 40-93 $2\theta$. ICP-OES spectra were collected with a Varian 710-ES Optical Emission Spectrometer.

### 2.2.6 X-ray Data Collection

For complexes **1**, **2**, and **5**, the X-ray diffraction data were collected on a Rigaku AFC12 diffractometer with a Saturn 724+ CCD using a Bruker AXS Apex II detector and

a graphite monochromator with MoKα radiation (λ = 0.71073 Å). Low temperatures were maintained using an Oxford Cryostream low temperature device. Data reduction was performed using the Rigaku Crystal Clear version 1.40.[159] Structures were solved by direct methods using SHELXT[160] and refined by full-matrix least-squares on $F^2$ with anisotropic displacement parameters for the non-H atoms using SHELXL-2014/7.[161] Structure analysis was aided by use of the programs PLATON[162] and WinGX.[163] For complexes **3, 4**, and $[Ni(I)_3(Sb^iPr_3)][NBu_4]$, the X-ray diffraction data were collected at –173 °C on a Nonius Kappa CCD diffractometer using a Bruker AXS Apex II detector and a graphite monochromator with MoKα radiation (λ = 0.71073Å). Reduced temperatures were maintained by use of an Oxford Cryosystems 700 low-temperature device. Data reduction was performed using SAINT V8.27B.[164] The structure was solved by direct methods using SHELXT[160] and refined by full-matrix least-squares on $F^2$ with anisotropic displacement parameters for the non-H atoms using SHELXL-2014/7.[161] Structure analysis was aided by use of the programs PLATON[162] and WinGX.[163]

### 2.2.7 DFT Calculations

Geometry optimizations for $\mathbf{4_{DFT}}$ and $\mathbf{5_{DFT}}$ were performed using the Firefly software package[165] with the mPW1PW91functional; the basis set of 6-31G(d) was used for H, C and Ni; 6-311G was used for I; and TZP for Sb. For spin state determinations, energy calculations of $\mathbf{4_{DFT}}$ and $\mathbf{5_{DFT}}$ were performed using B3LYP/3-21G using the coordinates obtained directly from the crystal structures. For the four putative Ni tricarbonyl complexes used to computationally evaluate the Tolman electronic parameter – i.e., $(^iPr_3Sb)Ni(CO)_3$, $(^iPr_2PhSb)Ni(CO)_3$, $(Me_2PhSb)Ni(CO)_3$ and $(MePh_2Sb)Ni(CO)_3$ – geometry optimizations were performed using the Firefly software package[165] with the

mPW1PW91functional; the basis set of 6-31G(d) was used for H, C and Ni; 6-311G was used for I; and TZP for Sb. IR calculations were accomplished using the same functional and basis sets. All IR calculations showed no imaginary frequencies. Graphical manipulations of the predicted spectra were performed with ChemCraft,[166] and structures were visualized with MacMolPlt.[167]

## 2.3 Results and Discussion

### 2.3.1 Synthesis and Rationale

Three of the ligands used in this work ($Sb^{i}Pr_3$, $SbMe_2Ph$, $SbMePh_2$) have been synthesized previously,[19,31] while the heteroleptic $Sb^{i}Pr_2Ph$ is reported here for the first time. In general, these syntheses utilize Grignard reagents to displace antimony chloride bonds with the desired alkyl substituents. The heteroleptic ligands require a fractional distillation purification, while the homoleptic ligands are analytically pure following an aqueous wash and can be used without further purification. These ligands have been used in several metalations;[168–170] however, the metal complexes of these ligands with nickel(II) have not been reported. Initially, metalations were performed in non-coordinating solvents to promote stable Sb–Ni bonding and to prevent competition for solvent binding at the metal site. The reactions were also successful when performed in the weakly coordinating solvent, THF, but could only be crystallized as solvent-free, antimony-bound complexes from non-coordinating solvents (e.g., FPh, pentane). We did see a reaction occur in $Et_2O$ and toluene, but those yields were quite low, and the reaction needed to be stirred for several days to see a faint color change. In contrast, the reaction of $NiI_2$ with $SbPh_3$ was unsuccessful in $Et_2O$, FPh or toluene. However, a reaction did occur in THF, yielding a dark yellow solution. But removal of solvent afforded a turquoise solid that was insoluble

in any non-coordinating solvents, unlike all cases with alkyl-substituted antimony ligands. We were never able to determine what exactly this complex was, but it clearly did not follow the same synthetic route that the other ligands afforded. More investigation into that compound could be warranted. A summary of the synthetic preparations of the ligands and metal complexes is shown in Schemes 2.1 and 2.2, respectively.

**Scheme 2.1** Preparation of Ligands.

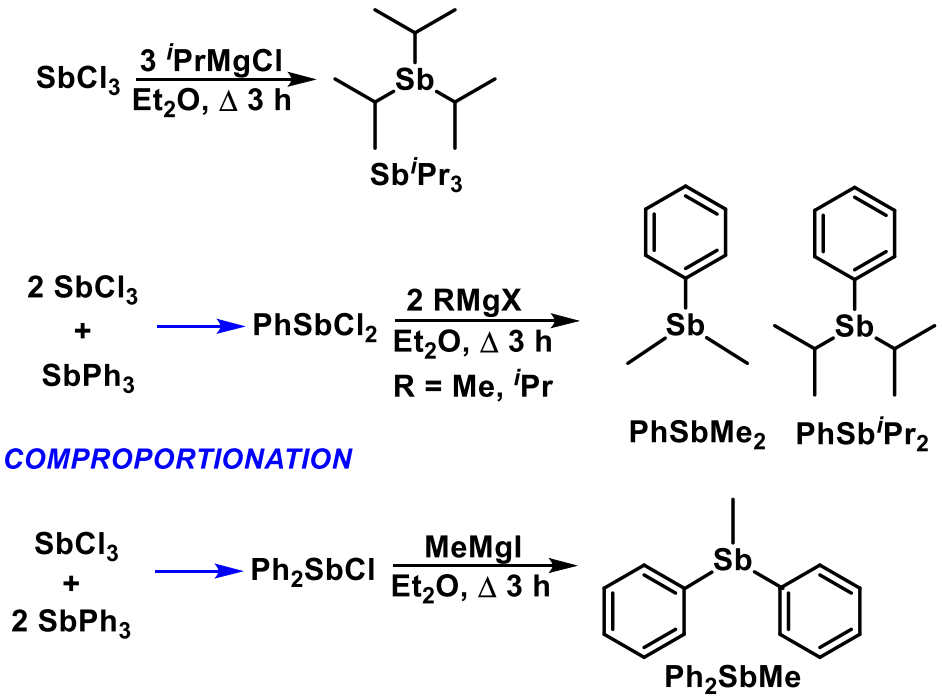


**Scheme 2.2** Preparation of Metal Complexes **1**-**6**.

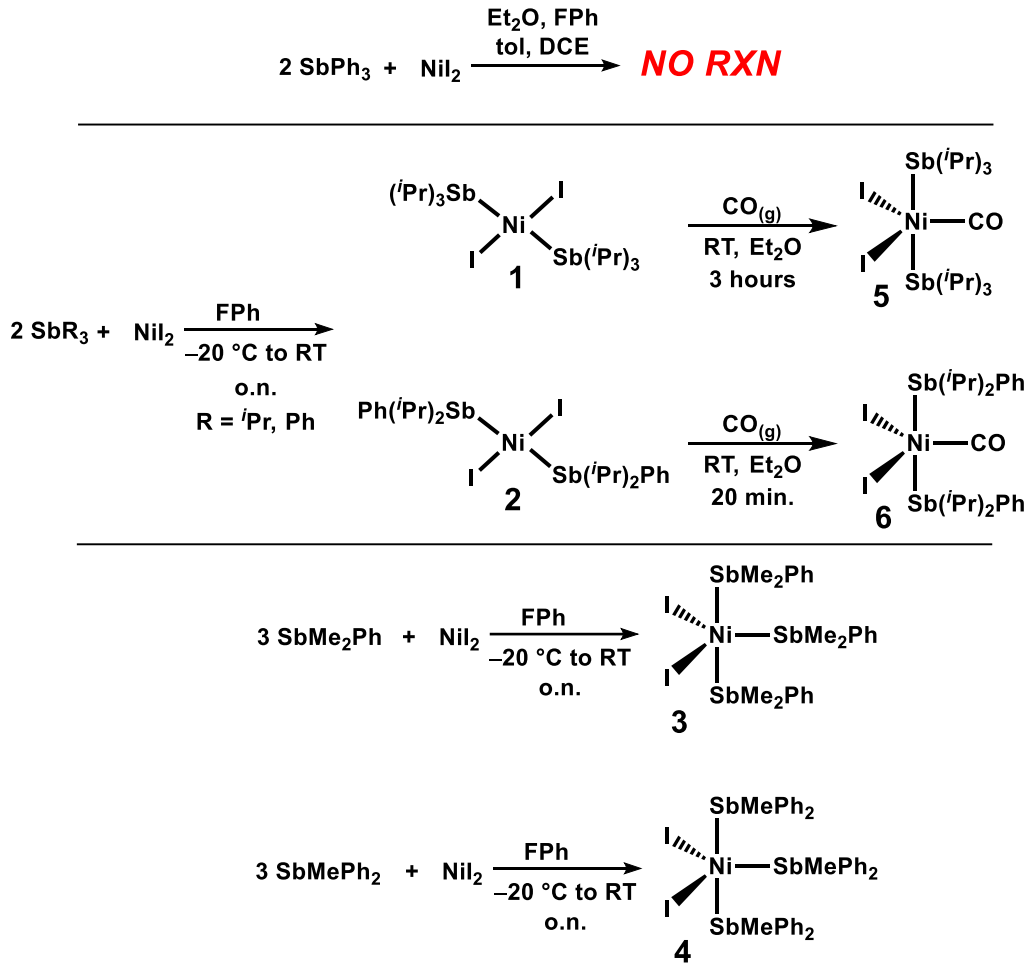


### 2.3.2 X-ray Structures and Steric Ligand Substituent Effects

#### *2.3.2.1 $Ni(I)_2(Sb^iPr_3)_2$ (1) and $Ni(I)_2(Sb^iPr_2Ph)_2$ (2)*

Figure 2.1 shows the crystal structures of $Ni(I)_2(Sb^iPr_3)_2$ (**1**) and $Ni(I)_2(Sb^iPr_2Ph)_2$ (**2**). Complex **1** has slightly distorted square planar geometry, and it has an average Ni–Sb bond length of 2.50(1) Å and a Sb–Ni–Sb bond angle of 177(3)°. The ligand cone angle for $Sb^iPr_3$ was calculated to be 155°.[171]

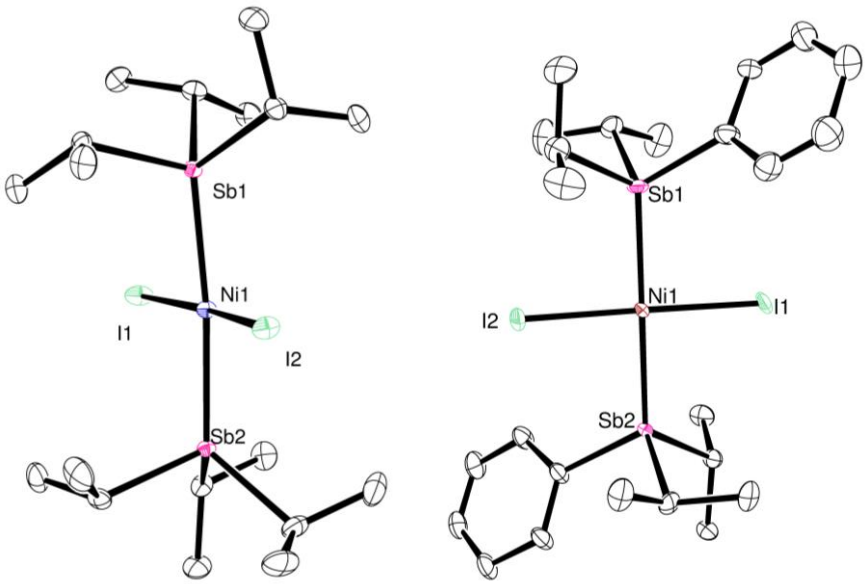


**Figure 2.1** ORTEP diagrams (50% thermal ellipsoids) for $Ni(I)_2(Sb^iPr_3)_2$ (**1**, *left*) and $Ni(I)_2(Sb^iPr_2Ph)_2$ (**2**, *right*).

Complex **2** exhibits a more ideal square planar geometry than **1**, with a Sb–Ni–Sb bond angle of 179.7(2)°. The Ni–Sb average bond distance is 2.487(2) Å. The ligand cone angle for diisopropylphenylantimony was calculated to be 147°. Complex **1** appears to be slightly distorted could be due to the increased steric bulk imposed by the $Sb^iPr_3$ ligand (155°) compared to the slightly smaller $Sb^iPr_2Ph$ ligand (147°). This phenomenon has been shown in several cases of square planar complexes with bulky ligands, such as $[V(DIPP)_4\{Li(THF)\}_2]$ (DIPP = diisopropylphenolate) and $(Ph_3P)_2Ni(o\text{-Tol})$(ISQ-Me) (ISQ = 4,6-di-tert-butyl-N-(2,6-di-methylphenyl)-*o*-iminobenzosemiquinonate).[172,173] However, complex **1** co-crystallizes with another molecule of $Ni(I)_2(Sb^iPr_3)_2$ in the asymmetric unit cell, which is nearly entirely planar (Figure 2.2). When averaging the bond distances and bond angles for these two molecules, the aforementioned structural deviations between **1** and **2** (2.50(1) vs. 2.487(2) Å and 177(3) vs. 179.7(2)° for Ni–Sb bond distance and Sb–Ni–Sb bond angles, respectively) become moot.

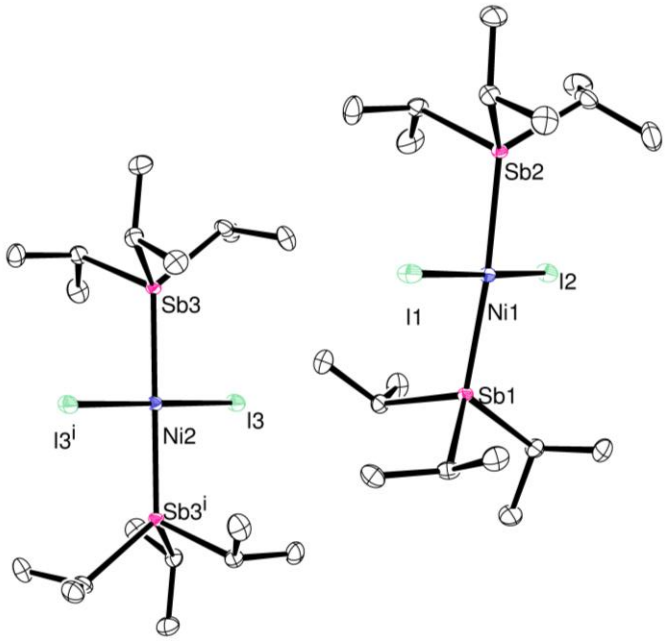


**Figure 2.2** ORTEP diagram (50% thermal ellipsoids) of the full crystal structure of **1**.

### *2.3.2.2 $Ni(I)_2(SbMe_2Ph)_3$ (3) and $Ni(I)_2(SbMePh_2)_3$ (4)*

Figure 2.3 shows the crystal structures of $Ni(I)_2(SbMe_2Ph)_3$ (**3**) and $Ni(I)_2(SbMePh_2)_3$ (**4**). $Ni(I)_2(SbMe_2Ph)_3$ has a trigonal bipyramidal geometry with a Ni–Sb average bond length of 2.44(1) Å. The average $Sb_{ax}$–Ni–$Sb_{ax}$ bond angle is 171(1)° and the average $Sb_{eq}$–Ni–$Sb_{ax}$ is 94.9(9)°. Interestingly, the TBP geometry accommodates the *three* smaller $SbMe_2Ph$ ligands (cone angle = 119°) around the nickel(II) center, thus expanding the coordination number from four to five (square planar to TBP) due to the decreased steric constraints as compared with the larger isopropyl-based ligands. Binding of five total ligands allows access to the presumably more stable eighteen electron species. In a similar vein, the reaction between nickel(II) iodide and diphenylmethylantimony (cone angle = 137°) yielded another trigonal bipyramidal complex (**4**). The average Ni–Sb bond

length for complex **4** was determined to be 2.45(1) Å. The $Sb_{ax}$–Ni–$Sb_{ax}$ bond angle is 174.1(1)° and the average $Sb_{eq}$–Ni–$Sb_{ax}$ bond angle is 92.4(6)°, affording a slightly distorted trigonal bipyramidal geometry similar to **3**. As with the comparison between the two isopropyl-based complexes, looking closer at the averaged Ni–Sb bond lengths (2.44(1) vs. 2.45(1) Å) and bond angles (171(1) vs. 174.1(1)° for $Sb_{ax}$–Ni–$Sb_{ax}$ and 94.9(9) vs. 92.4(6)° for $Sb_{eq}$–Ni–$Sb_{ax}$) between **3** and **4** reveal they are structurally similar.

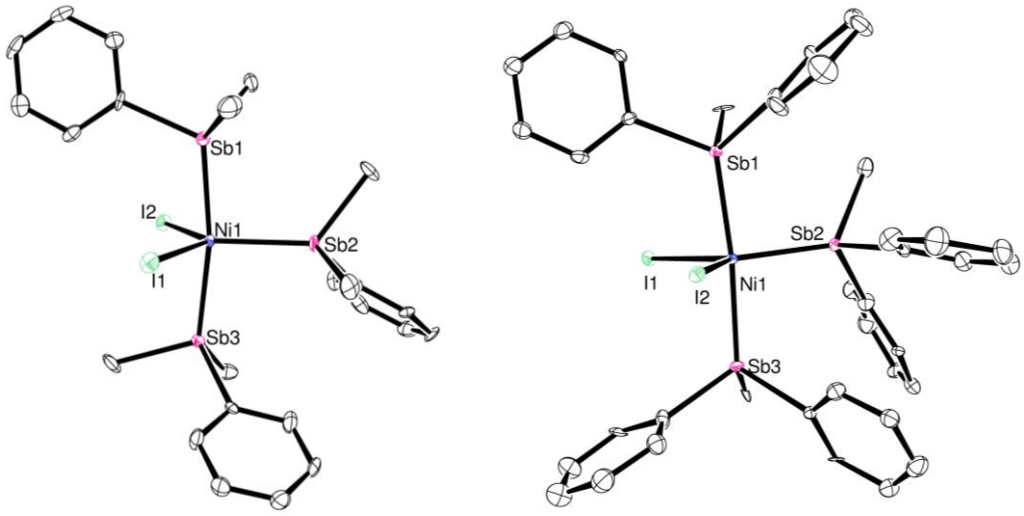


**Figure 2.3** ORTEP diagrams (30% thermal ellipsoids) for $Ni(I)_2(SbMe_2Ph)_3$ (**3**, *left*) and $Ni(I)_2(SbMePh_2)_3$ (**4**, *right*).

The relationships between ligand cone angle, complex geometry, and Ni–Sb bond length are summarized in Table 2.1. An additional parameter that can be used to classify these ligands is 'percent buried volume', which has been suggested to be a more accurate representation of steric hindrance of organic substituents in metal coordination complexes.[135] Percent buried volume is defined as the fraction of a sphere originating from the metal (first coordination sphere) that a given ligand occupies.[174] Although originally developed for NHC ligands, it has recently been used to quantify steric hindrance in bulky

phosphine ligands, and has scaled well with Tolman cone angles.[175,176] The percent buried volumes were calculated using the online web application SambVca developed by Cavallo et. al.[177] *This is a fantastic program and should be used whenever the steric bulk of a complex needs to be determined*. As evident in Table 1, the increase in ligand cone angle is directly correlated to the percent buried volume. The average Ni-Sb bond length appears to be split into two groups: isopropyl- and methyl-based ligands. The presence or number of phenyl substituents bound to the central antimony atom has no empirical effect on the Ni-Sb bond length, once standard deviations are accounted for. However, the isopropyl-based ligands with a Ni-Sb bond length of ~2.50 Å adopt a square planar geometry to account for the larger size of the ligands. The methyl-based ligands with an average Ni-Sb bond length of ~2.45 Å conform to trigonal bi-pyramidal geometry. There appears to exist a "cutoff" in both the Ni-Sb average bond length (> 2.45 Å) and the ligand cone angle parameters (> 137°) at which these nickel-antimony complexes revert to square planar geometry from TBP, although further investigation of stibine ligands of varying sizes between $SbMePh_2$ and $Sb^iPr_2Ph$ must be performed to reinforce that claim. Whether the ligand has electron-withdrawing or electron-donating organic substituents appears to have little effect on the bond lengths or geometries in the complexes: it is exclusively a steric effect.

**Table 2.1** Comparison between ligand cone angle, metal to ligand bond length, and metal complex geometry.

| Ligand | Ligand Cone Angle (°) | Percent Buried Volume (%) | Ni–Sb Bond Length (Å) | Complex Geometry |
|---|---|---|---|---|
| $Sb^iPr_3$ | 155 | 27.5 | 2.50(1) | Square planar |
| $Sb^iPr_2Ph$ | 147 | 26.9 | 2.487(2) | Square planar |
| $SbMePh_2$ | 137 | 25.8 | 2.45(1) | Trigonal bipyramidal |
| $SbMe_2Ph$ | 119 | 24.0 | 2.44(1) | Trigonal bipyramidal |

#### *2.3.2.3 $Ni(I)_2(Sb^iPr_3)_2CO$ (5)*

Although nickel(II) can only coordinate two larger antimony ligands ($Sb^iPr_3$, $Sb^iPr_2Ph$) in square planar geometry, these complexes can expand to a larger trigonal bipyramidal geometry by accommodating a fifth smaller ligand, such as CO. This has been observed with nickel phosphine complexes,[178,179] as well, and shows that – despite its weak σ-donating strength – the CO ligand will complete the coordination sphere without displacing either antimony ligand. Subjecting the square planar complex **1** to a CO atmosphere for a short amount of time affords a violet solid. This reaction is trickier than it looks, however. The CO(g) cannot be bubbled through the solution, or the excess CO will outcompete the antimony ligand and decompose the complex (likely giving toxic $Ni(CO)_4$). However, if the headspace of a small Schlenk tube is filled with a small amount of CO, the reaction appears to work. The reaction will not change color, but the distinctive IR spectrum is evidence for the reaction working. If the reaction changes color, too much CO was added or the reaction was allowed to proceed for too long. The complex is trigonal

bipyramidal geometry. This product was first serendipitously acquired and was the first Ni-Sb crystal structure determined in this project. The product was not intentional, the reaction that was performed was the reaction to generate complex **1** ($Ni(I)_2(Sb^iPr_3)_2$). However, during that time, a postdoc researcher was performing several reactions that displayed carbonyl ligands (nitrogenase biomimicking reactions). What likely occurred was the successfully formed complex **1** reacted with $CO_{(g)}$ that had flooded the glovebox atmosphere. As mentioned, this product can also be purposefully synthesized via addition of a headspace atmosphere of $CO_{(g)}$ to a solution of **1** in FPh. Figure 2.4 shows the crystal structure of $Ni(I)_2(Sb^iPr_3)_2CO$ (**5**), the result of the reaction of complex **1** with CO(g).

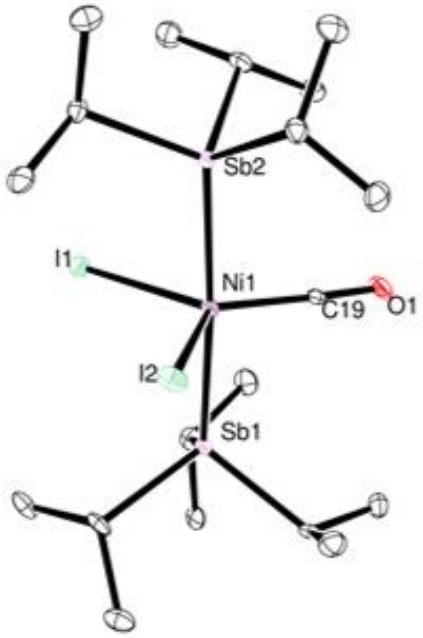


**Figure 2.4** ORTEP diagram (50% thermal ellipsoids) for $Ni(I)_2(Sb^iPr_3)_2CO$ (**5**).

The IR spectrum for complex **5** is shown alongside the IR spectrum of **1** in Figure 2.5, and it exhibits one strong CO feature at 1966 $cm^{-1}$; this matches the predicted number of CO stretches in complexes with $C_{2v}$ symmetry. Other than the presence of metal bound

CO feature, the IR of **5** is nearly identical to the IR spectrum of **1**. Although the spectra look like derivatives, they are typical transmittance IR spectra.

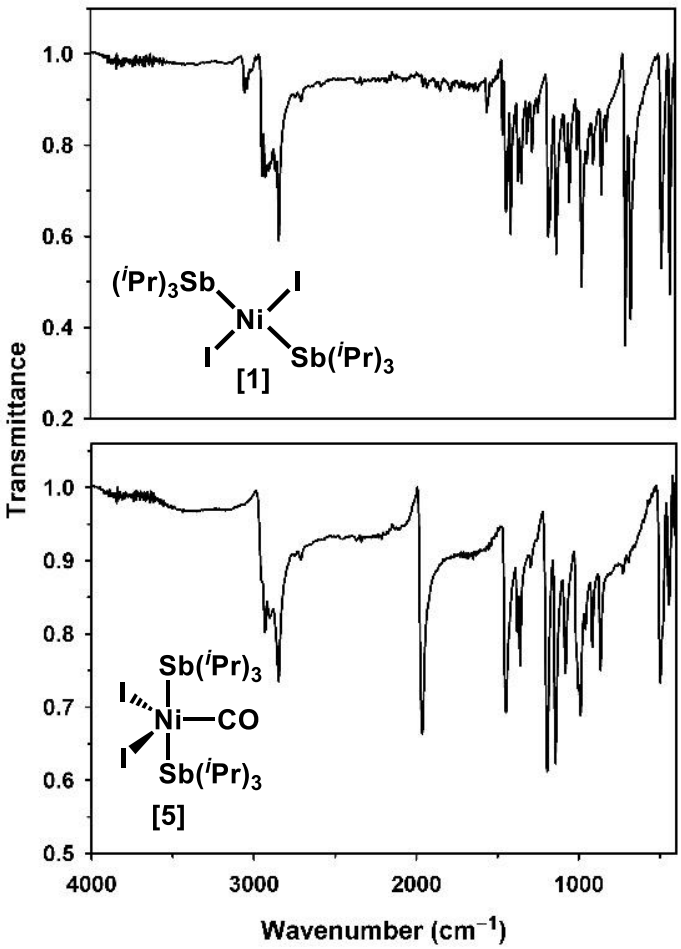


**Figure 2.5** Stacked IR spectra of **1** (top) and **5** (bottom) showing prominent CO peak.

### *2.3.2.4 $Ni(I)_2(Sb^iPr_2Ph)_2CO$ (6)*

Similarly, the TBP carbonyl complex **6** was generated via exposure of CO to the square planar complex **2**. We never achieved **6** serendipitously – we had to purposefully synthesize it from the beginning. However, it was found that the complex decomposed if

exposed to CO for longer than 30 minutes. This is likely due to the CO ligand having a greater probability of displacing the weaker $Sb^{i}Pr_2Ph$ ligand. Complex **1** could withstand a CO atmosphere for up to 2 hours, but not complex **2**. This makes complex **6** much more difficult to isolate and crystallize. Unfortunately, a crystal structure of **6** was never attained (following the same crystallization conditions that worked for complex **5**), yet spectroscopic measurements (IR and NMR) show some evidence the **6** was successfully synthesized. Figure 2.6 shows the stacked IR spectra of **2** and **6** showing two characteristic CO peaks.

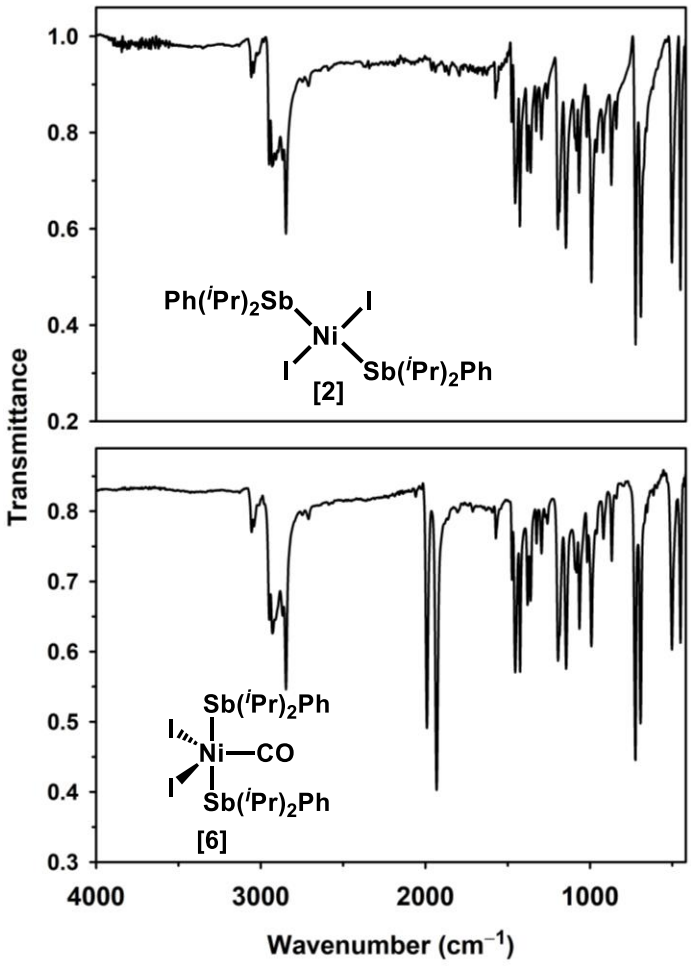

**Figure 2.6**. Stacked IR spectra of **2** (top) and **6** (bottom) showing two prominent CO peaks.

Although the number of CO peaks for **6** predicted by group theory is only one, there are several plausible reasons for the presence of two peaks. First, the examination of the IR spectra of analogous nickel(II) phosphine complexes also reveals the presence of two CO peaks, as found in the spectra of the two heteroleptic phosphine complexes, $Ni(Br)_2(PMe_2Ph)_2CO$ and $Ni(Br)_2(PMePh_2)_2CO$.[179] The additional stretch in each case was attributed to stereoisomerization derived from the heteroleptic ligands. This phenomenon has also been observed in similar cobalt nitrosyl phosphine complexes with the general formula $Co(Cl)_2(PR_3)_2NO$.[180] For **6**, the $^1H$ NMR also provides insight to the origin of the additional CO peak. The $^1H$ spectrum of $Sb^iPr_2Ph$ (see section 2.6 at end of chapter) exhibits two doublets at 1.33 and 1.22 ppm, whereas only one doublet is expected for a typical symmetric isopropyl-based ligand. Although the $^{13}C$ NMR is messy, there does appear to be only 1 CO stretch visible. The decreased molecular symmetry in the ligand (even in solution) likely breaks the idealized $C_{2v}$ symmetry one would presume for **6**, thus giving rise to two CO peaks. Solution IR spectra were collected for complexes **5** and **6** (Figures 2.7 – 2.9), and their similar features (and distinctness from the solution IR of **1**) imply both complexes are TBP-CO. A crystal structure of **6** was not obtained; however, it can be suggested from the spectroscopic data that **6** is structurally similar to **5**, with a formula of $Ni(I)_2(Sb^iPr_2Ph)_2CO$.

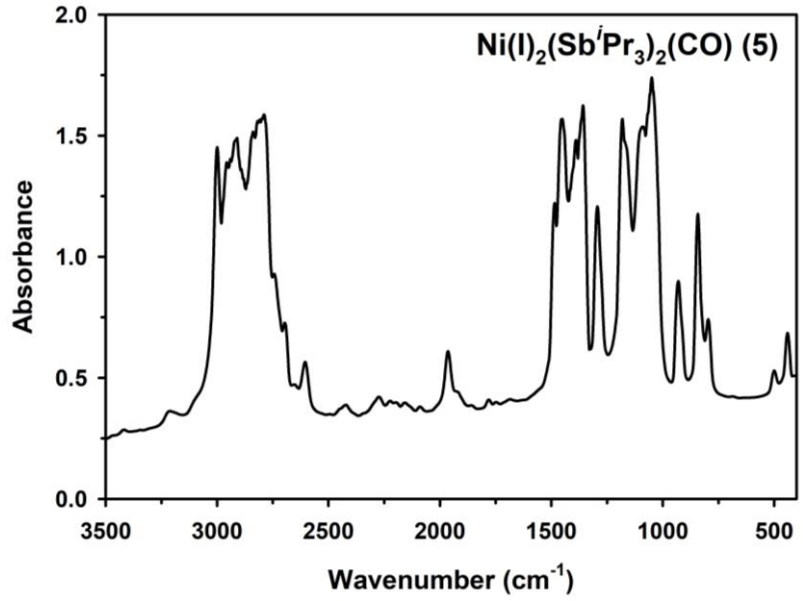


**Figure 2.7** Solution IR of **5** performed in $Et_2O$ at 298 K.

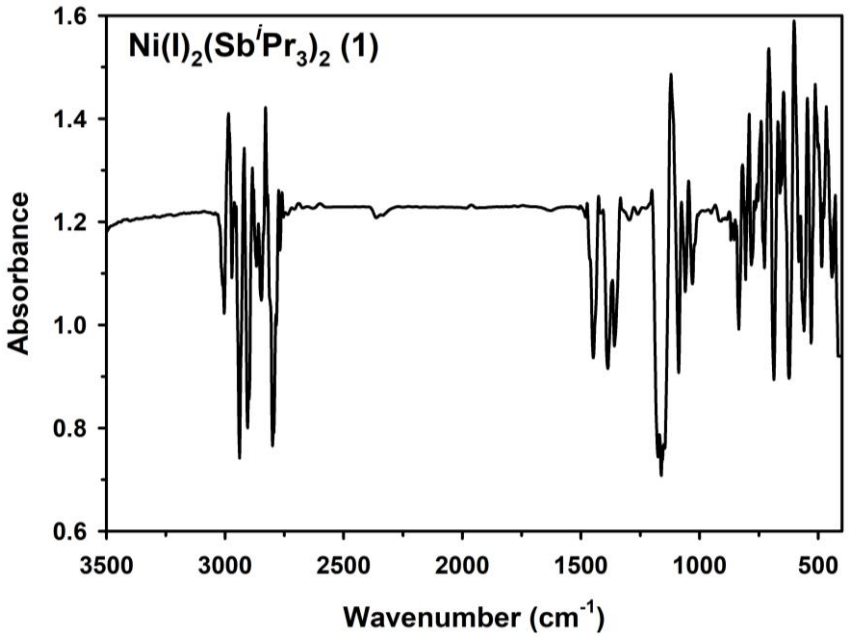


**Figure 2.8** Solution IR of **1** performed in $Et_2O$ at 298 K.

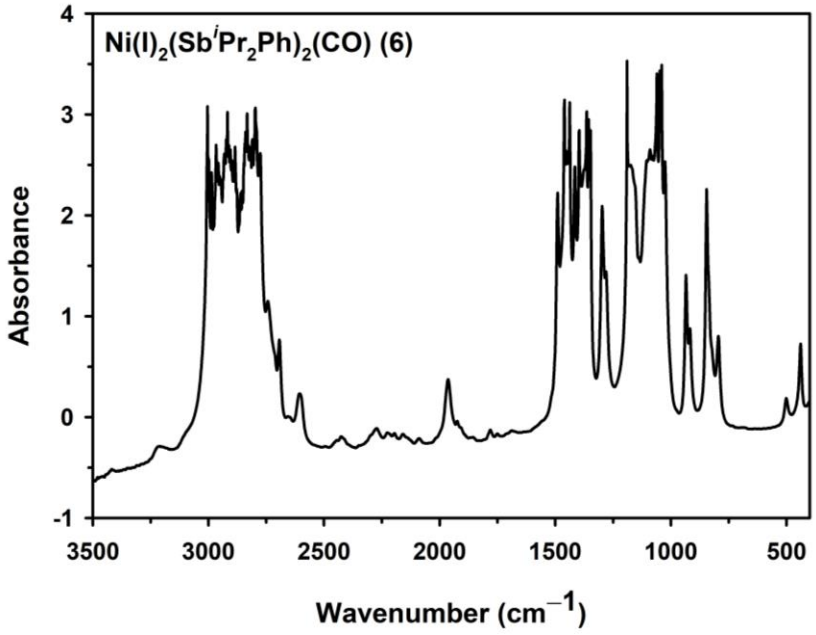


**Figure 2.9.** Solution IR of **6** performed in $Et_2O$ at 298 K.

### *2.3.2.5 Formation of tetrahedral [Ni(I)$_3$(Sb$^i$Pr$_3$)][NBu$_4$]*

We were able to add one CO ligand to the square planar complexes and were able to successfully crystallize and characterize complex **5**, derived from $Ni(I)_2(Sb^iPr_3)_2$. In a similar regard, we wanted to see if similar reactivity would occur with an iodination agent. Thus, tetrabutylammonium iodide was added to a solution of complex **1** in fluorobenzene with the hope of generating the square pyramidal charged complex, $[Ni(I)_3(Sb^iPr_3)_2][NBu_4]$. The reaction changed color from purple to red-brown, and crystals were obtained of the product from a FPh/pentane vapor diffusion. The crystal structure was not a square pyramidal complex, but a distorted tetrahedral complex of identity $[Ni(I)_3(Sb^iPr_3)][NBu_4]$. The third iodide ion did coordinate to the nickel center, but it also displaced a $Sb^iPr_3$ ligand. A preliminary crystal structure was obtained, but the quality is

not publication worthy and thus the exact determination of the complex still eludes us. The crystal structure of $[Ni(I)_3(Sb^iPr_3)][NBu_4]$ can be seen in Figure 2.10.

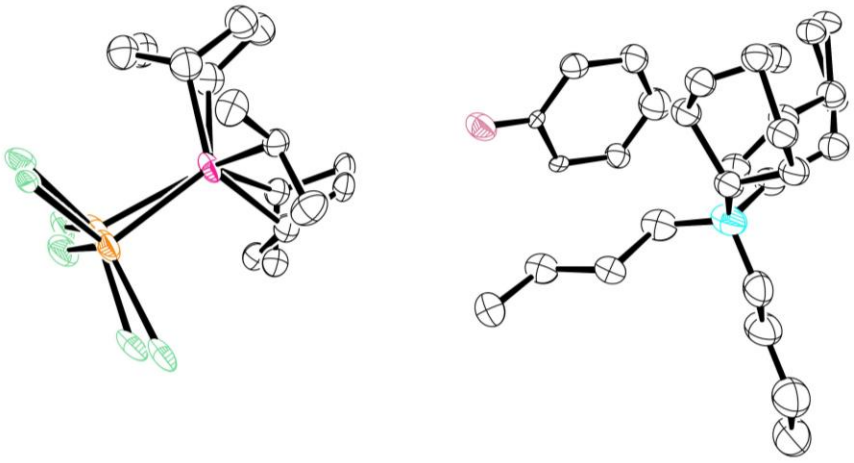

**Figure 2.10** ORTEP diagram of the crystal structure of $[Ni(I)_3(Sb^iPr_3)][NBu_4]$, obtained from a FPh/pentane vapor diffusion.

All of the complexes previously discussed were diamagnetic, and thus not able to be examined for the extent of spin-orbit-coupling on the nickel translationally donated from the antimony ligands. However, this new distorted tetrahedral complex could be paramagnetic, depending on the d-orbital splitting. Unfortunately, no magnetic studies have been performed with this complex – neither benchtop susceptibility nor SQUID. Still, this complex could be very intriguing for its magnetic properties, and the formation of a rare tetrahedral nickel complex is an interesting discovery on its own. Further investigation and the acquirement of a higher quality crystal structure are both required for this complex.

### 2.3.3 DFT Calculations and Tolman Electronic Parameters

To further understand the electronic contributions of the antimony ligands to the geometry and properties of the complexes, DFT calculations were performed to determine

their relative donor strengths, in a manner similar to the original Tolman electronic parameter developed for phosphine ligands.[78] In the original published report on electronic parameters of phosphine ligands, Tolman purports that the higher in energy the $A_1$ stretching frequency is for a $Ni(CO)_3(L)$ (L = phosphine ligand) complex, the greater the donor strength is of the phosphine ligand. When Tolman performed these calculations, he synthesized a variety of $Ni(CO)_3(L)$ complexes from $Ni(CO)_4$. As that is a highly toxic metal starting material, we decided it would be safer to merely simulate those complexes on Firefly. We simulated the structures of four model complexes with general formula $Ni(L)(CO)_3$ (L = $Sb^iPr_3$, $Sb^iPr_2Ph$, $SbMe_2Ph$, $SbMePh_2$) and calculated the carbonyl stretching frequencies for each complex (Tables 2.2 and 2.3). The most representative feature (the $A_1$ carbonyl stretch) for each corresponding complex is listed in Table 2.3.

**Table 2.2** DFT calculated $A_1$ carbonyl stretching frequencies for $Ni(L)(CO)_3$ (L = $Sb^iPr_3$, $Sb^iPr_2Ph$, $SbMe_2Ph$, $SbMePh_2$) determined using the functional of mPW1PW91. The basis set TZP was used on Sb, and 6-31G on the remaining elements.

| Sb Ligand | ν(CO) ($cm^{-1}$) |
|---|---|
| $Sb^iPr_3$ | 2060.8 |
| $Sb^iPr_2Ph$ | 2063.9 |
| $SbMe_2Ph$ | 2069.9 |
| $SbMePh_2$ | 2067.5 |

On this basis, the electronic donor properties of our ligands can be quantified, with $Sb^iPr_3$ representing the most strongly donating ligand (2061 $cm^{-1}$) and $SbMe_2Ph$ being the weakest ligand (2070 $cm^{-1}$). This is *somewhat* expected, as the corresponding phosphine analogues follow a similar trend both experimentally and computationally.[78,181] The isopropyl groups are more electron donating than the corresponding methyl groups, and

the phenyl groups serve as electron withdrawing substituents. In that regard, it was expected that $SbMe_2Ph$ would be a stronger donor than $SbMePh_2$; however, the opposite result was calculated by DFT. In related (experimental) phosphine work by Dartiguenave with identical R-group substituents,[179] the ν(CO) values were obtained for the TBP series of complexes analogous to those studied experimentally herein – namely of general formula $Ni(I)_2(PR^1R^2_2)(CO)$, where $PR^1R^2_2$ = $PMe_2Ph$, $PMePh_2$. Notably, our DFT-predicted substituent trend held true: the $PMe_2Ph$ ν(CO) value was observed at 2022 $cm^{-1}$, while the $PMePh_2$ ν(CO) feature was observed at slightly lower energy, 2018 $cm^{-1}$. However, the 2-4 $cm^{-1}$ difference between the $EMe_2Ph$ and $EMePh_2$ (E = P, Sb) cases is too small to definitively declare one ligand stronger or weaker. Inspection of the $A_1$ stretching frequencies for the analogous phosphine complexes with general structure $Ni(CO)_3L$ revealed the following values: $P^iPr_3$ = 2059 ± 1.4 $cm^{-1}$, $P^iPr_2Ph$ = 2066 ± 1.7 $cm^{-1}$, $PMe_2Ph$ = 2067 ± 2.7 $cm^{-1}$, $PMePh_2$ = 2068 ± 1.7 $cm^{-1}$.[182] Thus, in conjunction with existing tabulated values,[78,183] the collective data suggests that in the case of both antimony and phosphorus bound to nickel-carbonyl moieties, the methyl substituent is electronically equivalent to phenyl. These data call into question the apparent paradox between the successful metalation reaction of $NiI_2$ with $SbMe_2Ph$, but the failed reaction of $NiI_2$ with $SbPh_3$. If the methyl substituent is electronically equivalent to phenyl, $SbPh_3$ should be able to ligate in the same fashion as $SbMe_2Ph$. The answer could lie in the sterics and the phase of the two ligands. $SbMe_2Ph$ is much smaller than $SbPh_3$ (as detailed above via the percent buried volume data). This allows $SbMe_2Ph$ to coordinate three ligands to the nickel metal center, which will satisfy the electron density requirement of Ni(II). However, if $SbPh_3$ cannot sterically support three ligands coordinated to Ni(II), the nickel center is not electronically satisfied, and the simple coordination reaction will not occur. Another option

is the phase of the two ligands could afford different solubilities. $SbMe_2Ph$ is a liquid at room temperature (and at -20 °C), while $SbPh_3$ is a solid. The increased solubility of the liquid $SbMe_2Ph$ could push the reaction between it and nickel iodide to completion, while the same cannot be said for the solid $SbPh_3$. Clearly, more investigation into the electronic properties of methyl and phenyl substituents on antimony ligands is required to answer this predicament. Regardless, these results can serve as a useful reference for the design of future antimony-based ligands in transition metal complexes. Table 2.4 provides more bond metrics and gives the values for the other carbonyl stretches observed. There is not much information to be gleaned from this table other than the $A_1$ stretch, but it does prove that we performed the correct experiment in gathering all pertinent parameters and metrics.

**Table 2.3** Theoretical bond distances and carbonyl stretching frequencies for the four simulated nickel carbonyl complexes with antimony ligands.

| | **($^i$Pr$_3$Sb)Ni(CO)$_3$** | **($^i$Pr$_2$PhSb)Ni(CO)$_3$** | **(Me$_2$PhSb)Ni(CO)$_3$** | **(MePh$_2$Sb)Ni(CO)$_3$** |
|---|---|---|---|---|
| **Sb-Ni (Å)** | 2.436 | 2.429 | 2.423 | 2.423 |
| **Sb-C(≡O) (Å)** | 1.756 | 1.76 | 1.759 | 1.76 |
| | 1.757 | 1.757 | 1.758 | 1.759 |
| | 1.758 | 1.757 | 1.759 | 1.756 |
| **C≡O (Å)** | 1.169 | 1.169 | 1.168 | 1.167 |
| | 1.169 | 1.168 | 1.168 | 1.169 |
| | 1.169 | 1.169 | 1.168 | 1.168 |
| **ν(C≡O) cm$^{-1}$** | 1990.41 | 1991.66 | 2000.46 | 1994.43 |
| | 1992.54 | 1997.33 | 2000.82 | 2000.52 |
| | 2060.84 | 2063.94 | 2069.92 | 2067.49 |

### 2.3.4 Electronic Absorbance Spectra

The three unique coordination geometries (square planar, TBP-$Sb_3$ and TBP-$Sb_2CO$) of the complexes were analyzed for their electronic absorption spectra to further characterize these complexes. Low spin trigonal bipyramidal Ni(II) complexes such as

$[NiI\{1,2\text{-}C_6H_4(CH_2SbMe_2)_2\}_2](ClO_4)$ and $[Ni(TAP)Br]^+$ (TAP = tris[3-dimethylarsinopropyl]phosphine) typically display characteristic absorption features near 17,000 and 22,000 $cm^{-1}$,[50,184] while related square planar Ni(II) compounds such as $Ni(PEt_3)_2Br_2$ and $Ni(2,5\text{-}DMP)Br_2$ (2,5-DMP = 2,5-dimethylpyrazine) exhibit a single intense band within the broad range of 16,000-22,000 $cm^{-1}$, as well as a second band between 23,000-30,000 $cm^{-1}$.[185] The UV/vis absorption spectrum of **1** in pentane (Figure 2.11) exhibits an intense band at 17,860 $cm^{-1}$ ($\nu_2$, $\varepsilon$ = 4,330 $M^{-1}$ $cm^{-1}$) and a less intense band at 26,180 $cm^{-1}$ ($\nu_3$, $\varepsilon$ = 1,750 $M^{-1}$ $cm^{-1}$). We assign the 17,860 $cm^{-1}$ absorption as the [$b_{2g}(d_{xy}) \rightarrow b_{1g}(d_{x^2-y^2})$] transition and the 26,180 $cm^{-1}$ absorption as the [$a_{1g}(d_{z^2}) \rightarrow b_{1g}(d_{x^2-y^2})$] transition. There is another small feature on the shoulder of $\nu_2$ that is likely $\nu_1$. These transitions normally occur between 10,000-15000 $cm^{-1}$ and are quite weak as it is a spin forbidden transition. Another possible source of the small shoulder feature could be due to transitions from four non-bonding orbitals [$e(d_{xz}, d_{yz})$, $b_{2g}(d_{xy})$, $a_{1g}(d_z^2)$] to the high-lying $b_{1g}(d_{x^2-y^2})$ orbital. These transitions could cause additional non-obvious features and have been known to occur more commonly in complexes without $\pi$ bonding (which is the case for complex **1**).

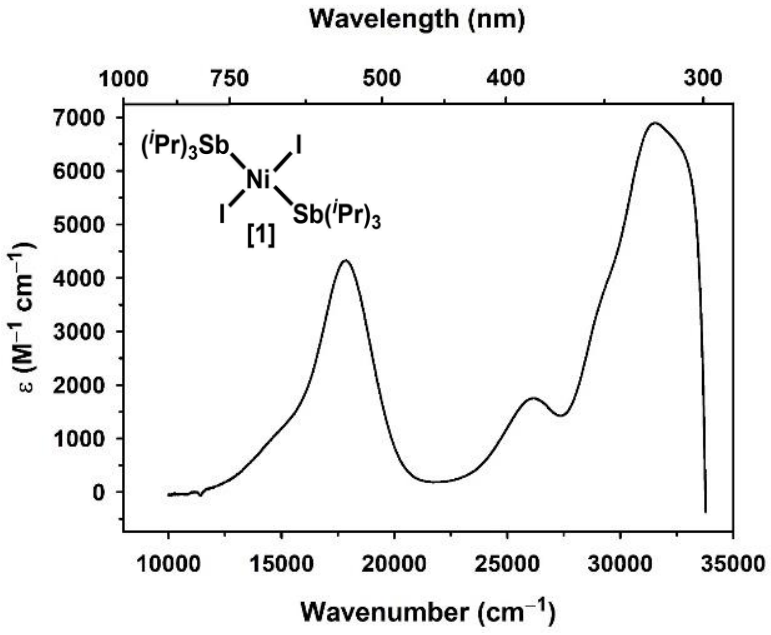


**Figure 2.11** UV/vis absorption spectrum of a solution of **1** in pentane at 298 K.

Although the violet color of the complex is not uncommon among square planar derivatives of nickel(II), the corresponding phosphine complexes with general formula $Ni(PR_3)_2(X)_2$ are generally red in color.[186] The violet colored solution in the present case is explained by the relatively low intensity of the absorption feature at 26,180 $cm^{-1}$. The higher energy band in Ni(II) square planar complexes is typically a more intense band than the lower energy absorption, which encompasses the higher energies of the visible spectrum.[185] We assign the ligand field transitions as $^1A_{2g} \leftarrow {}^1A_{1g}$ (17,860 $cm^{-1}$) and $^1B_{1g} \leftarrow {}^1A_{1g}$ (26,180 $cm^{-1}$). These energies are at the low end of the range for the two bands as previously described, which is indicative of the ligand field strength;[185] the presence of relatively weak $SbR_3$ and $I^-$ ligands is thus responsible for the lower energies of the absorption bands.

Figure 2.12 shows the UV/vis absorption spectra of **3** (TBP, no CO) and **5** (TBP, with CO) in pentane.

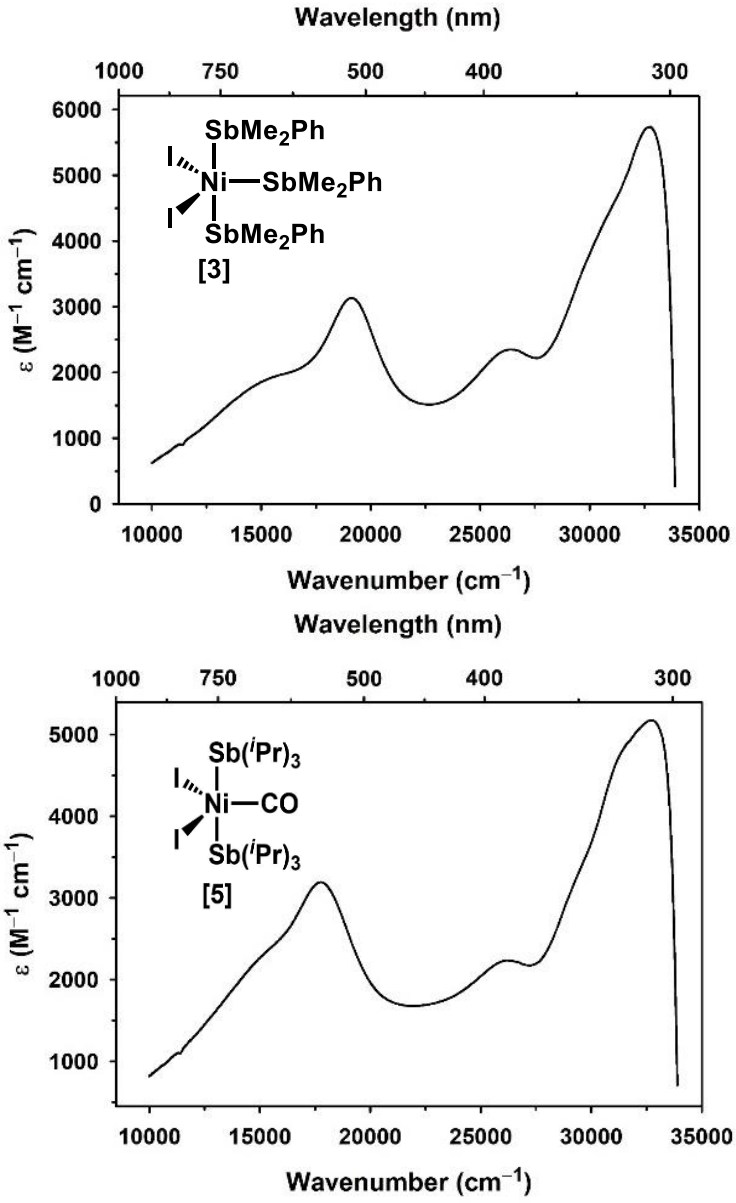


**Figure 2.12** UV/Vis spectra of pentane solutions of **3** (*top*) and **5** (*bottom*) obtained at 298 K.

Complex **3** exhibits an intense band at 19,120 $cm^{-1}$ ($\varepsilon$ = 3,135 $M^{-1}$ $cm^{-1}$) and a weaker band at 26,390 $cm^{-1}$ ($\varepsilon$ = 2,350 $M^{-1}$ $cm^{-1}$). From Lever, this is very typical of a low-spin Ni(II) $d^8$ system.[185] The ground state configuration of the diamagnetic trigonal bipyramidal complexes is $(e'')^4(e')^4$. Thus, the two excitations correspond to the $[(e'')^4(e')^4 \rightarrow (e'')^4(e')^3(a_1')]$ transition (19,120 $cm^{-1}$) and the $[(e'')^4(e')^4 \rightarrow (e'')^3(e')^4(a_1')]$ transition (26,390 $cm^{-1}$). We assign these transitions, respectively, as $^1E' \leftarrow {}^1A'_1$ (19,120 $cm^{-1}$) and $^1E'' \leftarrow {}^1A'_1$ (26,390 $cm^{-1}$). Complex **5** displays an intense band at 17,760 $cm^{-1}$ ($\varepsilon$ = 3,200 $M^{-1}$ $cm^{-1}$) and a less intense band at 26,180 $cm^{-1}$ ($\varepsilon$ = 2,230 $M^{-1}$ $cm^{-1}$). As with complex **3**, we assign the larger absorption feature to the $[(e'')^4(e')^4 \rightarrow (e'')^4(e')^3(a_1')]$ transition, and the less intense band to the $[(e'')^4(e')^4 \rightarrow (e'')^3(e')^4(a_1')]$ transition. Similarly, these transitions are assigned as $^1E' \leftarrow {}^1A'_1$ (17,760 $cm^{-1}$) and $^1E'' \leftarrow {}^1A'_1$ (26,180 $cm^{-1}$). In a similar manner to complex **1**, there is a progression/feature/shoulder around the low energy transition. However, the origin of the progressions in the TBP complexes is different than for the square planar complex. The likely origin is from a splitting of the excited $^1E'$ term into multiple states. This splitting would allow multiple transitions from the $^1A'$ ground state to the now-split $^1E'$ states. This splitting is actually not common among other nickel(II) TBP complexes, but is more commonly seen in Pd(II) or Pt(II) complexes. This was attributed to the distortion away from ideal trigonal bipyramidal due to the large size of the Pd or Pt metal centers. There is a large distortion away from ideal TBP geometry in our nickel-antimony complexes due to the antimony ligands. Thus, in our case the additional feature—not normally observed for nickel complexes—is due to the use of antimony ligands rather than the identity of the metal center.

It is important to comment on the visual similarity in the absorbance spectra between the square planar complex and the TBP complexes. We are confident in our

assignments of the transitions and the explanations for the origins of the transitions – especially the unique shoulders by the low energy transitions. We believe it to be merely coincidence that the square planar and TBP complexes show similar electronic absorbance spectra. However, it could be that the large structural distortions in our nickel-antimony complexes could lead to similar orbital degeneracies between the square planar and the TBP complexes. This may afford similar electronic absorbance spectra, especially when the complexes are in a fluctional liquid state. Regardless, our spectra look very similar to previously reported electronic absorbance spectra for square planar complexes (**1**) and trigonal bipyramidal complexes (**3** and **5**), lending credence that our complexes are pure, and their geometries are correctly assigned.

From a comparison of the UV/vis absorption spectra for **3** and **5** to known *high*-spin $d^8$ complexes, it is reasonably evident that **3** and **5** are low-spin. High-spin $d^8$ complexes exhibit multiple absorptions in the red region of the visible region with low molar intensities ($\varepsilon \approx$ 20-50 $M^{-1}$ $cm^{-1}$), as well as a more intense blue shifted band ($\varepsilon \approx$ 1,000 $M^{-1}$ $cm^{-1}$). These features are quite distinct from four-coordinate and low-spin five-coordinate nickel complexes, further supporting the low-spin state for all of the complexes herin.[185,187,188]

It is noted that NIR absorption spectra were also obtained for each complex to detect the presence of lower energy transitions. However, no metal-based absorption features were observed below 10,000 $cm^{-1}$ (compared with pentane solutions of ligand only). This is not entirely unexpected, as the large crystal field splitting between the HOMO and LUMO in both square planar and trigonal bipyramidal complexes should be greater than 10,000 $cm^{-1}$.[185]

### 2.3.5 Magnetism and Density Functional Theory

There are several reports of paramagnetic TBP nickel(II) complexes ligated by pnictogen donors.[187,189,190] However, all of the present set of trigonal bipyramidal complexes proved to be diamagnetic in solid-state, room-temperature magnetic susceptibility measurements – consistent with the UV/vis absorption spectra. To confirm the 0 K ground state configuration of the TBP complexes, DFT calculations were used to determine the lowest-energy spin multiplicity. Spin multiplicity calculations were performed on both the unoptimized X-ray coordinates and geometry-optimized structures of **4** and **5** under the presumptions of $S = 0$ and $S = 1$ configurations (see Table 2.4). The calculations performed using the X-ray coordinates of **4** and **5** clearly corroborated the findings from the benchtop magnetic susceptibility, determining that the diamagnetic configurations ($S = 0$) were more stable for both trigonal bipyramidal geometries (both with and without CO). For complexes **4** and **5**, the $S = 0$ configuration was 2.0 kcal/mol and 16.9 kcal/mol more stable than the $S = 1$ configuration, respectively.

**Table 2.4** DFT calculated energies for **4** and **5** regarding diamagnetic and paramagnetic spin multiplicities, and selected bond lengths on the *unoptimized* X-ray coordinates and geometry-*optimized* structures of **4** and **5** under at $S = 0$ and $S = 1$ configurations.

| | **X-ray Coordinates** | | **DFT Geometry Optimized** | |
|---|---|---|---|---|
| | $S = 0$ | $S = 1$ | $S = 0$ | $S = 1$ |
| **TBP–Sb3 (4)** | 0 | +2.0 kcal/mol | +10.3 kcal/mol | 0 |
| **Ni–Sb (Å)** | 2.451 ± 0.015 | | 2.377 ± 0.003 | 2.513 ± 0.028 |
| **TBP–CO (5)** | 0 | +5.0 kcal/mol | 0 | +16.9 kcal/mol |
| **Ni–Sb (Å)** | 2.473 ± 0.008 | | 2.407 ± 0.0004 | 2.594 ± 0.009 |
| **Ni–CO (Å)** | 1.798 | | 1.695 | 1.875 |

Interestingly, the geometry-optimized calculations provided slightly different results. The geometry optimized structure of carbonyl-bound **5** was similarly more stable in the $S = 0$ state by 4.9 kcal/mol, confirming its low-spin configuration. However, the geometry-optimized calculation of **4** (no CO bound) revealed an interesting result: the $S = 1$ configuration was 10.3 kcal/mole *more stable* than the $S = 0$ configuration. Evidently, the presence of three weakly donating $SbMePh_2$ ligands in **4** decreases the HOMO/LUMO gap to a small enough energy that a high-spin configuration is accessible – even dominant. In contrast, the strong-field CO ligand in **5** prevents any access to the high-spin state. It is important to note that the calculated bond distances and angles from the $S = 0$ optimizations of **4** and **5** afford better agreement with the parameters from the X-ray structures than do the $S = 1$ calculations (Table 2.4). In a comparison of x-ray coordinate bond distances to geometry-optimized bond distances, it appears universally (i.e. all measured bond distances) that the geometry optimized distances are shorter overall than the bond distances measured from the x-ray coordinates. This could be due to the relative temperatures these experiments are performed at. For the x-ray structure, data is collected at 100 K, but for the DFT geometry-optimized structures, data is "collected" at 0 K. A large decrease in temperature will shrink bond distances, especially if the vibrations are particularly anharmonic at higher temperatures. Given the significant distortions in the metal complex, and the likelihood that antimony ligands will lead to unique bond distances and angles, especially when compared to phosphine analogues, the bond vibrations in our Ni-Sb complexes could be quite anharmonic. A similar phenomenon is observed in the DFT calculations of complexes in Chapter 3. As the changes in bond distance were consistent for each bond metric tabulated, there is likely nothing drastically significant about the differences in bond distances between the calculated and observed data.

Notably, it has been recently suggested that paramagnetic nickel(II) TBP complexes with enhanced axial magnetic anisotropies (parameterized by the *D* values) can be obtained by maximizing axial anisotropy and minimizing equatorial distortions.[191–193] For example, the paramagnetic complex $[Ni(MDABCO)_2(Cl)_3]ClO_4$ exhibits uniquely high axial magnetic anisotropy ($D \approx -535$ cm$^{-1}$). However, the complexes reported herein are not paramagnetic due to their distortion from ideal TPB geometry – that is, due to the mixed donor set in the equatorial plane (two iodides and one antimony ligand). The potential use of even weaker stibine ligands (i.e. $SbMe_3$, $SbAr^F_3$) or multidentate antimony ligands with rigid organic scaffolding might afford complexes with interesting magnetic properties. Additionally, post synthetic iodination of **4** or **5** could lead to complexes with structures similar to that of $[Ni(MDABCO)_2(Cl)_3]ClO_4$.[191]

## 2.4 Nickel Metal Deposition

### 2.4.1 Empirical Depositions

We tested our metal complexes for nickel deposition on silicon wafers coated with 100 nm of copper. We were motivated to attempt these reactions after observing loss of violet color and the presence of a fine black powder when our complexes were subjected to heating. To elaborate on this story, and as mentioned in the prologue (section 2.0, above), we initially sent this manuscript out for publication without any of the nickel metal deposition work performed. The reviewers returned saying we should look for some practical purpose for these nickel-antimony complexes to improve the impact of the paper. Thinking on what to do about this matter, we recalled some reactivity studies we had performed several months prior. We were investigating if the nickel-antimony complexes would react with methane or dihydroanthracene, which would show signs of C-H activation

in these complexes (as that was the overall goal of this antimony project, see chapter 4 for more information on these reactions). Although the nickel-antimony complexes did not show any preliminary reactivity towards methane or DHA, when the complexes were heated to 80 °C, the complex appeared to decompose. The distinct purple color of the solutions disappeared, and a black precipitate deposited at the bottom of the flask that seemed to adhere to the stir bar. We wondered if that black precipitate could be nickel metal, and then we wondered if we could utilize that decomposition reaction to deposit that nickel metal onto a metal surface. Deposition of 3*d* transition metals is a critical process for the semiconductor industry, and if we could perform some semblance of that reaction with unique molecular starting materials and in organic solvents, these could be useful transformations for that industry and related fields. Additionally, any gained knowledge about antimony-metal complexes—especially their reactivity towards material substrates and at higher temperatures—could prove fruitful for future projects or industries.

The complexes were heated at 80 °C for 3 days in a pressure vessel containing the acetone-washed substrate. The SEM image and EDX scan results for the deposition of **1** (L = $Sb^iPr_3$) can be seen in Figure 2.13.

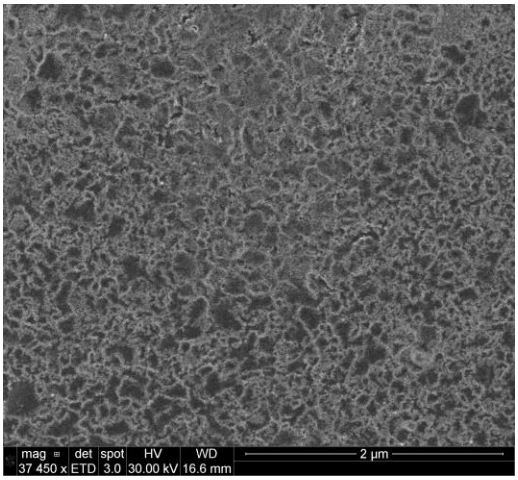

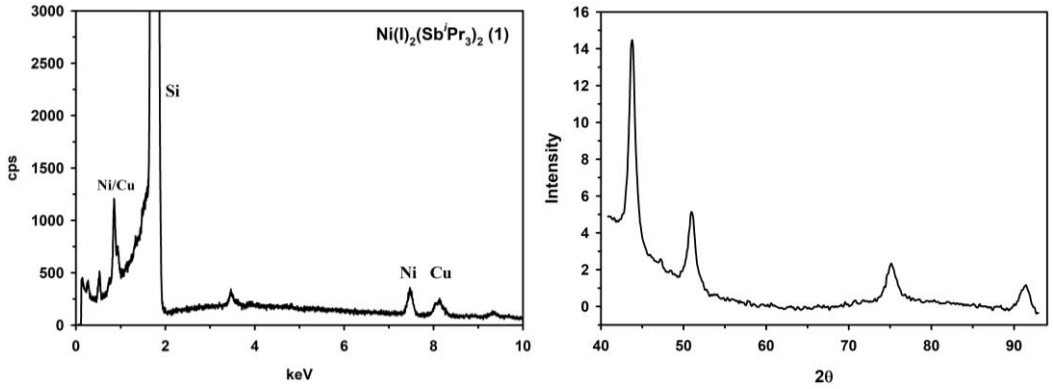


**Figure 2.13** SEM image (top), EDX spectrum (bottom left), and powder XRD spectrum (bottom right) of the deposition results from $Ni(I)_2(Sb^iPr_3)_2$ (**1**) on to a Si|Cu wafer.

The SEM image reveals a homogenous layer (in terms of elemental purity, not necessarily smoothness or evenness of the surface) that consists of nickel and copper, per the EDX spectrum. It is important to note that the surface is devoid of iodine/iodide, which could be expected from the iodide in the starting complex. The surface was tested with powder XRD (Figure 2.13, bottom right). Powder XRD similarly revealed no significant presence of iodine or CuI and showed four main features. The $2\theta$ values for these features reside in between the textbook $2\theta$ values for Cu and Ni metal, suggesting an alloy composition. The surface composition was further probed with ICP-OES, which found the mol ratio of Ni:Cu as 3.25:1, or as the alloy $Ni_{0.77}Cu_{0.23}$.

The Si|CuNi wafer resulting from the deposition of **1** was subjected to cross-sectional SEM analysis to provide the surface thickness and composition (Figure 2.14). The crystals are composed of both Cu and Ni and range from 10-20 μm thick. This data corroborates the powder XRD and ICP-OES regarding the alloyed nature of the deposited metal.

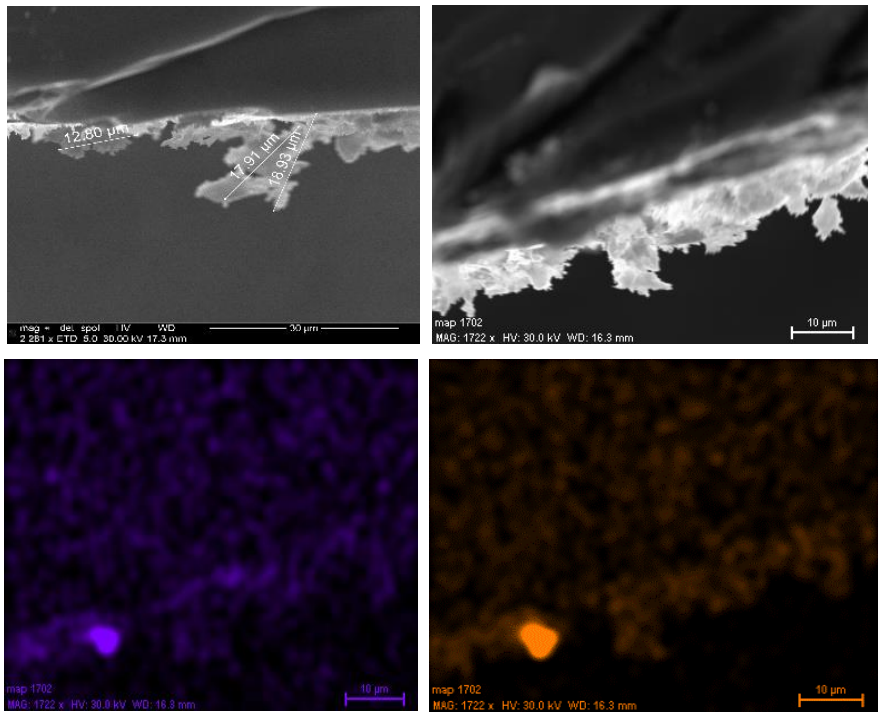


**Figure 2.14** SEM images (top) and EDX mapping images for Cu (bottom left) and Ni (bottom right) for the cross-sectional view of a sliced wafer after the deposition reaction of $Ni(I)_2(Sb^iPr_3)_2$. Top right image and bottom images were obtained from the same area on the wafer.

Complexes **2**, **3**, and **5** (L = $Sb^iPr_2Ph$; $SbMe_2Ph$; and $Sb^iPr_3$ + CO, respectively) were also tested for nickel deposition under the identical conditions. While some extent of nickel deposition was observed as with **1**, a large amount of iodine was also deposited (SEM, EDX for **2**, **3** and **5**: Figure 2.15). The surface composition of these iodinated surfaces was probed via powder XRD, and it was determined that the crystalline units were copper iodide (Figure 2.16).

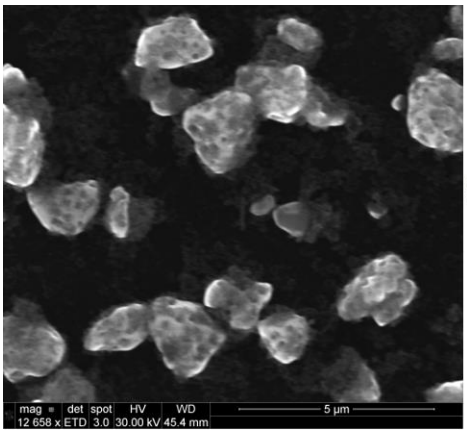
mag det spot HV WD 5 µm
12 658 x ETD 3.0 30.00 kV 45.4 mm

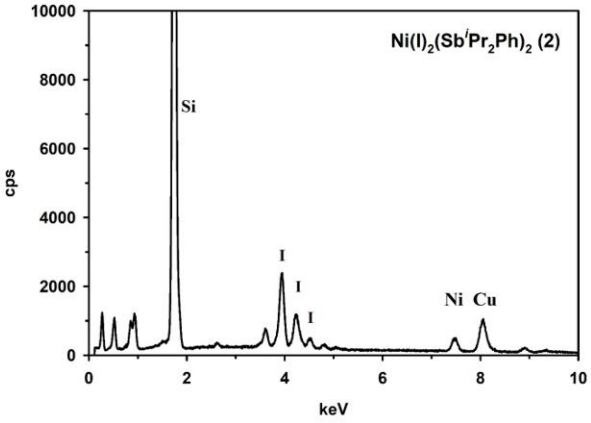
Ni(I)2(SbiPr2Ph)2 (2)
cps
keV
Si
I
I
I
Ni Cu
0
2000
4000
6000
8000
10000
0 2 4 6 8 10

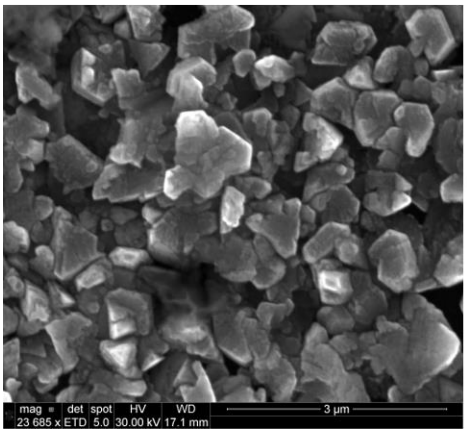
mag det spot HV WD 3 µm
23 685 x ETD 5.0 30.00 kV 17.1 mm

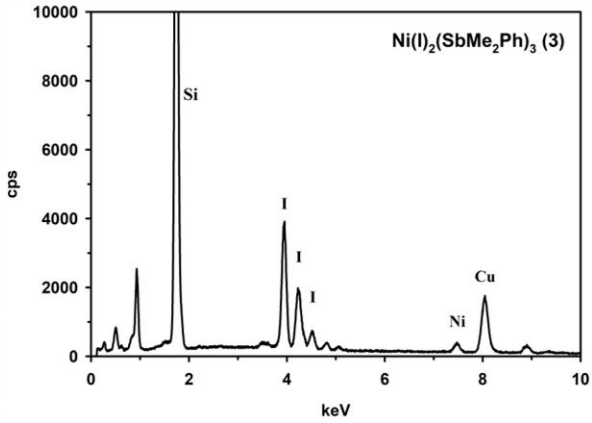
Ni(I)2(SbMe2Ph)3 (3)
cps
keV
Si
I
I
I
Ni
Cu
0
2000
4000
6000
8000
10000
0 2 4 6 8 10

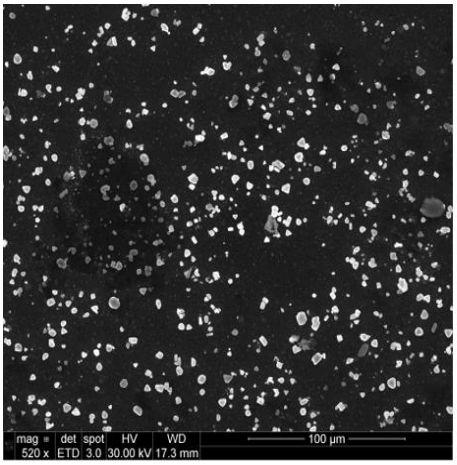
mag det spot HV WD 100 µm
520 x ETD 3.0 30.00 kV 17.3 mm

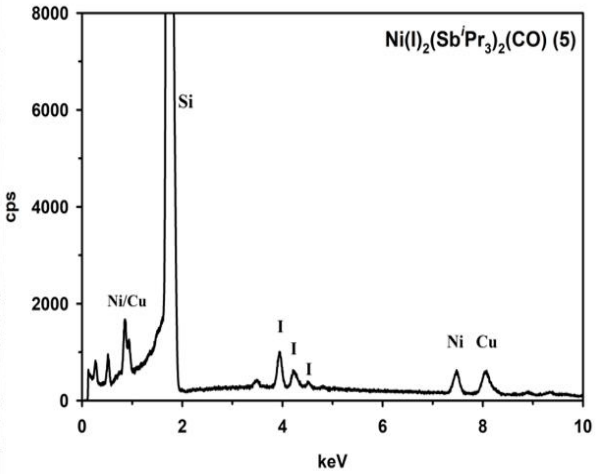
Ni(I)2(SbiPr3)2(CO) (5)
cps
keV
Si
Ni/Cu
I
I
I
Ni Cu
0
2000
4000
6000
8000
0 2 4 6 8 10

**Figure 2.15** SEM image (top left) and EDX spectrum (top right) of the deposition results from $Ni(I)_2(Sb^iPr_2Ph)_2$ on to a Cu|Si wafer. SEM image (middle left), EDX spectrum (middle right) of the deposition results from $Ni(I)_2(SbMe_2Ph)_3$. SEM image (bottom left), EDX spectrum (bottom right) of the deposition results from $Ni(I)_2(Sb^iPr_3)_2CO$.

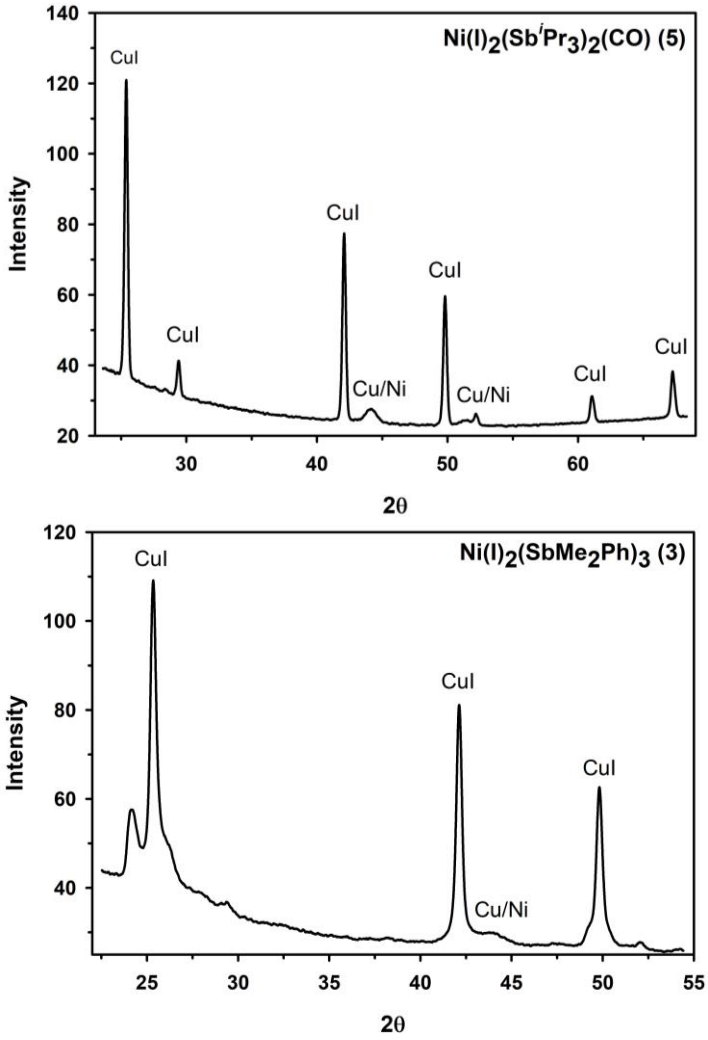


**Figure 2.16** Powder XRD spectra for the deposition results of $Ni(I)_2(Sb^iPr_3)_2(CO)$ (**5**) (*top*) and $Ni(I)_2(SbMe_2Ph)_3$ (**3**) (*bottom*).

### 2.4.2 Deposition Mechanism

In attempts to remove iodine deposition when using **2**, **3** and **5**, we used thallium tetrakis[3,5-bis(trifluoromethyl)phenyl)]borate, $Tl(BAr^{F}{}_{4})$ (a common halide-extraction reagent), to abstract the iodide ions, followed by the standard deposition protocol (80 °C, 3 days). More information on the deposition mechanism can be found in the experimental section of this chapter, but the three-day heating was probably longer than necessary. The loss of purple color in the solution was observed starting at four hours and the solution was nearly entirely colorless after 24 hours. However, the first reaction performed with a Cu|Si wafer was heated for 3 days, and a deviation in procedure could cause skewed results. In order to keep all results consistent and comparable, each reaction was heated for 3 days, even if the reactions were likely complete after one day. Figure 2.17 shows the EDX spectra of the deposition results from the thallium treated reactions of complexes **1**, **3** and **5**.

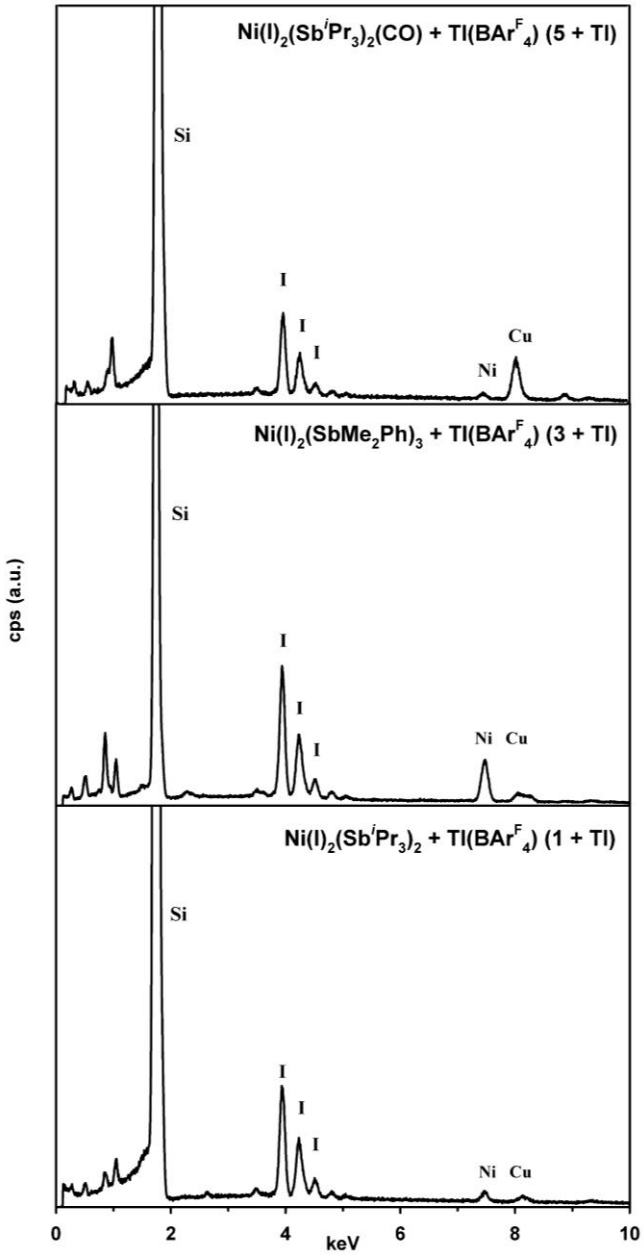


**Figure 2.17** EDX spectra of the thallium-treated deposition reactions of $Ni(I)_2(Sb^iPr_3)_2$ (bottom), $Ni(I)_2(SbMe_2Ph)_3$ (middle), and $Ni(I)_2(Sb^iPr_3)_2(CO)$ (top).

It was found that the thallium treatment moderately increased the amount of nickel deposited in the case of **3**. However, the iodine remained evident in the EDX spectrum.

Interestingly, for **1** and **5** the amount of nickel deposited *decreased* when compared with the non-thallium treated reactions. In the case of **1**, the EDX presence of iodine is unexpected in the thallium-treated reaction as there was no iodine observed in the deposition of **1** without thallium treatment. The SEM image of the surface of complex **1** + Tl shows the presence of CuI which then renders the results similar to those for **2**, **3** and **5**. Although unexpected from a chemical perspective, this result does reveal evidence for a potential mechanism of deposition (Scheme 2.3).

We postulate that at higher temperatures, the ligand(s) disassociate from the $Ni^{2+}$ center, lowering the reduction potential and rendering the $Ni^{2+}$ susceptible to reduction by the bound $I^-$ ions. The resulting $Ni^0$ is suitable for nucleation and deposition; the stoichiometric and oxidized byproduct ($I_2$) then reacts with the $I_2$ acceptor $Sb^{III}(^iPr_3)$ (strongest σ donor), thus forming $Sb^{V}(^iPr_3)(I)_2$. This scheme appears plausible, as antimony has been shown to be an excellent Lewis acid, especially in the case of halides.[69,70] For example, Gabbaï has demonstrated that fluoride will preferably bind to a stibine ligand over a metal center in both Pt and Au complexes.[25,194] The balanced reaction and proposed mechanism for iodine scavenging by $Sb^iPr_3$ is delineated in Scheme 2.3. However, the exact order, kinetics and synergism between the elementary steps are not addressed in the present work.

**Scheme 2.3** Proposed Mechanism for Nickel Metal Deposition from **1**.

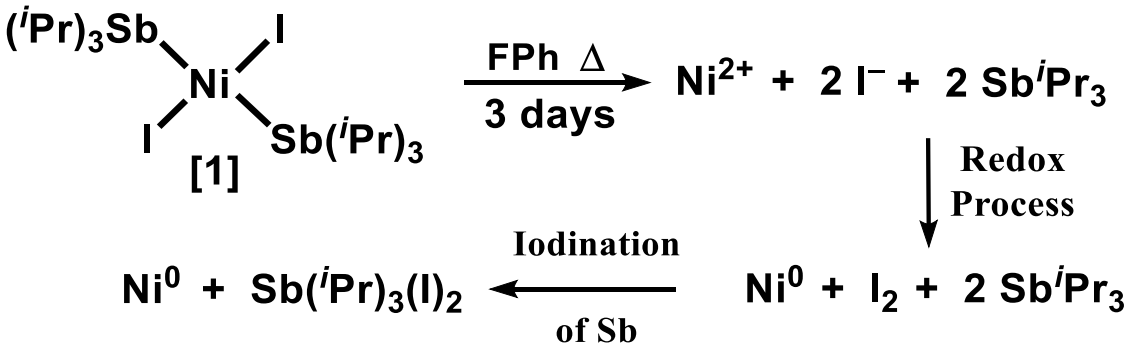


To test this hypothesis, we analyzed the filtrate after a deposition procedure using **1** for the presence of $Sb(^{i}Pr)_3(I)_2$, which is soluble in fluorobenzene. The $^{1}H$ NMR for the deposition product does indeed show the presence of $Sb(^{i}Pr)_3(I)_2$, which was compared to a sample of the independently synthesized $Sb(^{i}Pr)_3(I)_2$ [synthesized from the addition of ethereal iodine to a solution of $Sb^{i}Pr_3$ under nitrogen] (Figure 2.18).

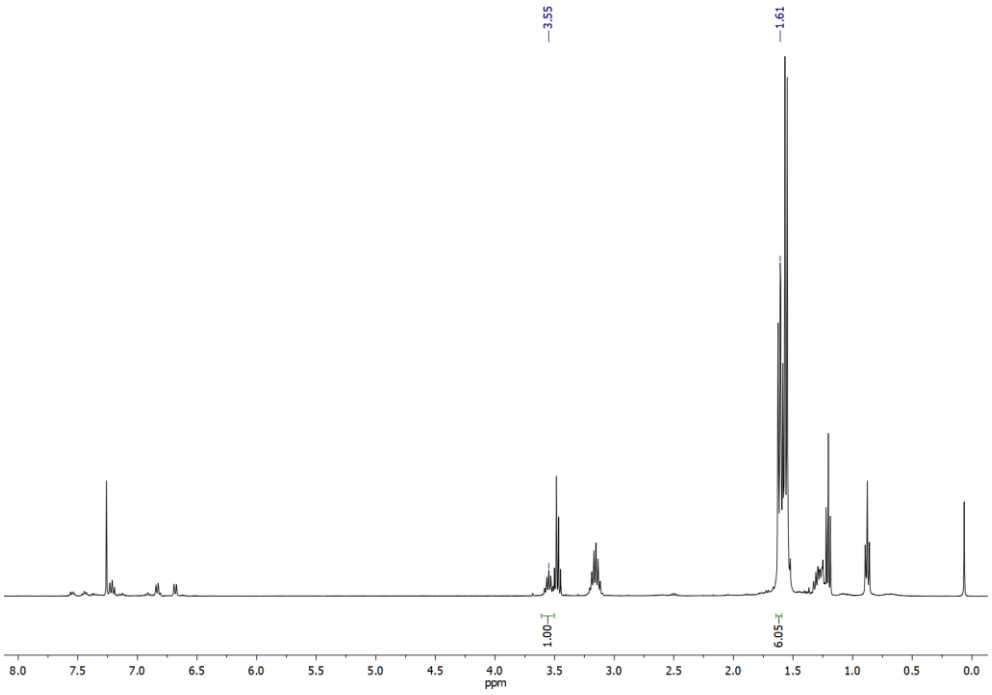

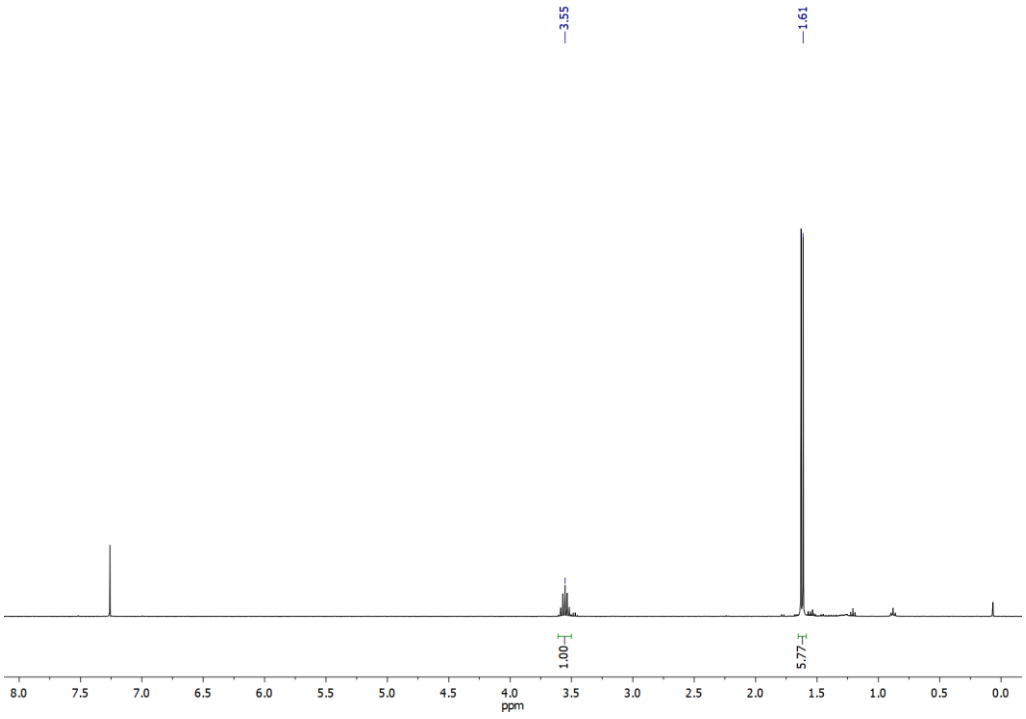


**Figure 2.18** $^{1}$H NMR of the filtrate after the deposition reaction of **1** in $CDCl_3$ at 400 MHz (*top*). $^{1}$H NMR of independently synthesized $Sb^{i}Pr_3I_2$ in $CDCl_3$ at 400 MHz (*bottom*).

The CI mass spectra for both the deposition product and the synthesized $Sb(^{i}Pr)_3(I)_2$ are nearly identical (Figure 2.19) and correspond to the theoretical ionization pattern of $[Sb(^{i}Pr)_3(I)]^{+}$ (Figure 2.19, bottom).

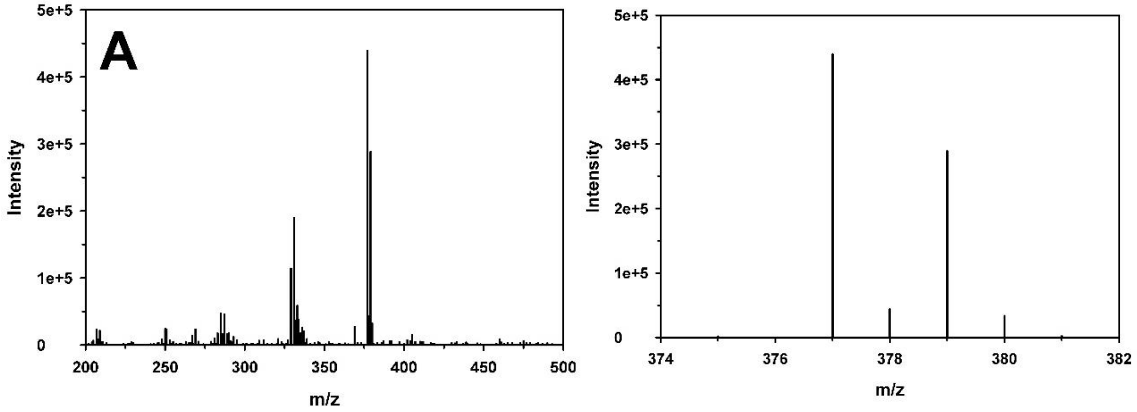

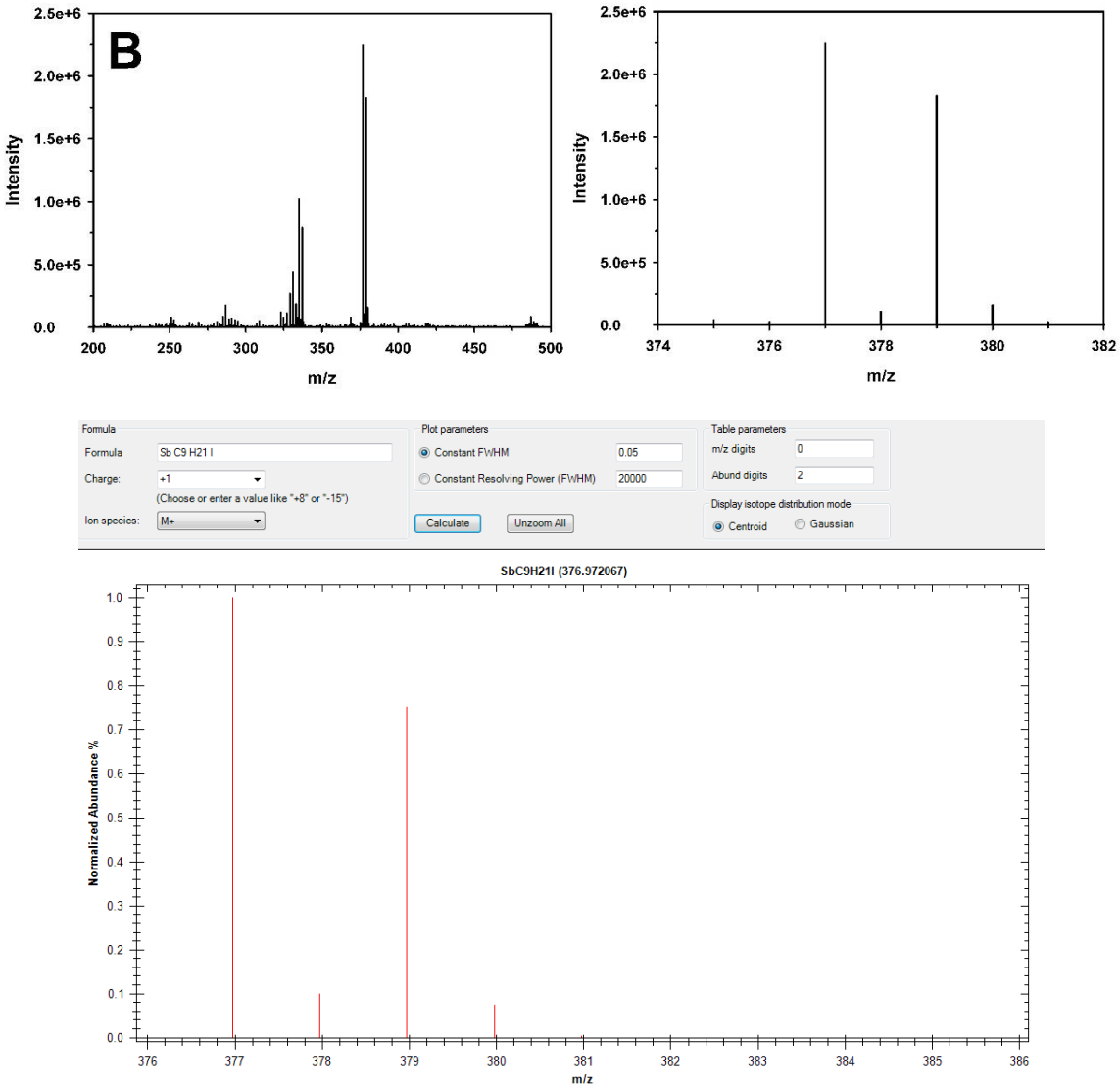


**Figure 2.19** *(Top)* CI mass spectrum of the filtrate following nickel metal deposition from **1** *(A)* and of the independently synthesized $Sb(^{i}Pr_3)(I)_2$ *(B)*. The main feature at 377/379 *m*/*z* is $[Sb(^{i}Pr_3)I]^+$ , which results from the loss of $I^-$ during the ionization and injection process. The lower spectra in both images are the expanded view in the *m*/*z* region of interest. (*Bottom*) Theoretical mass spectrum of $[Sb^{i}Pr_3I]^+$.

*It is critical to note that the deposition results accurately reflect the computational work used to determine the Tolman electronic parameter of each of the ligands.* The

strongest σ-donating ligand, $Sb^{i}Pr_3$, was best able to scavenge iodine from solution [→$Sb(^{i}Pr_3)(I)_2$] and prevent the formation of CuI, thus allowing for the cleanest deposition of nickel metal (ultimately as NiCu alloy) on the Si|Cu wafers. In contrast, the weakest donating and therefore least reactive $I_2$ acceptor ($SbMe_2Ph$) showed minimal efficacy in removing $I^-/I_2$, and the resulting surface exhibited a significant extent of CuI. It can be inferred from our data that in order to exclusively deposit nickel – desirable for any industrial or semiconductor deposition process – a strongly donating antimony ligand bound to the nickel is required. Any extraneous factors – such as $Tl(BAr^F_4)$ or a CO ligand – hinder the deposition process. The use of even more strongly donating antimony ligands, such as $Sb(^{t}Bu)_3$ or $Sb(Cy)_3$, bound to nickel(II) may result in cleaner depositions, milder conditions, and shorter reaction times for deposition on the Si|Cu wafers.

## 2.5 CONCLUSION

The findings of this work are manifold and can be summarized as follows:

(1) Commercially available triphenyl antimony ($SbPh_3$) does not bind or react with Ni under any tested condition in non-coordinating solvents (polar or non-polar) or coordinating solvents (THF, MeCN) due to its combination of moderately weak σ-donor strength and moderately large cone angle.

(2) Substitution of even a single phenyl unit in $SbPh_3$ for a *smaller* yet *electron-withdrawing* substituent [Ph→Me; see point (5) below] induces binding to $NiI_2$ due to the decreased cone angle (Sb more available for metal binding). This proves that the lack of $SbPh_3$ binding to $NiI_2$ (or other metals) is not *exclusively* due to its weak σ-donor strength.

(3) A range of synthetic, alkyl-substituted antimony ligands of the homoleptic (R = $^{i}$Pr, Me) and heteroleptic (R = $^{i}$Pr, Me, Ph) variety stably bind $NiI_2$ to form complexes that are square planar (2 Sb ligands) or trigonal bipyramidal (3 Sb ligands).

(4) The steric size of these antimony R-groups – as determined by 'classical' Tolman cone angle (119-155°), and the newly calculated percent buried volume (PBV = 24.0-27.5%) – is an effective determinant of the complex geometry (trigonal-bipyramidal < 26% PBV [140 °] < square-planar).

(5) DFT calculations provide the Tolman electronic parameter for this set of ligands (2060-2070 $cm^{-1}$), which demonstrates the unexpected electron-withdrawing nature of the methyl substituent relative to the phenyl substituent in this case.

(6) Despite their TBP geometry, complexes **3** and **4** were *experimentally* determined (solid state: magnetic susceptibility; solution: NMR, UV/vis) to be diamagnetic; this is attributed to the asymmetry of donors in the equatorial plane (two iodides and one $SbR_3$) versus the previously reported and more symmetric TBP complex $[Ni(MDABCO)_2(Cl)_3]ClO_4$ ($S$ = 1).[191] Intriguingly, DFT calculations on the *geometry-optimized* structure of $\mathbf{4_{DFT}}$ indicate a more stable paramagnetic state ($S$ = 1) versus the diamagnetic configuration at zero point energy ($S$ = 0, +10 kcal/mol).

(7) Overall, and in concert with a published report,[191] this study provides guidelines to design a paramagnetic, TBP Ni(II) complex derived from heavy-atom pnictogen ligands.

(8) Deposition of a clean Ni/Cu alloy using mild conditions in an organic solvent on a Si|Cu substrate is possible with a nickel-antimony complex that has strong enough σ donating ligands (i.e., $Sb^{i}Pr_3$) to scavenge $I^{-}/I_2$ from solution. The use of a weaker σ donating ligands (e.g., $SbMe_2Ph$) promotes the undesired deposition of iodine-containing species (CuI).

(9) More broadly, this work refutes the dogma that antimony can be categorically described as a poor or ineffective σ donor for divalent 3*d* metals, and this report illustrates that judicious selection of alkyl substituents can greatly enhance the practical binding ability of antimony(III) ligands.

## 2.6 REFERENCES


(131) Bianchini, C.; Fornasiero, P. A Synthetic Nickel Electrocatalyst with a Turnover Frequency above 100000 $s^{-1}$ for $H_2$ Production. *ChemCatChem* **2012**, *4*, 45–46.

(132) Bini, L.; Müller, C.; Wilting, J.; Von Chrzanowski, L.; Spek, A. L.; Vogt, D. Highly Selective Hydrocyanation of Butadiene toward 3-Pentenenitrile. *J. Am. Chem. Soc.* **2007**, *129*, 12622–12623.

(133) Speiser, F.; Braunstein, P.; Saussine, L. New Nickel Ethylene Oligomerization Catalysts Bearing Bidentate P,N-Phosphinopyridine Ligands with Different Substituents a to Phosphorus. *Organometallics* **2004**, *23*, 2625–2632.

(134) Baber, R. A.; Haddow, M. F.; Middleton, A. J.; Orpen, A. G.; Pringle, P. G.; Haynes, A.; Williams, G. L.; Papp, R. Ligand Stereoelectronic Effects in Complexes of Phospholanes, Phosphinanes, and Phosphepanes and Their Implications for Hydroformylation Catalysis. *Organometallics* **2007**, *26*, 713–725.

(135) Clavier, H.; Nolan, S. P. Percent Buried Volume for Phosphine and N-Heterocyclic Carbene Ligands: Steric Properties in Organometallic Chemistry. *Chem. Commun.* **2010**, *46*, 841–861.

(136) Fukin, G. K.; Guzei, I. A.; Baranov, E. V.; Domrachev, G. A. Analysis of the Supramolecular Structures of Sb(III) and Sb(V) Catecholate Complexes from the Viewpoint of Ligand Solid Angles. *Struct. Chem.* **2009**, *20*, 643–654.

(137) Poddel'Sky, A. I.; Smolyaninov, I. V.; Berberova, N. T.; Fukin, G. K.; Cherkasov, V. K.; Abakumov, G. A. Triaryl/Trialkylantimony(V) Catecholates with Electron-Acceptor Groups. *J. Organomet. Chem.* **2015**, *789–790*, 8–13.

(138) Jones, J. S.; Wade, C. R.; Yang, M.; Gabbaï, F. P. On the Coordination Non-Innocence of Antimony in Nickel(II) Complexes of the Tetradentate (*o*-$(Ph_2P)C_6H_4)_3Sb$ Ligand. *Dalt. Trans.* **2017**, *46*, 5598–5604.

(139) Imyanitov, N. S. Electronic and Steric Effects of Ligands in Square-Planar, Trigonal Bipyramidal, and Octahedral Complexes. *Koord. Khimiia* **1992**, *18*, 1127–1138.

(140) Breunig, H. J.; Ghesner, I. Coordination Compounds with Organoantimony and $Sb_n$ Ligands. *Adv. Organomet. Chem.* **2003**, *49*, 95–131.

(141) Werner, H.; Schwab, P.; Heinemann, A.; Steinert, P. Bis(Triisopropylarsan) - Und Bis(Triisopropylstiban)-Rhodium(I)-Komplexe Mit Isonitrilen, Olefinen, Alkinen Und Diinen Als Liganden. *J. Organomet. Chem.* **1995**, *496*, 207–216.

(142) Grünwald, C.; Laubender, M.; Wolf, J.; Werner, H. Acetato and Acetylacetonato Ruthenium(II) Complexes Containing $Sb^iPr_3$, $P^iPr_3$ and $PCy_3$ as Ligands. *J. Chem. Soc. Dalt. Trans.* **1998**, 833–840.

(143) Yang, J.; Li, P.; Zhang, Y.; Wang, L. A New Library of Arsine, Stibine-Stabilized N-Heterocyclic Carbene Palladium Complexes: Synthesis, Structures and Activities in C-C and C-N Coupling Reactions. *Dalt. Trans.* **2014**, *43*, 14114–14122.

(144) Gomes, C. S. B.; Krishnamoorthy, P.; Silva, L. C.; Costa, S. I.; Gomes, P. T.; Jiménez-Tenorio, M.; Valerga, P.; Puerta, M. C. First Examples of Neutral and Cationic Indenyl Nickel(II) Complexes Bearing Arsine or Stibine Ligands: Highly Active Catalysts for the Oligomerisation of Styrene. *Dalt. Trans.* **2015**, *44*, 17015–17019.

(145) Mlynek, P. D.; Dahl, L. F. New Nickel-Antimony Carbonyl Clusters : Stereochemical Analyses of the $[Ni_{10}(SbR)_2(CO)_{18}]_2$ - Dianions (R) Me, Et, $^i$Pr, $^t$Bu, *p*-$FC_6H_4$) Containing Empty 1,12-$Ni_{10}Sb_2$ Icosahedral Cages and of the Unprecedented Stibinido-Bridged. *Organometallics* **1997**, *16*, 1641–1654.

(146) Desenfants, R. E.; Gavney, J. A.; Hayashi, R. K.; Rae, A. D.; Dahl, L. F. Reactions of the $[Ni(CO)R_2]^{2-}$ Dianion with Stibine and Bismuthine Reagents : Synthesis and Stereophysical Characterization of the $(Ni_1(SbPh)_2(CO)Is]$* - Dianion Containing a Noncentered Icosahedral Ni, Sb, Core and Ni*$(CO)P_2$, *J. Organomet. Chem.* **1990**, *2033*, 543–572.

(147) Goicoechea, J. M.; Hull, M. W.; Sevov, S. C. Heteroatomic Deltahedral Clusters: Synthesis and Structures of Closo-$[Bi_3Ni_4(CO)_6]^{3-}$, Closo-$[Bi_4Ni_4(CO)_6]^{2-}$, the

Open Cluster $[Bi_3Ni_6(CO)_9]^{3-}$, and the Intermetalloid Closo-$[Ni_x@\{Bi_6Ni_6(CO)_8\}]^{4-}$. *J. Am. Chem. Soc.* **2007**, *129*, 7885–7893.

(148) Albano, V. G.; Demartin, F.; Iapalucci, M. C.; Laschi, F.; Longoni, G.; Sironi, A.; Zanello, P. Icosahedral Carbonyl Clusters $[Ni_{10}Sb_2(M_{12}\text{-}Ni)\{Ni(CO)_3\}^{2-}(CO)_{18}]^{n-}$ (n = 2, 3 or 4); Synthesis, Spectroscopic, Electrochemical and Bonding Analysis. Crystal Structures of $[Ni_{10}Sb_2(M_{12}\text{-}Ni)\{Ni(CO)_3\}_2(CO)_{18}]^{n-}$ (n = 2 or 3). *J. Chem. Soc. Dalt. Trans.* **1991**, 739–748.

(149) Charles, S.; Eichhorn, B. W.; Bott, S. G. Synthesis and Structure of $[Sb_7Ni_3(CO)_3]^{3-}$: A New Structural Type for Nido 10-Vertex Polyhedral Clusters. *J. Am. Chem. Soc.* **1993**, *115*, 5837–5838.

(150) Moses, M. J.; Fettinger, J. C.; Eichhorn, B. W. $[Ni_5Sb_{17}]^{4-}$ Transition-Metal Zintl Ion Complex: Crossing the Zintl Border in Molecular Intermetalloid Clusters. *Inorg. Chem.* **2007**, *46*, 1036–1038.

(151) Charton, M. Substituent Effects of Arsenic, Antimony, and Bismuth Groups. In *Organic Arsenic, Antimony, and Bismuth Compounds*; Patai, S., Ed.; John Wiley & Sons, Ltd: West Sussex, 1994; pp 367–439.

(152) Casares, J. A.; Espinet, P.; Martín-Alvarez, J. M.; Martínez-Ilarduya, J. M.; Salas, G. Stable Nickel Catalysts for Fast Norbornene Polymerization: Tuning Reactivity. *Eur. J. Inorg. Chem.* **2005**, *2005*, 3825–3831.

(153) Tolman, C. A. Steric Effects of Phosphorus Ligands in Organometallic Chemistry and Homogeneous Catalysis. *Chem. Rev.* **1976**, *77*, 313–348.

(154) Ferguson, G.; Roberts, P. J.; Alyea, E. C.; Khan, M. Cone Angle and Ligand Profile Calculations for Bulky Phosphine Ligands. *Inorg. Chem.* **1978**, *17*, 2965–2967.

(155) Wu, K.; Doyle, A. G. Parameterization of Phosphine Ligands Demonstrates Enhancement of Nickel Catalysis via Remote Steric Effects. *Nat. Chem.* **2017**, *9*, 779–784.

(156) Mallory, G. O.; Hajdu, J. B. *Electroless Plating: Fundamentals and Applications*; William Andrew, 1990.

(157) Djokie, S. Electroless Deposition Deposition of of Cobalt Cobalt Using Using Hydrazine Hydrazine as an Electroless Reducing Agent. *J. Electrochem. Soc.* **1997**, *144*, 2358–2363.

(158) Paunovic, M.; Schlesinger, M. *Fundamentals of Electrochemical Deposition, 2nd Edition*; Wiley and Sons, 2006.

(159) CrystalClear 1.40. CrystalClear 1.40 (2008). Rigaku Americas Corporation: The Woodlands, TX 2008.

(160) Sheldrick, G. M. SHELXT - Integrated Space-Group and Crystal-Structure Determination. *Acta Crystallogr. Sect. A Found. Crystallogr.* **2015**, *71*, 3–8.

(161) Sheldrick, G. M. Crystal Structure Refinement with SHELXL. *Acta Crystallogr. Sect. C Struct. Chem.* **2015**, *71*, 3–8.

(162) Spek, A. L. Structure Validation in Chemical Crystallography. *Acta Crystallogr. Sect. D Biol. Crystallogr.* **2009**, *65*, 148–155.

(163) Farrugia, L. J. WinGX and ORTEP for Windows: An Update. *J. Appl. Crystallogr.* **2012**, *45*, 849–854.

(164) Saint V8.27 B. SAINT V8.27B Bruker AXS Inc, (2012): Madison, WI.

(165) Granovsky, A. A. Firefly v. 7, www http://classic.chem.msu.su/gran/firefly/index.html.

(166) Andrienko, G. A. Chemcraft, https://www.chemcraftprog.com.

(167) Bode, B. M.; Gordon, M. S. MacMolPlt: A Graphical User Interface for GAMESS. *J. Mol. Graph. Model.* **1998**, *16*, 133–138.

(168) Herber, U.; Weberndörfer, B.; Werner, H. Formation of Novel Dinuclear Mixed-Valence Rhodium Complexes by Intramolecular Migration of a Chelating Ligand. *Angew. Chemie Int. Ed.* **1999**, *38*, 1609–1613.

(169) Chan, K. H.; Leong, W. K.; Hang, K.; Mak, G. Thermolysis of the Osmium - Antimony Clusters $Os_3(CO)_{11}(SbMe_2Ar)$: Higher Nuclearity Clusters and Arrested Ortho Metalation. *Organometallics* **2006**, *25*, 250–259.

(170) Taylor, W. V.; Soto, U. H.; Lynch, V. M.; Rose, M. J. Antimony-Supported $Cu_4I_4$Cuboid with Short Cu-Cu Bonds: Structural Premise for Near-Infrared Thermoluminescence. *Inorg. Chem.* **2016**, *55*, 3206–3208.

(171) Imyanitov, N. S. Cone Angle of Ligands - Group IV and V Compounds. *Koord. Khimiya* **1985**, *11*, 1171–1178.

(172) Scott, M. J.; Christian, W.; Wilisch, A.; Armstrong, W. H. Unprecedented Example of Four Coordination at a Vanadium(II) Center. Synthesis, Structure, and Properties of a Reactive, Nearly Planar V(II) Phenolate Complex, $[V(DIPP)_4\{Li(THF)\}_2]$ (DIPP = 2,6-Diisopropylphenolate). *J. Am. Chem. Soc.* **1990**, *112*, 2429–2430.

(173) Poddel'Sky, A. I.; Cherkasov, V. K.; Bubnov, M. P.; Abakumova, L. G.; Abakumov, G. A. EPR Study of Mono-*o*-Iminobenzosemiquinonato Nickel(II) Complexes with Ni-C σ-Bond. *J. Organomet. Chem.* **2005**, *690*, 145–150.

(174) Falivene, L.; Credendino, R.; Poater, A.; Petta, A.; Serra, L.; Oliva, R.; Scarano, V.; Cavallo, L. SambVca 2. A Web Tool for Analyzing Catalytic Pockets with Topographic Steric Maps. *Organometallics* **2016**, *35*, 2286–2293.

(175) Kendall, A. J.; Zakharov, L. N.; Tyler, D. R. Steric and Electronic Influences of Buchwald-Type Alkyl-JohnPhos Ligands. *Inorg. Chem.* **2016**, *55*, 3079–3090.

(176) Riley, L. E.; Krämer, T.; McMullin, C. L.; Ellis, D.; Rosair, G. M.; Sivaev, I. B.; Welch, A. J. Large, Weakly Basic Bis(Carboranyl)Phosphines: An Experimental and Computational Study. *Dalt. Trans.* **2017**, *46*, 5218–5228.

(177) Poater, A.; Cosenza, B.; Correa, A.; Giudice, S.; Ragone, F.; Scarano, V.; Cavallo, L. SambVca: A Web Application for the Calculation of the Buried Volume of N-Heterocyclic Carbene Ligands. *Eur. J. Inorg. Chem.* **2009**, *13*, 1759–1766.

(178) Garrou, P. E.; Heck, R. F. The Mechanism of Carbonylation of Halo(Bis Ligand)Organoplatinum(II), -Palladium(II), and -Nickel(II) Complexes. *J. Am. Chem. Soc.* **1976**, *98*, 4115–4127.

(179) SaintJoly, C.; Mari, A.; Gleizes, A.; Dartiguenave, M.; Dartiguenave, Y.; Galy, J. Reaction of Monodentate (Tertiary Phosphine)Nickel(II) Complexes $NiX_2(PR_3)_2$, $NiX_2(PMe_3)_3$, and $(NiX(PMe_3)_4)(BF_4)$ with Carbon Monoxide. Crystal and Molecular Structure of $NiI_2(CO)(PMe_3)_2$. *Inorg. Chem.* **1980**, *19*, 2403–2410.

(180) Brock, C. P.; Collman, J. P.; Dolcetti, G.; Farnham, P. H.; Ibers, J. A.; Lester, J. E.; Reed, C. A. A Bent vs. Linear Nitrosyl Paradox. Infrared and X-Ray Photoelectron Spectra of $CoCl_2(NO)L_2$ and Crystal Structure with L = $P(CH_3XC_6H_5)_2$. *Inorg. Chem.* **1973**, *12*, 1304–1313.

(181) Ardizzoia, G. A.; Brenna, S. Interpretation of Tolman Electronic Parameters in the Light of Natural Orbitals for Chemical Valence. *Phys. Chem. Chem. Phys.* **2017**, *19*, 5971–5978.

(182) Bjorsvik, H. R.; Hansen, U. M.; Carlson, R. Principal Properties of Monodentate Phosphorus Ligands. Predictive Model for the Carbonyl Absorption Frequencies in $Ni(CO)_3L$ Complexes. *Acta Chem. Scand.* **1997**, *51*, 733–741.

(183) Flener Lovitt, C.; Frenking, G.; Girolami, G. S. Donor-Acceptor Properties of Bidentate Phosphines. DFT Study of Nickel Carbonyls and Molecular Dihydrogen Complexes. *Organometallics* **2012**, *31*, 4122–4132.

(184) Benner, G. S.; Hatfield, W. E.; Meek, D. W. Five-Coordinate Nickel(II) Complexes with Tris(3-Dimethylarsinopropyl)Phosphine. *Inorg. Chem.* **1964**, *3*, 1544–1549.

(185) Lever, A. B. P. *Inorganic Electronic Spectroscopy*, 1st ed.; Elsevier Publishing Company: Amsterdam, 1984.

(186) Coussmaker, C. R. C.; Hely Hutchinson, M.; Mellor, J. R.; Sutton, L. E.; Venanzi, L. M. Tetrahedral Nickel(II) Complexes and the Factors Determining Their Formation. Part II.* Complexes with Dibutylphenylphosphine and Butyldiphenylphosphine. *J. Chem. Soc.* **1961**, 2705–2713.

(187) Ciampolini, M.; Nardi, N. Five-Coordinated High-Spin Complexes of Bivalent Cobalt, Nickel, and Copper with Tris(2-Dimethylaminoethyl)Amine. *Inorg. Chem.* **1966**, *5*, 41–44.

(188) Gray, H. B. Electronic Structures of Square Planar Metal Complexes. *Transit. Met. Chem. A Ser. Adv.* **1965**, *1*, 239–287.

(189) Dubois, T. D.; Meek, D. W. Five-Coordination. IV. Nickel(II) Complexes Of Diphenyl(o-Diphenylarsinophenyl)Phosphine. *Inorg. Chem.* **1967**, *6*, 1395–1398.

(190) Bröring, M.; Prikhodovski, S.; Brandt, C. D. The First (Tripyrrinato)Nickel(II) Complexes, TrpyNiX with X = Cl, Br, I: Synthesis, Structures and Solvent Coordination. *J. Chem. Soc., Dalt. Trans.* **2002**, 4213–4218.

(191) Marriott, K. E. R.; Bhaskaran, L.; Wilson, C.; Medarde, M.; Ochsenbein, S. T.; Hill, S.; Murrie, M. Pushing the Limits of Magnetic Anisotropy in Trigonal Bipyramidal Ni(II). *Chem. Sci.* **2015**, *6*, 6823–6828.

(192) Ruamps, R.; Maurice, R.; Batchelor, L.; Boggio-Pasqua, M.; Guillot, R.; Barra, A. L.; Liu, J.; Bendeif, E. E.; Pillet, S.; Hill, S.; et al. Giant Ising-Type Magnetic Anisotropy in Trigonal Bipyramidal Ni(II) Complexes: Experiment and Theory. *J. Am. Chem. Soc.* **2013**, *135*, 3017–3026.

(193) Gruden-Pavlovic, M.; Peric, M.; Zlatar, M.; Garcia-Fernandez, P. Theoretical Study of the Magnetic Anisotropy and Magnetic Tunnelling in Mononuclear Ni(II) Complexes with Potential Molecular Magnet Behavior. *Chem. Sci.* **2014**, *5*, 1453–1462.

(194) Yang, H.; Gabbal, F. P. Activation of a Hydroamination Gold Catalyst by Oxidation of a Redox-Noninnocent Chlorostibine Z-Ligand. *J. Am. Chem. Soc.* **2015**, *137*, 13425–13432.

## 2.7 NMR SPECTRA

### 2.7.1 Ligand NMR Spectra

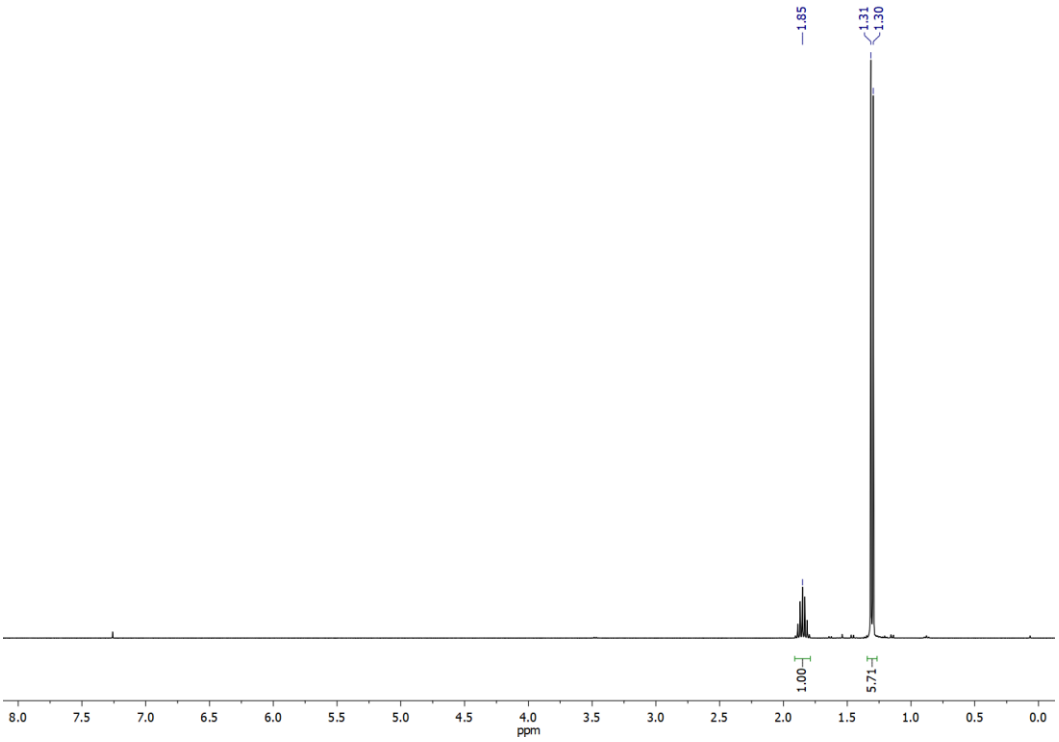


**Figure 2.20** $^{1}$H NMR spectrum of Sb$^{i}$Pr$_3$ in $CDCl_3$ obtained at 400 MHz.

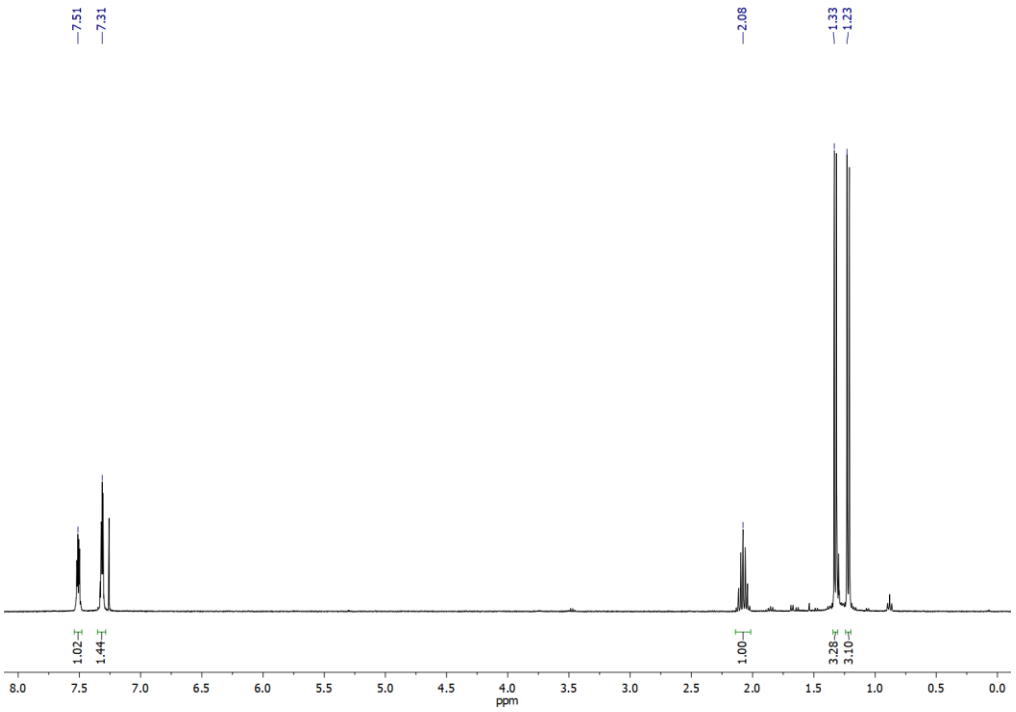


**Figure 2.21** $^{1}$H NMR spectrum of Sb$^{i}$Pr$_2$Ph in $CDCl_3$ obtained at 400 MHz.

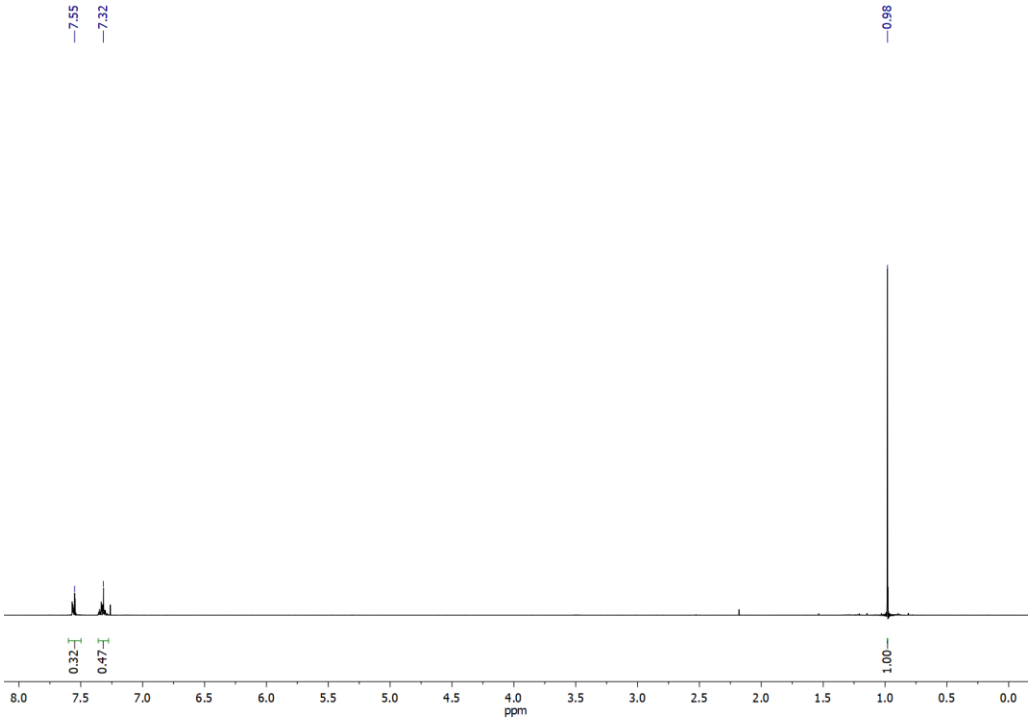

**Figure 2.22** $^{1}$H NMR spectrum of $SbMe_2Ph$ in $CDCl_3$ obtained at 400 MHz.

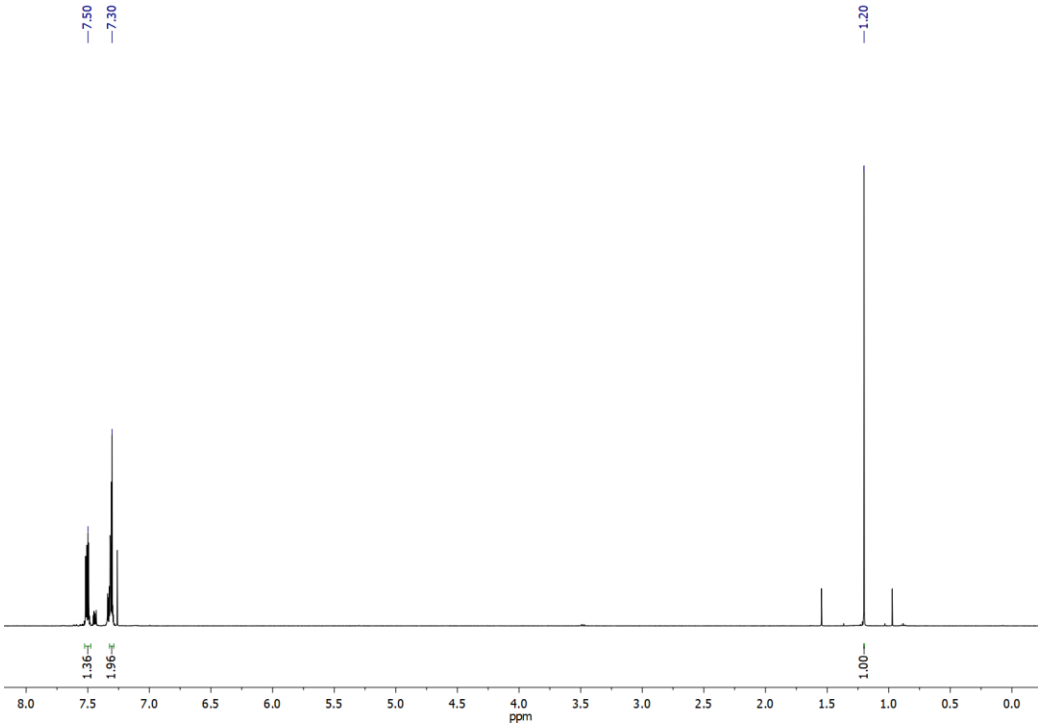


**Figure 2.23** $^{1}$H NMR spectrum of $SbMePh_2$ in $CDCl_3$ obtained at 400 MHz.

### 2.7.2 Metal Complex NMR Spectra

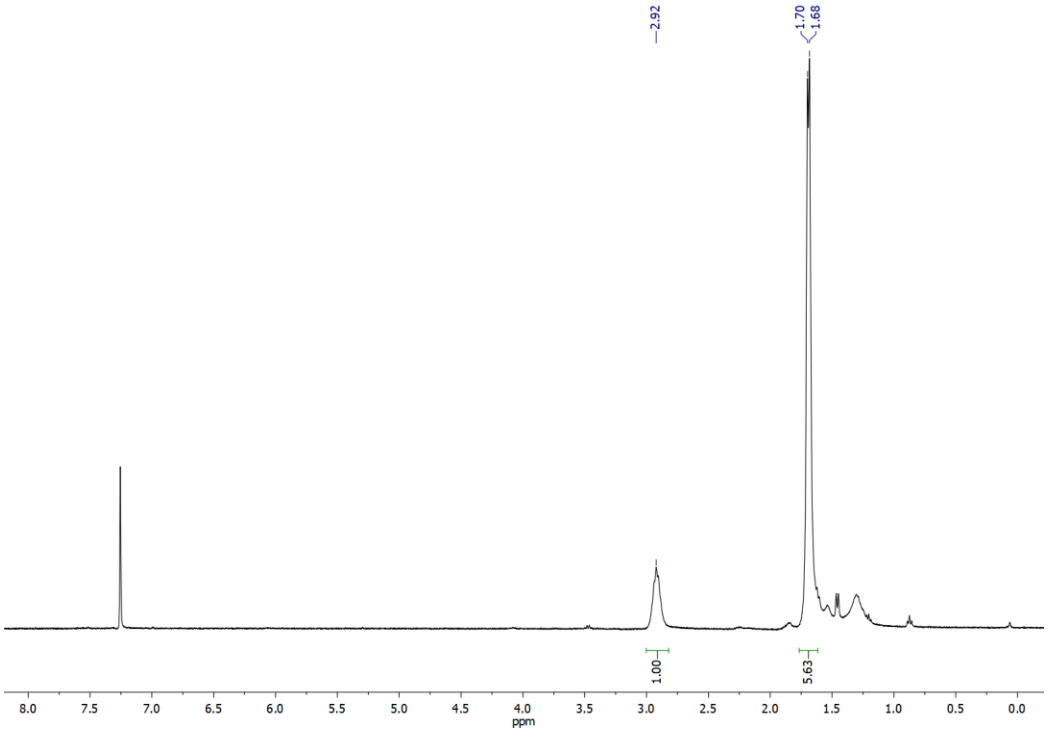


**Figure 2.24** $^{1}$H NMR spectrum of $Ni(I)_2(Sb^{i}Pr_3)_2$ [**1**] in $CDCl_3$ obtained at 400 MHz.

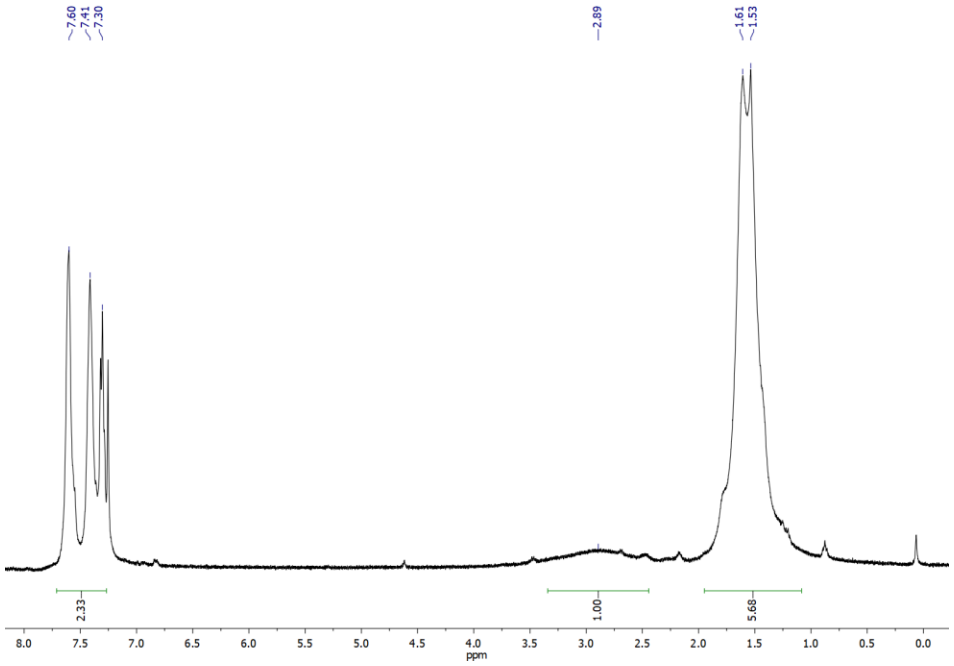

**Figure 2.25** $^{1}$H NMR spectrum of $Ni(I)_2(Sb^{i}Pr_2Ph)_2$ [**2**] in $CDCl_3$ obtained at 400 MHz.

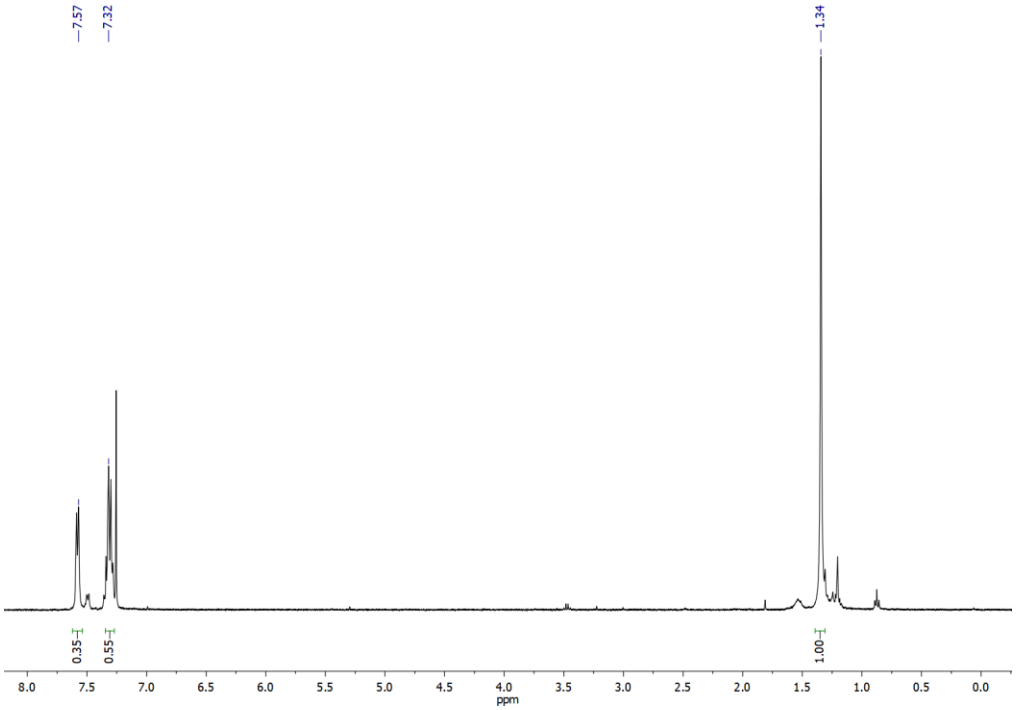


**Figure 2.26** $^{1}$H NMR spectrum of $Ni(I)_2(SbMe_2Ph)_3$ [**3**] in $CDCl_3$ obtained at 400 MHz.

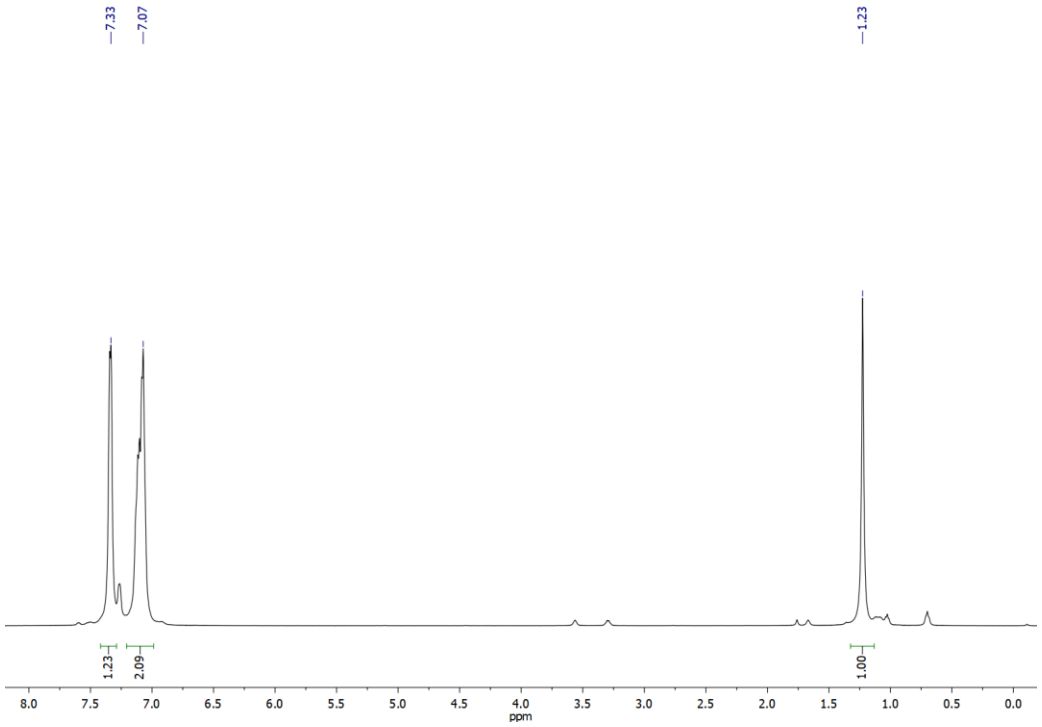


**Figure 2.27** $^{1}$H NMR spectrum of $Ni(I)_2(SbMePh_2)_3$ [**4**] in $CDCl_3$ obtained at 400 MHz.

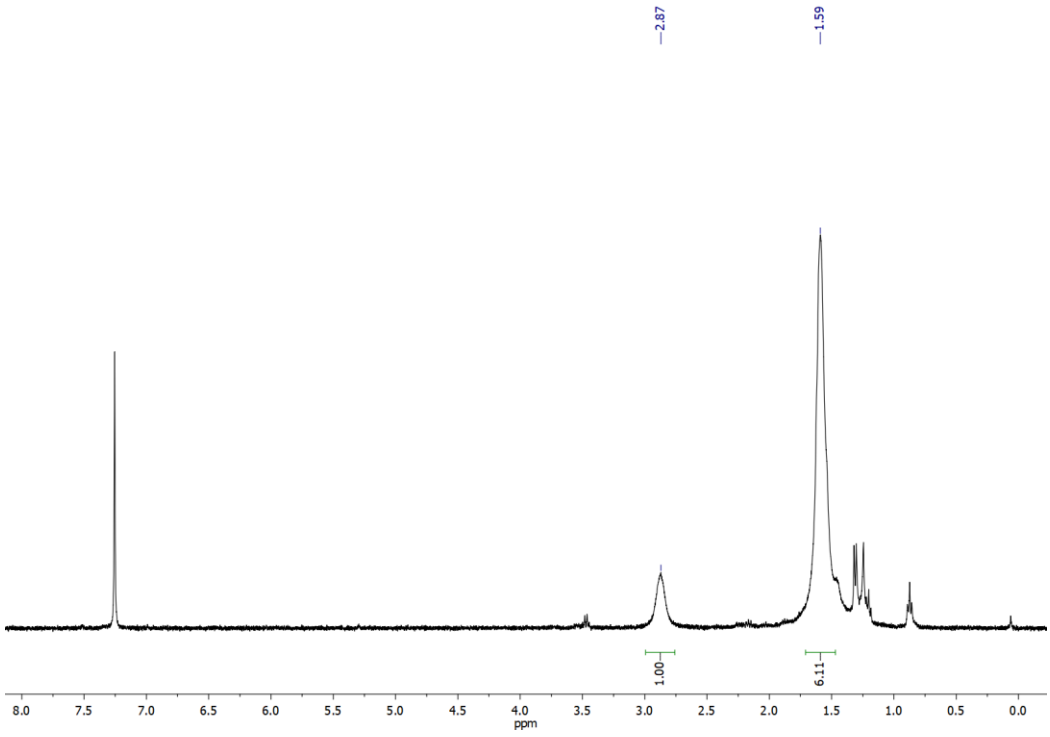

**Figure 2.28** $^{1}$H NMR spectrum of $Ni(I)_2(Sb^{i}Pr_3)_2CO$ [**5**] in $CDCl_3$ obtained at 400 MHz.

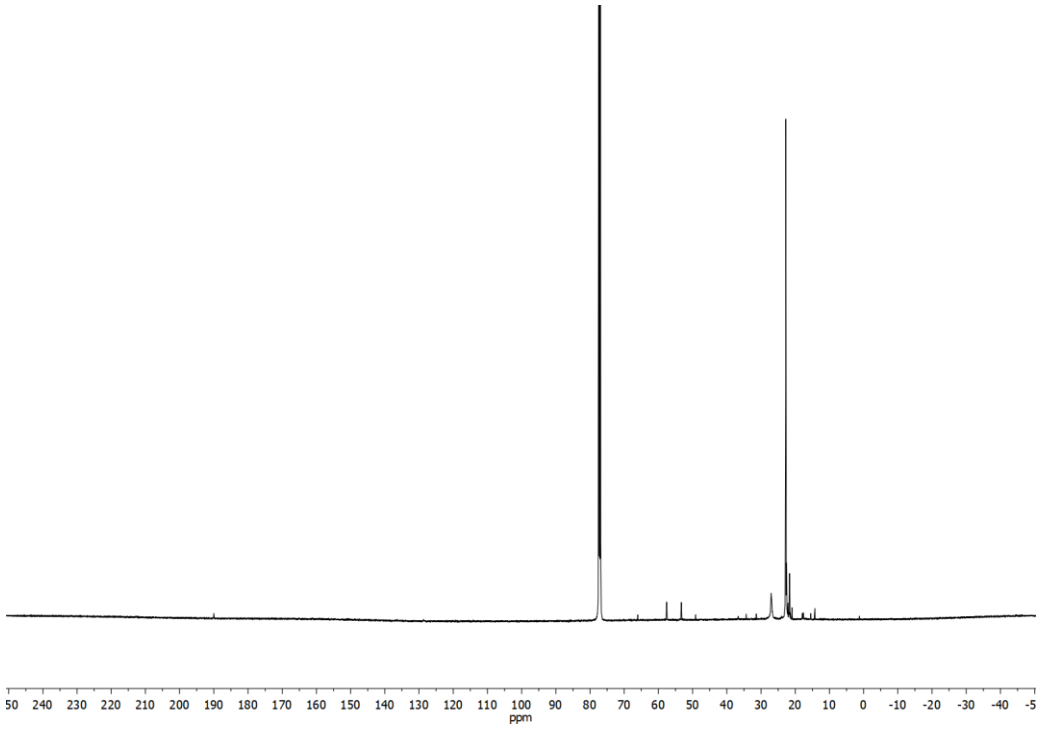


**Figure 2.29** $^{13}$C NMR spectrum of $Ni(I)_2(Sb^{i}Pr_3)_2CO$ [**5**] in $CDCl_3$ obtained at 500 MHz.

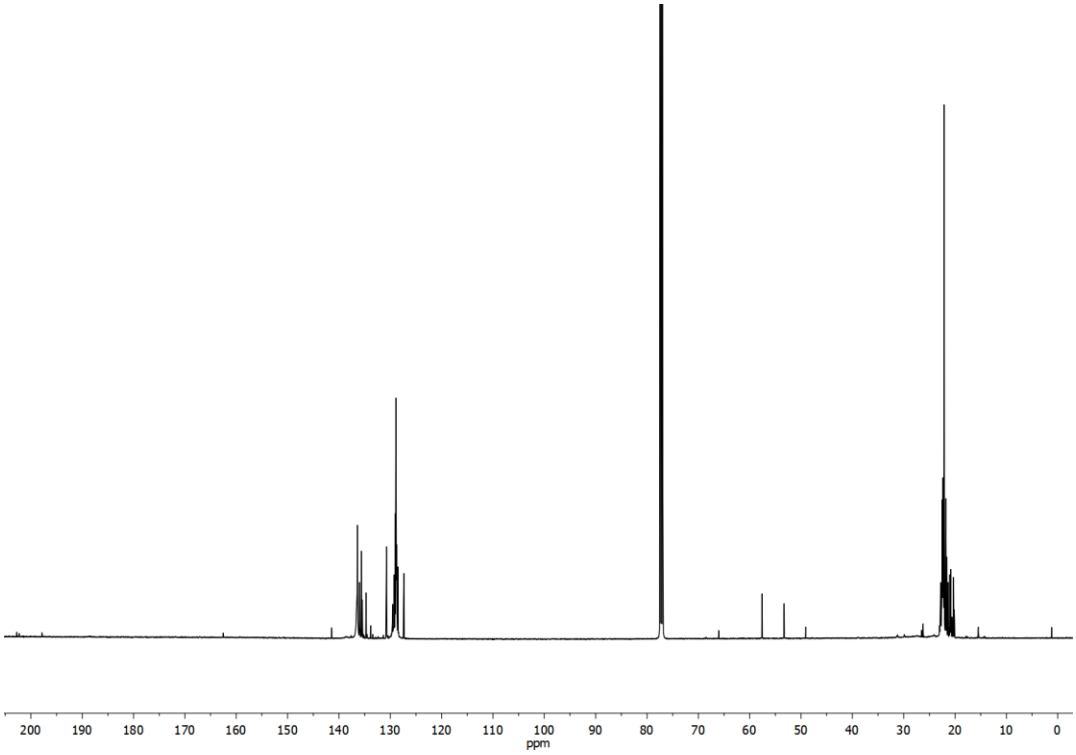


**Figure 2.30** $^{13}C$ NMR spectrum of $Ni(I)_2(Sb^iPr_2Ph)_2CO$ [**6**] in $CDCl_3$ obtained at 500 MHz.

## 2.8 CRYSTAL TABLE AND REFINEMENT PARAMETERS

The full crystallographic data and refinement parameters for complexes **1**-**5** are tabulated in Table 2.5.

| | $Ni(I)_2(Sb^iPr_3)_2$ (1) | $Ni(I)_2(Sb^iPr_2Ph)_2$ (2) | $Ni(I)_2(SbMe_2Ph)_3$ (3) | $Ni(I)_2(SbMePh_2)_3$ (4) | $Ni(I)_2(Sb^iPr_3)_2CO$ (5) |
|---|---|---|---|---|---|
| Formula | $C_{27}H_{63}I_3Ni_{1.5}Sb_3$ | $C_{24}H_{38}I_2NiSb_2$ | $C_{24}H_{33}I_2NiSb_3$ | $C_{19.5}H_{19.5}INi_{0.5}Sb_{1.5}$ | $C_{19}H_{42}I_2NiOSb_2$ |
| FW | 1221.79 | 882.55 | 999.26 | 592.73 | 842.53 |
| Color | Violet | Violet | Violet | Violet | Violet |
| Habit | Needle | Needle | Needle | Needle | Needle |
| Size ($mm^3$) | 0.2 × 0.2 × 0.15 | 0.3 × 0.1 × 0.1 | 0.4 × 0.1 × 0.1 | 0.3 × 0.1 × 0.1 | 0.33 × 0.15 × 0.08 |
| T (K) | 100 (2) | 100 (2) | 100 (2) | 100 (2) | 100 (2) |
| Lattice | Triclinic | Monoclinic | Monoclinic | Triclinic | Triclinic |
| Space Group | *P*-1 | *Cc* | $P_{21/n}$ | *P*-1 | *P*-1 |
| a (Å) | 8.9343(10) | 7.9090(13) | 9.8565(9) | 13.0086(10) | 8.515(2) |
| b (Å) | 12.7490(12) | 22.337(4) | 17.638(2) | 13.6381(12) | 12.156(3) |
| c (Å) | 18.464(2) | 16.527(3) | 34.677(4) | 16.2879(15) | 13.751(3) |
| α (deg) | 83.570(4) | 90.0 | 90 | 70.758(6) | 90.908(5) |
| β (deg) | 88.241(3) | 94.584(4) | 98.17 | 71.584(5) | 91.517(6) |
| γ (deg) | 69.632(6) | 90.0 | 90 | 66.784(5) | 106.541(5) |
| V ($Å^3$) | 1959.1(4) | 2910.4(8) | 5967.3(11) | 2449.0(4) | 1363.6(6) |
| Z | 2 | 4 | 8 | 4 | 2 |
| $d_{calc}$ ($g/cm^3$) | 2.071 | 2.014 | 2.225 | 1.608 | 2.052 |
| μ ($mm^{-1}$) | 5.130 | 4.614 | 5.388 | 3.296 | 4.921 |
| GOF on $F^2$ | 1.130 | 1.082 | 0.841 | 1.037 | 1.129 |
| R indices [I > 2σ(I)] | $R_1$ = 0.0160<br>$wR_2$ = 0.0411 | $R_1$ = 0.0634<br>$wR_2$ = 0.1788 | $R_1$ = 0.0290<br>$wR_2$ = 0.0580 | $R_1$ = 0.0808<br>$wR_2$ = 0.1949 | $R_1$ = 0.0908<br>$wR_2$ = 0.2726 |
| R indices all data | $R_1$ = 0.0180<br>$wR_2$ = 0.0418 | $R_1$ = 0.0658<br>$wR_2$ = 0.1823 | $R_1$ = 0.0495<br>$wR_2$ = 0.0606 | $R_1$ = 0.1400<br>$wR_2$ = 0.2214 | $R_1$ = 0.0966<br>$wR_2$ = 0.2756 |

**Table 2.5** Crystallographic data and refinement parameters for the antimony-nickel complexes **1**-**5**.

# Chapter 3: Thermoluminescent Copper-Antimony Complexes – NIR Emissions through High Crystallographic Symmetry and Structure-Luminescence Correlations[2]

## 3.1 INTRODUCTION

Transition metal complexes and clusters with luminescent properties have found utility in fields ranging from OLEDs, bioimaging devices, and pressure-sensing devices (mechanochromism).[195–197] In addition, the discovery of new molecules and materials that achieve near-IR (NIR) emission is desirable for applications such as deep-tissue bio-imaging, photodynamic therapy, and novel two-photon and triplet-transfer solar technologies.[198–200] Long-lived NIR emission (phosphorescence) is difficult to achieve due to the closer proximity of lower-lying triplet states to thermally excited ground states.[201,202] Additionally, the presence of high energy oscillators (such as O-H and C-H bonds) cause vibrational quenching in NIR emitters and limit long-lived emissions.[203,204] While a number of examples of organic-based dyes and sensors for NIR emission and sensing have been reported,[205,206] these are largely limited to short-lived fluorescence rather than longer-lived phosphorescence, which has a higher possibility for persistent emission past initial excitation.[207]

The use of transition metals and — in conjunction, heavy atoms to enhance intersystem crossing — could afford new classes of bright, long-lived phosphors for biological and energy applications. However, there is a need for fundamental studies of transition metal-based NIR phosphorescent complexes, clusters and materials. In

[2] Portions of this chapter were published in:
Taylor, W.V., Soto, U.H., Lynch, V.M., Rose, M.J., *Inorg. Chem.*, **2016**, *55*, 3206-3208.
Taylor, W.V., Cammack, C.X., Shubert, S.A., Rose, M.J., *Inorg. Chem.*, *Accepted* (**DOI**: 10.1021/acs.inorgchem.9b00229).
My contributions included the syntheses, structures, and analyses of luminescence measurements and other data for all copper-antimony complexes. Mike Rose and I wrote > 99 % of the manuscripts together.

particular, copper-based complexes are intriguing for their low cost and relative stability. Luminescent copper complexes exist in the form of monomers, dimers, tetramers, and polymeric species—and their emission wavelengths span the entire visible spectrum.[208,209] An interesting subset of luminescent copper-halide compounds are the cubes with general structure $Cu_4X_4L_4$ (where X = halide; L = pnictogen ligand). These complexes, which take on the form of a cubane as the $Cu_4X_4$ motif forms the core and the pnictogen donors ligate to the copper vertices, exhibit a unique property known as luminescent thermochromism. Luminescent thermochromism is a phenomenon in which emission intensity and energy fluctuate as a function of temperature. First discovered by Hardt,[210] luminescent thermochromism is classically explained as being derived from two triplet excited states: one originating at the center of the copper cluster ($^3$CC) and one originating from charge transfer from the halide to the ligand ($^3$XLCT).[211] Typically, a low energy (LE) band is observed at room temperature and corresponds to the CC transition; whereas at low temperatures, this band is abolished and the presence of a high energy (HE) band emerges, corresponding to the XLCT process. As the excitation wavelength is usually located in the near-UV or near visible region, these compounds will luminesce when exposed to a simple blacklight – and changing the temperature can cause them to change colors. Notably, neither band (specifically, the LE band) has been reported to occur in the near-infrared (NIR) region.

There have been several luminescent copper iodide cubanes with supporting phosphorus-based ligands. For example, elegant work by Benito et al. has demonstrated that the copper-iodo-phosphine cube $[Cu_4(I)_4(PPh_3)_4]$ exhibits several emission features, including a LE band at 535 nm and an HE band at 425 nm.[212] Both the intensity and energy of these bands were modulated by temperature. Additionally, these authors showed a correlation between decreased Cu–Cu distances and increased luminescence (ligand and

metal based). A summary of their complex and its luminescent properties – that can hopefully serve as an example of a copper-based luminescent thermochromism emission portfolio – can be seen in Figure 3.1.

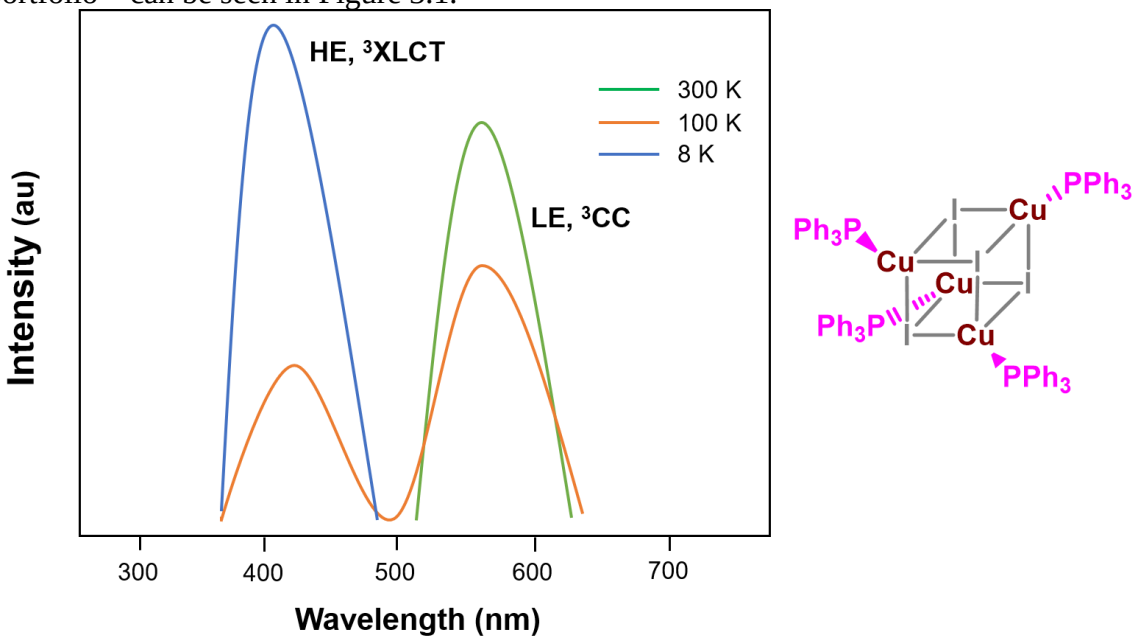


**Figure 3.1** (Left) Pictorial depiction of a variable temperature emission spectra of $Cu_4(I)_4(PPh_3)_4$, highlighting the thermochromic nature of these complexes. (Right) Structure of $Cu_4(I)_4(PPh_3)_4$ showing the cubane geometry.

Extensive literature on phosphine-supported $Cu_4I_4$ cubes has elucidated a number of structure-activity design principles. In general, phosphine-supported cubes exhibit luminescent properties at ambient temperatures, regardless (without known exception) of the phosphine substituents. Second, the emissive properties of these cubes are dependent on temperature – primarily via thermochromism; that is, two competing emissive states (LE = 500-600 nm, HE = 400-500 nm; see paragraphs above) can be proportionally accessed depending on the temperature. Studies have shown that thermochromic properties (i.e. the presence of the HE XLCT band) are dependent on the identity of the phosphine

substituents. Namely, the presence of *two* phenyl substituents (e.g. $PPh_2Pr$, $PPh_2OEt$, $PPh_2CH_2CH{=}CH_2$)[211,213,214] appears to be required to impart thermochromism, whereas *one* phenyl unit is insufficient. For example, the $PPhMe^iPr$ supported cube is simply luminescent (LE emission only, RT→77 K).[215]

Among published thermochromic copper cubes, the $Cu_4I_4$ core remains constant for the most part, but the supporting ligand can be modulated. Although a select number of arsenic-based copper iodide cubes have been synthesized, these complexes were not vetted for thermochromic properties.[216,217] Additionally, the arsenic-supported cubanes retain the rigid cube-like structure of their phosphorus congeners. Several chalcogen based luminescent cubanes have been reported as well. [218,219] To date, there have been no reported copper-iodide cubanes with antimony as supporting ligand. Indeed, antimony presents several interesting properties that could affect cube geometry and therefore luminescence. For example, heavy atoms have been shown to red-shift both absorption and emission features.[220,221] Additionally, the diffuse 5*p* lone pair of Sb results in a weak σ-donor strength,[222] which could promote longer Cu–L(Sb) bonds and correspondingly shorter Cu–Cu bonds. Thus, we sought to synthesize new copper-iodide cubanes with antimony ligands to investigate the "heavy-atom effect" as well as observe any structural or physical modulations that may affect the luminescent properties of this class of compounds.

## 3.2 EXPERIMENTAL

### 3.2.1 Physical Measurements

NMR ($^1H$ and $^{13}C$) measurements were obtained using a 500 MHz Bruker AVANCE III NMR (supported by NSF grant 1 S10 OD021508-01); $CDCl_3$ was referenced to 7.26 ppm and 77.2 ppm for $^1H$ and $^{13}C$ spectra, respectively. Elemental analyses (C, H) were performed by Midwest Microlab, IN Absorption spectra were recorded on a Varian

Cary 6000i UV-VIS-NIR spectrophotometer using Starna Quartz Fluorometer Cells with path lengths of 10 mm. Luminescence measurements were recorded on a Photon Technology International QM 4 spectrofluorimeter. BryteBox interface using FeliX32 software. Luminescence spectra were excited using a xenon short-arc lamp (USHIO, UXL-75XE) and recorded with a PTI detection system (model 814) and photomultiplier tube (Hamamatsu, R928P) connected to a PTI lamp power supply (LPS-250B). Time-resolved spectra were excited with a xenon flash lamp (Hamamatsu, L4633) and recorded using a photomultiplier tube (Hamamatsu, R562) connected to a PTI XenoFlash power supply.

### 3.2.2 X-ray Data Collection

For complexes **1**, **2**, **3**, **4**, and **7**, the X-ray diffraction data were collected on a Rigaku AFC12 diffractometer with a Saturn 724+ CCD using a Bruker AXS Apex II detector and a graphite monochromator with MoKα radiation (λ = 0.71073 Å). Low temperatures were maintained using an Oxford Cryostream low temperature device. Data reduction was performed using the Rigaku Crystal Clear version 1.40.[159] Structures were solved by direct methods using SHELXT[160] and refined by full-matrix least-squares on $F^2$ with anisotropic displacement parameters for the non-H atoms using SHELXL-2014/7.[161] Structure analysis was aided by use of the programs PLATON[162] and WinGX.[163] For complexes **5** and **6**, the X-ray diffraction data were collected at –173 °C on a Nonius Kappa CCD diffractometer using a Bruker AXS Apex II detector and a graphite monochromator with MoKα radiation (λ = 0.71073Å). Reduced temperatures were maintained by use of an Oxford Cryosystems 700 low-temperature device. Data reduction was performed using SAINT V8.27B.[164] The structure was solved by direct methods using SHELXT[160] and refined by full-matrix least-squares on $F^2$ with anisotropic displacement parameters for the

non-H atoms using SHELXL-2014/7.[161] Structure analysis was aided by use of the programs PLATON[162] and WinGX.[163]

### 3.2.3 DFT, Tolman Angle and Percent Buried Volume (%$V_B$) Calculations

The program Firefly[165] was used for DFT calculations using the B3LYP functional with the following basis sets per atom: Sb, TZP; I, 6-311G; Cu, C and H: 6-31G**. The ground state structure was geometry optimized from the X-ray coordinates, and the excited state triplet was, in turn, optimized from the ground state structure. The resulting structures were visualized with MacMolPlt.[167] The orbital energy diagram was constructed in Mathematica. Tolman cone angles were calculated using the Mathematica package FindConeAngle developed by Allen et. al.[223] Percent buried volumes were calculated using SambVca (Cavallo et. al).[41]

### 3.2.4 Ditertbutylphenylantimony ($Sb^tBu_2Ph$)

Tert-butyl magnesium chloride solution (2.0 M in $Et_2O$, 20.8 mL, 41.7 mmol) was added dropwise to a stirring solution of $SbCl_2Ph$ in $Et_2O$ (5 g, 18.5 mmol, 125 mL) on ice. The solution was refluxed for three hours, then allowed to cool to room temperature. The solution was quenched with degassed water (70 mL). Under completely inert atmosphere, the organic layer was separated, dried over sodium sulfate and filtered. The solvent was removed *in vacuo* to produce a slightly yellow oil. A distillation was performed at 130 °C to afford the product as a colorless clear oil (1.7 g, 5.4 mmol). Yield: 30 %. $^1$H NMR ($CDCl_3$): 1.31 (s 18H, -C*H*$_3$), 7.31 (mult 3H, aromatic C*H*), 7.61 (mult 2H, aromatic C*H*). $^{13}$C NMR ($CDCl_3$): δ = 31.6, 34.6, 128.4, 129.1, 135.6, 137.5.

### 3.2.5 Tritertbutylantimony ($Sb^tBu_3$)

A solution of $SbCl_3$ in $Et_2O$ (3 g, 13.1 mmol, 100 mL) was added dropwise to a stirring solution of tert-butyl magnesium chloride solution (2.0 M in $Et_2O$, 26.3 mL, 52.6 mmol) on ice. The solution was refluxed for three hours, then allowed to cool to room temperature. The solution was quenched with degassed water (70 mL). Under completely inert atmosphere, the organic layer was separated, dried over sodium sulfate and filtered. The solvent was removed *in vacuo* to produce a slightly yellow oil. A distillation was performed at 100 °C to provide the product as a slightly yellow oil (1.0 g, 3.4 mmol). Yield: 26%. $^1$H NMR ($CDCl_3$): 1.33 (s 18H, -C*H*$_3$). $^{13}$C NMR ($CDCl_3$): δ = 32.3, 34.7.

### 3.2.6 Tricyclohexylantimony ($SbCy_3$)

A solution of $SbCl_3$ in $Et_2O$ (2.5 g, 10.9 mmol, 100 mL) was added dropwise to a stirring solution of cyclohexyl magnesium chloride solution (1.0 M in $Et_2O$, 38.3 mL, 38.3 mmol) on ice. The solution was refluxed for three hours, then allowed to cool to room temperature. The solution was quenched with degassed water (70 mL). Under completely inert atmosphere, the organic layer was separated, dried over sodium sulfate and filtered. The solvent was removed *in vacuo* to produce a white solid (2.7 g, 7.2 mmol). Yield: 66 %. $^1$H NMR ($CDCl_3$): 1.31 (mult 12H, -C*H*$_2$), 1.48 (mult 3H, -C*H*), 1.73 (mult 18H, -C*H*$_2$). $^{13}$C NMR ($CDCl_3$): δ = 27.1, 28.2, 29.0, 32.9.

### 3.2.7 $[Cu_4(I)_4(Sb^iPr_3)_4]$ (1)

A suspension of copper (I) iodide (0.285 g, 1.49 mmol) in fluorobenzene was added to a solution of triisopropylantimony (1.50 g, 5.96 mmol) in fluorobenzene at –20 °C. The solution was allowed to warm to room temperature and stirred overnight. The solution was then filtered and the solvent removed *in vacuo*. The residue was extracted into pentane, filtered, and then the solution was placed into a freezer at –20 °C, where crystals of the

desired complex crashed out of the pentane solution (0.495 g, 19% yield). $^{1}$H NMR ($C_6D_6$): δ 1.49 (d, 72H, -$CH_3$), 2.05 (hept, 12H, -CH). Anal. cald (% wt.) for $Cu_4I_4Sb_4C_{36}H_{84}$: C, 24.49; H, 4.79. Found: C, 24.19; H, 4.79.

### 3.2.8 $Cu_4(I)_4(SbCy_3)_4$ (2)

Copper iodide (0.14 g, 0.74 mmol) was added to $SbCy_3$ (0.28 g, 0.74 mmol) in 15 mL fluorobenzene at –20 °C under an inert argon atmosphere. The reaction was allowed to warm to room temperature and stirred overnight. The clear, slightly yellow solution was filtered, and the solvent was removed *in vacuo* to afford a light yellow oil and a white precipitate. The product was washed several times with pentane to remove the oil, leaving the desired product as white solid (0.15 g, 0.07 mmol). Yield: 36%. Crystals suitable for X-ray crystallography were obtained via slow vapor diffusion of pentane into a DCM solution of the product at –20 °C. $^{1}$H NMR: ($CDCl_3$): 1.27 (mult 18H, -C$H_2$), 1.73 (mult 12H, -C$H_2$), 1.95 (mult 3H, -C*H*). $^{13}$C NMR ($CDCl_3$): δ = 26.9, 29.0, 29.2, 32.3. Anal. cald (% wt.) for $Cu_4I_4Sb_4C_{72}H_{132}$: C, 38.49; H, 5.92. Found: C, 38.37; H, 5.95.

### 3.2.9 $Cu_4(I)_4(Sb^tBu_3)_4$ (3)

Copper iodide (0.08 g, 0.42 mmol) was added to $Sb^tBu_3$ (0.5 g, 1.7 mmol) in 15 mL fluorobenzene at –20 °C under an inert argon atmosphere. The reaction was allowed to warm to room temperature and stirred overnight to provide a colorless solution and a white precipitate. The solution was decanted off and the white solid was washed several times with pentane to remove impurities, leaving behind the purified desired product as a white solid (0.051 g, 0.03 mmol). Yield: 25%. Crystals suitable for X-ray crystallography were obtained via slow vapor diffusion of pentane into a DCM solution of the product at –20 °C.

$^{1}$H NMR ($CDCl_3$): 1.47 (s 18H, -C$H_3$). $^{13}$C NMR ($CDCl_3$): δ = 32.6, 35.6. Anal. cald (% wt.) for $Cu_4I_4Sb_4C_{48}H_{108}$: C, 29.81; H, 5.63. Found: C, 29.78; H, 5.74.

### 3.2.10 $Cu_4(I)_4(Sb^tBu_2Ph)_4$ (4)

Copper iodide (0.08 g, 0.42 mmol) was added to $Sb^tBu_2Ph$ (0.53 g, 1.7 mmol) in 15 mL fluorobenzene at –20 °C under an inert argon atmosphere. The reaction was allowed to warm to room temperature and stirred overnight to yield a clear colorless solution. The solution was filtered, and the solvent was removed *in vacuo* to generate a light yellow oil. The oil was washed several times with pentane, which precipitated out the product as a white solid (0.065 g, 0.03 mmol). Yield: 31%. Crystals suitable for X-ray crystallography were obtained via slow vapor diffusion of pentane into a DCM solution of the product at –20 °C. $^{1}$H NMR ($CDCl_3$): 1.49 (s 18H, -C$H_3$), 7.33 (mult 3H, aromatic C*H*), 7.90 (mult 2H, aromatic C*H*). $^{13}$C NMR ($CDCl_3$): δ = 32.0, 34.7, 128.5, 129.1, 134.0, 138.1. Anal. cald (% wt.) for $Cu_4I_4Sb_4C_{56}H_{92}$: C, 33.39; H, 4.60. Found: C, 33.17; H, 4.62.

### 3.2.11 $Cu_2(I)_2(Sb^iPr_2Ph)_4$ (5)

Copper iodide (0.04 g, 0.22 mmol) was added to $Sb^iPr_2Ph$ (0.26 g, 0.88 mmol) in 15 mL fluorobenzene at –20 °C under an inert argon atmosphere. The reaction was allowed to warm to room temperature and stirred overnight, yielding a clear, colorless solution. The solvent was removed *in vacuo* to yield a light brown oil and a white precipitate. The oil was dissolved into pentane and placed into the freezer at –20 °C to yield the dimer product as a white crystalline solid (0.03 g, 0.02 mmol). Yield: 16%. Crystals suitable for X-ray crystallography were obtained via slow evaporation of a pentane solution of the product at –20 °C. $^{1}$H NMR: δ 1.39 (d 6H, -C$H_3$), 1.28 (d 6H, -C$H_3$), 2.24 (hept 2H, -C*H*), 7.60 (mult 2H, aromatic C*H*), 7.32 (mult 3H, aromatic C*H*). $^{13}$C NMR ($CDCl_3$): δ = 20.1, 21.9, 128.5,

128.8, 136.3, 136.5. Anal. cald (% wt.) for $Cu_2I_2Sb_4C_{48}H_{76}$: C, 37.90; H, 5.04. Found: C, 37.46; H, 4.56.

### 3.2.12 $Cu_2(I)_2(SbMe_2Ph)_4$ (6)

Copper iodide (0.14 g, 0.75 mmol) was added to $SbMe_2Ph$ (0.68 g, 3.00 mmol) in 15 mL fluorobenzene at –20 °C under an inert argon atmosphere. The reaction was allowed to warm to room temperature and stirred overnight to generate a clear, colorless solution. The solvent was removed *in vacuo* to afford a clear oil. The product was dissolved into pentane and placed into the freezer at –20 °C to yield the product as a white solid (0.11 g, 0.08 mmol). Yield: 23%. Crystals suitable for X-ray crystallography were obtained via slow evaporation of a pentane solution of the product at –20 °C. $^1$H NMR: ($C_6D_6$): 0.85 (s 6H, -C*H*$_3$), 7.10 (mult 3H, aromatic C*H*), 7.53 (mult 2H, aromatic C*H*). $^{13}$C NMR ($CDCl_3$): δ = -1.7, 128.8, 128.9, 134.7, 135.1. Anal. cald (% wt.) for $Cu_2I_2Sb_4C_{32}H_{44}$: C, 29.64; H, 3.42. Found: C, 29.41; H, 3.47.

### 3.2.13 $Cu_2(I)_2(SbPh_3)_4$ (7)

The product $Cu_2(I)_2(SbPh_3)_4$ was prepared according to a published procedure.[224] $^1$H NMR: ($C_6D_6$): 7.23 (mult 2H, aromatic C*H*), 7.34 (mult 3H, aromatic C*H*). $^{13}$C NMR ($CDCl_3$): δ = 128.8, 129.1, 136.4, 138.5. Anal. cald (% wt.) for $Cu_2I_2Sb_4C_{72}H_{60}$: C, 48.23; H, 3.37. Found: C, 45.10; H, 3.25.

### 3.2.14 $Cu_4(I)_4(Sb^iPr_2Ph)_4$ (8)

Copper iodide (0.04 g, 0.22 mmol) was added to $Sb^iPr_2Ph$ (0.06 g, 0.22 mmol) in 15 mL fluorobenzene at –20 °C under an inert argon atmosphere. The reaction was allowed to warm to room temperature and stirred overnight, yielding a clear, colorless solution. The solvent was removed in vacuo to yield a light brown oil and a white precipitate. The product

was washed several times with pentane to remove the oil, leaving the desired product as a white solid (0.09 g, 0.04 mmol). Yield: 51%. $^{1}$H NMR: δ 1.48 (d 6H, -C*H*$_3$), 1.35 (d 6H, -C*H*$_3$), 2.38 (hept 2H, -C*H*), 7.70 (mult 2H, aromatic C*H*), 7.33 (mult 3H, aromatic C*H*). $^{13}$C NMR ($CDCl_3$): δ = 20.8, 21.9, 128.6, 128.9, 136.4, 136.8. Anal. cald (% wt.) for $Cu_4I_4Sb_4C_{48}H_{76}$: C, 30.31; H, 4.03. Found: C, 29.79; H, 3.98.

### 3.3 Results and Discussion For the First Cube – $Cu_4(I)_4(Sb^iPr_3)_4$

#### 3.3.1 Prologue

It must be stated that our work on this project was serendipitous – we did not intend to synthesize these copper cubanes with antimony ligands, or even know of the existence of luminescent thermochromic complexes. We were simply interested in investigating the binding properties of alkyl-antimony ligands to 3*d* transition metals. We had expected a simple tris-ligated $Cu(I)(Sb^iPr_3)_3$ complex but were pleasantly surprised when we solved the crystal structure of $Cu_4(I)_4(Sb^iPr_3)_4$ (**1**, see below) to reveal it was an odd cubane structure. In fact, we didn't know what to do with the compound until reading more about the phosphine analogues of these cubes and seeing the potential for an intriguing luminescence study. Thus, a multi-year project was born, and we have hopefully added to the field in a meaningful way both through novel complexes and a detailed investigation of the correlation between structure and the cluster-centered emission of luminescent copper cubes.

#### 3.3.2 $Cu_4(I)_4(Sb^iPr_3)_4$ – the first cube

The copper-iodo cluster was generated by addition of anhydrous CuI to a solution of $Sb^iPr_3$ in fluorobenzene. The solvent was removed *in vacuo* and the crude material was extracted into pentane, filtered through celite, and the solvent removed *in vacuo* to afford

the antimony-copper-iodo cluster $[Cu_4(I)_4(Sb^iPr_3)_4]$ (**1**) as a white solid (19% yield). Initially, we believed the solid that precipitates out of solution with the addition of pentane was unreacted CuI. However, after working further with these clusters, it was likely not CuI, but rather the main product, **1**. The $Sb^iPr_3$ version of these cubes is soluble in pentane, but only partially. Most of these cubes are not soluble in pentane and (relatively pure) bulk material can be collected by washing the crude material with pentane. That relatively pure bulk material can be further purified by crystallization, but this is a useful tool when one needs to collect a decent amount of material without worrying about crystallizing the complex. Crystals of **1** suitable for X-ray analysis were obtained from a pentane solution of the complex stored at –20 °C.

**Scheme 3.1** Synthesis of $Sb^iPr_3$ and $[Cu_4(I)_4(Sb^iPr_3)_4]$ (**1**).

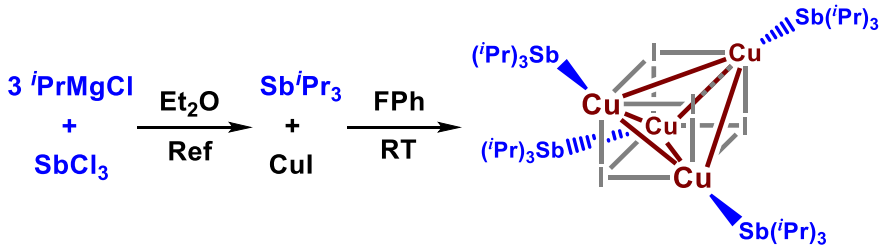


The crystal structure of **1** (100 K, Figure 3.2) reveals that the center of the cuboid is anchored by a tetrahedron comprised of interconnected copper centers. Each copper ion is similarly connected via bridging $\mu_3$-iodides, and each Cu vertex is bound to a capping $Sb^iPr_3$ ligand. The interconnected $Cu_4$ tetrahedron bonding motif in **1** is unique among the existing set of reported copper-iodide-pnictogen cubanes. This appears to be a really interesting aspect of these cubes – the interconnected copper "bonds" are truly differentiated from copper-phosphine cubes, of which there are many. It could be an indication of stronger interactions between the copper atoms (an increased cuprophilicity

in the complex). However, the formal or informal nature of those contacts is ambiguous, as the bonds are rendered in WinGX/ORTEP using a programmed bond distance. Regardless, it is still an indication of short Cu-Cu contacts inside **1**. Additionally, there is no crystallographic asymmetric distortion in the cuboid: the Cu–Cu bond distance of 2.761(3) Å (at 100 K) is uniform throughout the cluster, which is significantly shorter than the copper-copper contacts found in the phosphorous and arsenic analogues [$PPh_3$: ~2.905 Å; $AsPh_3$: ~2.833 Å]. It is important to note that some nitrogen analogues of these cubes do have shorter Cu-Cu bond distances: as low as ~2.65 Å!

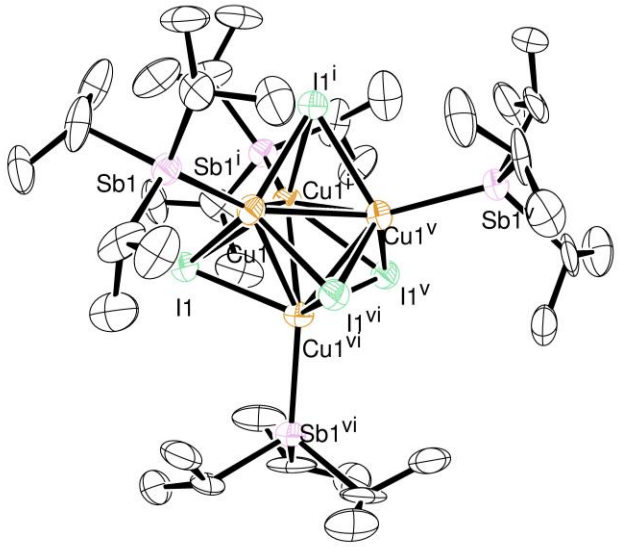


**Figure 3.2** The perspective view (30% thermal ellipsoids) of $[Cu_4(I)_4(Sb^iPr_3)_4]$ (**1**) at 100 K. Selected bond lengths (Å): Cu–Cu = 2.761(3), Cu–Sb = 2.571(2), Cu–I = 2.707(2).

Previous reports of luminescent thermochromism of phosphorous-copper-iodo cubanes prompted us to investigate the solid-state emissive properties of **1**. When exposed to UV light at ambient temperatures, colorless crystals of the complex display no luminescence (Figure 3.3, left). Although it appears to be weak luminescence, that is

merely the reflection of the blacklight on the glass NMR tube/sample. However, at lower temperatures (195 K; Figure 3.3, middle), the complex demonstrates noticeable phosphorescence, and the intensity of the emission increased further as the temperature decreased (77 K; Figure 3.3, right) to afford a bright pink color. This process proved to be reversible, as the luminescence was repeatedly switched 'on' and 'off' with decreases and increases of temperature, respectively. These figures were obtained by preparing 50-100 mg of **1** inside an NMR tube in the glove box, removing the tube from the box, and taking pictures of the sample over a blacklight. It is readily evident that these compounds exponentially increase their emission intensity as the temperature is lowered – the photos may not do the brightness of the sample sufficient justice.

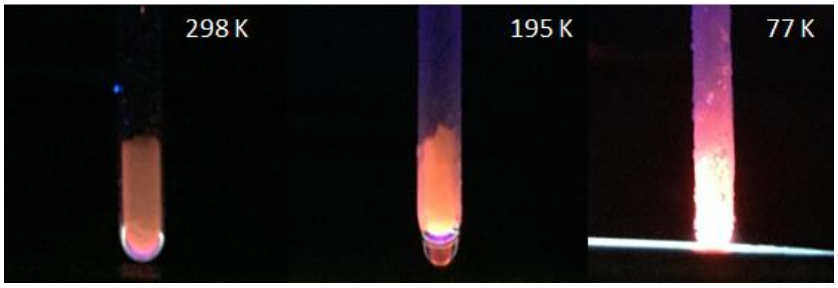


**Figure 3.3** Solid state thermoluminescence of $[Cu_4(I)_4(Sb^iPr_3)_4]$ (**1**) ($\lambda_{Ex}$ = 390 nm) at the temperatures as indicated.

To quantify these observations, solid state emission and excitation spectra were recorded for the complex at 77 K (Figure 3.4, right). More information on how these data were collected and details on the fluorimeter used can be found in the experimental section at the end of this chapter. For the emission data of **1**, most notable is that (*i*) only a single emission feature is observed, and that (*ii*) the emission maximum ($\lambda_{Em}$ = 711 nm) is red-

shifted into the far-Vis/NIR range as compared to the analogous phosphorous cluster $[Cu_4(I)_4(PPh_3)_4]$ ($\lambda_{Em}$ = 535 nm).

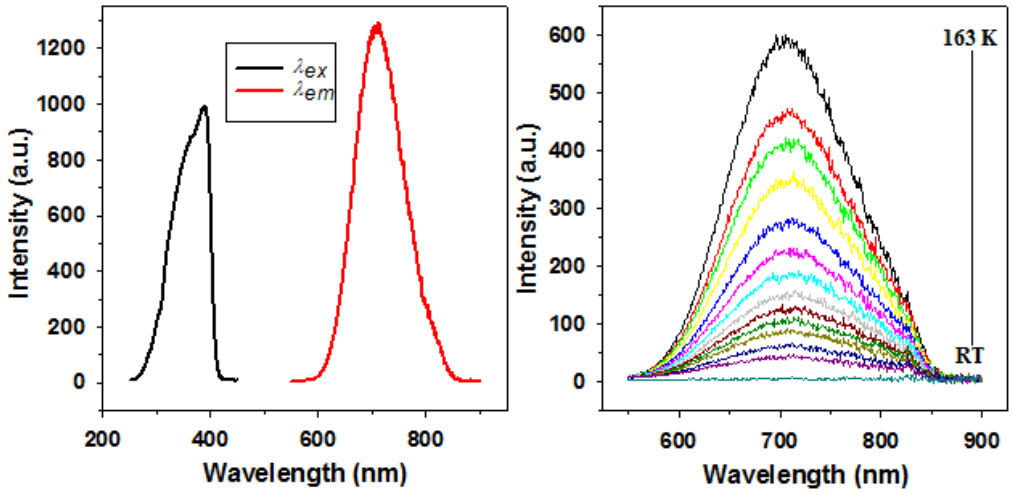


**Figure 3.4** (*Left*) Solid state excitation and emission data at 77 K. (*Right*) Temperature dependence of emission intensity.

To the first point, it is notable that there is no high energy band (or shoulder) in the spectrum, and – consequently – there is no thermo*chromism* observed as the complex cools to lower temperatures. Recent reports have suggested that, at room temperature, the LE band should be the most intense feature in the spectrum, but that the LE band diminishes significantly as the temperature is lowered and the emission becomes dominated by the HE band.[211] Our emission profile shows the LE band is not observable at room temperature and becomes stronger as the temperature decreases, and there is no evidence of a higher energy band appearing at any temperature, seemingly contradicting the previous notion. This could be due to a combination of effects. The lack of a HE band is attributable to the fact that there are no conjugated substituents present on the antimony ligand ($\pi \rightarrow \pi^*$ transitions). In $PPh_3$-based cubes, the phenyl moieties allow for $\pi$ electronic transitions and thus XLCT. Both of these points will be extrapolated on later on in the chapter.

To the second point, the red-shift to the far-visible/NIR is (at least) partially attributable to the 'heavy atom effect', which has been shown to red-shift optical properties and increase the probability of singlet→triplet crossover.[220,221] To further elucidate the luminescence properties of the complex, emission lifetimes were determined for the complex at room temperature and at low temperature (77 K). The lifetime value at room temperature was 1.28 +/- 0.09 μs, while the lifetime at 77 K was 7.7 +/- 0.4 μs. These longer lifetimes and the change in lifetimes at these temperatures are characteristic of phosphorescence and suggest the emission is based on relaxation from a cluster centered triplet excited state. If the emission were fluorescence in origin, the lifetimes would be at a much faster timescale (nanoseconds). A second contributing factor to the low-energy emission is the close proximity of copper nuclei in the cluster, inside of the copper van der Waals radii (vide infra). It has been previously postulated that short Cu-Cu bonds directly correlate with emission energy due to the stronger orbital overlap between the copper atoms. To quantify the decrease in emission intensity, spectra were recorded as the temperature was systematically increased from 163 K to room temperature (Figure 3.4, left). This measurement was conducted using a liquid nitrogen/pentane bath (-163 °C), then allowing the bath to slowly warm up to room temperature and acquiring an emission reading in 5 °C intervals.

This temperature-dependent observation, coupled with hypothesis that the close Cu–Cu contacts in the cuboid could be modulated by temperature, led us to collect single crystal XRD data at six temperatures (100, 150, 200, 250, 273, 300 K) spanning the range of emissive intensities. This measurement was quite facile via the Agilent instrument (UT Austin's Agilent SuperNova has both Mo and Cu microfocus X-ray tubes with an AtlasS2 CCD detector and an Oxford Cryostream 700 low temperature device) and programming it as necessary. One crystal was mounted, the data was collected at the first temperature,

then the temperature was raised 50 °C and the data was collected again. This continued until room temperature was reached. Overall, the core structure of the Sb-Cu-I cuboid remained qualitatively intact. However, the Cu–Cu bond distance systematically increased from 2.761(3) → 2.779(2) → 2.795(3) → 2.821(4) → 2.829(6) → 2.836(4) Å. However, over the same range of temperatures, the Cu–I and Cu–Sb bond distances remained largely invariant (Table 3.1). This strongly suggests that the change in emissive properties is due to thermal modulation of the Cu–Cu bond distance, and in relation, the size of the Cu-Cu core *volume*. The triplet cluster centered excited state is derived from the overlap of the s/p atomic orbitals from the four metals. As the temperature is lowered, the volume of the Cu tetrahedron core decreases and the orbital overlap increases, thus increasing the intensity of the luminescence.[225]

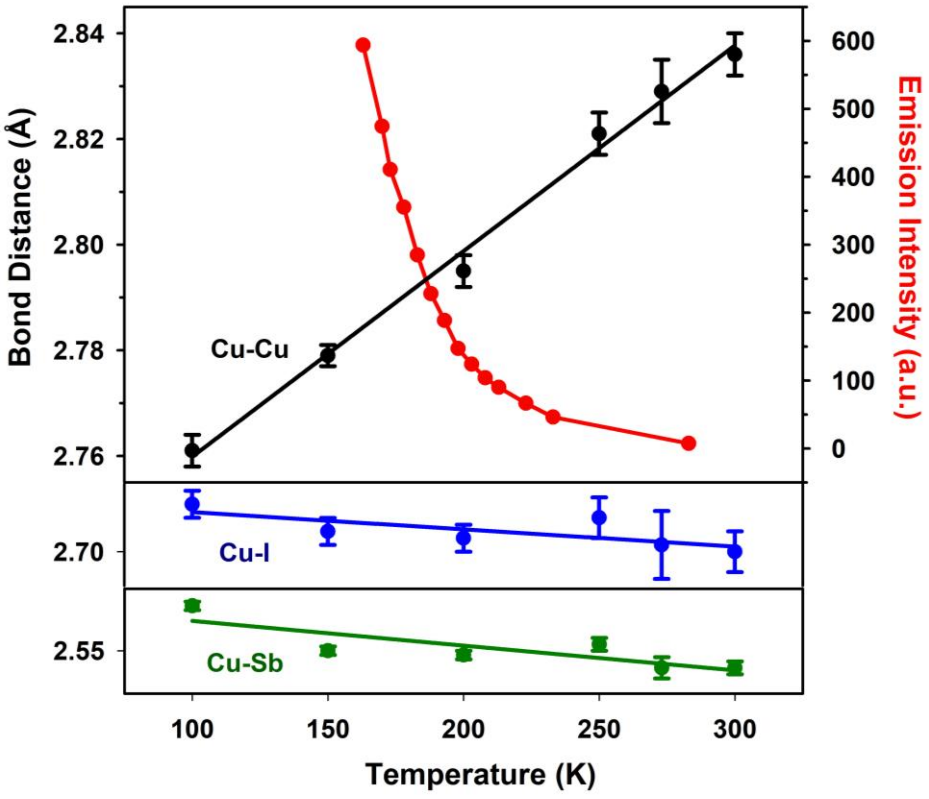

**Figure 3.6** Correlation between the temperature dependent changes in (*i*) Cu–Cu, Cu–Sb or Cu–I bond distances (single crystal XRD) and (*ii*) the emission intensity.

**Table 3.1** Selected bond distances for $[Cu_4(I)_4(Sb^iPr_3)_4]$ (**1**) at various temperatures.

| Temperature | Cu–Cu (Å) | Cu–Sb (Å) | Cu–I (Å) |
|---|---|---|---|
| 100 K | 2.761(3) | 2.571(2) | 2.707(2) |
| 150 K | 2.779(2) | 2.550(2) | 2.703(2) |
| 200 K | 2.795(3) | 2.548(2) | 2.702 (2) |
| 250 K | 2.821(4) | 2.553(3) | 2.705(3) |
| 273 K | 2.829(6) | 2.542(5) | 2.701(5) |
| 300 K | 2.836 (4) | 2.542(3) | 2.700(3) |

To best visualize this effect, Figure 3.6 depicts an overlayed plot of the changes in Cu–Cu bond distance and the emission intensity as a function of temperature. From the data, it is clear that a Cu–Cu distance of ~2.80 Å represents the 'cross-over point', shorter than which the luminescent behavior becomes highly visible. The emission rapidly quenches as the intramolecular copper distance approaches 2.80 Å, which is twice the van der Waals radius for copper and has been suggested to be the upper limit for Cu–Cu bond distance to meaningfully impact the emission energy.[212,218,219] It has been shown that attractive metallophilic interactions are obtained in clusters where Cu-Cu distances are less than 2.80 Å, which could help explain the sudden increase in luminescence.[226] However, the mere presence of luminescence is not precluded on the existence of Cu-Cu distances below 2.80 Å. Several phosphine clusters exhibit luminescent properties with Cu-Cu bond

distances as long as 3.5 Å. Still, our data strongly suggests that the lifetime and/or existence of the $Cu_4$-based triplet state is strongly correlated with the metal-metal bonding motif.

In conclusion, the novel antimony-based copper-iodide cuboid $[Cu_4(I)_4(Sb^iPr_3)_4]$ (**1**) exhibits thermoluminescence in the far-visible/NIR. The close Cu···Cu contacts in the ground state of **1** gave rise to a pseudo-metallic $Cu_4$ tetrahedron at the core of the cuboid, with a ~2.76 Å distance between all copper ions (crystallographically defined) at 100 K. The red-shifted emission feature ($\lambda_{Em}$ > 700 nm), exhibits significant increases in intensity at low temperatures. This increased emission intensity is strongly correlated with short Cu–Cu bond distances of < 2.80 Å (determined by XRD), which appears to be the 'cross-over' point in Cu–Cu distances that support brightly emissive $Cu_4$-based triplet states. Crystal structure solutions for **1** at varying temperatures between 100-300 K revealed a distinct structure-emission correlation between shorter Cu···Cu distances [low T: 2.761(3)→2.836(4) Å, high T] and increased luminescence. Indeed, as the Cu···Cu distance crossed 2× van der Waals radius of copper (~2.80 Å), the emission *intensity* exponentially increased. It is also notable that the Cu···Cu distance found in **1** (~2.76 Å) is distinctly shorter than the average Cu···Cu distance found in phosphine-supported cubes (~2.85-3.15), suggesting that close intermetallic contacts are required for shifting the emission *energy* to the NIR. In contrast, our own data for **1** regarding the structure-emission correlation (temperature dependence) suggests that the Cu···Cu distance controls the emission *intensity*, not the emission *energy*. Thus, based on all of the information presented above, our research goals following this initial discovery and investigation of **1** were to (*i*) shift the emission profile further into the NIR (*ii*) resolve the apparent paradox involving the correlation between Cu···Cu contacts and emission energy/intensity, and (*iii*) develop a fundamental understanding of the correlations among ligand identity, clusters structure, and emission properties.

### 3.4 Towards New Cubes: Thermochromism, NIR emission, and Structure-Luminescence Correlations

It is known (and confirmed in this work) that $SbPh_3$ does not form cube or cuboid structures, and thus further ligand design and synthetic rationale was required to access the cuboid motif. Therefore, to fully elucidate the structure-activity relationships within this class of $Sb_4Cu_4I_4$ clusters, it was necessary to synthesize and employ a wide range of antimony-based ligands — including those with and without phenyl units, larger and smaller cone angles, stronger or weaker donor strength, as well as varying extents of symmetry.

For this next chapter of work, we targeted ligands sterically both larger and smaller than $Sb^iPr_3$, and with stronger and weaker donor strengths to investigate the full range of ligand effects on emission wavelength. However, we had some cause for concern regarding the impact of electronic ligand effects on the LE emission that **1** solely displays. Specifically, a study on electronic ligand effects in phosphine-supported thermochromic cuboids determined that while the ligand donor strength had the expected effect on the high-energy (HE, $^3$XLCT) emission (weaker ligand = lower energy emission), there was no correlation with low-energy (LE, $^3$CC) emission.[227] Perruchas et. al. (currently the most prolific and leading research group studying thermochromic copper clusters) examined the luminescent properties of three copper clusters synthesized with $PPh_3$ ligands modified with varying para-substituents on the phenyl rings. Although there was a correlation between the more electron withdrawing substituents and shorter Cu-Cu distances, they definitively concluded, "One the other hand, there is no direct correlation between the LE emission wavelength and the ligand nature as expected from to the 'Cluster Centered' nature of the corresponding excited state."[227] This was primarily determined by examining two isomers of $Cu_4(I)_4(PPh_3)_4$ that differed in Cu-$Cu_{avg}$ bond distances but not in electronic

ligand effects (as they contain the same $PPh_3$ ligand). The two isomers displayed very different emission energies that corresponded to the LE $^3$CC emission (determined via DFT). Although they did conclude electronic ligand effects do modulate the HE $^3$XLCT emission, we are primarily interested in the LE $^3$CC emission and can rule out the possibility that electronic ligand effects play a meaningful role in determining and accessing NIR emission energies for these Cu-Sb luminescent clusters. Additionally, the lack of access to a family $Sb_4Cu_4I_4$ cuboids derived from *para*-substituted $SbPh_3$ derivatives (R = OMe, $CH_3$, H, $CF_3$)[227] — due to the inability of $SbPh_3$ to support the cuboid motif — prevented the development of a classical Hammett relationship between donor strength and emission properties.

Secondly, the inclusion of a single phenyl unit in the ligand design would greatly amplify the breadth of synthetically accessible heteroleptic ligands with relative ease. In the pursuit of exclusively NIR emitters, we carefully considered whether a proposed series of $SbR_2Ph$ ligands (R = alkyl) would impart the undesirable HE band observed in $PPh_3$-based $Cu_4I_4$ cubes. For example, nearly all reported phenylphosphine-supported copper-halide cubes exhibit LE→HE thermochromism (high temp → low temp) due to the *nb*(I)→π*(Ph) XLMCT.[211,228] However, deeper inspection of the literature reveals that the presence of *two* phenyl substituents (e.g. $PPh_2Pr$, $PPh_2OEt$, $PPh_2CH_2CH{=}CH_2$)[211,213,214] is *actually* required to imbue thermochromism, whereas *one* phenyl unit is insufficient. For example, the $PPhMe^iPr$ supported cube is simply luminescent (LE emission only, RT→77 K).[215] Similarly, no detectable HE emission was observed in a $Cu_4I_4$ cluster without *any* aromatic substituent (L = $Pcyp_3$; cyp = cyclopentyl), but the cluster did exhibit thermoluminescence (like **1** derived from $Sb^iPr_3$).[229] Notably, there are several other examples of alkyl-only phosphorus-based cubes, but these were not investigated for their luminescent properties.[230,231] Therefore, we confidently pursued the synthesis of several

'mono-phenyl' substituted $SbPhR_2$ ligands with the premise of only steric consequences on LE emission.

Although we initially sought to achieve thermochromism with Cu-Sb cuboids, with this new 'mono-phenyl' revelation, we turned our attention to minimizing the NIR emission wavelength and studying the effects that modulate emission wavelength, rather than multiple emissions.

### 3.4.1 Steric Ligand Effects.

We hypothesized that as the steric bulk of the ligand decreased, the $\{Cu–SbR_3\}$ unit would be drawn closer to the cluster center due to fewer steric interactions with the neighboring $SbR_3$ ligands and the iodide ions. Consequently, we postulated smaller size would decrease the average Cu-Cu bond distance, thereby red-shifting the emission derived from the $^3$CC excited state in accordance with published trends.[170,227,228,232] Although our work is exclusively performed with antimony ligands, these findings might apply to any copper-based luminescent clusters. Additionally, by focusing on just one photophysical aspect of these clusters (how sterics modulate the emission energy of the LE emission), we can ensure a thorough analysis without muddying the results with excessive factors.

### 3.4.2 Synthetic Method of Ligands and Clusters.

Antimony ligands with only one aryl group, such as $SbMe_2Ph$ and $SbEt_2Ph$, have been synthesized previously, and others can be synthesized by following a similar procedure.[19,31] Although the synthetic techniques of heteroleptic ligands were covered in previous chapters, it is still valuable to mention critical details for ligands used in this chapter. Each ligand was synthesized by reaction of the appropriate Grignard reagent with either $SbCl_3$ or $SbCl_2Ph$ (crystallized to improve purity, see chapter 2 for more detail on

this technique). The heteroleptic ligands ($SbMe_2Ph$, $Sb^iPr_2Ph$, $Sb^tBu_2Ph$) and $Sb^tBu_3$ required distillations to purify, while the homoleptic ligands did not require additional purification. The copper metalation conditions in fluorobenzene (FPh) are similar to that previously reported for **1** ($Sb^iPr_3$-based). However, the *tert*-butyl based clusters (**3** and **4**) precipitated from FPh, while cluster **2** proved insoluble in pentane during washing of the crude solid. Both of these observations could be due to the decreased solubility caused by the bulkier ligands. For crystallizing the copper cubes, a vapor diffusion of pentane into DCM at -20 °C was successful for complexes **2**-**4** and **8**. As noted previously, **1** is soluble in pentane and crystals can be grown from slow evaporation at -20 °C. All of the dimers are soluble in pentane and can be crystallized from slow evaporation of a pentane solution at -20 °C. The difference in solubility between the dimers and cubes was critical in separating product **5** from **8** (both synthesized from $Sb^iPr_2Ph$). Although the initial reaction conditions will favor the formation of one compound over the other (excess ligand produces dimer, 1:1 CuI to $Sb^iPr_2Ph$ produces cube), the undesirable compound will still appear in the products as an impurity. Copious washing of **8** with pentane will remove **5**, leaving a white precipitate as the final pure product. To obtain **5**, the crude oil can be washed with pentane and that pentane solution can be filtered and placed in a -20 °C freezer to precipitate or crystallize pure **5**. A summary of the synthetic preparations of the ligands and metal complexes is depicted in Schemes 2 and 3, respectively.

**Scheme 3.2** Synthetic preparations of the homoleptic and heteroleptic antimony ligands used in this chapter.

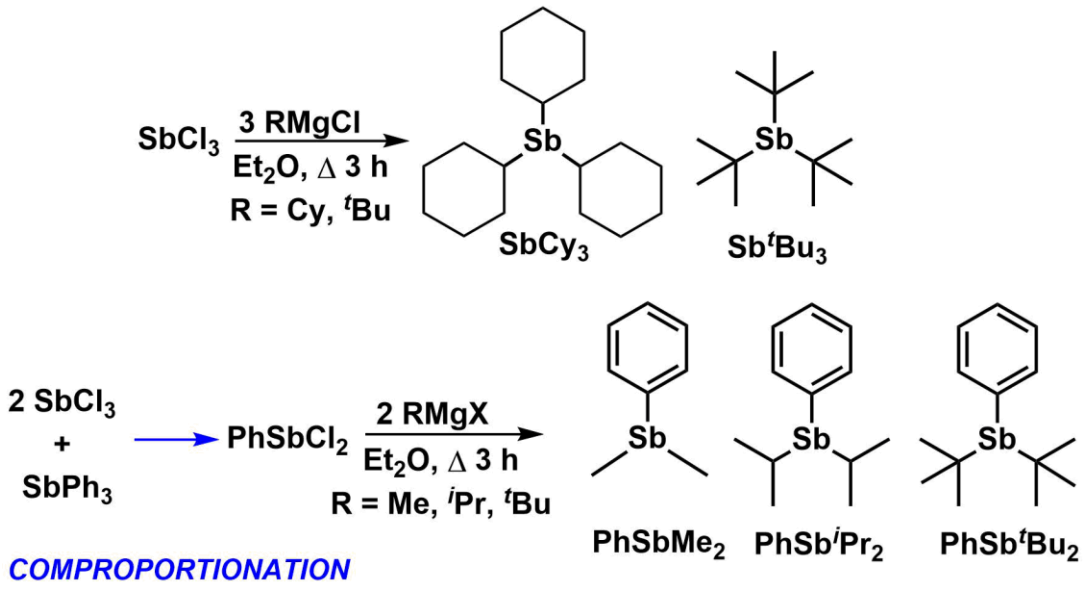


**Scheme 3.3** Synthetic preparations of the copper-antimony cubes and dimers.

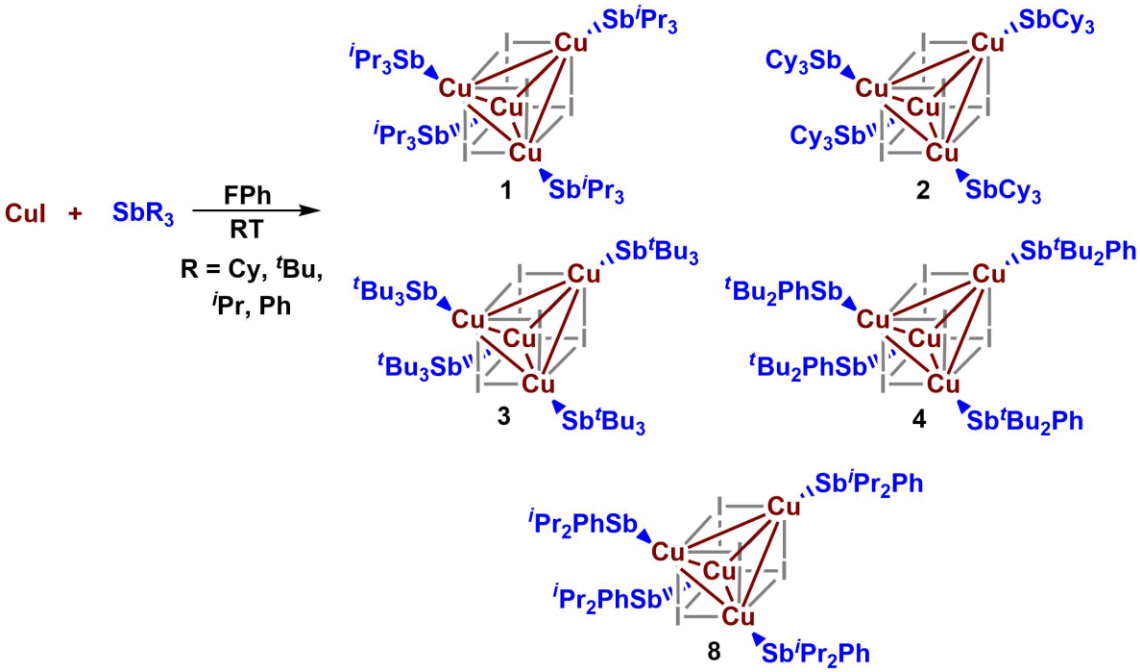


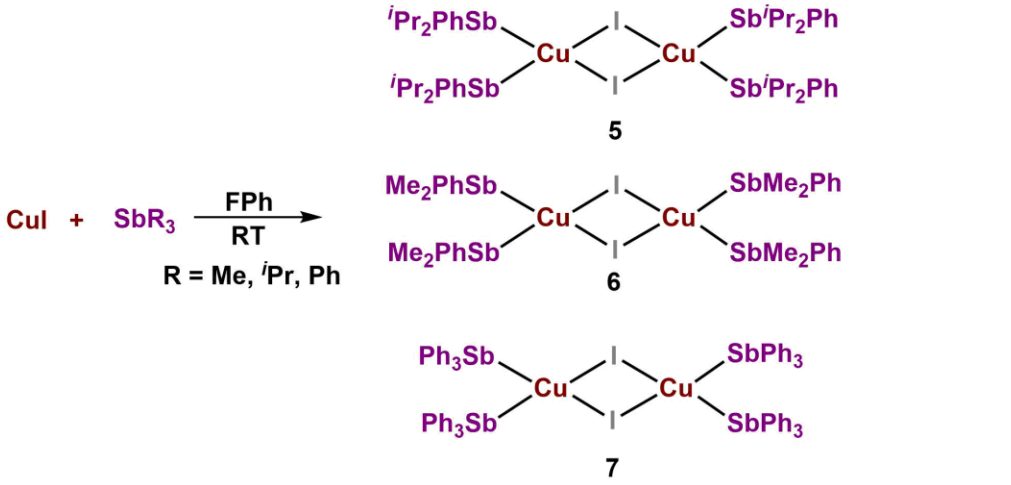





### 3.4.2 X-Ray Structures and Ligand Steric Effects

#### *3.4.2.1 Dimeric Complexes. $Cu_2(I)_2(Sb^iPr_2Ph)_4$ (5), $Cu_2(I)_2(SbMe_2Ph)_4$ (6) and $Cu_2(I)_2(SbPh_3)_4$ (7).*

Following on our initial hypothesis that the steric size of the ligand dictates emission wavelength, we attempted to synthesize cuboids using smaller antimony ligands.

The expectation was that smaller antimony ligands would allow the copper core to contract when the steric constraints of the ligands were minimized. Despite analogous reaction conditions to the synthesis of **1**, this subset of antimony ligands bearing phenyl substituents provided dimers (Figure 3.7) rather than cuboid structures. The cone angles of the three ligands in this series ($SbMe_2Ph$ = 119° < $Sb^iPr_2Ph$ = 147° < $SbPh_3$ = 155°, $Sb^iPr_3$ = 155°; see next paragraph for discussion of the two 155° ligands) were calculated using the Cartesian coordinates from the crystal structures with the Mathematica program Exact Ligand Cone Angle.[223] Such small cone angles allow two ligands per copper atom, providing a dimer instead of a cuboid (cuboid = 1 $SbR_3$ ligand per copper). Thus, the evidence suggests that the cuboid motif can only be accessed with ligands that have a relatively large cone angle (~ ≥155°). Dimeric complexes are not accessible with large cone angle ligands, as the copper ion could not support two close-proximate Sb-ligands without significant steric clashing. These results also indicate the copper atoms are starved for electron density and will readily accommodate a second weakly coordinating antimony ligand if the opportunity arises. Similarly, if a sterically unencumbered ligand is not accessible for dimer formation, the copper atoms will cluster and form the cubane motif.

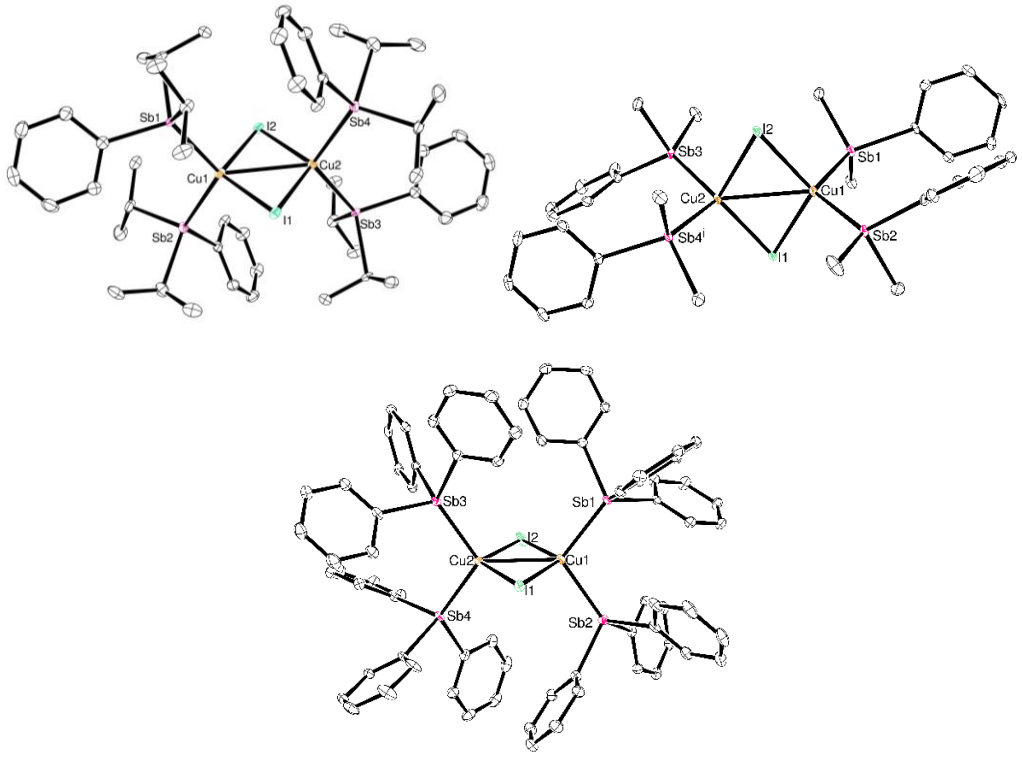


**Figure 3.7** ORTEP diagrams (30% ellipsoids) for $Cu_2(I)_2(Sb^iPr_2Ph)_4$ (**5**) (*top left*), $Cu_2(I)_2(SbMe_2Ph)_4$ (**6**) (*top right*), $Cu_2(I)_2(SbPh_3)_4$ (**7**) (*bottom*).

### *3.4.2.2 Tolman Cone Angle vs. Percent Buried Volume*

An apparent discrepancy occurs when examining the calculated ligand cone angles for both $SbPh_3$ and $Sb^iPr_3$. Both cone angles were calculated to be 155°, yet two $SbPh_3$ ligands were able to coordinate in the case of **7**, while only one $Sb^iPr_3$ ligand is bound per copper atom in cluster **1**, implying that $Sb^iPr_3$ is sterically larger. This discrepancy can be rationalized by parameterizing the ligands based on the percent buried volume ($\%V_B$), as discussed in chapter 2.[135] The percent buried volumes of the four ligands were calculated using SambVca (Cavallo et. al),[174] affording the following values: $SbMe_2Ph$ = 23.3% < $SbPh_3$ = 25.8% <$Sb^iPr_2Ph$ = 26.0% < $Sb^iPr_3$ = 27.0% (Table 3.2). The SambVca program is a web-based program and only requires the cartesian coordinate (xyz) file obtained from

the crystal structure and is quite simple to operate. Thus, the $\%V_B$ values more accurately reflect the functional nature of the ligand sterics, and compares favorably to the steric rankings of the analogous phosphine ligands.[153]

The $\%V_B$ was equally accurate in predicting the propensity for larger ligands (cone angle ~ ≥155°; $\%V_B$ > 27.0%) to form the desired cuboid structures (see X-ray section, next paragraph); there were no exceptions. The traditional cone angle method provided the following: $SbCy_3$, 152° < $Sb^iPr_3$, 155° < $Sb^tBu_2Ph$, 161° < $Sb^tBu_3$, 163°. [Note: our calculated ligand cone angles differ slightly from previously reported numbers ($Sb^iPr_3$ = 157°; $SbCy_3$, $Sb^tBu_2Ph$ = 166°; $Sb^tBu_3$ = 177°)].[171] However, the $\%V_B$ calculations for these ligands provided a close match to the previously published cone angles. Overall, the clear $\%V_B$ cutoff (27.0 %) between cube and dimer formation suggests that $\%V_B$ is the most reliable parameter. From the combination of these results and the nickel $\%V_B$ results, *it is highly recommended to use the percent buried volume to accurately predict steric bulk of ligands*.

#### *3.4.2.3 Cuboid Structures. $Cu_4(I)_4(SbCy_3)_4$ (2), $Cu_4(I)_4(Sb^tBu_3)_4$ (3), $Cu_4(I)_4(Sb^tBu_2Ph)_4$ (4).*

The formation of dimers rather than cuboids from smaller antimony ligands prompted us to employ sterically bulkier antimony ligands. Following our original hypothesis, we couldn't directly obtain further-NIR emitting clusters using sterically bulkier ligands. However, we could still garner interesting trends and confirm our hypothesis that short Cu-Cu bonds (due to sterically less encumbered Sb ligands) red-shift emissions. The crystal structures of the resulting antimony-supported copper-iodo cuboids **1**-**4** are depicted in Figure 3.8 (**1** is displayed again for ease of comparison). At the core of each cuboid is a copper-based tetrahedron wherein the four copper atoms reside at the

vertices. Each copper ion is bound to three iodine atoms, which in turn are each ligated in $\eta_3$ fashion to three copper ions. Each copper vertex is externally capped by an antimony ligand. The large steric bulk of the antimony ligand restricts the ligation of one (weak) antimony ligand per copper ion, which presumably drives the copper centers to assemble the cluster core. [*Note:* herein crystallographically unique bonds are presented in the conventional fashion; bond distance *averages* are stated in the format avg ± s.d. for the *n* number of bond instances in the cluster.] Cluster **2** ligated by $SbCy_3$ has an average Cu–Cu distance of 2.83 ± 0.14. Å, an average Cu–Sb distance of 2.51 ± 0.008 Å, and an average Cu–I bond distance of 2.68 ± 0.02 Å. Despite derivation from a homoleptic ligand similar to **1**, the tetrahedron core of **2** is not as symmetric as found in the four-fold symmetric $Cu_4$ core of $Cu_4(I)_4(Sb^iPr_3)_4$ (**1**, in cubic *I*23 space group), in which the unique crystallographic Cu–Cu bond length is 2.761(3) Å. In fact, each Cu–Cu distance in **2** is distinct from the other five Cu–Cu distances, with the shortest distance of 2.675(1) Å and the longest of 3.104(1) Å. In fact, the set of Cu–Cu distances for **2** represent (*i*) the broadest range of distances and (*ii*) both the shortest *and* the longest distances found in any cluster herein! Thus, these two extremes of high ligand symmetry and low crystallographic symmetry demonstrate that *the selection of homoleptic ligand does not ensure access to a highly symmetric $Cu_4$ core in the (emissive) solid state*.

In fact, varying extents of $Cu_4$ core symmetry can be arbitrarily accessed with both homoleptic and heteroleptic antimony ligands. For example, the homoleptic ligand $Sb^tBu_3$ gives rise to the partially asymmetric $Cu_4$ core in $Cu_4(I)_4(Sb^tBu_3)_4$ (**3**), which exhibits two sets (*n* = 3) of crystallographic Cu–Cu bonds at 2.9478(6) and 3.0032(6) Å. Similarly, the cuboid derived from heteroleptic $Sb^tBu_2Ph$ [$(Cu_4(I)_4(Sb^tBu_2Ph)_4$, **4**] also exhibits an albeit less numerically symmetric two sets of crystallographic Cu–Cu bonds at 2.8037(7) (*n* = 4) and 2.8618(8) Å (*n* = 2). It is notable that the differences in bond length between the

shortest and longest Cu–Cu bonds in **3** and **4** are not nearly as exaggerated as in **2**. From a crystallographic perspective, cluster **4** is unique in the fact that the asymmetric unit cell is Cu(I)(Sb$^t$Bu$_2$Ph). In Mercury or WinGX (crystal determination software), when the "Grow Fragments" command is issued and the entire structure is expanded from the asymmetric part of the unit cell, the cubane structure of **4** is revealed. The only other cluster that behaves similarly is **1** – the highly symmetric cluster occupying a cubic crystal system. However, **4** occupies the tetragonal crystal system, and although structurally similarly to **1**, is lower in symmetry, as dictated by the two sets of crystallographic Cu-Cu bonds (**1** has only one set of Cu-Cu bonds – all 2.76 Å). All of these data reinforce the notion that ligand symmetry is not a (predictable) determinant of crystallographic cluster symmetry. All relevant bond distances for each of the three cuboids as well as Cu$_4$(I)$_4$(Sb$^i$Pr$_3$)$_4$ (for ease of comparison) are tabulated in Table 3.2.

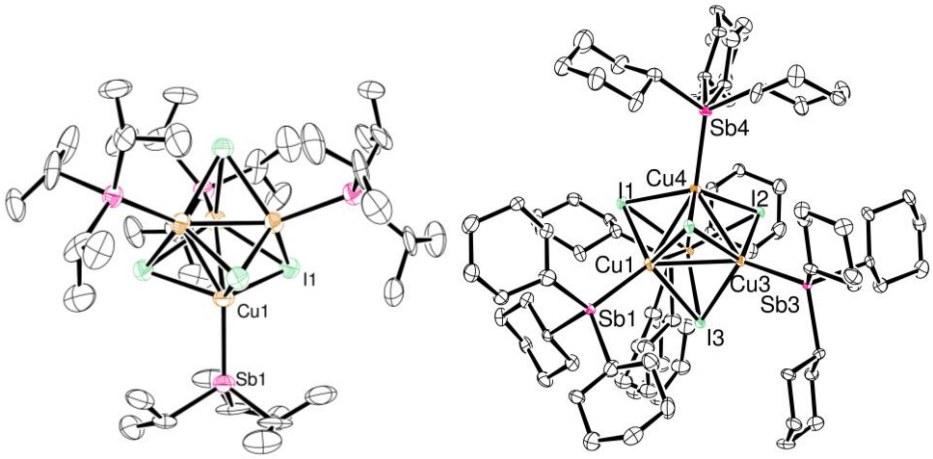

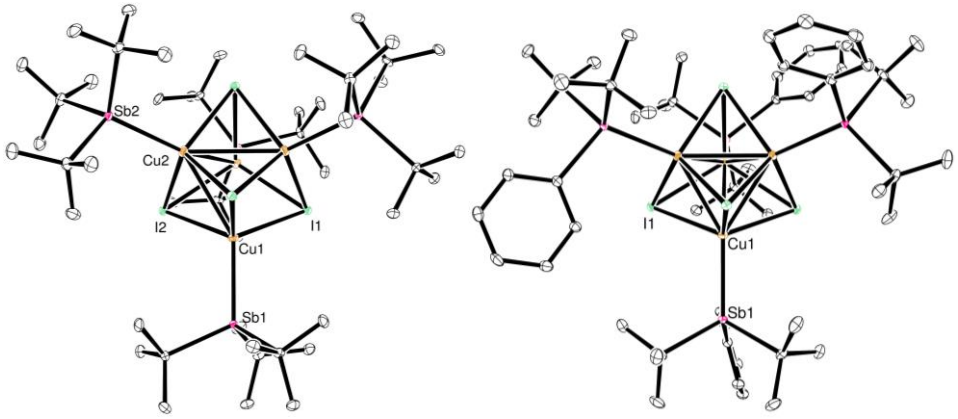


**Figure 3.8.** ORTEP diagrams (30% ellipsoids) for $Cu_4(I)_4(Sb^iPr_3)_4$ (**1**, previously reported, *top left*)[170], $Cu_4(I)_4(SbCy_3)_4$ (**2**, *top right*), $Cu_4(I)_4(Sb^tBu_3)_4$ (**3**, *bottom left*), and $Cu_4(I)_4(Sb\,^tBu_2Ph)_4$ (**4**, *bottom right*).

**Table 3.2.** Average Cu–Cu, Cu–Sb, and Cu–I bond distances (Å) for complexes **1-7**. Also listed are the shortest and longest Cu–Cu bond distances for each complex as well as the cone angle and the percent buried volume parameter for each ligand.

| | $Cu–Cu_{avg}$ | $Cu–Cu_{shortest}$ | $Cu–Cu_{longest}$ | $Cu–Sb_{avg}$ | $Cu–I_{avg}$ | Cone Angle (θ) | $\%V_B$ |
|---|---|---|---|---|---|---|---|
| **Cuboids** | | | | | | | |
| **$Cu_4(I)_4(Sb^iPr_3)_4$ (1)** | 2.761(3) | 2.761(3) | 2.761(3) | 2.571(2) | 2.707(2) | 155 | 27.0 |
| **$Cu_4(I)_4(SbCy_3)_4$ (2)** | 2.83 ±0.14 | 2.675(1) | 3.104(1) | 2.51 ±0.008 | 2.68 ±0.02 | 152 | 28.5 |
| **$Cu_4(I)_4(Sb^tBu_3)_4$ (3)** | 2.98 ±0.03 | 2.9478(6) | 3.0032(6) | 2.55 ±0.00004 | 2.69 ±0.006 | 163 | 31.6 |
| **$Cu_4(I)_4(Sb^tBu_2Ph)_4$ (4)** | 2.82 ±0.03 | 2.8037(7) | 2.8618(8) | 2.5381(5) | 2.69 ±0.01 | 161 | 29.9 |
| **Dimers** | | | | | | | |
| **$Cu_2(I)_2(Sb^iPr_2Ph)_4$ (5)** | 2.88 ±0.03 | — | — | 2.54 ±0.004 | 2.64 ±0.01 | 147 | 26.0 |
| **$Cu_2(I)_2(SbMe_2Ph)_4$ (6)** | 2.95 ±0.04 | — | — | 2.53 ±0.01 | 2.64 ±0.02 | 119 | 23.3 |
| **$Cu_2(I)_2(SbPh_3)_4$ (7)** | 2.7255(5) | — | — | 2.54 ±0.007 | 2.63 ±0.01 | 155 | 25.8 |

The bond metric data indicates that irrespective of ligand choice, ligand symmetry, or crystallographic symmetry, there are only relatively small changes in the average Cu–Sb bond distances (2.51-2.57 Å), and virtually no change in Cu–I distances (2.68-2.71 Å). The Cu–Sb distances are typical for copper complexes with antimony ligands (~2.5 Å), and are understandably longer than average distances of Cu–P (~2.25 Å) or Cu–As (~2.35 Å) bonds in the respective analogues.[71,233] Lastly, the Cu–I bond distances are akin to any copper-pnictogen cuboid (~2.6-2.7 Å); there is no clear relationship between Cu–I distance and ligand design.[227,230] As discussed in the previous paragraphs, there appears to be a direct relationship between ligand design and Cu-Cu bond distances. If the hypothesis on the correlation between Cu-Cu distances and emission wavelengths is valid, it should be evident when examining the luminescence properties of these complexes.

### 3.4.3 Luminescence

Each cuboid with Cu-Cu contacts was tested for its luminescent properties. The excitation and emission profiles of four cuboids (**1**-**4**) at 77 K are depicted in Figure 3.9 (**1**: $Sb^{i}Pr_3$; **2**: $SbCy_3$; **3**: $Sb^{t}Bu_3$; **4**: $Sb^{t}Bu_2Ph$). Compared with phosphine-supported copper cubes at 77 K, only a single emission is observed for **1**-**4** – analogous to the low-energy (LE) band typically exhibited in the 500-600 nm region for $P_4Cu_4I_4$ cubes. Notably absent from the emission spectra of **1**-**4** is the characteristic high energy (HE) band found in thermochromic phosphine-supported cubes, which is generally observed in the 400-500 nm range. At the first approximation, the lack of the HE band in **1**-**4** can be attributed to the lack of phenyl groups as antimony substituents (i.e, the phenyl-based *nb*(I)→($\pi^*$)Ph XLCT triplet state is obviated). The single exception to this is cluster **4** (derived from $Sb^{t}Bu_2Ph$); however, previous work using a *single-phenyl* phosphine (namely, $PPh^{i}PrMe$) also did not display the HE band, suggesting that multiple aryl units are required to activate

the XLCT pathway, as explained and hypothesized in the Electronic Ligand Effects sub-section above. Overall, considering the excitation profiles of the colorless samples of **1**-**4** ($\lambda_{ex} \approx 350$; similar to phosphine cubes), this results in a very large Stokes shift of ~250 nm. Modulation of the $\lambda_{ex}$ did not result in any noticeable change in the emission profiles of **1**-**4**; namely, the appearance of the HE band was never observed.

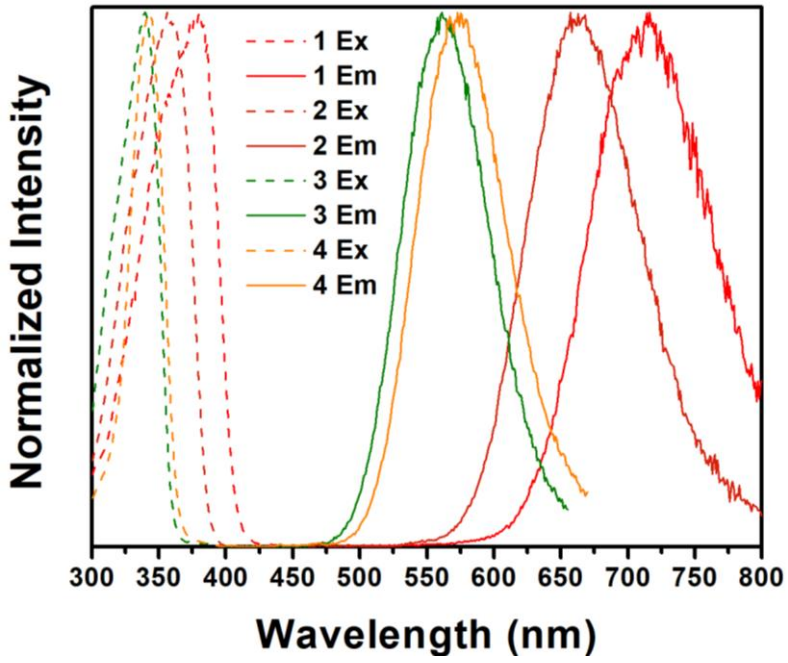


**Figure 3.9.** Excitation and emission maxima for complexes **1**-**4** at 77 K.

However, the room temperature emission spectra of **1**-**4** do not exhibit any appreciable luminescence compared with the low temperature spectra (Figure 3.10). This is in stark contrast to the ambient temperature emission from phosphine-supported cubes, in which a dominant LE band (500-600 nm) is preserved. An illustrative comparison is the case of $[Cu_4(I)_4(PPh^iPrMe)_4]$, a phosphine-supported cube reported by Harvey (with no XLCT) that exhibits *room temperature* luminescence at 580 nm (LE band);[215] the phenyl-

free cluster $[Cu_4(I)_4(Pcpent_3)_4]$ reported by Perruchas exhibits similar properties ($\lambda_{em} \approx 520$ nm).[229] Such emission from these complexes can be attributed exclusively to the cluster-centered ($^3CC$) emission mechanism. By comparison, cluster **3** exhibits a similar (intermediate) emission energy ($\lambda_{em} \approx 560$ nm), and yet does not emit at room temperature. Thus, the room temperature quenching of emission in **1**-**4** cannot exclusively be due to the red-shifted emission profiles.

Our main argument for the lack of room temperature emission in our Cu-Sb clusters is the increased probability of non-radiative decay pathways present at warm temperatures. It can be postulated that lower energy emissive states generally have shorter lifetimes due to increased probability of non-radiative decay pathways.[234,235] As the clusters cool, those decay pathways are "frozen out". It could be plausible that this phenomenon increases the probability of the intersystem crossing occurring, which leads to the phosphorescent-based emission. Further evidence for this postulate lies in the solution-state behavior of these clusters. As an experiment, two solutions of **1** were prepared: one in benzene and another in 2-methyl-THF (often used in frozen solution fluorimetry due to its proclivity to form a transparent frozen glass). Both samples were non-emissive under a long-wave UV light at room temperature. However, when the samples were frozen in liquid nitrogen and exposed to the UV light, both emitted the characteristic bright pink color a la Figure 3.3. The benzene frozen solution retained its emission for longer (a.k.a. at higher temperatures), but we believe that is due to the high freezing point of benzene compared to 2-methyl-THF (5 °C vs. -136 °C). The clusters are known to remain intact in solution (via NMR spectroscopy). Even in solution-state where there exists a higher probability of non-radiative decay pathways, the frozen sample still emitted at the same wavelength. It is important to note that at dilute concentrations (μM), the frozen sample in 2-Me-THF did not show any emission. Albeit, given this unique property of Cu-Sb luminescent clusters,

we are unable to definitively determine the cause of the non-emissive room temperature nature. Yet it is clear in this case that the precise identity (P vs Sb) and coordinates (long vs short bonds, *vide infra*) of atoms in this family of clusters is critical in determining the accessible photoactive states.

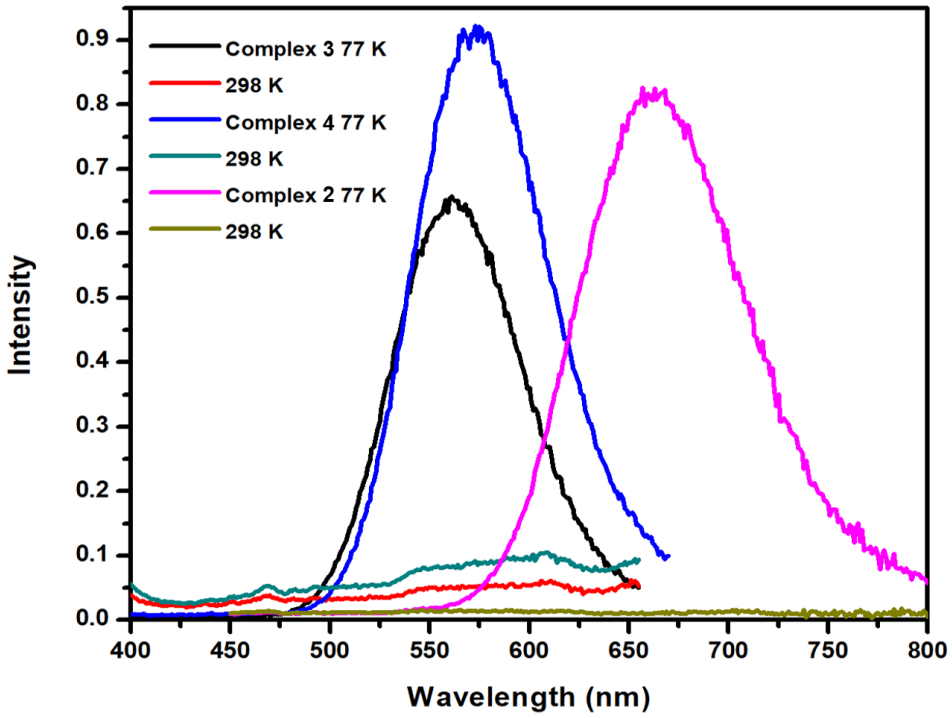


**Figure 3.10.** Emission profiles for complexes **2**-**4** at RT and 77 K.

To clearly showcase the precise temperature dependence and the lack of multiple emissions at other temperatures, variable temperature luminescence measurements were collected in the same manner as **1**. The variable temperature fluorimetry data for clusters **2** and **4** are depicted in Figure 3.11. The luminescent LE bands for **2** and **4** are quite prominent at –120 °C (liq $N_2$/pentane bath; 153 K), but for each cluster the luminescence intensity decreases to baseline as the temperature increases to 298 K. There is a slight shift in the $\lambda_{em}$ of **2** from 661 nm (low temp) to 681 nm (RT), whereas a negligible $\lambda_{em}$ shift

occurs for cluster **4** in the same temperature regime. The emission from both **2** and **4** become essentially non-emissive above 230 K. The small shift in $\lambda_{em}$ for **2** (20 nm) is interesting but not indicative of the authentic dual emission found in thermochromic systems. Such small shifts in $\lambda_{em}$ (< ~50 nm) have been observed in many cuboids and have been postulated to originate from symmetry distortions inside the $Cu_4$ core, rather than a change in emission mechanism.[236–238] Intriguingly, the structural data for **4** reveal some extent of homogeneity among its Cu-Cu bond distances (4 × 2.80 Å; 2 × 2.86 Å), while cluster **2** exhibits *six* unique bond lengths – one for every Cu-Cu interaction. Similarly, the originally reported cluster **1** — which exhibits *complete* homogeneity of Cu-Cu contacts: 6 × 2.76 Å — also did not exhibit any significant shift in $\lambda_{em}$ across variable temperatures (see Figure 3.4, above).[170] Thus, our data is consistent with the previously asserted connection between cluster symmetry and a small wavelength shift in the LE emission.[236–238] As a result, this technique allows one to determine the relative symmetry in the complex without having access to the crystal structure – the variable temperature luminescence data is a crucial experiment for characterizing these copper clusters.

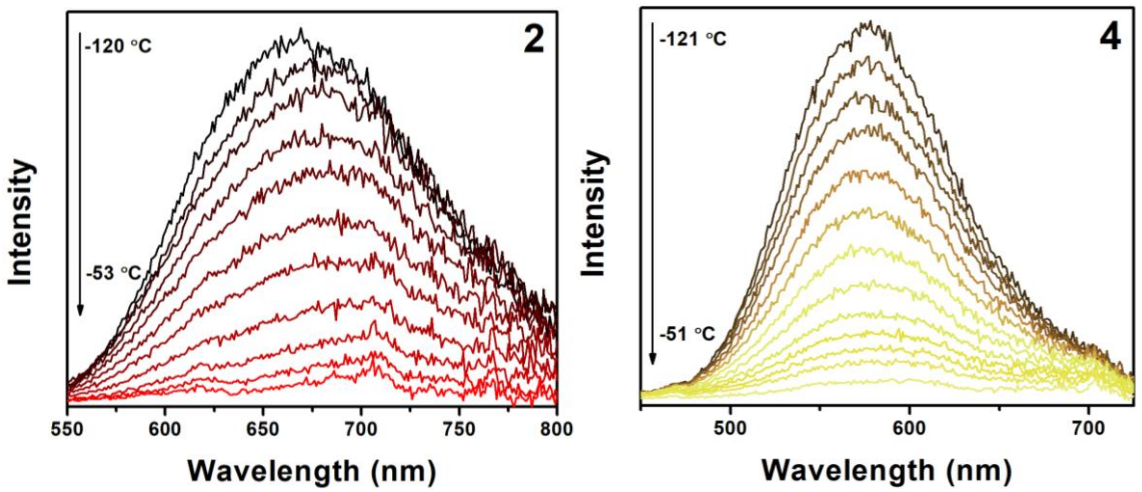

**Figure 3.11.** Variable temperature (153 to 222 K) luminescence of clusters **2** and **4**.

Cluster **3** was also tested for its luminescent properties, wherein it exhibited a similar extent of luminescence to **2** and **4** at 77 K. However, variable temperature measurements under the same conditions as those used for **2** and **4** at –120 °C (liq $N_2$/pentane bath; 153 K) revealed a greatly diminished intensity compared with the 77 K measurement. Thus, another temperature bath regime was used at –152 °C (liq $N_2$/isopentane; 121 K) to obtain the thermal decay of emission intensity (Figure 3.12). A liquid nitrogen/isopentane bath is the coldest temperature bath that is accessible with typical solvents. Although a temperature bath may exist between 77 K and 121 K, we were unable to find it in the literature. For future experiments, the use of a cryostat is required, and some labs at UT possess one. The emission feature in the resulting data for **3** rapidly declines as a function of increasing temperature, and the emission intensity when warmed from –152 to –120 °C is approximately 25% of the emission intensities from **2** and **4** at the same temperature. The emission at 121 K for **3** appears to be rapidly increasing with respect to the emission at slightly warmer temperatures. If a low temperature bath could be accessed that was merely 10-20 degrees colder, a more resolved variable temperature curve could be plotted (similar to complexes **2** and **4**). Still, useful knowledge and trends can be gained from these data as will be seen in future sections.

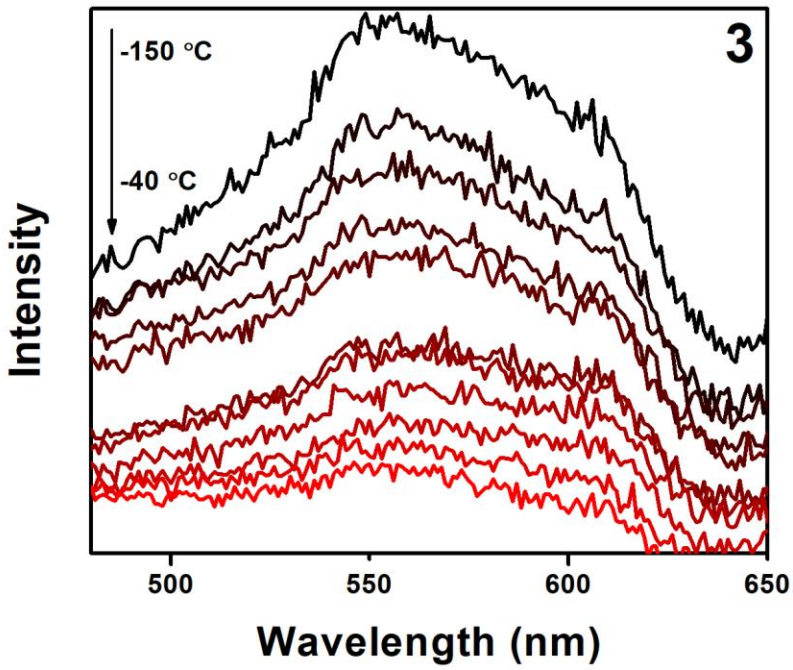


**Figure 3.12** Variable temperature (123 to 233 K) luminescence of cluster **3**.

## 3.5 Structure-Luminescence Correlations

### 3.5.1 Temperature Dependent Structures and Emission

The marked difference of **3** in its diminished luminescence intensity (from **1**, **2** and **4**) motivates the exploration of any possible correlation between structural parameters and luminescence properties. Out of all of the clusters studied herein, cluster **3** is most notable in that it exhibits the longest average Cu-Cu distances (2.98 Å) by a wide margin – significantly longer than the next closest Cu-$Cu_{avg}$ value (2.83 Å, for **2**). Previously, it was suggested that 2 × the van der Waals radius of copper (2.80 Å) was the theoretical cutoff for copper-centered LE emission, as beyond that distance cuprophilic interactions cease.[238,239] However, that has been disproven in the case of phosphine-supported cubes,

wherein LE emission ($\lambda_{em}$ = 500 nm) has been observed up to Cu-$Cu_{avg}$ = 3.47 Å, as in the case of $[Cu_4(I)_4(tmp)_4]$ — where tmp = tris(3-methylphenyl)phosphine.[240]

Previously it was shown that crystal structures of **1** (derived from $Sb^iPr_3$) solved across a range of temperatures (100-300 K) established a correlation between Cu-Cu bond length and emission intensity; for clarity, an updated version of this plot is presented herein as Figure 3.13 (*left*). The biggest difference between the plots in Figure 3.13 and 3.6 is the right-side y-axis. In Figure 3.13, the emission intensity is plotted as percentage of maximum intensity. The percentage of max intensity was calculated by first determining the full width at half max (FWHM) for each intensity measurement taken at each temperature reading during the variable temperature experiment as well as at 77K (max intensity). Then, each intensity reading (at each temperature) was divided by the corresponding FWHM to acquire a ratio of FWHM:Intensity. Finally, we calculated the percentage of max intensity by dividing the FWHM:Intensity ratio at a warmer temperature to the FWHM:Intensity ratio at 77 K. This analysis was performed to semi-quantitatively compare intensity measurements between our emissive cuboids without quantum yield data. Due to the limitations of our instrument (no integrating sphere), we were unable to determine the quantum yield for each cuboid at low temperatures.

It was notable for **1** that the only significant changes in bond distances from 100-300 K occurred in the Cu-Cu contacts, and the Cu–I and Cu–Sb bond lengths remained relatively invariant. Due to the vastly different temperature profile of **3** (temperature of emission 'turn-on', $T_{em}$ = 100-125 K) compared with the other cuboids (**1**, **2** and **4**: $T_{em} \approx$ 200 K), we determined the structure-luminescence correlation for **3** using the same variable temperature X-ray structure method (Figure 3.13, *right*).

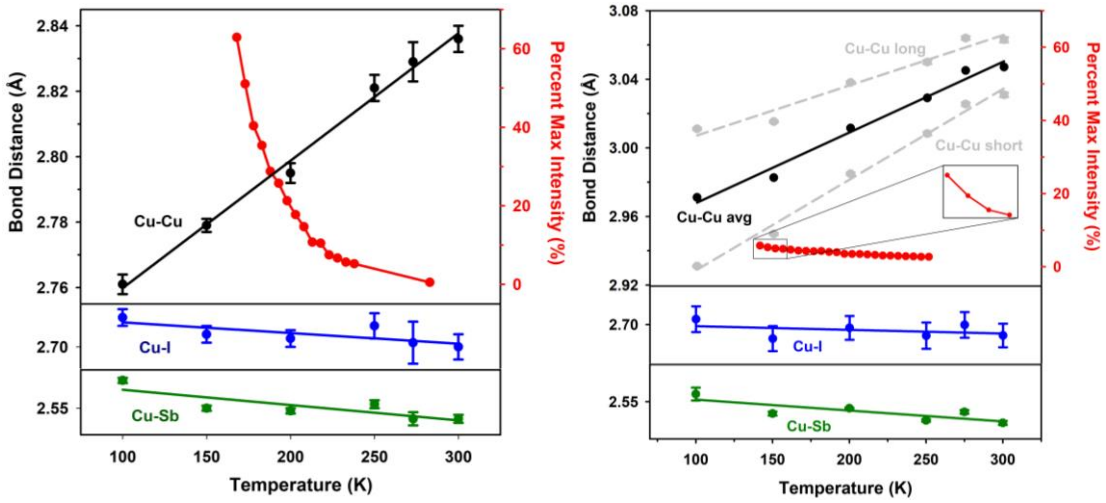


**Figure 3.13** For cuboids **1** (*left*) and **3** (*right*), correlation between the temperature dependent changes in X-ray structure (Cu–Cu, Cu–Sb or Cu–I bond distances) and percent of maximum intensity (red data points).

Regarding the temperature dependent X-ray structure metrics, the same general trends are observed for **3** as for **1**. The Cu–I and Cu–Sb bonds remain relatively constant across the 200 K range. As cluster **3** possesses two sets of crystallographic Cu–Cu distances, each individual dataset is plotted (gray) as well as the average distances and trendline (black). Notably, the change in Cu–Cu distances for **3** across the temperature range is 0.08 Å, nearly identical to that for **1**. However, all of the Cu–Cu distances found in **3** are longer than those for **1** irrespective of any temperature considerations. Regarding the emission, it is important to note that both **1** and **3** exhibit comparably strong luminescence at 77 K, but they exhibit different characteristic 'turn-on' temperatures ($T_{em}$) upon cooling. The $T_{em}$ was collected by determining the ratio of the luminescence intensity at varying temperatures (collected during the variable temperature luminescence measurements) to the intensity at 77 K, affording a parameter defined as 'percent max intensity'. From Figure 3.13, it can be clearly seen that cluster **3** displays a much weaker emission intensity than **1** at comparable temperatures. It could even be argued that **3** is non-

emissive above 150 K, where the emission starts to slowly increase at temperatures lower than 150 K, as per the inset in the left-most graph. A full graphical representation of each cuboid's percent max intensity at varying temperatures can be found in Figure 3.14. Determining the exact $T_{em}$ from these data is somewhat ambiguous, but it can tentatively be assigned as the temperature at which the emission reaches 25% of the max intensity achieved at 77 K. From Figure 3.14, one can definitively determine the $T_{em}$ for clusters **1**, **2**, and **4**, which all occur around -80 °C. Complex **8** has a much higher $T_{em}$ and this will be discussed in further detail shortly. However, the $T_{em}$ for cluster **3** is indeterminable from Figure 3.14. Despite the very low temperature used in a controlled cooling bath (isopentane/liq $N_2$; 123 K), cluster **3** remains weakly emissive compared with **1** at an even higher temperature (pentane/liq $N_2$; 163 K). As a result, the exact emission 'turn-on' temperature remains elusive for **3** but is likely in the 100-125 K range, which is correlated with Cu–$Cu_{avg}$ ≈ 2.96 Å. It is thus evident that the 2.80 Å van der Waals 'cutoff' is not a litmus test indicator for luminescence, but instead there is a correlation between the Cu-$Cu_{avg}$ and characteristic $T_{em}$ value (shorter Cu-$Cu_{avg}$ = higher $T_{em}$).

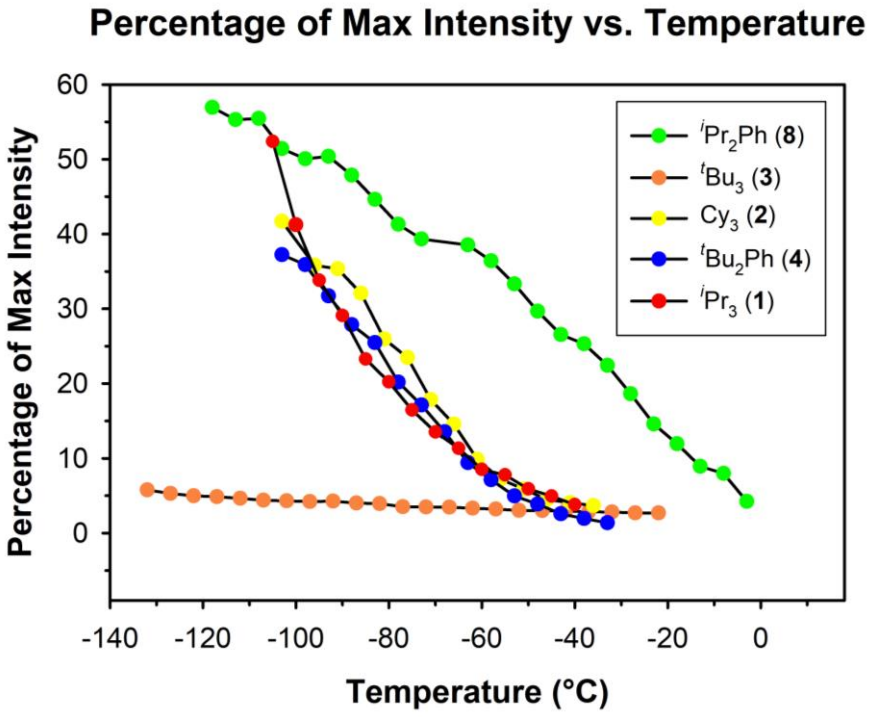


**Figure 3.14.** Percentage of Max Intensity vs. Temperature for the five cubes.

### 3.5.2 Effect of Phenyl Substituents on Thermochromism versus Thermoluminescence.

Complexes **1**, **2** and **3** lack any aromatic character in the ligand backbone, which has been proven necessary to observe the competing $^3$CC↔$^3$XLCT(aryl) emissions that are present in dual-emitting thermochromic compounds. Therefore, purely thermo*luminescent* properties are expected and, indeed, observed. Although this issue of multiple phenyl substituents has been discussed previously, it is an important one to rationalize the non-existence of thermochromism in any of our compounds. Regarding cluster **4** (L = Sb$^t$Bu$_2$Ph), it has been observed that in phosphine-based systems, *two* aryl substituents are required for thermochromism (L = PPh$_2$Pr, PPh$_2$OEt, PPh$_2$CH$_2$C=CH$_2$),[211,213,214] whereas *one* phenyl substituent (L = PPhMe$^i$Pr)[215] is insufficient to impart thermochromism. The

temperature dependent emission for cluster **4** (Figure 3.11) clearly exhibits a single emission feature at all temperatures, consistent with the expectation of thermoluminescence only. It thus appears that the 'two-phenyl' rule for thermochromism remains constant from phosphine to stibine systems. However, we do note that the counter-example of an $SbPh_2R$-supported cuboid has yet remained synthetically inaccessible. As seen in chapter 2, $SbPh_2Me$ was successfully synthesized, but the percent buried volume was smaller than $Sb^iPr_2Ph$ ($\%V_B$ = 25.8), suggesting it would form a dimer over a cube. Thus, the copper metallation reaction with $SbPh_2Me$ was never attempted. $SbPh_2{}^iPr$ would potentially form a cuboid with thermochromic properties, however, $SbPh_2{}^iPr$ (and by extension, $SbPh_2{}^tBu$) is very difficult to purify post-Grignard due to the very high boiling point, which renders the distillation unsafe with our laboratory apparatus. An effort to synthesize antimony ligands with multiple phenyl groups that are bulky enough to form cuboids over dimers could provide fascinating insight into the effect of antimony-based ligands on the HE emission for these clusters.

### 3.5.3 Correlation between Steric Bulk and Emission Energy.

A correlation is evident between the steric size of the ligand and the maximum emission wavelength (Table 3.3, Figure 3.15). Of all cuboids presented so far, **1**-**4**, the lowest-energy emitting cuboid is the original complex, $Cu_4(I)_4(Sb^iPr_3)_4$ (**1**), with $\lambda_{em}$ = 711 nm, which also exhibits the lowest $\%V_B$ at 27.0%. As tabulated in Table 2 and illustrated in Figure 3.15, for clusters **1-4** an increasing $\%V_B$ is correlated with decreasing $\lambda_{em}$ values vis a vis blue-shifted emission energies. The cuboids synthesized with $SbCy_3$ ($\%V_{bur}$ = 28.5%), $Sb^tBu_2Ph$ ($\%V_{bur}$ = 29.9%), and $Sb^tBu_3$ ($\%V_B$ = 31.6%) have emission wavelengths of 661, 575, and 558 nm, respectively. This trend is also structurally correlated to the *average* Cu-Cu bond distances in the cluster, wherein sterically smaller ligands result

in shorter Cu-$Cu_{avg}$ distances (lower emission energies). As it has been previously postulated that Cu-$Cu_{avg}$ bond distance is the sole contributor in determining LE emission wavelength, our results appear to corroborate this notion. The correlation between smaller ligands and shorter Cu-$Cu_{avg}$ distances likely arises because the entire {Cu–$SbR_3$} unit is best able to approach the center of the cluster when {Cu–$SbR_3$} is small. Notably, the overall importance of steric effects in this series of copper dimers/clusters is evident in that any ligands smaller than $Sb^iPr_3$ resulted in dimer formation (which accommodates *cis* $SbR_3$ ligands) rather than forming tetramers ($SbR_3$ is too big for *cis* motif).

**Table 3.3** Comparative table of ligand cone angles, average Cu-Cu bond distance, emission wavelengths and other pertinent bond distances for complexes **1-4**.

| | **$Cu_4(I)_4(Sb^iPr_3)_4$ (1)** | **$Cu_4(I)_4(SbCy_3)_4$ (2)** | **$Cu_4(I)_4(Sb^tBu_2Ph)_4$ (4)** | **$Cu_4(I)_4(Sb^tBu_3)_4$ (3)** |
|---|---|---|---|---|
| **$\%V_B$** | **27.0** | **28.5** | **29.9** | **31.6** |
| **Emission (λ)** | **711** | **666** | **575** | **558** |
| **Cu–Cu avg (Å)** | **2.761** | **2.826** | **2.822** | **2.975** |
| **Shortest Cu–Cu** | **2.761** | **2.679** | **2.803** | **2.997** |
| **Longest Cu–Cu** | **2.761** | **3.097** | **2.861** | **3.003** |
| **# of unique (crystallographic) Cu-Cu bonds** | **1** | **6** | **2** | **2** |

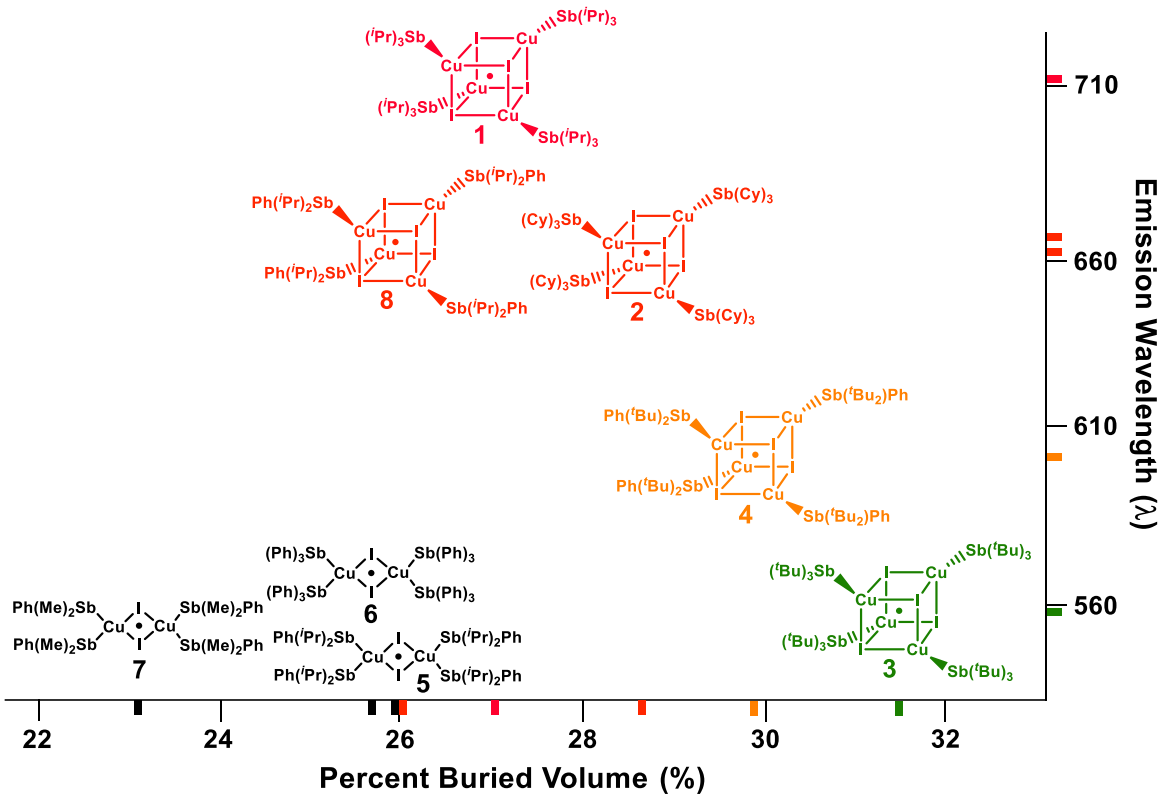


**Figure 3.15.** Graphical summary comparing percent buried volume to emission wavelength.

An interesting caveat to this data resides in the comparison of cluster **2** with cluster **4**: these clusters exhibit nearly identical Cu-$Cu_{avg}$ distances (2.826±0.14 and 2.822±0.03 Å, respectively), and yet exhibit 100 nm difference in emission wavelength (666 and 575 nm, respectively). This implies the existence of another subtle structural reason for the vast difference in emission energy. As Perruchas has demonstrated that ligand donor strengths in phosphine-based cubes have no trend-wise effect on LE emission,[227] we postulate that the explanation can again be found in the structural metrics. Closer inspection reveals that **2** exhibits the shortest Cu-Cu bond (2.679 Å) found in *any* of the clusters. In contrast, the shortest Cu-Cu bond in **4** resides at 2.803 Å. DFT calculations reveal that the LUMO in the $^3$CC transition is due to an MO that is highly delocalized across the cluster center, as

opposed to an individual lowest lying molecular orbital.[241,242] While it has been shown that short Cu-Cu bond distances do red-shift the emission, it is not clear whether the presence of a few particularly short Cu-Cu bonds in a cluster center will similarly adjust the maximum emission wavelength in these complexes.[243,244] Put another way, are emission energies dictated by the *average* Cu-Cu bond distance inside the cluster, or can a *few particularly short* Cu-Cu bonds skew the emission wavelength that is expected from a cluster with its Cu-$Cu_{avg}$ distance? Indeed, there is some precedent for this phenomenon.[237,238,244–246] Kim et. al synthesized two crystallographic isoforms of the same cubane (derived from 2-(cyclohexylthio)-1-thiomorpholinoethanone) that differed in their solvation state (desolvated versus MeCN solvate). The two structures had similar Cu-$Cu_{avg}$ distances (2.70 vs. 2.71 Å), but the range of Cu-Cu bond lengths within the cluster ranged from 2.607–2.773 Å for the desolvated cluster versus 2.643–2.771 Å for the $CH_3CN$ solvated cluster. The presence of the shorter Cu-Cu bond distance in the desolvated structure resulted in a red-shifted $\lambda_{em}$ = 600 nm, compared with the 540 nm emission of the cluster with the *longer* shortest Cu-Cu distance.[244] In another case, the copper cluster $Cu_4(I)_4(PPh_2py)_2$ ($PPh_2py$ = 2-(diphenylphosphino)pyridine) was synthesized alongside its solvated analogue, $Cu_4(I)_4(PPh_2py)_2$•0.5 $CH_2Cl_2$. The two complexes exhibited similar average Cu-$Cu_{avg}$ distances (2.95 Å vs. 2.97 Å, solvated vs. unsolvated respectively), yet the solvated species had a larger range of Cu-Cu distances in both directions than the unsolvated complex (2.52–3.82 Å (solvated) vs. 2.57–3.78 (unsolvated)). Similarly, this affected the emission wavelength for the two complexes, with the solvated species (shorter Cu-Cu bond) exhibiting red-shifted $\lambda_{em}$ = 576 nm, whereas the unsolvated cluster emitted at 527 nm.[246] Lastly, another case was two closely related luminescent clusters with different ligand sets: $Cu_4(I)_4(py)_4$ (py = pyridine) and $Cu_4(I)_4(quin)_4$ (quin = quinuclidine). The pyridine analogue exhibited Cu-$Cu_{avg}$ = 2.69 Å, Cu-$Cu_{min}$ = 2.61 Å, $\lambda_{em}$ = 570 nm. In

contrast, despite a nearly identical Cu-$Cu_{avg}$ (2.70 Å), the quinuclidine structure exhibited a longer Cu-$Cu_{min}$ (2.67 Å) and as a result blue-shifted emission ($\lambda_{em}$ = 540 nm).[247] *Overall, these examples plus the work described herein (notably, **2** and **4**) suggest that the average Cu-Cu distance provides a first approximation rank-order correlation between structure and emission wavelength (shorter distance = red-shifted $\lambda_{em}$). However, when similar Cu-$Cu_{avg}$ values are present, the shortest Cu-$Cu_{min}$ results in the more red-shifted emission profile.* This is another tool in the belt of an aspiring chemist that wants to design a copper cluster to emit at a certain energy.

### 3.5.4 Correlation between Crystallographic Symmetry and Emission Energy.

Based on the metrics discussed above showing that clusters supported by the smallest $SbR_3$ ligand resulted in the most red-shifted NIR emission, we synthesized the next smallest ligand in the series — namely $Sb^iPr_2Ph$. Correspondingly, this intermediate-sized $SbR_3$ ligand was the only case where we isolated both a dimer (**5**) and tetranuclear cluster (**8**) by varying the ligand equivalents (excess versus 1:1, respectively). This synthesis and discovery need more attention. When initially performing reactions to synthesize new cubes, excess ligand was always added to CuI as per the original reaction to synthesize **1**. When working with $Sb^iPr_2Ph$, this reaction scheme will lead to the dimer (**5**); however, the cuboid **8** will precipitate out after the pentane wash during the workup. The dimer was discovered much prior to **8** because the product of the reaction was assumed to lie in the pentane layer. However, **8** is insoluble in pentane, but can be crystallized and purified by a DCM/pentane vapor diffusion. This "mystery" product was the last cluster synthesized for the project and is the reason this section is written as it is. We had clusters **1**-**4** synthesized and their luminescent properties studied prior to the discovery of **8**. We had initially believed the emission energies were purely dictated by the Cu-$Cu_{avg}$ bond

distance inside the cluster core, and that that distance was determined by the steric size of the ligand. However, the discovery and analysis of **8** revealed that initial hypothesis to be not entirely true.

The co-result of dimer and cube for the ligand $Sb^{i}Pr_2Ph$ suggests that the $\%V_B$ of $Sb^{i}Pr_2Ph$ (26.0%) is of truly intermediate steric bulk between the small set [$\%V_B \leq 25.8\%$ ($SbPh_3$,)] and large set [$\%V_B \geq 27.0\%$ ($Sb^{i}Pr_3$)] of antimony ligands. Another (unintended) difference was the lower symmetry of $Sb^{i}Pr_2Ph$ versus $Sb^{i}Pr_3$. Unfortunately, due to competing space groups of crystallization the exact structure of the $Sb^{i}Pr_2Ph$ cuboid **8** could not be precisely determined, although several partial structure solutions unambiguously support the cuboidal structure and Cu–Cu bond lengths in the 2.7-2.8 Å range, and on average are about equal to the 2.76 Å Cu-Cu bond distance in **1**. A collection of ball-and-stick representations of the $Sb_4Cu_4I_4$ core of **8** were collected from several partial structure solutions and is provided in Figure 3.16. Presumably as a result of the lower symmetry of $Sb^{i}Pr_2Ph$ versus $Sb^{i}Pr_3$, the partial structures can be solved in triclinic, tetragonal or rhombohedral space groups — but all of these are of lower symmetry than that of $Sb^{i}Pr_3$ supported **1** (cubic, *I*23). Another potential issue with crystallization could have been the co-crystallization of **5**, however that was ideally removed through several pentane washes. As a corollary, while cluster **1** exhibits just a *single* crystallographically unique Cu-Cu bond, the partial structures of **8** reveal the following sets of unique Cu-Cu bonds: six sets of 1 (triclinic, a.k.a. all bonds were unique), two sets of 3 (rhombohedral), or one set of 2 plus one set of 4 (tetragonal). Complex **8** was very easy to crystallize via DCM/pentane vapor diffusion and the crystals looked excellent under the microscope. Alternative solvent combinations (THF/pentane, $CHCl_3$/pentane) provided crystals as well, but the same issue occurred. The structure is definitively a cube, but the absolute structure could never be resolved. It is acknowledged that conjecturing on bond distances (but perhaps not

symmetry) is difficult without having a full structure, but we believe we had enough data to declare **8** was less symmetric than **1** while possessing Cu-$Cu_{avg}$ bond lengths in the same range (or lower) as **1**.

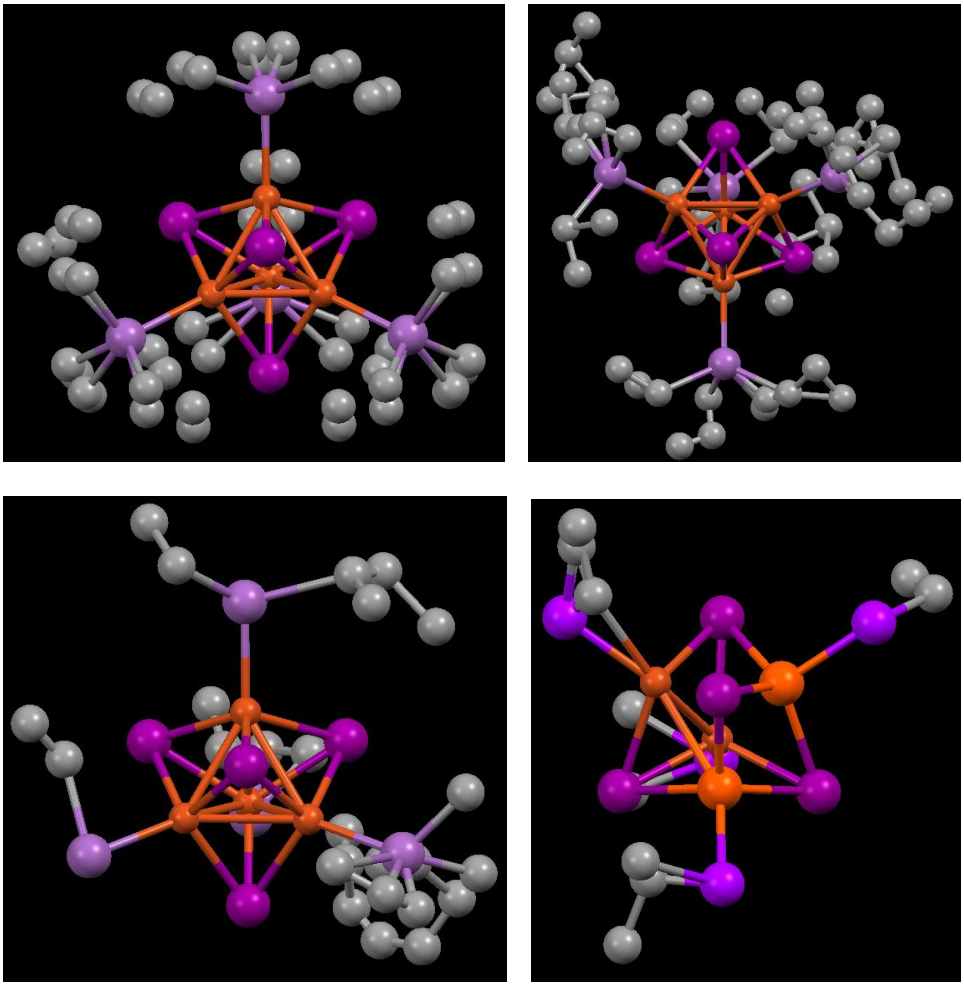

**Figure 3.16** Collection of ball and stick models for the partial structure of **8**.

The luminescence properties of this cuboid (Figure 3.17) reveals several intriguing insights. First, while **8** emits in the red-shifted region (670 nm) in this series (558-711 nm), cluster **1** still emits 40 nm further into the NIR. Additionally, **8** is the only cluster that is

detectably emissive at room temperature, as evidenced by the VT and $T_{em}$ emission profiles seen in Figure 3.17 and Figure 3.14. Additionally, lower temperatures blue-shifted the emission energy by ~15 nanometers, which can be attributed to the symmetry-imposed distortions in the Cu core, and as explained previously in the case of complex **2** (vide supra **Luminescence**, and Figure 3.11). That shifting in emission energy during the variable temperature luminescence experiment is further evidence that **8** is not very symmetric. Although crystallographically it could not be definitively determined, this measurement provides further evidence to the asymmetry in **8**, especially compared to **1**. The average nominal Cu-Cu bond distance in **8** is roughly ~2.7 Å, which would imply the emission of this complex would be similar to **1** if the emission deriveth purely from the length of the Cu-Cu bonds in the cluster center. Overall, **8** clearly follows the $\lambda_{em}$ trend established by the ligand sterics and Cu-Cu bond lengths found in **2**, **3** and **4**. Indeed, the result of this analysis *firmly places **1** as the outlier in the series*. Notably, **1** is the only cubic (space group) structure in the series with just a single crystallographically unique Cu-Cu bond. A closer investigation into the connection between luminescence and symmetry is required.

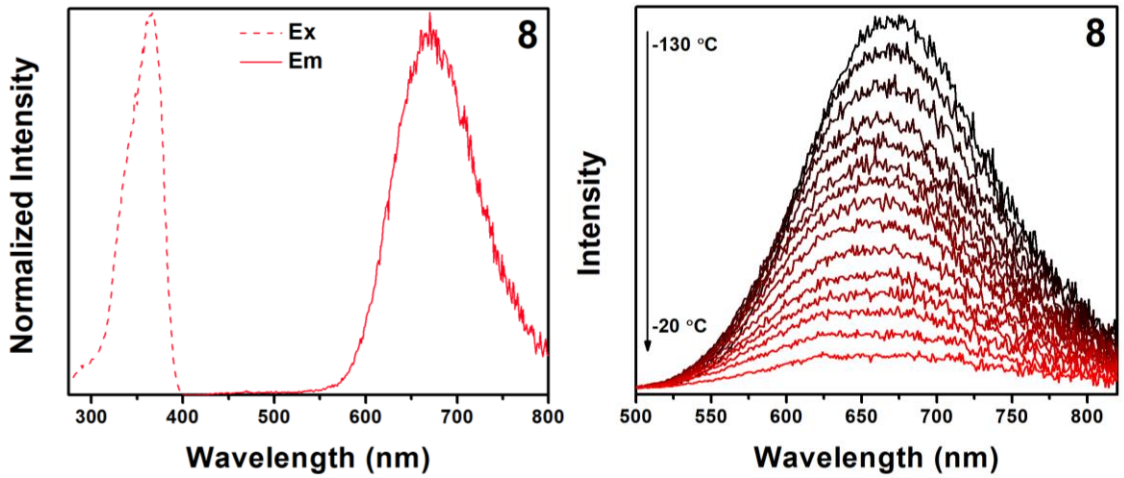

**Figure 3.17** (*Left*) Excitation and emission features (77 K) for complex 8 showing $\lambda_{em}$ = 670 nm; (*right*) Variable temperature luminescence (143 to 253 K) for **8**.

A relationship between the LE emission and crystal symmetry was first suggested by Hardt and Pierre, who noticed the presence of a 4-fold symmetry element led to red-shifting of emissions.[236] Later, Holt and coworkers synthesized several luminescent clusters with general structure $Cu_4(I)_4(CH_3CN)_2(L)_2$ (L = aniline derivative). One complex with L = 2,6-dimethylaniline had no internal symmetry element, a Cu-$Cu_{avg}$ bond distance of 2.706 Å, and a $\lambda_{em}$ = 568 nm. Another complex with L = *p*-anisidine had a Cu-$Cu_{avg}$ = 2.716 Å but did contain an internal 2-fold symmetry element. The latter cluster displayed an emission of 608 nm, significantly red-shifted as compared to the lower symmetry compound.[238] In a separate instance, two polymorphs of the luminescent cluster, $Cu_4(I)_4(PPh_2OEt)_4$, were synthesized – one with tetragonal symmetry, and the other monoclininc. Although the Cu-$Cu_{avg}$ bond distance for the two were drastically different (3.056 Å for tetragonal, 2.871 Å for monoclinic), the two compounds displayed remarkably similar emission profiles for the LE emission ($\lambda_{em}$ = 570 and 580 nm for the tetragonal and monoclinic structures, respectively).[213] These examples, along with our current findings, provide further evidence for the correlation between symmetry and $\lambda_{max}$ for the LE emission. Importantly, there does not appear to be a correlation between symmetry and $T_{em}$ or FWHM at variable temperatures.

### 3.5.5 Correlation between Electronic Ligand Effects and Emission Energy.

In early 2018, Perruchas et. al. determined that there was no discernable correlation between the electronic properties of the ligand and the energy of emission originating from the cluster center ($^3$CC).[227] Although we did not seek to study those effects initially, our results appear to corroborate those findings. Using the classical Tolman electronic parameter (TEP) to define the electronic strength of our antimony ligands, it was previously

shown that the addition of a single phenyl group does lower the TEP versus an all-alkyl analogue, while higher aliphatic organic substituents increased the TEP (i.e. isopropyl versus methyl, see previous chapter).[248] Although it is difficult to quantify the TEP for the bulkier ligands (e.g. $Sb^tBu_3$, $SbCy_3$), we can extract useful information by examining analogous phosphine compounds ($P^tBu_{3TEP}$ = 2056 $cm^{-1}$; $PCy_{3TEP}$ = 2056 $cm^{-1}$).[78] Thus, an approximate order of Sb-ligand strength would follow as $Sb^tBu_3 = SbCy_3 > Sb^tBu_2Ph > Sb^iPr_3 > Sb^iPr_2Ph$. If electronic effects were crucial in determining the $^3CC$ $\lambda_{em}$, it would be expected that the emission energies follow this trend as well. *However, the emission energies do not, in fact, follow this trend*, as the emission for complex **1** is further red-shifted versus complex **8** and similarly for complexes **2** and **3**. Although from both our results and those of Perruchas, there does appear to be a trend between increasing electron withdrawing ligand effects and decreasing Cu-Cu bonds, there does not appear to be a definitive correlation between said effects and the emission energy originating in the Cu-Cu core.

Lastly, lifetime measurements were collected for all of the clusters and are tabulated in Table 3.4. Based on the relatively long microsecond lifetime in each case in a narrow range (5.4-9.8 μs), it is clear that all of the clusters undergo the same phosphorescence-based emission process. At room temperature, the lifetimes decrease by an order of magnitude. No apparent trend is evident between the ligands, complexes, or emission wavelengths with the lifetimes. However, the stark difference between the room temperature and low temperature lifetimes partially explains the lack of luminescence at room temperature. Additionally, the non-radiative decay pathways are mitigated as the temperature is lowered, thus accessing the phosphorescent emissions.

**Table 3.4** Lifetime measurements for clusters **1-4** and **8** at low temperature and room temperature.

| Cluster | 77 K $\lambda_{ex}$ (nm) | 77 K $\lambda_{em}$ (nm) | 77 K $\tau$ (μs) | 298 K $\tau$ (μs) |
|---|---|---|---|---|
| **$Cu_4(I)_4(Sb^iPr_3)_4$ (1)** | 380 | 711 | 7.7 ± 0.4 | 1.2 ± 0.09 |
| **$Cu_4(I)_4(Sb^iPr_2Ph)_4$ (8)** | 369 | 670 | 7.7 ± 0.05 | 0.36 ± 0.05 |
| **$Cu_4(I)_4(SbCy_3)_4$ (2)** | 355 | 666 | 9.8 ± 0.05 | 0.43 ± 0.04 |
| **$Cu_4(I)_4(Sb^tBu_2Ph)_4$ (4)** | 341 | 575 | 5.4 ± 0.8 | 0.42 ± 0.06 |
| **$Cu_4(I)_4(Sb^tBu_3)_4$ (3)** | 339 | 558 | 5.9 ± 0.03 | 0.39 ± 0.05 |

### 3.6 DENSITY FUNCTIONAL THEORY (DFT) CALCULATIONS FOR 1

DFT calculations undertaken on the ground state singlet (based on X-ray structure) and excited state triplet (geometry optimized $S = 1$ state) describe the electronic states available in the phosphorus-based luminescent copper cuboids, and they have been performed and reported.[241,242] We performed such calculations to gain a better understanding of the orbitals involved in the luminescence as well as theoretically determine the lack of HE emission in our Cu-Sb clusters. The calculations performed on one of the first thermochromic compounds, $[Cu_4(I)_4(pyridine)_4]$ cluster, elucidated the origins of the lower energy XLCT excited state and the higher energy CC excited state, and determined that the pyridine $\pi^*$ orbitals were the LUMO responsible for the XLCT transition. Although this is consistent with the lack of a second emission band in our first thermoluminescent compound (**1**), a full DFT study on the singlet and triplet states of that and related compounds are critical to understand the origins of the copper-antimony cuboid luminescence. Thus, DFT calculations were performed on the singlet and triplet states of **1**. The geometries for both the ground and excited state were optimized using B3LYP functional with the following basis sets per atom: Sb, TZP; I, 6-311G; Cu, C and H: 6-31G**. Such a mixture of high-level basis sets was critical in obtaining converged solutions. When the calculation was attempted with one high level basis set used for every atom, the calculation failed as the computer used to perform these calculations ran out of available memory. Although it is customary to use one basis set for every atom, it is not

uncommon (and typically not an issue) if a mixture of basis sets is used. Lastly, despite the high crystallographic symmetry of **1**, calculations were performed without any symmetry impositions.

Figure 3.19 depicts the ensemble of MOs resulting from the $S_0$ (*left*) and $T_1$ optimized geometries; both the α and β spin manifolds of $T_1$ are represented (*middle* and *right*, respectively). From the MO diagram of the ground state ($S_0$), the HOMO consists primarily of the Cu 3*d*-orbitals with a small contribution from the iodine 5*p* orbitals. These assignments are purely speculative based on the orbital parentage images derived from the DFT calculation, but it is important to note that DFT is not $\psi$-based, and it cannot directly calculate orbital contributions. At slightly lower energy, the occupied MOs are a cluster of orbitals resulting from various admixtures of the Cu and I orbitals, with small contributions from the Sb 5*p* set. The LUMO of the ground state ($S_0$) consists almost entirely of Cu-Cu bonding character (4*s*) with an incredibly symmetric profile, with a small extent of I parentage (5*p*). This highly symmetric orbital was labeled $A_1$ to reflect that property. The lack of any contribution from the antimony R groups provides insight for the lack of the HE band (XLCT, ligand-based) in the emission profile. The next higher energy group of unoccupied MOs resides on the antimony atoms, with some extension onto the isopropyl carbons. This data suggests that a second (HE) emission band may be possible provided the presence of more aromatic character on ligand. However, from the previous discussion, we have determined it would require multiple (≥2) aryl substituents to decrease the energies of those orbitals to a level competitive with the copper-based emission.

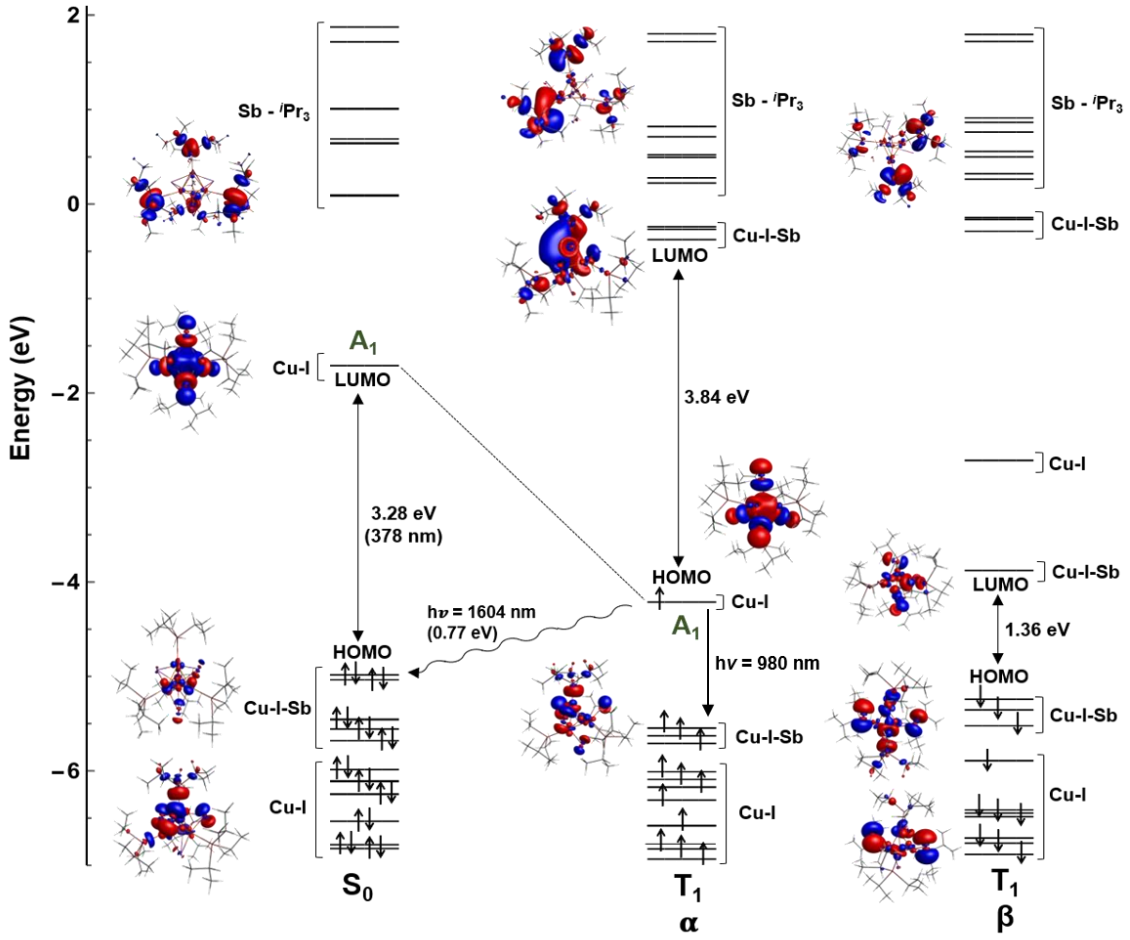


**Figure 3.19.** Represented molecular orbital diagram of **1** showing the ground and excited states, along with relevant orbital parentage images.

The $T_1$ state of **1** was geometry optimized in the $S = 1$ configuration. Obtaining this geometry optimized structure required a slow progression at low basis set levels away from the $S_0$ geometry, followed by higher level calculations that converged on the final calculated structure for the $T_1$ state. The conversion from ground state singlet to excited state triplet often enacts large geometric distortions, especially among the Cu-Cu and Cu-I bond lengths.[241,242] The relevant bond distance data are tabulated in Table 3.5, along with the experimental distances acquired from the crystal structure. In the DFT calculated system, the Cu-Cu bonds are contracted in the excited state – just as they contract in the

experimental cluster as temperature decreases. The most notable difference between the DFT calculated ground state for **1** and the X-ray structure of **1** is the discrepancies in Cu-Cu bond lengths [DFT: 2.424±0.004; X-ray: 2.761(3)]. This highlights the fact that the $Cu_4$ core is especially elastic with respect to temperature, considering the temperature of X-ray data collection (100 K) versus the "temperature" of DFT calculation (0 K). Upon conversion from $S_1$ to $T_1$, the excited state exhibits contracted Cu-Cu contacts (2.36±0.04 versus 2.424±0.004) and expanded Cu-I bonds (3.09±0.29 versus 2.839±0.007) that compensate for the contracted $Cu_4$ core. Interestingly, upon moving from the ground to excited states, the degree of contraction of the Cu-Cu distances is nearly the same for the calculated and experimental clusters (0.065 Å, calculated; 0.075 Å, experimental). This agreement suggests the calculation was successful and that DFT calculations are a reliable tool for more closely examining the physical origin of copper cluster emission. There is little change in the Cu-Sb bond lengths between ground and excited states, which is common even among Cu-P based cubes.[228] Overall, it is clear from both the calculated and experimental data that the origin of luminescence for all the Cu-Sb clusters presented herein is centered within the cluster.

**Table 3.5.** Relevant bond distances for the calculated singlet and triplet states, and the associated experimental (X-ray) bond distances for **1**.

| | **Cu-Cu (Å)** | **Cu-I (Å)** | **Cu-Sb (Å)** |
|---|---|---|---|
| **$S_0$ (DFT)** | **2.424 ± 0.004** | **2.839 ± 0.007** | **2.544 ± 0.002** |
| **$T_1$ (DFT)** | **2.36 ± 0.04** | **3.09 ± 0.29** | **2.52 ± 0.02** |
| **Experimental (X-ray)** | **2.761(3)** | **2.707(2)** | **2.571(2)** |

Most importantly, the highest SOMO of the excited state consists of an incredibly symmetric and delocalized set of Cu 3d orbitals, with minor contributions the iodine 5*p* orbitals. This can be visually seen in the orbital image next to the SOMO of $T_1$ α. The

highest SOMO of $T_1$ exhibits decreased energy relative to the $S_0$ LUMO by nearly 2.5 eV (both denoted with the $A_1$ symmetry label, reflecting the similar origins from the $Cu_4$ core). This phenomenon of energy stabilization of the Cu-Cu electron density responsible for the CC excited state between ground and excited states has been observed in calculations on the analogous pyridine supported cube, with a similar degree of energy stabilization in the pyridine case (~ 2.5 eV).[242] For the pyridine cube, the stabilization lowers the energies of these orbitals past the $\pi^*$ orbitals of the pyridine ring, which are the original LUMOs in the ground state and the LUMOs for the second (HE) transition (X/MLCT). In contrast, our system exhibits orbital properties similar to other cubes without phenyl substituents, and the calculated MO diagram appears similar, too.[229] The stabilization of this orbital is quite fascinating and is a trademark of luminescent copper clusters. These systems display a unique single low-lying triplet state and it is clear that occupation of only one triplet state is plausible. The LUMO of the $T_1$ excited state in **1** (the excited state of the excited state) displays significant Sb character, with an additional large amount of electron density located along the Cu-I core. The LUMO+4 is comprised of primarily of Sb 4*p* orbitals with some additional interaction with the Cu 3*d* orbitals, which interestingly is very similar to the LUMO+1 cluster of orbitals in the ground state. The previous HOMO of the ground state, consisting of Cu (3*d*) and I (5*p*) parentage is the new HOMO-2 cluster in the triplet excited state, showcasing the consistency between the two calculations for cluster **1**. The energy difference between the $T_0$ HOMO and the highest energy SOMO of $T_1$ represents the energy of the phosphorescent emission from the LE band that is experimentally observed. The corresponding calculated emission wavelength was determined to be 980 nm, which is quite red-shifted from the experimental value (711 nm). Such a deviation from experimental spectroscopic energies is not uncommon in DFT calculations on multinuclear transition metal complexes in general,[249] and for B3LYP in particular,[250]

however these deviations are usually blue-shifted. However, it must be stated that this shift is significant and could be a sign that the calculation could be improved upon. Overall, this was the only discrepancy in the calculation, suggesting this to be a satisfactory theoretical model of our system.

**Conclusion**

In conclusion, copper-antimony cuboid clusters can be synthesized with a multitude of different antimony ligands with varying steric size, but only ligands with enough steric bulk ($\geq$ 26.0 $\%V_B$, R = $^{i}Pr_3$, $^{t}Bu_3$, $^{t}Bu_2Ph$, $Cy_3$, $^{i}Pr_2Ph$) will form cubes. Smaller ligands ($\leq$ 25.8 $\%V_B$, R = $Ph_3$, $Me_2Ph$) only form dimeric structures. In this work, only the cuboid structures are luminescent and only show one emission band whose intensity varies with temperature. There is a distinct structure-luminescence correlation present in this class of compounds. Similar to other work on copper cubes, we find cubes derived from ligands with 0 or 1 phenyl unit(s) do not exhibit thermochromism; rather, only thermoluminescence is observed. In contrast to previously-held theories that Cu-Cu distances are the only reliable metric for emission energy, our work has revealed that the *combination of short Cu-Cu bonds with a $Cu_4$ core possessing highest crystallographic symmetries is required for NIR emission*. A small, but important, conclusion drawn from this work is that among cubes with similar average Cu-Cu bonds, the presence of a *single* short Cu-Cu bond red-shifts the $\lambda_{em}$ value. Lastly, shorter average Cu-Cu bonds (regardless of symmetry) lead to higher $T_{em}$ values — that is, luminescence at temperatures closer to ambient conditions.

From DFT calculations, it is clear the two critical orbitals involved in the $S_1 \rightarrow T_1$ intersystem crossing process — as well as the $T_1 \rightarrow S_0$ emission process — are highly symmetric, Cu(3*d*) based MOs whose delocalization and resultant energy are dependent on the symmetry of the cluster. Such interpretation of the DFT calculations are consistent with

the experimental observation that the cluster with the highest symmetry (**1**) allows for the population of the most symmetric and lowest energy MOs in a $Cu_4I_4Sb_4$ system. We conclude that the extremely high crystallographic symmetry of **1** — in conjunction with the small $\%V_B$ of $Sb^iPr_3$ and corresponding short $Cu\text{-}Cu_{avg}$ bond distances — result in cluster **1** exhibiting the lowest energy NIR emission (711 nm) in this series of clusters. This work convincingly relays that future designs for NIR emissive $Cu_4$ clusters must obtain shorter Cu-Cu bonds while retaining the highest possible (cubic) crystallographic symmetry — likely via the clever design of smaller, cuboid-supporting homoleptic ligands derived from main group elements.

## 3.7 REFERENCES


(195) Elie, M.; Renaud, J.-L.; Gaillard, S. N-Heterocyclic Carbene Transition Metal Complexes in Light Emitting Devices. *Polyhedron* **2018**, *140*, 158–168.

(196) Zhang, K. Y.; Yu, Q.; Wei, H.; Liu, S.; Zhao, Q.; Huang, W. Long-Lived Emissive Probes for Time-Resolved Photoluminescence Bioimaging and Biosensing. *Chem. Rev.* **2018**, *118*, 1770–1839.

(197) Shan, X.-C.; Jiang, F.-L.; Chen, L.; Wu, M.-Y.; Pan, J.; Wan, X.-Y.; Hong, M.-C. Using Cuprophilicity as a Multi-Responsive Chromophore Switching Color in Response to Temperature, Mechanical Force and Solvent Vapors. *J. Mater. Chem. C* **2013**, *1*, 4339–4349.

(198) Reineck, P.; Gibson, B. C. Near-Infrared Fluorescent Nanomaterials for Bioimaging and Sensing. *Adv. Opt. Mater.* **2016**, *5*, 1600446.

(199) Wang, W.; Lei, X.; Gao, H.; Mao, Y. Near-Infrared Quantum Cutting Platform in Transparent Oxyfluoride Glass–ceramics for Solar Sells. *Opt. Mater. (Amst).* **2015**, *47*, 270–275.

(200) Liu, Y.; Zhang, P.; Fang, X.; Wu, G.; Chen, S.; Zhang, Z.; Chao, H.; Tan, W.; Xu, L. Near-Infrared Emitting Iridium(III) Complexes for Mitochondrial Imaging in Living Cells. *Dalt. Trans.* **2017**, *46*, 4777–4785.

(201) Otto, S.; Dorn, M.; Förster, C.; Bauer, M.; Seitz, M.; Heinze, K. Understanding and Exploiting Long-Lived near-Infrared Emission of a Molecular Ruby. *Coord. Chem. Rev.* **2018**, *359*, 102–111.

(202) Wagenknecht, P. S.; Ford, P. C. Metal Centered Ligand Field Excited States: Their Roles in the Design and Performance of Transition Metal Based Photochemical Molecular Devices. *Coord. Chem. Rev.* **2011**, *255*, 591–616.

(203) Peng, Y.; Hu, J. X.; Lu, H.; Wilson, R. M.; Motevalli, M.; Hernández, I.; Gillin, W. P.; Wyatt, P. B.; Ye, H. Q. Functionalisation of Ligands through Click Chemistry: Long-Lived NIR Emission from Organic Er(III) Complexes with a Perfluorinated Core and a Hydrogen-Containing Shell. *RSC Adv.* **2017**, *7*, 128–131.

(204) Tan, R. H. C.; Motevalli, M.; Abrahams, I.; Wyatt, P. B.; Gillin, W. P. Quenching of IR Luminescence of Erbium, Neodymium, and Ytterbium β-Diketonate Complexes by Ligand C−H and C−D Bonds. *J. Phys. Chem. B* **2006**, *110*, 24476–24479.

(205) Zampetti, A.; Minotto, A.; Squeo, B. M.; Gregoriou, V. G.; Allard, S.; Scherf, U.; Chochos, C. L.; Cacialli, F. Highly Efficient Solid-State Near-Infrared Organic Light-Emitting Diodes Incorporating A-D-A Dyes Based on α,β-Unsubstituted "BODIPY" Moieties. *Sci. Rep.* **2017**, *7*, 1611.

(206) Park, S.; Fukuda, K.; Wang, M.; Lee, C.; Yokota, T.; Jin, H.; Jinno, H.; Kimura, H.; Zalar, P.; Matsuhisa, N.; et al. Ultraflexible Near-Infrared Organic Photodetectors for Conformal Photoplethysmogram Sensors. *Adv. Mater.* **2018**, *30*, 1802359.

(207) Skoog, D. A.; Holler, F. J.; Crouch, S. R. *Principles of Instrumental Analysis*, 6th ed.; Thomson Brooks Cole: Belmont, CA, 2007.

(208) Ford, P. C.; Cariati, E.; Bourassa, J. Photoluminescence Properties of Multinuclear Copper(I) Compounds. *Chem. Rev.* **1999**, *99*, 3625–3648.

(209) Bai, S.-Q.; Ke, K. L.; Young, D. J.; Hor, T. S. A. Structure and Photoluminescence of Cubane-like $[Cu_4I_4]$ Cluster-Based 1D Coordination Polymer Assembled with Bis(Triazole)Pyridine Ligand. *J. Organomet. Chem.* **2017**, *849–850*, 137–141.

(210) Hardt, H. D.; Pierre, A. Fluorescence Thermochromism of Pyridine Cu Iodide and Copper Iodide. *Z. Anorg. Allg. Chem*. **1973**, *42*, 107–112.

(211) Perruchas, S.; Goff, X. F. L.; Maron, S.; Maurin, I.; Guillen, F.; Garcia, A.; Gacoin, T.; Boilot, J. P. Mechanochromic and Thermochromic Luminescence of a Copper Iodide Cluster. *J. Am. Chem. Soc.* **2010**, *132*, 10967–10969.

(212) Benito, Q.; Goff, X. F. Le; Nocton, G.; Fargues, A.; Garcia, A.; Berhault, A.; Kahlal, S.; Saillard, J.-Y.; Martineau, C.; Trébosc, J.; et al. Geometry Flexibility of Copper Iodide Clusters: Variability in Luminescence Thermochromism. *Inorg. Chem.* **2015**, *54*, 4483–4494.

(213) Benito, Q.; Maurin, I.; Cheisson, T.; Nocton, G.; Fargues, A.; Garcia, A.; Martineau, C.; Gacoin, T.; Boilot, J. P.; Perruchas, S. Mechanochromic Luminescence of Copper Iodide Clusters. *Chem. - A Eur. J.* **2015**, *21*, 5892–5897.

(214) Tard, C.; Perruchas, S.; Maron, S.; Goff, X. F. Le; Guillen, F.; Garcia, A.; Vigneron, J.; Etcheberry, A.; Gacoin, T.; Boilot, J. Thermochromic Luminescence of Sol-Gel Films Based on Copper Iodide Clusters. **2008**, *5*, 7010–7016.

(215) Lapprand, A.; Dutartre, M.; Khiri, N.; Levert, E.; Fortin, D.; Rousselin, Y.; Soldera, A.; Jug, S.; Harvey, P. D. Luminescent P-Chirogenic Copper Clusters. *Inorg. Chem.* **2013**, *52*, 7958–7967.

(216) Churchill, M. R.; Kalra, K. L. Molecules With an $M_4X_4$ core. III. Comparison of the x-ray crystallographically determined molecular structures of tetrameric triethylphosphinecopper(I) iodide and triethylarsinecopper(I) Iodide. *Inorg. Chem.* **1974**, *13*, 1899–1904.

(217) Churchill, M. R.; Youngs, W. J. (Triphenylarsine)Copper(I). *Inorg. Chem.* **1979**, *18*, 0–5.

(218) Knorr, M.; Bonnot, A.; Lapprand, A.; Khatyr, A.; Strohmann, C.; Kubicki, M. M.; Rousselin, Y.; Harvey, P. D. Reactivity of CuI and CuBr toward dialkyl sulfides RSR: From discrete molecular $Cu_4I_4S_4$ and $Cu_8I_8S_6$ clusters to luminescent copper(I) coordination polymers *Inorg. Chem.* **2015**, *54*, 4076–4093.

(219) Knorr, M.; Khatyr, A.; Aleo, A. D.; Yaagoubi, A. El; Strohmann, C.; Kubicki, M. M.; Rousselin, Y.; Aly, S. M.; Fortin, D.; Lapprand, A.; et al. Copper(I) Halides (X = Br, I) Coordinated to Bis(Arylthio)Methane Ligands: Aryl Substitution and Halide Effects on the Dimensionality, Cluster Size, and Luminescence Properties of the Coordination Polymers. *Cryst. Growth Des.* **2014**, *14*, 5373–5387.

(220) Rose, M. J.; Mascharak, P. K. Photosensitization of Ruthenium Nitrosyls to Red Light with an Isoelectronic Series of Heavy-Atom Chromophores: Experimental and Density Functional Theory Studies on the Effects of O-, S- and Se-Substituted Coordinated Dyes. *Inorg. Chem.* **2009**, *48*, 6904–6917.

(221) Li, P.-F.; Schon, T. B.; Seferos, D. S. Thiophene, Selenophene, and Tellurophene-Based Three-Dimensional Organic Frameworks. *Angew. Chemie Int. Ed.* **2015**, *54*, 9361–9366.

(222) Dobbs, K. D.; Boggs, J. E.; Cowley, A. H. Trends in Structure and Reactivity of Group 15 Alkyls, Alkylidenes, and Alkylidynes. *Chem. Phys. Lett*. **1987**, *141*, 372–375.

(223) Bilbrey, J. A.; Kazez, A. H.; Locklin, J.; Allen, W. D. Exact Ligand Cone Angles. *J. Comput. Chem.* **2013**, *34*, 1189–1197.

(224) Paizanos, K.; Charalampou, D.; Kourkoumelis, N.; Kalpogiannaki, D.; Hadjiarapoglou, L.; Spanopoulou, A.; Lazarou, K.; Manos, M. J.; Tasiopoulos, A.

J.; Kubicki, M.; et al. Synthesis and Structural Characterization of New Cu(I) Complexes with the Antithyroid Drug 6-*n*-Propyl-Thiouracil. Study of the Cu(I)-Catalyzed Intermolecular Cycloaddition of Iodonium Ylides toward Benzo[*b*]Furans with Pharmaceutical Implementations. *Inorg. Chem.* **2012**, *51*, 12248–12259.

(225) Kitagawa, H.; Ozawa, Y.; Toriumi, K. Flexibility of Cubane-like $Cu_4I_4$ Framework : Temperature Dependence of Molecular Structure and Luminescence Thermochromism of $[Cu_4I_4(PPh_3)_4]$ in Two Polymorphic Crystalline States W. *Chem. Commun.* **2010**, *4*, 6302–6304.

(226) Sculfort, S.; Braunstein, P. Intramolecular $d^{10}$-$d^{10}$ Interactions in Heterometallic Clusters of the Transition Metals. *Chem. Soc. Rev.* **2011**, *40*, 2741–2760.

(227) Huitorel, B.; El Moll, H.; Utrera-Melero, R.; Cordier, M.; Fargues, A.; Garcia, A.; Massuyeau, F.; Martineau-Corcos, C.; Fayon, F.; Rakhmatullin, A.; et al. Evaluation of Ligands Effect on the Photophysical Properties of Copper Iodide Clusters. *Inorg. Chem.* **2018**, *57*, 4328–4339.

(228) Benito, Q.; Le Goff, X. F.; Nocton, G.; Fargues, A.; Garcia, A.; Berhault, A.; Kahlal, S.; Saillard, J. Y.; Martineau, C.; Trébosc, J.; et al. Geometry Flexibility of Copper Iodide Clusters: Variability in Luminescence Thermochromism. *Inorg. Chem.* **2015**, *54*, 4483–4494.

(229) Perruchas, S.; Tard, C.; Le Goff, X. F.; Fargues, A.; Garcia, A.; Kahlal, S.; Saillard, J.-Y.; Gacoin, T.; Boilot, J.-P. Thermochromic Luminescence of Copper Iodide Clusters: The Case of Phosphine Ligands. *Inorg. Chem.* **2011**, *50*, 10682–10692.

(230) Churchill, M. R.; Kalra, K. L. Molecules with an $M_4X_4$ Core. III. Comparison of the X-Ray Crystallographically Determined Molecular Structures of Tetrameric Triethylphosphinecopper(I) Iodide and Triethylarsinecopper(I) Iodide. *Inorg. Chem.* **1974**, *13*, 1899–1904.

(231) Medina, I.; Mague, J. T.; Fink, M. J. Tetra-$\mu_3$-iodo-tetrakis[(tri-*tert*-butylphosphine)copper(I)]. *Acta Crystallogr. Sect. E* **2005**, *61*, m1550-m1552.

(232) Sculfort, S.; Braunstein, P. Intramolecular $d^{10}$-$d^{10}$ Interactions in Heterometallic Clusters of the Transition Metals. *Chem. Soc. Rev.* **2011**, *40*, 2741–2760.

(233) Shou, R.-E.; Chai, W.-X.; Song, L.; Qin, L.-S.; Shi, H.-S.; Wang, T.-G. Three Luminescent Copper(I) Iodide Clusters with Phosphine Ligands: Synthesis, Structure Characterization, Properties and TD-DFT Calculations. *J. Clust. Sci.* **2017**, *28*, 2185–2203.

(234) Lakowicz, J. R. *Principles of Fluorescence Spectroscopy*, 3rd ed.; Springer: New York, 2006.

(235) Steiner, U. E. Fundamentals of Photophysics, Photochemistry, and Photobiology. In *Photodynamic Therapy*; Abdel-Kader, M. H., Ed.; Springer-Verlag: Berlin, 2014; pp 25–58.

(236) Hardt, H. D.; Pierre, A. Fluorescence Thermochromism and Symmetry of Copper(I) Complexes. *Inorganica Chim. Acta* **1977**, *25*, L59–L60.

(237) Rath, N. P.; Holt, E. M.; Tanimura, K. Fluorescent Copper(I) Complexes: Structural and Spectroscopic Characterization of Bis(*p*-Toluidine)Bis(Acetonitrile)Tetraiodotetracopper and Bis[(*p*-Chloroaniline)(Acetonitrile)Diiododicopper] Tetrameric Complexes of Mixed-Ligand Character. *Inorg. Chem.* **1985**, *24*, 3934–3938.

(238) Hu, G.; Mains, G. J.; Holt, E. M. Correlation of Structure and Emission in Solid State Copper(I) Complexes; $[Cu_4I_4(CH_3CN)_2(L)_2]$, L = Aniline Derivative. *Inorganica Chim. Acta* **1995**, *240*, 559–565.

(239) Vogler, A.; Kunkely, H. Photoluminescence of Tetrameric Copper(I) Iodide Complexes Solutions. *J. Am. Chem. Soc.* **1986**, *108*, 7211–7212.

(240) Yang, K.; Li, S.-L.; Zhang, F.-Q.; Zhang, X.-M. Simultaneous Luminescent Thermochromism, Vapochromism, Solvatochromism, and Mechanochromism in a C3-Symmetric Cubane $[Cu_4I_4P_4]$ Cluster without Cu–Cu Interaction. *Inorg. Chem.* **2016**, *55*, 7323–7325.

(241) Vega, A.; Saillard, J. Y. Bonding in Tetrahedral $Cu_4(M^{3-}X)_4L_4$ Copper(I) Clusters: A DFT Investigation. *Inorg. Chem.* **2004**, *43*, 4012–4018.

(242) De Angelis, F.; Fantacci, S.; Sgamellotti, A.; Cariati, E.; Ugo, R.; Ford, P. C. Electronic Transitions Involved in the Absorption Spectrum and Dual Luminescence of Tetranuclear Cubane $[Cu_4I_4(Pyridine)_4]$ Cluster: A Density Functional Theory/Time-Dependent Density Functional Theory Investigation. *Inorg. Chem.* **2006**, *45*, 10576–10584.

(243) Kitagawa, H.; Ozawa, Y.; Toriumi, K. Flexibility of Cubane-like $Cu_4I_4$ Framework: Temperature Dependence of Molecular Structure and Luminescence Thermochromism of $[Cu_4I_4(PPh_3)_4]$ in Two Polymorphic Crystalline States. *Chem. Commun.* **2010**, *46*, 6302–6304.

(244) Kim, T. H.; Shin, Y. W.; Jung, J. H.; Kim, J. S.; Kim, J. Crystal-to-Crystal Transformation between Three CuIcoordination Polymers and Structural Evidence for Luminescence Thermochromism. *Angew. Chemie - Int. Ed.* **2008**, *47*, 685–688.

(245) Ryu, C. K.; Vitale, M.; Ford, P. C. Photoluminescence Properties of the Structurally Analogous Tetranuclear Copper(I) Clusters $Cu_4X_4(Dpmp)_4$ (X = I, Br, Cl; Dpmp = 2-(Diphenylmethyl)Pyridine). *Inorg. Chem.* **1993**, *32*, 869–874.

(246) Chen, K.; Shearer, J.; Catalano, V. J. Subtle Modulation of $Cu_4X_4L_2$ Phosphine Cluster Cores Leads to Changes in Luminescence. *Inorg. Chem.* **2015**, *54*, 6245–6256.

(247) Mazzeo, P. P.; Maini, L.; Petrolati, A.; Fattori, V.; Shankland, K.; Braga, D. Phosphorescence Quantum Yield Enhanced by Intermolecular Hydrogen Bonds in $Cu_4I_4$ Clusters in the Solid State. *J. Chem. Soc. Dalt. Trans.* **2014**, *43*, 9448–9455.

(248) Taylor, W. V.; Xie, Z.; Cool, N.; Shubert, S.; Rose, M. J. Syntheses, Structures and Characterization of Nickel(II) Stibines: Steric and Electronic Rationale For Metal Deposition. *Inorg. Chem.* **2018**, *57*, 10364–10374.

(249) Chantzis, A.; Kowalska, J. K.; Maganas, D.; DeBeer, S.; Neese, F. Ab Initio Wave Function-Based Determination of Element Specific Shifts for the Efficient Calculation of X-Ray Absorption Spectra of Main Group Elements and First Row Transition Metals. *J. Chem. Theory Comput.* **2018**, *14*, 3686–3702.

(250) Shou, R. E.; Chai, W. X.; Song, L.; Qin, L. S.; Shi, H. S.; Wang, T. G. Three Luminescent Copper(I) Iodide Clusters with Phosphine Ligands: Synthesis, Structure Characterization, Properties and TD-DFT Calculations. *J. Clust. Sci.* **2017**, *28*, 2185–2203.

### 3.8 NMR SPECTRA

Note: Some spectra have a few extra peaks, but these are only solvent peaks. The peaks correspond to n-pentane (0.88 ppm, t; 1.27 ppm, m), diethyl ether (1.21 ppm, t; 3.48 ppm, q), water (1.56 ppm, s), acetone (2.17 ppm, s), dichloromethane (5.30 ppm, s), silicon grease (0.07 ppm, s), or tetrahydrofuran (1.85 ppm, m; 3.76 ppm, m). Each spectrum caption is labeled to denote the presence of solvent peaks.

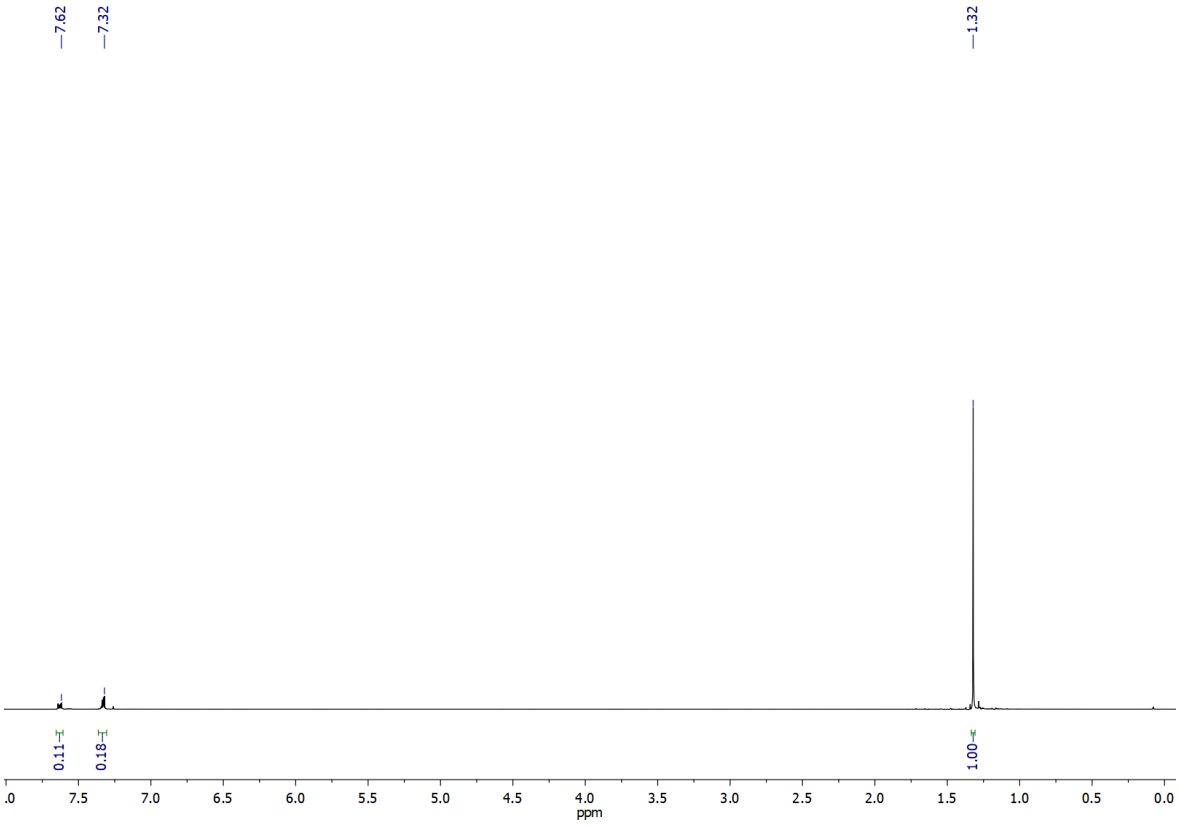


**Figure 3.20** $^{1}$H NMR spectrum of Sb$^{t}$Bu$_2$Ph in $CDCl_3$ obtained at 400 MHz.

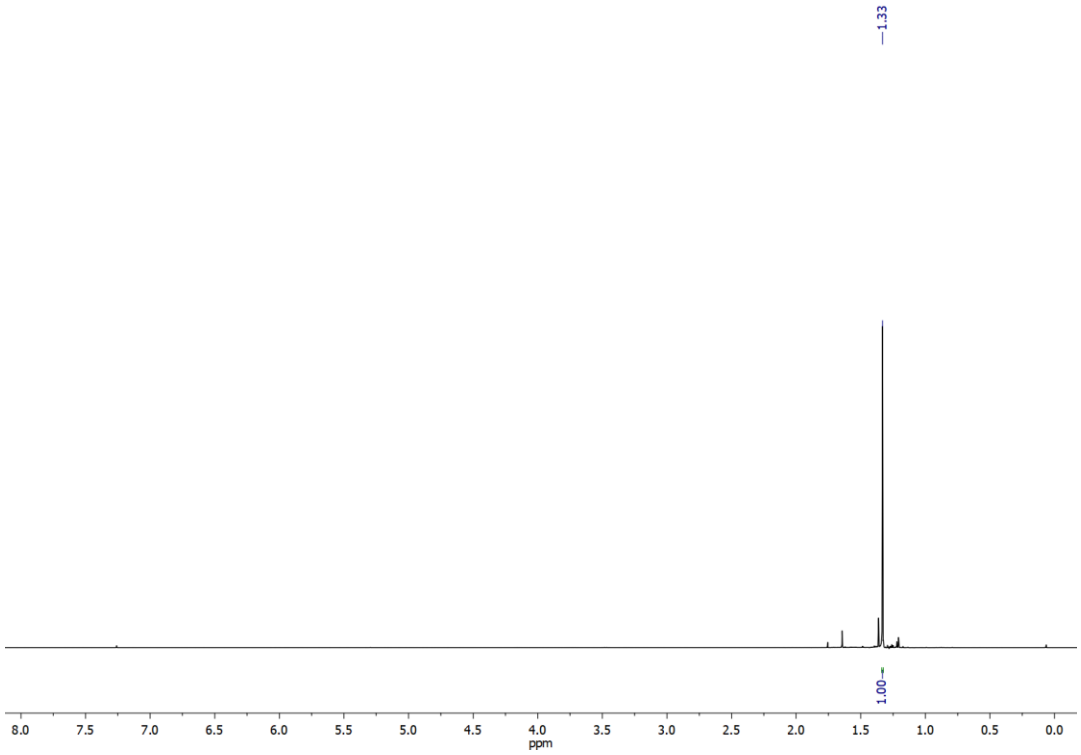


**Figure 3.21** $^{1}$H NMR spectrum of Sb$^{t}$Bu$_3$ in CDCl$_3$ obtained at 400 MHz.

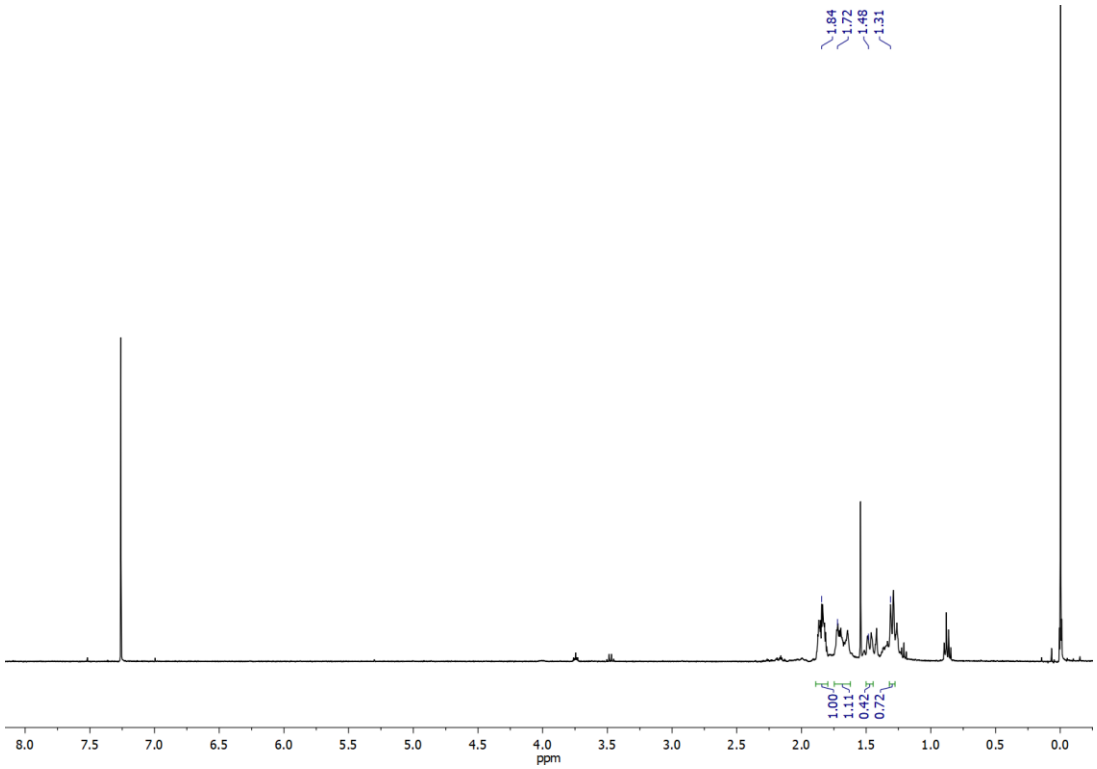


**Figure 3.22** $^{1}H$ NMR spectrum of $SbCy_3$ in $CDCl_3$ obtained at 400 MHz. Small solvent peaks of n-pentane (0.88 ppm, t; 1.27 ppm, m), diethyl ether (1.21 ppm, t; 3.48 ppm, q), tetrahydrofuran (1.85 ppm, m; 3.76 ppm, m), and silicon grease (0.07 ppm, s) are present in the spectrum.

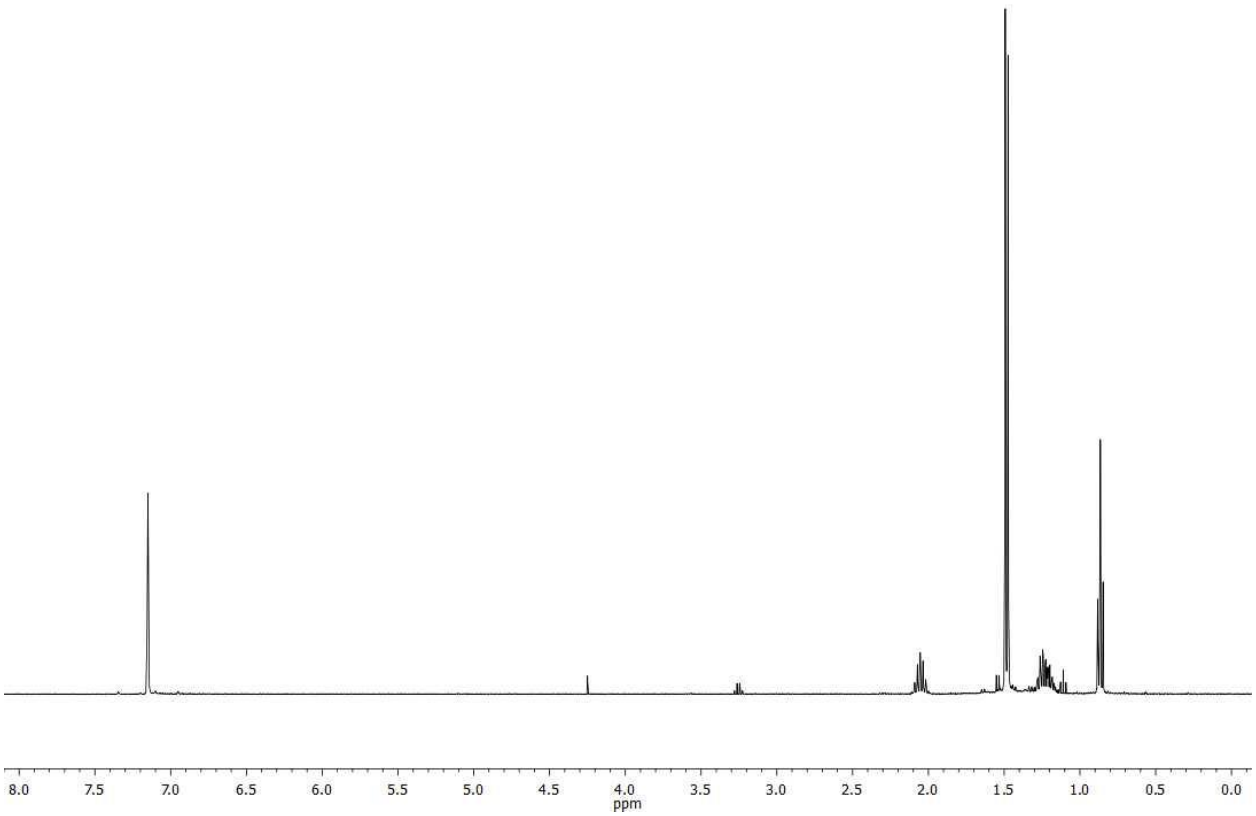


**Figure 3.23** $^{1}$H NMR of $[Cu_4(I)_4(Sb^iPr_3)_4]$ (**1**) in $C_6D_6$ obtained at 400 MHz. Small solvent peaks of n-pentane (0.87 ppm, t; 1.23 ppm, m) and diethyl ether (1.11 ppm, t; 3.26 ppm, q) are present in the spectrum.

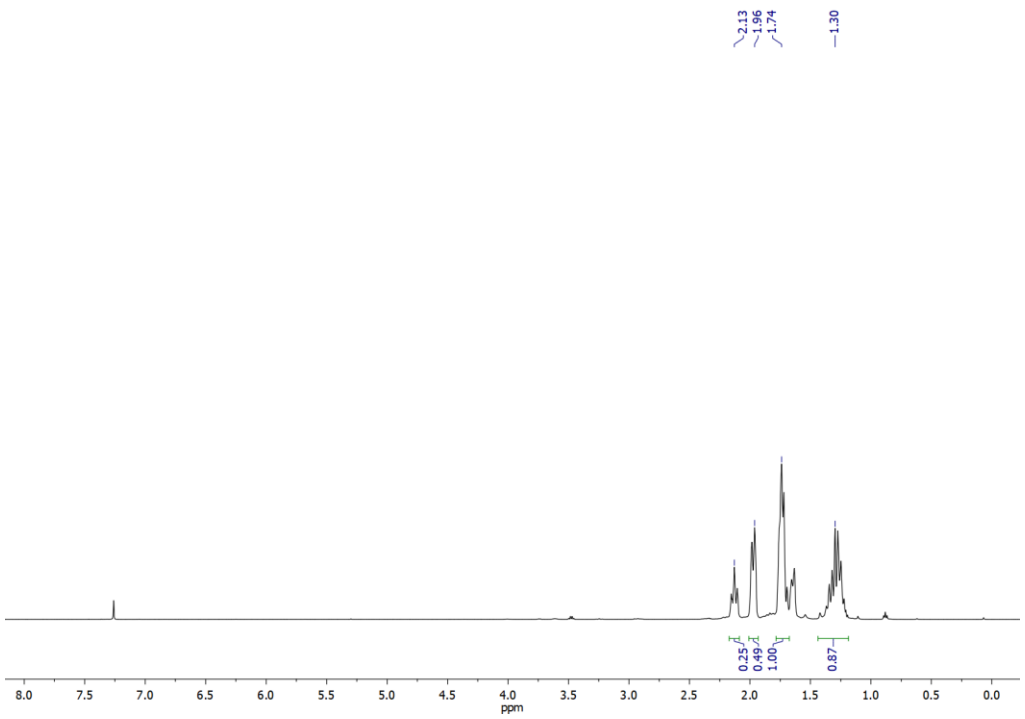


**Figure 3.24** $^{1}$H NMR spectrum of $Cu_4(I)_4(SbCy_3)_4$ [**2**] in $CDCl_3$ obtained at 500 MHz. Small solvent peaks of n-pentane (0.88 ppm, t; 1.27 ppm, m) and diethyl ether (1.21 ppm, t; 3.48 ppm, q) are present in the spectrum.

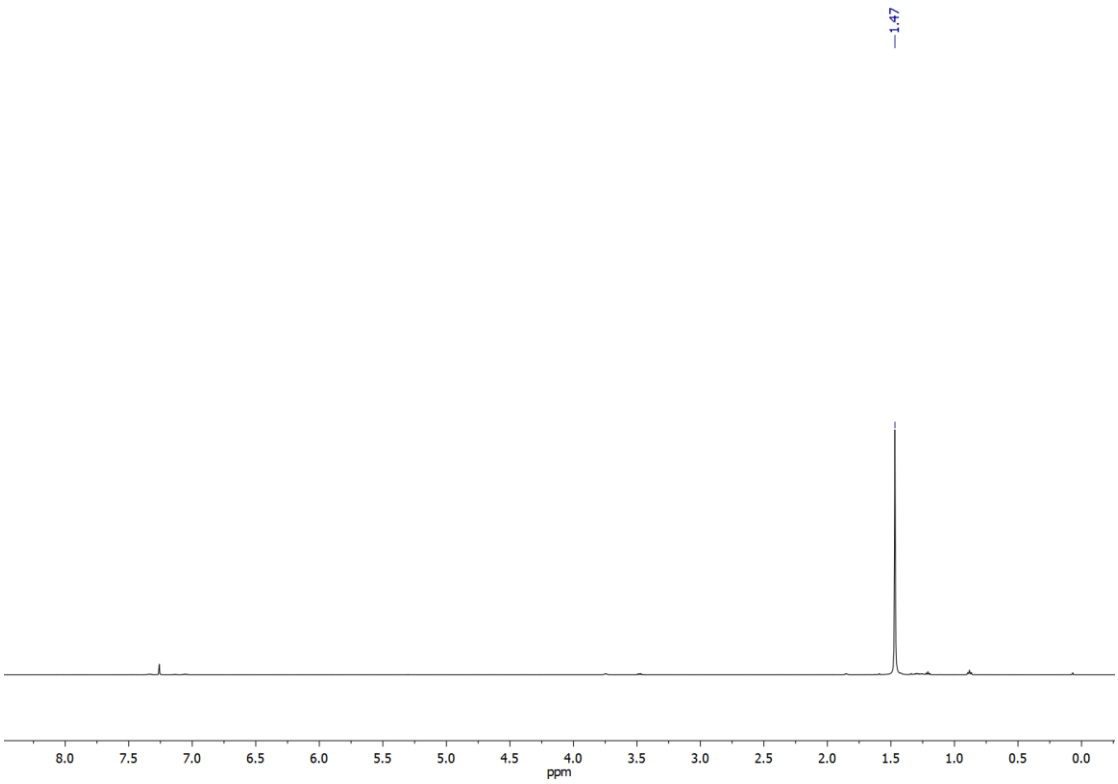


**Figure 3.25** $^{1}$H NMR spectrum of $Cu_4(I)_4(Sb^tBu_3)_4$ [**3**] in $CDCl_3$ obtained at 500 MHz. Small solvent peaks of n-pentane (0.88 ppm, t; 1.27 ppm, m) and diethyl ether (1.21 ppm, t; 3.48 ppm, q) are present in the spectrum.

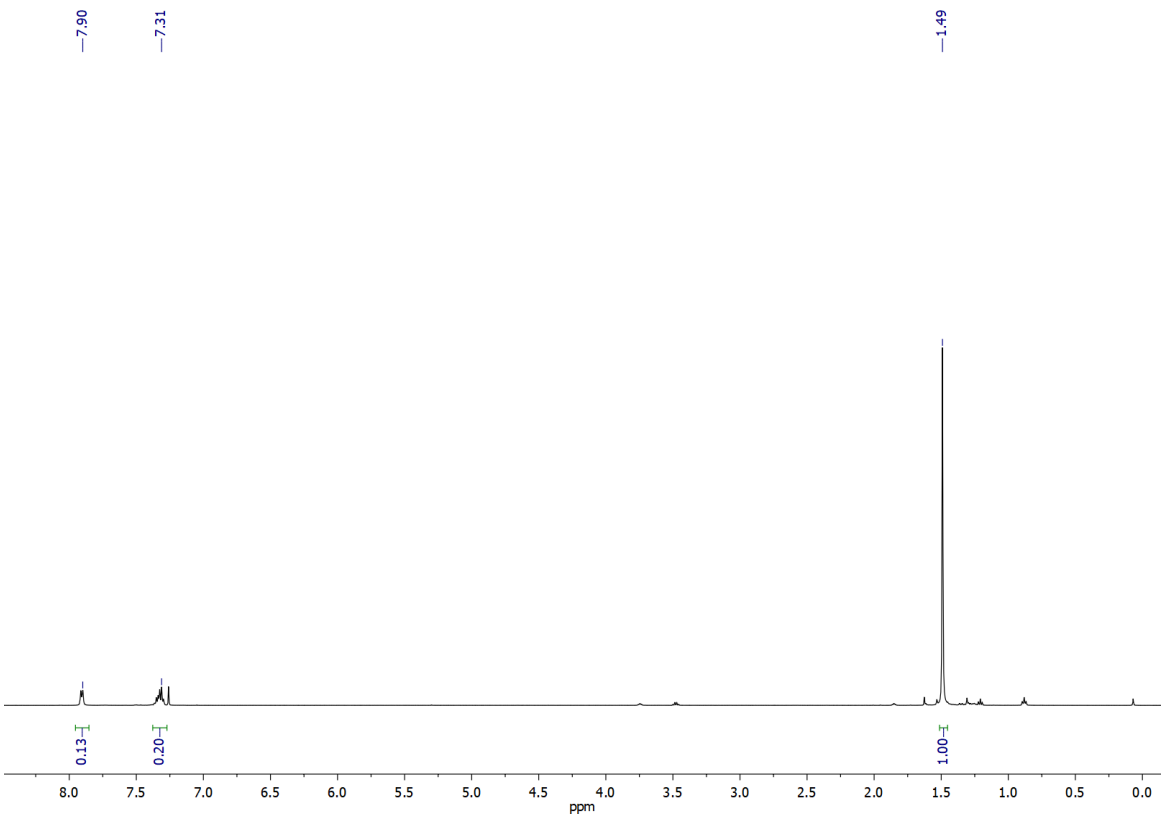


**Figure 3.26** $^{1}$H NMR spectrum of $Cu_4(I)_4(Sb^tBu_2Ph)_4$ [**4**] in $CDCl_3$ obtained at 500 MHz. Small solvent peaks of n-pentane (0.88 ppm, t; 1.27 ppm, m), diethyl ether (1.21 ppm, t; 3.48 ppm, q), tetrahydrofuran (1.85 ppm, m; 3.76 ppm, m), and silicon grease (0.07 ppm, s) are present in the spectrum.

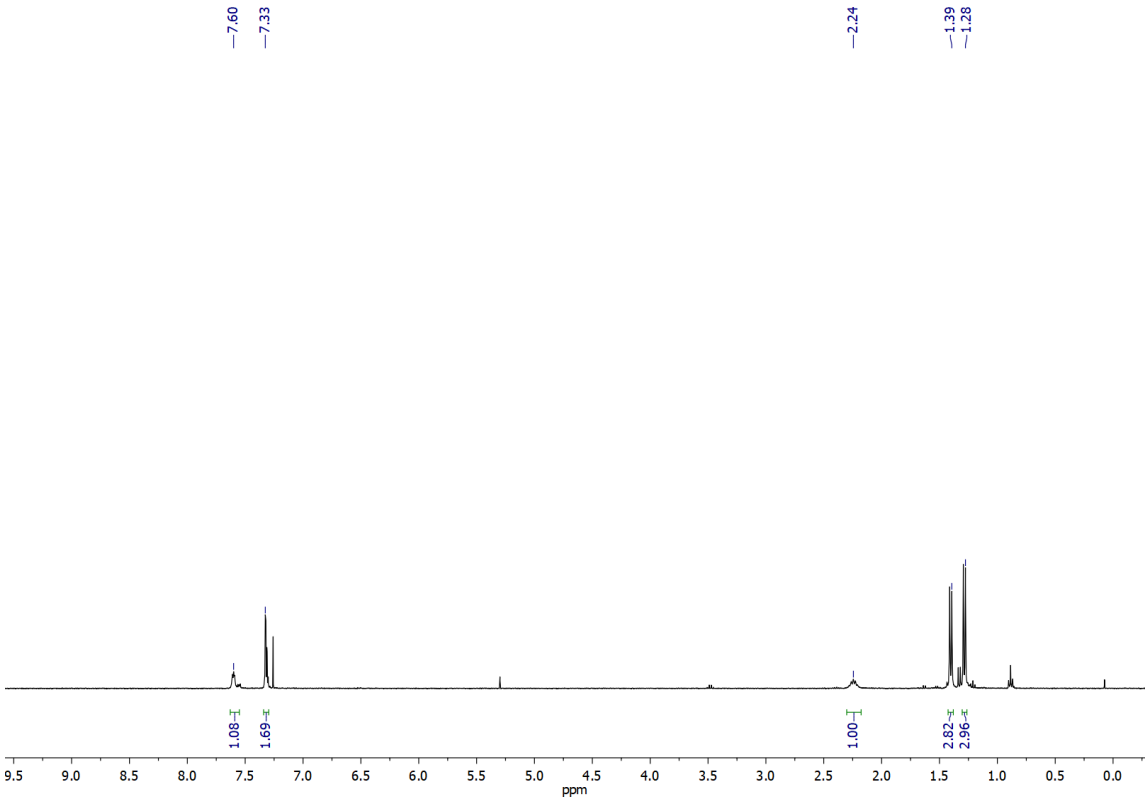


**Figure 3.27** $^{1}$H NMR spectrum of $Cu_2(I)_2(Sb^{i}Pr_2Ph)_4$ [**5**] in $CDCl_3$ obtained at 500 MHz. Small solvent peaks of n-pentane (0.88 ppm, t; 1.27 ppm, m), diethyl ether (1.21 ppm, t; 3.48 ppm, q), dichloromethane (5.30 ppm, s), and silicon grease (0.07 ppm, s) are present in the spectrum.

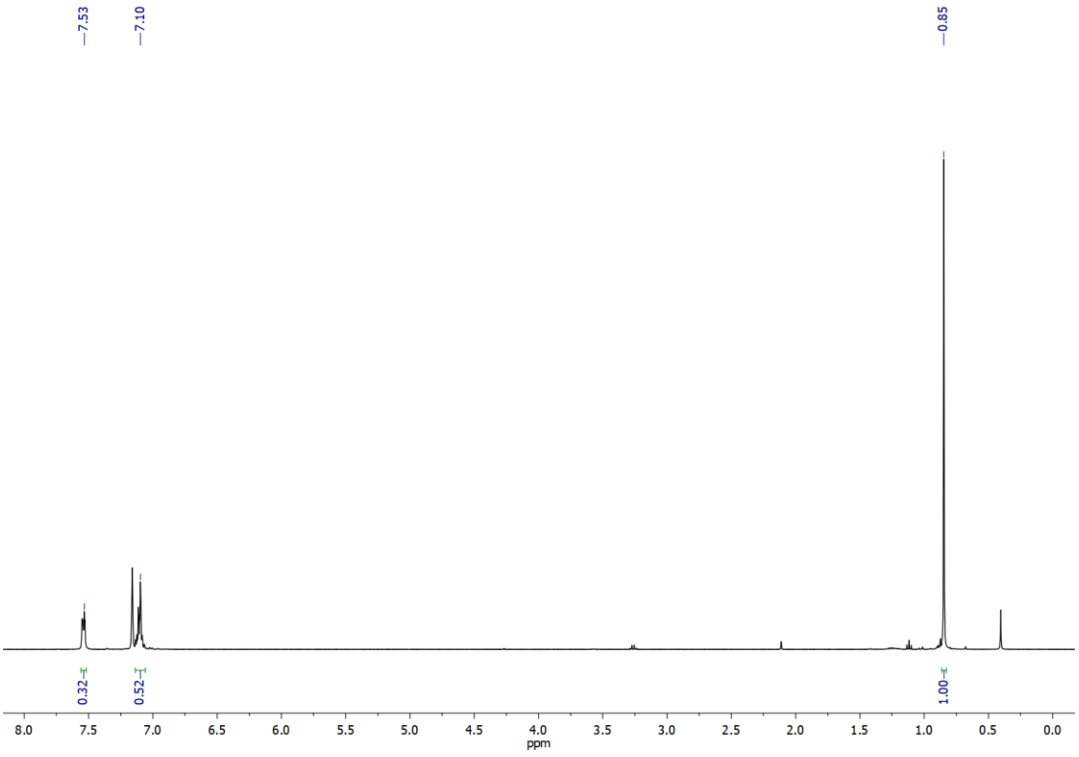


**Figure 3.28** $^{1}$H NMR spectrum of $Cu_2(I)_2(SbMe_2Ph)_4$ [**6**] in $C_6D_6$ obtained at 500 MHz. Small solvent peaks of water (0.40 ppm, s) and diethyl ether (1.11 ppm, t; 3.26 ppm, q) are present in the spectrum.

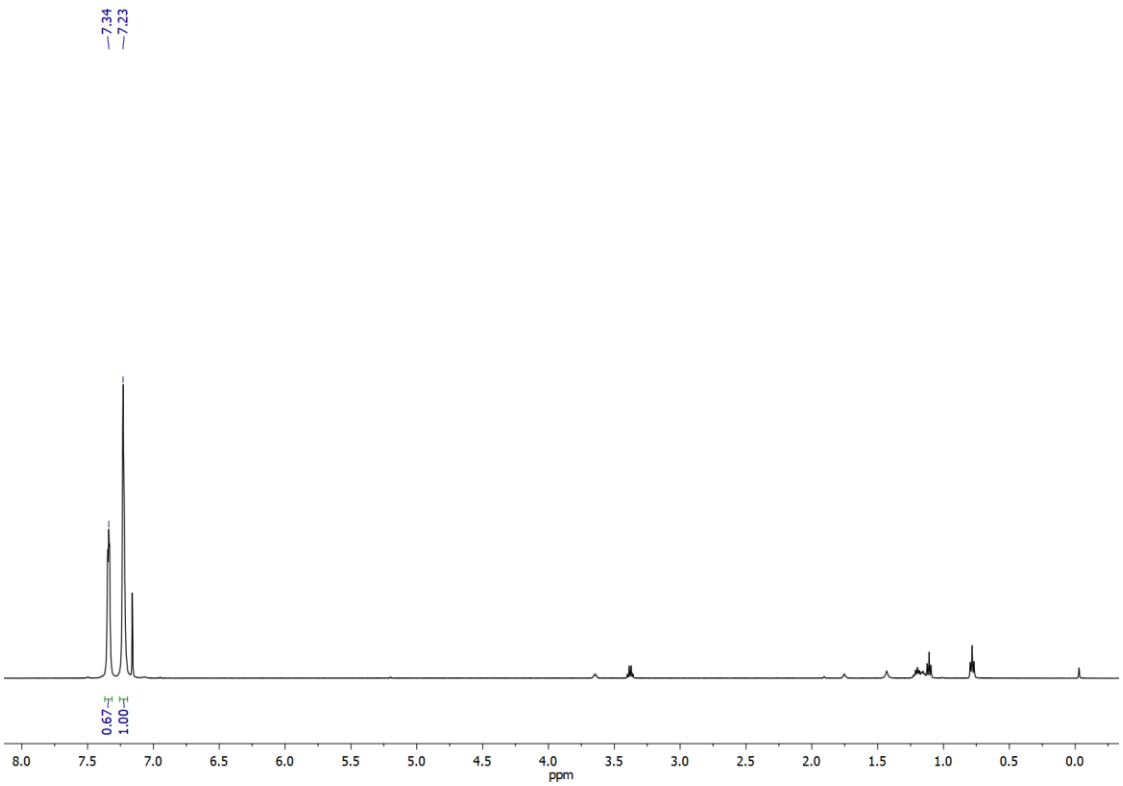


**Figure 3.29** $^{1}$H NMR spectrum of $Cu_2(I)_2(SbPh_3)_4$ [**7**] in $C_6D_6$ obtained at 500 MHz. Small solvent peaks of n-pentane (0.87 ppm, t; 1.23 ppm; m), diethyl ether (1.11 ppm, t; 3.26 ppm; q), tetrahydrofuran (1.40 ppm, m; 3.57 ppm, m) are present in the spectrum.

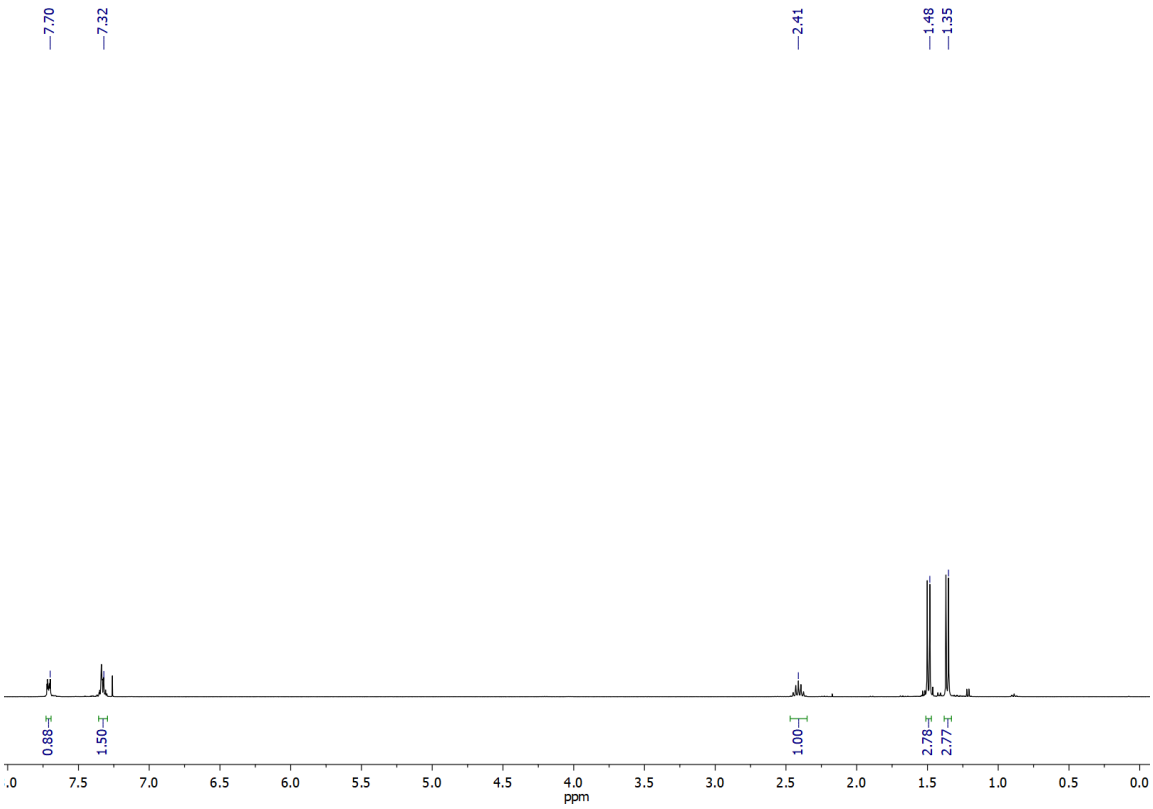


**Figure 3.30** $^{1}$H NMR spectrum of $Cu_4(I)_4(Sb^{i}Pr_2Ph)_4$ [**8**] in $CDCl_3$ obtained at 500 MHz. Small solvent peaks of pentane (n-pentane (0.88 ppm, t; 1.27 ppm, m) and acetone (2.17 ppm, s) are present in the spectrum.

## 3.9 Crystal Tables and Refinement Parameters for Cu-Sb complexes

**Table 3.6** Selected Crystal Data for $[Cu_4(I)_4(Sb^iPr_3)_4]$ (**1**) at 150 K.

| **Empirical formula** | **$C_9H_{21}CuISb$** |
|---|---|
| **Formula weight** | 1765.87 |
| **Temperature** | 150 K |
| **Wavelength** | 1.54184 Å |
| ***a*, Å** | 14.0760(2) Å |
| ***b*, Å** | 14.0760(2) Å |
| ***c*, Å** | 14.0760(2) Å |
| **α, deg** | 90° |
| **β, deg** | 90° |
| **γ, deg** | 90° |
| **Volume** | 2788.93(12) $Å^3$ |
| ***Z*** | 12 |
| **Density (calculated)** | 2.103 $Mg/m^3$ |
| **Absorption coefficient** | 34.276 $mm^{-1}$ |
| **Goodness-of-fit on $F^2$** | 1.082 |
| **Final R indices [I > 2σ (I)]** | R1 = 0.0345<br>wR2 = 0.0903 |
| **R indices (all data)** | R1 = 0.0360<br>wR2 = 0.0913 |

| | $Cu_4(I)_4(SbCy_3)_4$ **(2)** | $Cu_4(I)_4(Sb^tBu_3)_4$ **(3)** | $Cu_4(I)_4(Sb^tBu_2Ph)_4$ **(4)** | $Cu_2(I)_2(Sb^iPr_2Ph)_4$ **(5)** | $Cu_2(I)_2(SbMe_2Ph)_4$ **(6)** | $Cu_2(I)_2(SbPh_3)_4$ **(7)** |
|---|---|---|---|---|---|---|
| Formula | $C_{72}H_{132}C_{l4}Cu_4I_4Sb_4$ | $C_{48}$ $H_{108}$ $Cu_4I_4Sb_4$ | $C_{56}H_{92}Cu_4I_4Sb_4$ | $C_{48}H_{76}Cu_2I_2Sb_4$ | $C_{24}H_{33}Cu_{1.50}I_{1.50}Sb_3$ | $C_{36}H_{30}CuISb_2$ |
| FW | 2388.33 | 1934.10 | 2014.05 | 1520.96 | 972.41 | 896.54 |
| Color | Colorless | Colorless | Colorless | Colorless | Colorless | Colorless |
| Habit | Prism | Block | Block | Block | Plates | Plates |
| Size ($mm^3$) | 0.2 × 0.2 × 0.15 | 0.15 × 0.15 × 0.12 | 0.25 × 0.2 × 0.1 | 0.2 × 0.15 × 0.1 | 0.18 × 0.12 × 0.07 | 0.1 × 0.08 × 0.05 |
| T (K) | 100 (2) | 100 (2) | 100 (2) | 100 (2) | 100 (2) | 100 (2) |
| Lattice | Orthorhombic | Trigonal | Tetragonal | Triclinic | Triclinic | Monoclinic |
| Space Group | *P*212121 | *R*-3 | *I*-4 | *P*-1 | *P*-1 | *P*21/c |
| a (Å) | 14.4780(15) | 14.2779(13) | 15.889(2) | 13.0699(9) | 10.4433(5) | 24.3954(15) |
| b (Å) | 24.208(3) | 14.2779(13) | 15.889(2) | 13.8976(8) | 12.2143(6) | 13.8760(9) |
| c (Å) | 24.835(3) | 61.986(6) | 13.3892(16) | 16.7487(12) | 26.2003(12) | 20.2060(12) |
| α (deg) | 90 | 90.0 | 90 | 89.660(3) | 92.152(2) | 90 |
| β (deg) | 90 | 90.0 | 90 | 84.836(4) | 101.319(2) | 111.165(2) |
| γ (deg) | 90 | 120 | 90 | 63.596(3) | 114.095(2) | 90 |
| V ($Å^3$) | 8704.4(18) | 10943(2) | 3380.0(9) | 2711.8(3) | 2965.5(2) | 6378.6(7) |
| Z | 4 | 6 | 2 | 2 | 4 | 8 |
| $d_{calc}$ ($g/cm^3$) | 1.822 | 1.761 | 1.979 | 1.863 | 2.178 | 1.867 |
| μ ($mm^{-1}$) | 3.756 | 4.317 | 4.664 | 3.901 | 5.331 | 3.334 |
| GOF on $F^2$ | 1.037 | 1.235 | 1.207 | 1.025 | 1.069 | 0.949 |
| R indices [I > 2σ(I)] | $R_1$ = 0.0160<br>$wR_2$ = 0.0411 | $R_1$ = 0.0233<br>$wR_2$ = 0.0378 | $R_1$ = 0.0111<br>$wR_2$ = 0.0273 | $R_1$ = 0.0204<br>$wR_2$ = 0.0418 | $R_1$ = 0.0306<br>$wR_2$ = 0.0622 | $R_1$ = 0.0191<br>$wR_2$ = 0.0413 |
| R indices all data | $R_1$ = 0.0180<br>$wR_2$ = 0.0418 | $R_1$ = 0.0259<br>$wR_2$ = 0.0383 | $R_1$ = 0.0111<br>$wR_2$ = 0.0273 | $R_1$ = 0.0276<br>$wR_2$ = 0.0435 | $R_1$ = 0.0411<br>$wR_2$ = 0.0652 | $R_1$ = 0.0210<br>$wR_2$ = 0.0421 |

**Table 3.7** Crystallographic data and refinement parameters for the antimony-copper complexes **2-7**.

# Chapter 4: Magnetic Properties of Cobalt-Antimony Complexes – Syntheses, Structures, and C-H Catalytic Activity

## 4.0 PROLOGUE

Following our successful metallations with Ni(II) metal salts, we knew we could synthesize complexes with high valent late 3*d* transition metals. As the overall goal of this project – detailed in Chapter 1 – was to synthesize complexes with enhanced magnetic properties (as compared to analogous complexes with lighter donor atoms) and describe their catalytic properties, we proceeded to Co(II) metal sources. Co(II) salts are $d^7$ complexes and will afford paramagnetic species in nearly any mononuclear geometry. As spin-orbit-coupling (SOC) requires at least $S \neq 0$ (among other criteria), we knew these complexes were to be investigated for their magnetic and catalytic properties. During the timeline of this dissertation work, this was the final project undertaken, and although the complexes were synthesized earlier on, the magnetic and catalytic studies were slightly abbreviated. Thus, this chapter will detail all of the work completed on these complexes, but it should be noted that a more in-depth investigation of the magnetic results and reactivity is likely required for future advancement and/or publication.

## 4.1 INTRODUCTION

In Chapter 1, we discussed the origin and applications of spin-orbit-coupling, the effect it could have on catalysis, and the theoretical phenomenon that heavy donor atoms could "donate" some portion of their spin-orbit-coupling to a metal center. In this chapter and in this introduction, we will delve deeper into molecular magnetism and the relationships between the spin Hamiltonian, spin-orbit-coupling, and zero-field-splitting to provide a baseline of knowledge in the field of molecular magnetism for the interested

synthetic chemist. The following paragraphs are built from summarizing three core sources: *Ch. 10: The Magnetic Properties of Complex Ions* in Introduction to Ligand Fields by Figgis,[107] Ch. 1-3 of Molecular Magnetism by Kahn,[106] and *Theory and Application of PHI* by Chilton.[112] These resources are essential learning materials for any reader interested in molecular magnetism and it is highly recommended to study these in-depth.

If a complex possesses unpaired spins, when it is exposed to a magnetic field, the field will align those unpaired spins in one direction. How that complex reacts to that magnetic field determines the magnetic susceptibility of the complex and from the susceptibility, the magnetic moment of a material can be derived. In molecular magnetism, the magnetic moment dictates the magnetic strength of the molecule, but it can also be used to ascertain useful characterizations of a complex, including oxidation states, number of unpaired electrons, and molecular geometry. Typically, the first and simplest equation learned when studying molecular magnetism is the spin-only magnetic moment equation, shown in equation 4.1.

$$\mu_{so} = \sqrt{4S(S+1)} \qquad \text{(Eq. 4.1)}$$

With knowledge of only the number of unpaired electrons ($S$ = u.p.e./2), one can calculate the spin-only magnetic moment. As the name implies, the spin-only magnetic moment equation does not factor in orbital angular momentum (it is sometimes referred to as the 'undergraduate approach'), and as discussed in Chapter 1, the spin and orbital angular momenta are coupled to each other through spin-orbit-coupling, *J*. To correct the spin-only magnetic moment for orbital angular momentum, a new equation is formed, called the effective magnetic moment equation (equation 4.2).

$$\mu_{eff} = \sqrt{L_{eff}\left(L_{eff}+1\right) + 4S(S+1)} \qquad \text{(Eq. 4.2)}$$

In the $\mu_{eff}$ equation, $L_{eff}$ is equal to 0 when the complex possesses an A or E term ground state, but $L_{eff}$ equals 1 if the complex normally exists in a T state. This is due to the orbital angular momentum being quenched in A and E terms. Orbital angular momentum about an axis is associated with the ability to rotate an orbital about an axis to give a geometrically *identical* and energetically *degenerate* orbital. Among A, E, and T terms, only the T term can satisfy that requirement, as $d_{x^2-y^2}$ and $d_{z^2}$ differ in shape such that no rotation can transform the $d_{x^2-y^2}$ orbital into the $d_{z^2}$ orbital.[107] From the $\mu_{eff}$ equation, when orbital angular momentum is quenched, $\mu_{eff}$ effectively becomes $\mu_{so}$. Although the ligand field does quench orbital angular momentum, in the presence of spin-orbit-coupling, this quenching effect for A and E terms cannot be completed. And although the spin-orbit-coupling is difficult to determine in non-T terms, it is still present and can be determined via multiple methods. These will be discussed in more detail in later sections.

A third equation to determine magnetic moment is $\mu_J$, given in Equation 4.3. $\mu_J$ incorporates spin-orbit-coupling, *J*, but can only be used for a system which consists only of ground states that are split by J-J coupling rather than the conventional Russel-Saunders L-S coupling scheme. As such, it is only useful for lanthanide complexes where SOC is so large that states away from the ground state are inaccessible. As this project deals primarily with 3*d* transition metals, $\mu_J$ is not very useful.

$$\mu_J = g\sqrt{J(J+1)} \quad \text{where} \quad g = \frac{3}{2} + \frac{(S(S+1)-L(L+1))}{2J(J+1)} \qquad \text{(Eq. 4.3)}$$

Although these three equations for determining magnetic moment are useful in theory, they are not detailed enough to accurately predict and model magnetic susceptibility in experimental data. A more thorough approach is necessary – namely the van Vleck equation. The van Vleck formula does not lean on any approximations and is considered the most fundamental expression that underpins molecular magnetism (Equation 4.4).

$$\chi = N\sum_n \left(\frac{E_n^{(1)2}}{kT} - 2E_n^{(2)}\right) e^{E_n^{(0)}/kT} / \sum_n e^{E_n^{(0)}/kT} \qquad \text{(Eq. 4.4)}$$

$$E_n^{(1)} = \langle n|\widehat{H_{ZE}}|n\rangle \qquad E_n^{(2)} = \frac{\langle n|\widehat{H_{ZE}}|m\rangle^2}{E_n^{(0)} - E_m^{(0)}}$$

$E_n^1$ and $E_n^2$ are expressions that can be determined through perturbation theory. The Hamiltonian in those two expressions is the Zeeman operator, which accounts for the interaction between the magnetic field and the electronic angular momenta. The Zeeman operator is given in Equation 4.5.

$$\widehat{H_{ZE}} = \beta\sum_i (I_i + g_e S_i)H \qquad \text{(Eq. 4.5)}$$

In this equation, $\beta$ is the Bohr magneton, $I_i$ is the orbital momentum of the electron i, $S_i$ is the spin momentum of the same electron, $g_e$ is the gyromagnetic factor for a free electron, and $H$ is the magnetic field. Using this operator, the eigenvalues must be determined for the van Vleck formula. This is a long process, and a more in-depth step-by-step procedure for this mathematical approach can be accessed in the tutorial *Theory and Application of PHI*.[112] In summary, a Hilbert space group is constructed, and basis states are formed using the $m_L$ and $m_S$ values for the working system. The matrix of the Hamiltonian can then be generated to span the Hilbert space of the system. Once the matrix is formed, it is then diagonalized and the eigenvalues are determined from the diagonalization. This can be performed manually for simple systems (e.g. $S = 1$, $L = 0$), but for more complicated systems, the matrix gets very complicated very quickly. Thankfully, several software programs exist that can perform these manipulations. The software used in this dissertation has already been referenced several times: PHI.[112] PHI uses the full Spin Hamiltonian to determine more accurate eigenvalues and thus more trustworthy fits of experimental data. Experimental data is fit with a least-squares procedure using the Spin Hamiltonian and, from that fit, the underlying parameters can be determined that accurately

characterize the experimental data. The full Spin Hamiltonian that PHI accesses to fit the system is given in Equation 4.6, along with labelled parameters.

$$\hat{H}\varphi = E\varphi$$

$$\widehat{H_{spin}} = \widehat{H_{ZE}} + \widehat{H_{CF}} + \widehat{H_{SO}} + \widehat{H_{EX}} \qquad \text{(Eq. 4.6)}$$

$$\widehat{H_{ZE}} = \beta \sum_{i=1}^{N} \left(\sigma_i \hat{L}_\iota I + g_i \hat{S}_\iota\right) \vec{B}$$

$$\widehat{H_{CF}} = \sum_{i}^{N} \sum_{k=2,4,6} \sum_{q=-k}^{k} B_{ki}^{q} \theta_k \hat{O}_q^k$$

$$\widehat{H_{SO}} = \sum_{i=1}^{N} \sum_{i=1}^{2S_i} \lambda_{ji} (\sigma_i \hat{L}_i \hat{S}_\iota)^j$$

$$\widehat{H_{ZE}} = Zeeman\ Hamiltonian$$

$$\widehat{H_{CF}} = Crystal\ Field\ Splitting\ Hamiltonian$$

$$\widehat{H_{SO}} = Spin\ Orbit\ Coupling\ Hamiltonian$$

$$\widehat{H_{EX}} = Exhange\ Hamiltonian$$

$$\sigma_i = orbital\ reduction\ factor$$

$$\hat{S}_\iota = Spin\ operator$$

$$\hat{L}_\iota = Orbit\ operator$$

$$B_{ki}^{q}\theta_k = Crystal\ Field\ Parameters$$

$$\hat{O}_q^k = Operators\ (containing\ orbital\ reduction\ parameter)$$

$$\lambda_{ji} = spin\ orbit\ coupling\ parameter$$

Details for the exchange Hamiltonian were not given as it is only important for molecules with multiple paramagnetic metal ions. From the full Spin Hamiltonian, it is clear that SOC in a system can alter the eigenvalues derived from the Hamiltonian, through either the spin-orbit-coupling parameter, or the inherent coupling of *L* and *S* that derives *J*.

PHI is also useful when solving for zero-field-splitting (ZFS) in a complex, because of an important connection between ZFS and the crystal-field-splitting (CFS) Hamiltonian. Essentially, the zero-field-splitting Hamiltonian (commonly used in EPR fittings) and the $\hat{O}_q^k$ operator in the CFS Hamiltonian commute with certain values of *k* and *q*. A full breakdown can be seen in Equation 4.7.

ZFS Hamiltonian (from EPR):

$$\hat{S} \cdot \overline{\overline{D}} \cdot \hat{S} = D\left(\widehat{S_z^2} - \frac{1}{3}S(S+1)\right) + E(\widehat{S_+^2} + \widehat{S_-^2})$$

$\hat{O}_k^q$ operator from CFS Hamiltonian for (*k* = 0, *q* = 2) and (*k* = 2, *q* = 2):

$$\hat{O}_2^0 = 3\widehat{S_z^2} - S(S+1)$$

$$\hat{O}_2^2 = \widehat{S_+^2} + \widehat{S_-^2}$$

Therefore:

$$B_2^0\theta_2 = \frac{D}{3} \qquad \text{(Eq. 4.7)}$$

$$B_2^2\theta_2 = E$$

Thus, by solving for $B_2^0\theta_2$ and $B_2^2\theta_2$ in the PHI fittings, we can quantitatively determine the *D* (axial) and *E* (transversal or rhombal) zero-field-splitting parameters for our complexes. From the discussion in Chapter 1, SOC and *D* are directly related, especially in the case of 3*d* transition metals where SOC is the largest factor of *D*. Although axial zero field splitting can have many other different contributors (e.g. magnetic anisotropy, distortions in complex geometry, orbital spacing and splitting), spin-orbit-coupling is the largest contributor. Examining the sign and magnitude of zero-field-splitting—determined through the mathematical fitting of susceptibility and magnetization data—is a quantifiable and agreed-upon solution to determine the extent of SOC in a complex,[124–126] especially if two analogous complexes can be compared to each other.

In this chapter, we report the syntheses of three new cobalt-antimony complexes and examine their electronic properties (susceptibility, field-dependent magnetization, and NIR electronic absorbance) to determine the enhancement of spin-orbit-coupling at the cobalt(II) center versus their phosphorus analogues. From a practical standpoint, magnetic materials have several promising applications in modern society, namely in data storage, quantum computing, and modeling of biological systems.[251–253] Magnetically enriched complexes could also play a role in increasing the catalytic activity of specific sub-sections of catalysts. In particular, and as mentioned in Chapter 1, a substantial increase to the extent of spin-orbit-coupling on a catalytically inert cobalt center could incite C-H activation activity via increased probability of the necessary spin-orbit induced spin-crossing along the reaction coordinate. The end of this chapter will also detail some preliminary reactivity studies performed with these complexes as possible C-H activation catalysts, but those results are brief.

As a refresher from Chapter 1, one pathway towards enhancing magnetic properties of molecular complexes is by increasing the spin-orbit-coupling of those complexes through ligand effects. Through a phenomenon called translational spin-orbit-coupling, the overall extent of SOC on the paramagnetic metal center has the potential to be heightened via covalent ligation of heavy donor atoms.[122] This effect has been experimentally determined previously, first shown by Cotton.[123] More recently, seminal work by Long and Dunbar revealed that the stepwise increase in the atomic number ($Z$) of the donor atom in coordination complexes led to an increase in the magnitude of the axial zero-field-splitting parameter ($D$) of the complex.[124,125,129] Zero-field-splitting is comprised of a combination of effects, including ligand field, molecular symmetry, magnetic anisotropy, and spin-orbit-coupling.[106,124,127] In previous reports, however, SOC has been connected to the

extent of axial zero-field-splitting in a complex, and the amount of SOC in a complex can be estimated by investigating the magnitude of *D*, and quantitatively determined in combination with other spectroscopies.[124–126,129,254]

In the effort to synthesize organometallic complexes with heavy main group donor atoms, previous compounds have been reported with elements as heavy as As, Se, and other main group elements, but not heavier than n = 4 elements due to the associated synthetic difficulties of ligating soft elements like Sb to 3*d* metals—with the 5*s* "inert pair" effect serving as the primary roadblock.[124,125,128] Paramagnetic complexes derived from 3*d* metals and heavy main group donor ligands are rare, and the translational spin-orbit-coupling effect of antimony ligands has not been investigated. Antimony has a spin-orbit-coupling constant nearly four times larger than arsenic—on par with late 5*d* transition metals.[22,130] Thus, investigating any enhanced magnetic properties that antimony ligands impart on paramagnetic 3*d* metal centers could have important effects on the fields of single-molecular magnetism or organometallic catalysis.

## 4.2 Experimental

### 4.2.1 Reagents and General Procedure

All reactions were conducted under a dry dinitrogen atmosphere with a Schlenk line (ligand syntheses and phosphine metal complex syntheses) or under a dry argon atmosphere in a drybox (antimony metal complex syntheses). Dry solvents were HPLC-grade and purified over alumina using a Pure Process Technology solvent purification system. The starting materials trichloroantimony and triphenylantimony were purchased from Strem Chemicals and used without further purification. Cobalt iodide (Strem

Chemicals), fluorobenzene (Oakwood Chemical), triphenylphosphine (Acros Organics) were purchased and used as received without purification.

### 4.2.2 Ligand Synthesis

All antimony ligands have been previously synthesized and detailed ligand syntheses can be found in Chapters 2 and 3.

### 4.2.3 Metal Complex Synthesis

#### *4.2.3.1 $Co(I)_2(Sb^iPr_2Ph)_2$ (1)*

Diisopropylphenylantimony (0.73 g, 2.5 mmol) was added to a solution of cobalt(II) iodide (0.39 g, 1.27 mmol) in 15 mL of fluorobenzene (FPh) at –20 °C. The reaction was allowed to warm to room temperature and stirred for 12 hours. The deep red solution was filtered through Celite and the solvent was removed *in vacuo* to yield a deep red oil. The red oil was dissolved in 5 mL pentane and filtered through Celite and the final concentrated pentane solution was placed in a freezer at –20 °C. The final product crystallized out of the concentrated pentane solution to yield dark red crystals suitable for X-ray crystallography (0.21 g). Yield: 19 %.

#### *4.2.3.2 $Co_2(I)_4(Sb^iPr_3)_2$ (2)*

Triisopropylantimony (0.25 g, 1.0 mmol) was added to a solution of cobalt(II) iodide (0.16 g, 0.5 mmol) in 15 mL of toluene at –20 °C. The reaction was allowed to warm to room temperature and stirred for 12 hours. The dark red solution was filtered through Celite and the solvent was removed *in vacuo* to yield a dark red oil. The oil was dissolved in 5 mL pentane and filtered through Celite and the final concentrated pentane solution was

placed in a freezer at –20 °C. The final product crystallized out of the concentrated pentane solution to yield dark red crystals suitable for X-ray crystallography (0.26 g). Yield: 46 %.

#### *4.2.3.3 $Co(I)_2(SbMe_2Ph)_4$ (5)*

Dimethylphenylantimony (1.1 g, 4.7 mmol) was added to a solution of cobalt(II) iodide (0.37 g, 1.2 mmol) in 15 mL of fluorobenzene at –20 °C. The solution was allowed to warm to room temperature and stirred for 12 hours. The dark purple solution was filtered through Celite, and the solvent was removed *in vacuo* to yield a dark purple oil. The oil was re-dissolved in 10 mL of pentane and placed in a freezer at –20 °C. The final product crystallized out of the concentrated pentane solution to yield black crystals suitable for x-ray crystallography (0.15 g). Yield: 10 %.

#### *4.2.3.4 $Co(I)_2(PPh_3)_2$ (3)*

Triphenylphosphine (0.16 g, 0.6 mmol) was added to a solution of cobalt(II) iodide (1.0 g, 3.1 mmol) in 25 mL of toluene. The solution was refluxed under inert and dry conditions for two hours. The solution was filtered hot and the solvent was removed i*n vacuo* to yield a dark brown solid. The solid was washed with pentane to remove unreacted triphenylphosphine and yield the final product as a brown solid (0.25 g). Yield: 45 %. Crystals suitable for x-ray crystallography were collected via a DCM/pentane vapor diffusion.

#### *4.2.3.5 $Co_2(I)_4(PPh_3)_2$ (4)*

This product was synthesized following the previously reported procedure.[255] Triphenylphosphine (0.17 g, 0.65 mmol) was added to a stirring solution of cobalt(II) iodide (1.1 g, 3.4 mmol) in 25 mL of benzene. The solution was refluxed under inert and

dry conditions for two hours. The solution was filtered hot and then allowed to cool to room temperature and then the solvent was removed *in vacuo* to yield an orange solid. The solid was washed with pentane to remove unreacted triphenylphosphine. The final product was crystallized via a benzene/pentane vapor diffusion at room temperature, and those crystals were suitable for x-ray crystallography (0.09 g). Yield: 13 %.

### 4.2.4 Magnetic Measurements – SQUID and Benchtop Magnetic Susceptibility

Magnetic susceptibility measurements were taken using a SQUID magnetometer for complexes **1**, **2**, **3**, and **5**. Susceptibility measurements were never taken for complex **4** due to a lack of enough material and a lack of interest in gathering in-depth magnetic data for **4**. At the University of Texas, the SQUID is owned and operated by the lab group of Jianshi Zhou (jszhou@mail.utexas.edu). Communication with that group is critical to gain access to the SQUID. The queue is often long so it is recommended to get time on the instrument ASAP. SQUID samples are 50-80 mg of crystalline compound – do not crush up the crystals (Dr. Zhou's advice). It is possible to perform the experiment with less than 50 mg, but it is not recommended. Samples are packed in a small plastic pill capsule, then protected with cotton to fill in the capsule. The capsule is lodged inside a plastic straw in order to fit inside the SQUID instrument. Performing this procedure inside the glovebox with precious compound is *very difficult* and it is recommended to clear out other lab members from the box and to be extremely careful and deliberate. Once at the SQUID instrument, utilize a graduate student from the Zhou group to assist for the first run or two, however, the instrument is quite facile to use.

For benchtop magnetic susceptibility, the instrument used in the Rose lab is not correctly calibrated to "zero", but the use of a chemical standard before each run allows for

reasonably-accurate determination of the room temperature magnetic moment. It should be stated that SQUID magnetometry is a much more precise determinant of magnetic moment, but the benchtop susceptibility is recommended for initial measurements. A substantial amount of material is needed for this measurement – roughly 80-100 mg. However, the sample tube can be adjusted (raised up or down in the sample insert) to obtain an accurate measurement without possessing the requisite 80 mg for analysis.

### 4.2.5 PHI fitting

Magnetic susceptibility and magnetization SQUID raw data measurements were fit using the program PHI, which has been noted several times previously in this dissertation. PHI is free to download from the creator's website (http://www.nfchilton.com/phi.html). It is a user-friendly software that has a GUI interface. It also has an excellent tutorial on molecular magnetism that includes everything from the full Spin Hamiltonian, how to solve the Hamiltonian for the eigenvalues, and tips for using the program. Additionally, PHI has an excellent and detailed manual that gives instructions on how to construct experimental files and scripts to analyze experimental data. Although the manual gives good instruction on constructing scripts, I will further describe it in this experimental section to hopefully save the reader some time and frustration learning the program.

An example of a PHI input script is shown in Figure 4.1. I will go through each important line of the script in order to give a personal insight.

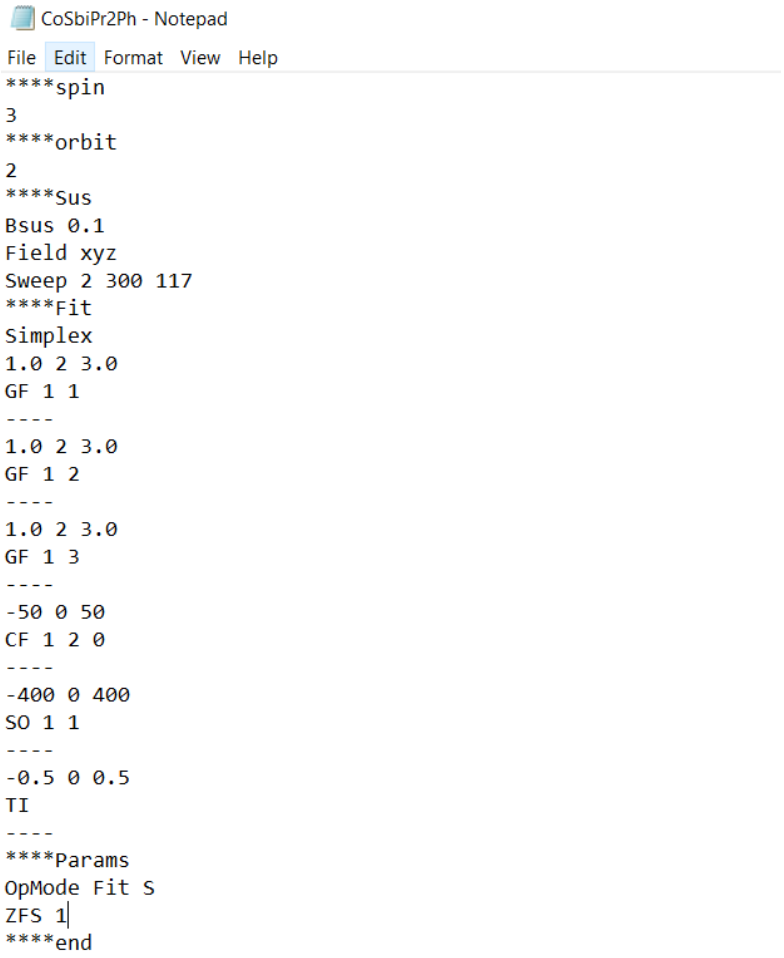


**Figure 4.1** PHI input script.

In a PHI script, the identity of the complex must be described, as well as the experiment performed, and finally the parameters one wishes to modify and ascertain with the fit. In Figure 4.1, the script tells PHI that the spin of the system is equal to 3/2 and the orbital angular momentum is equal to 1 (the molecular quantum numbers are always ½ of what is listed in the script). The "Sus" section tells PHI that the experimental data is from a susceptibility measurement. The field strength of 0.1 T is listed as "BSus 0.1", "Field xyz" means the field was not aligned in one particular direction and "Sweep 2 300 117"

means the temperature range was swept from 2-300 K and there were 117 data points in the experimental file. The "Fit" section tells PHI we would like to fit the data, as opposed to running simulations or surveys on the data—other available operations. In the "Fit" block, the syntax is such that the first line details the allowable numerical range the program can operate in while searching for a best fit on the desired parameter. For example, the two lines reading 1.0 2 3.0 // GF 1 1 means we would like to vary the *g*-factor in the x direction from 1.0 to 3.0 and search for a value for $g_x$ that gives a best fit for the data (lowest residual value). For another example, the line -50 0 50 // CF 1 2 0 means we would like to search for a value of $B_2^0\theta_2$ in the range of -50 – 50 $cm^{-1}$ that gives a best fit for the data. As a reminder, that value is equal to *D*/3, and is in the PHI script to ascertain a value for the axial ZFS parameter for this data. The "Params" block is necessary to communicate what the user wants PHI to do. In this case, the operation mode selected is "Fit S", which asks it to fit the susceptibility. The ZFS 1 command will multiply the final $B_2^0\theta_2$ value by 3 in order to get an accurate value for *D*. Finally, an "end" command is given at the end of the script to complete the input file. In Figure 4.1, the anisotropic *g*-factors ($g_x \neq g_y \neq g_z$), the *D* parameter, the spin-orbit-coupling parameter (SO), and the temperature independent paramagnetism parameter (TI) were all parameters that were determined from the best fit of this data. If the final fitting determines a parameter to be at the extreme of the given range (e.g. if the fitting determines a value of -50 $cm^{-1}$ for *D* in this script), the fitting is a bad fit and the range must be expanded. In conclusion, PHI is an excellent, user-friendly program that affords accurate fits and good estimates of any parameter the user is interested in determining.

### 4.2.6 NIR Electronic Absorbance Measurements

Electronic absorbance measurements were performed to better characterize our complexes and to gain a more quantitative measure of spin-orbit-coupling in our systems. For tetrahedral systems, the *d*-orbital splitting energies are quite small, meaning scans must be expanded to low energies in order to observe the transitions. Scans were performed in deuterated benzene out to 3000 $cm^{-1}$ or in non-deuterated dichloromethane out to 4000 $cm^{-1}$. Complexes **3** and **5** did not dissolve in benzene, so we selected to use non-deuterated dichloromethane to perform the measurements. However, because detectable transitions only occurred out to 5000 $cm^{-1}$, the absorptions and stretches from C-H bonds were a non-issue. Electronic absorbance measurements were conducted with an air-free quartz cuvette that was affixed with a sealable CHEM-CAP metering plug and control knob to avoid oxidation. In order to see the weakly absorbing $\nu_2$ transition for complexes **1**-**4**, concentrated samples were used (1 mM).

### 4.2.7 Physical Measurements

Magnetic susceptibility measurements were conducted using a SQUID magnetometer (Quantum Design) from 2-300 K at 0.1 T. Room temperature benchtop magnetic moment measurements were conducted using an MSB-1 Magnetic Susceptibility Balance from Sherwood Scientific. The balance was calibrated using Mohr's salt, $Fe(NH_4)_2(SO_4)_2 \cdot 6\ H_2O$. Electronic absorbance spectra were collected using a Cary 5000 UV-Vis NIR Spectrometer.

### 4.2.8 X-ray data collection

For complex **2**, the X-ray diffraction data were collected on a Rigaku AFC12 diffractometer with a Saturn 724+ CCD using a Bruker AXS Apex II detector and a

graphite monochromator with MoKα radiation (λ = 0.71073 Å). Low temperatures were maintained using an Oxford Cryostream low temperature device. Data reduction was performed using the Rigaku Crystal Clear version 1.40.[159] Structures were solved by direct methods using SHELXT[160] and refined by full-matrix least-squares on $F^2$ with anisotropic displacement parameters for the non-H atoms using SHELXL-2014/7.[161] Structure analysis was aided by use of the programs PLATON[162] and WinGX.[163] For complexes **1**, **3, 4** and **5**, the X-ray diffraction data were collected at –173 °C on a Nonius Kappa CCD diffractometer using a Bruker AXS Apex II detector and a graphite monochromator with MoKα radiation (λ = 0.71073Å). Reduced temperatures were maintained by use of an Oxford Cryosystems 700 low-temperature device. Data reduction was performed using SAINT V8.27B.[164] The structure was solved by direct methods using SHELXT[160] and refined by full-matrix least-squares on $F^2$ with anisotropic displacement parameters for the non-H atoms using SHELXL-2014/7.[161] Structure analysis was aided by use of the programs PLATON[162] and WinGX.[163]

## 4.3 Results and Discussion

### 4.3.1 Structures and Synthesis

Synthetically, very few Co(III)-Sb complexes—*and no Co(II)-Sb complexes*—have been previously reported, likely due to the previously discussed difficulties associated with ligating commercially available and weakly *σ*-donating $SbPh_3$ to electron deficient metal centers.[65,67] By increasing the electron donating strength of the antimony donor atom via alkyl substituents, we have previously reported successful metalation of monodentate antimony ligands to $M^{2+/1+}$ late 3*d* metal centers.[248] We have already discussed these topics in detail in Chapters 1 and 2.

Complexes **1** and **2** were synthesized in an analogous manner via addition of two equivalents of ligand to one equivalent of cobalt(II) iodide (**1**: $Sb^{i}Pr_2Ph$; **2**: $Sb^{i}Pr_3$) in fluorobenzene. Complex **2** was also successfully synthesized using toluene as the solvent. These reactions are fairly straightforward; one trick is to filter the pentane-dissolved product to give a homogenous concentrated solution. This concentrated solution will afford crystals after a few nights in a -20 °C freezer; the technique worked for all Co-Sb complexes (**1**, **2**, and **5**).

Crystal structures of **1** and **2** are shown in Figure 4.2. Evidently, the steric bulk of the ligand dictates the number of ligands per cobalt center, as well as the formation of dimeric or monomeric species. The smaller $Sb^{i}Pr_2Ph$ ligand ($\%V_{bur}$ = 26.0) results in two coordinated ligands to the Co center, affording the monomer $Co(I)_2(Sb^{i}Pr_2Ph)_2$ (**1**), where the $Sb^{i}Pr_2Ph$ ligands bind in the obligate *cis* fashion in the tetrahedron. However, the bulkier $Sb^{i}Pr_3$ ligand ($\%V_{bur}$ = 27.0) results in only one supported ligand per cobalt. To accommodate this, two cobalt centers dimerize through bridging iodides, affording $Co_2(I)_4(Sb^{i}Pr_3)_2$ (**2**). This motif was similarly seen in Chapter 3, when the sterically bulky ligands only coordinated one ligand per copper center. To compensate, multiple metal centers connected through bridging iodides. In another similar manner, the nickel complexes from Chapter 2 also afforded different geometries and coordinated number depending on the steric bulk of the ligand. As such, it is clear that the size of the antimony ligand dictates the coordination number and overall geometry of 3*d* metal-antimony complexes.

Both cobalt complexes exhibit a distortion away from perfect tetrahedral geometry. In **1**, the I1-Co-I2 angle is 122.6°, while the Sb1-Co-Sb2 angle is 111.6°. For **2**, the average I1-Co-I2 angle is 116.7° (± 0.1), and the average I3-Co-Sb angle is 107.6° (± 1.5). The Co-

Sb bond distances in the two structures range from 2.59 – 2.66 Å, which are elongated from typical Co-Sb bonds (~2.55 Å).[67,256] A small elongation is presumed for both tetrahedral complexes due to the doubly occupied $e_g$* orbitals in each. Both of these structures are highly distorted tetrahedral complexes, especially when compared to phosphine and arsine analogous (**P**: I1-Co-I2 = 111.4°; P1-Co-P2 = 108.3° // **As**: I1-Co-I2 = 116.8°; As1-Co-As2 = 105.1°). Distortions away from ideal tetrahedral geometry (especially tetragonal distortions) are a sign of magnetic anisotropy in the complex and can contribute to axial zero-field-splitting. In a comparison of the two tetrahedral complexes **1** and **2**, it is clear complex **1** exhibits more tetragonal distortion away from ideal tetrahedral geometry than complex **2**. This could be due to the number of antimony ligands coordinated in **1** vs **2**; multiple antimony donors contribute to greater distortion. Additionally, the bridging iodides in **2** could stabilize the metal center and limit distortions away from ideal tetrahedral geometry. Regardless, tetrahedral cobalt-antimony crystal structures are quite rare, as among previously reported crystal structures of Co-Sb complexes, there exists only one other such complex in tetrahedral geometry ($Co(CO)_2(NO)(SbPh_3)$), which has a low valent $Co^0$ center.[257]

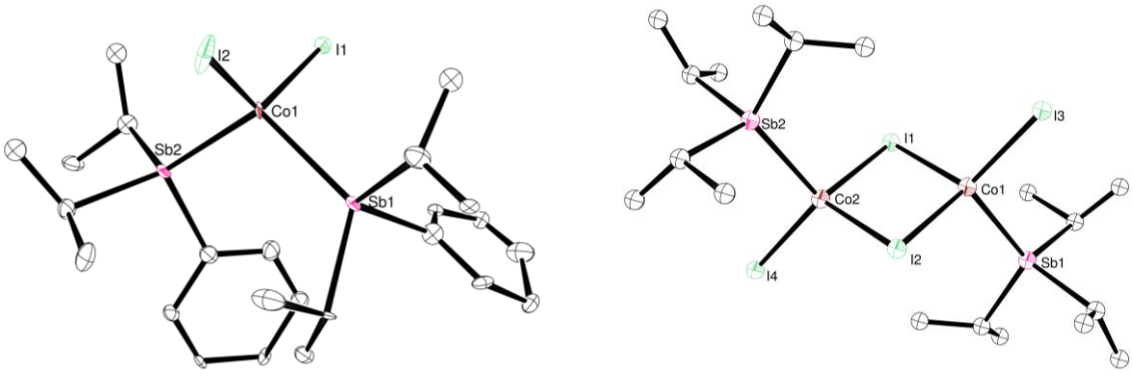


**Figure 4.2** ORTEP diagrams (30 % ellipsoids) of the crystal structures of $Co(I)_2(Sb^iPr_2Ph)_2$ (**1**, left) and $Co_2(I)_4(Sb^iPr_3)_2$ (**2**, right).

Both monomer and dimer analogous compounds with triphenylphosphine are previously reported.[125,255] For an unambiguous comparison of the translational spin-orbit-coupling effects between antimony and its lighter phosphorus congeners, we synthesized and crystallized the two analogous $PPh_3$ compounds. The reproduced crystal structures of complexes **3** and **4** are shown in Figure 4.3. As both of these complexes have already been reported, there is not much information to be gained by thoroughly examining the structural and synthetic aspects of these compounds. It is important to note, however, that complex **3** was synthesized in the same manner as complex **4**, but with toluene instead of benzene. Although this was slightly different than the reported method, this synthetic route was viable, affording pure crystalline product following a DCM/pentane vapor diffusion.[125] Complex **4** co-crystallizes with one molecule of benzene, and it is important to perform the re-crystallization in benzene (with pentane vapor diffusion) to ensure the correct crystallized structure of the dimer. These compounds were merely synthesized so we could have a direct comparison of the magnetic and catalytic properties versus our antimony complexes.

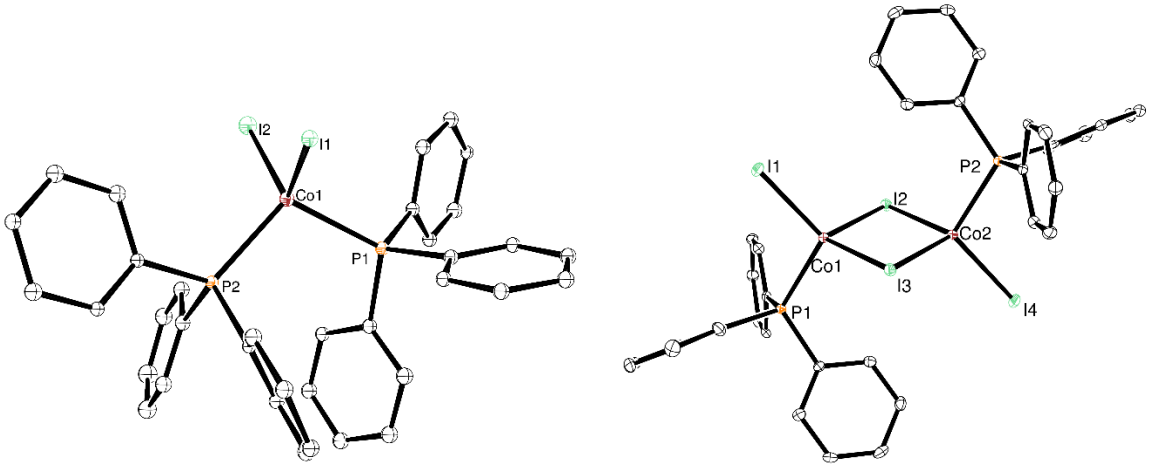

**Figure 4.3:** ORTEP crystal structures of $Co(I)_2(PPh_3)_2$ (**3**, left) and $Co_2(I)_4(PPh_3)_2$ (**4**, right) at 50% ellipsoids. The co-crystallized benzene molecule in **4** is not shown for simplicity.

The last complex in the antimony-cobalt(II) set was synthesized in the same manner as the other antimony complexes above, but with four equivalents of $SbMe_2Ph$ to one equivalent of $CoI_2$ in fluorobenzene to give $Co(I)_2(SbMe_2Ph)_4$ (**5**). The crystal structure of **5** can be seen in Figure 4.4. Notably, the smallest $SbMe_2Ph$ ligand ($\%V_{bur}$ = 23.3) can coordinate up to four antimony ligands around the Co(II) center, along with two bound iodides, affording an octahedral geometry. Similar to how the size difference between $Sb^iPr_2Ph$ and $Sb^iPr_3$ caused the formation of a monomeric or dimeric tetrahedral complex, the use of a significantly smaller antimony ligand once again changed the coordination number and geometry in the final cobalt complex. Complex **5** exhibits a tetragonal distortion away from ideal octahedral geometry with axial distortions in the I-Co-Sb bond angles. The range of I-Co-Sb bond angles range from 83.5 ° at the most acute to 100.9 ° at the most obtuse angle. Following on the previous analysis of Co-Sb compounds, this could be further evidence that heavy donor atoms increase axial distortions in these types of complexes. This motif of four monodentate pnictogen ligands bound in octahedral fashion to a cobalt-halogen center is actually quite rare among previously reported complexes. The only available structures in the CCDC with general formula $CoX_2(P)_4$ (P = phosphine donor) utilize bidentate phosphine ligands to access this motif.[258,259] As such, obtaining the light atom structural or magnetic congeners of **5** was difficult to obtain for this work. Among published structures in the CCDC, this is the only known Co(II)-Sb octahedral crystal structure.

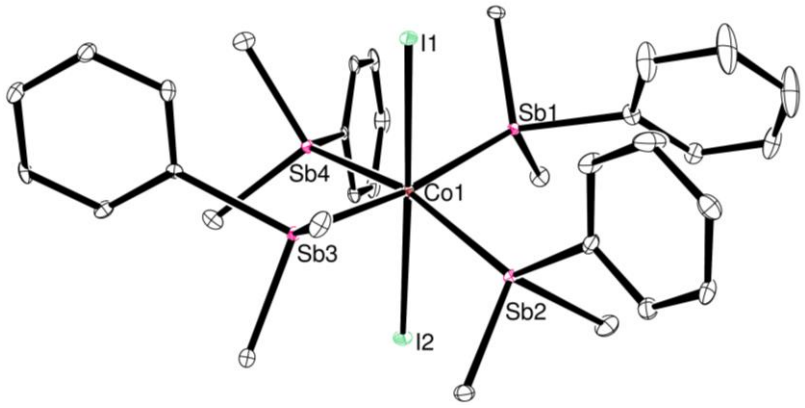


**Figure 4.4:** ORTEP diagram (30 % ellipsoids) of complex **5**, $Co(I)_2(SbMe_2Ph)_4$.

### 4.3.2 Magnetic Susceptibility and Data Fittings

#### *4.3.2.1 Tetrahedral Monomers: $Co(I)_2(Sb^iPr_2Ph)_2$ (1) vs. $Co(I)_2(PPh_3)_2$ (3)*

Variable temperature magnetic susceptibility measurements were obtained for the monomeric, tetrahedral complexes **1** (Sb) and **3** (P) using packed polycrystalline samples. DC Susceptibility measurements were performed at 0.1 T over a temperature range of 2 – 300 K and the data was corrected for diamagnetic contributions.[260] Figure 4.5 shows the susceptibility data (in $\chi$T vs. T) along with the associated fitting curves determined via *PHI*.[112]

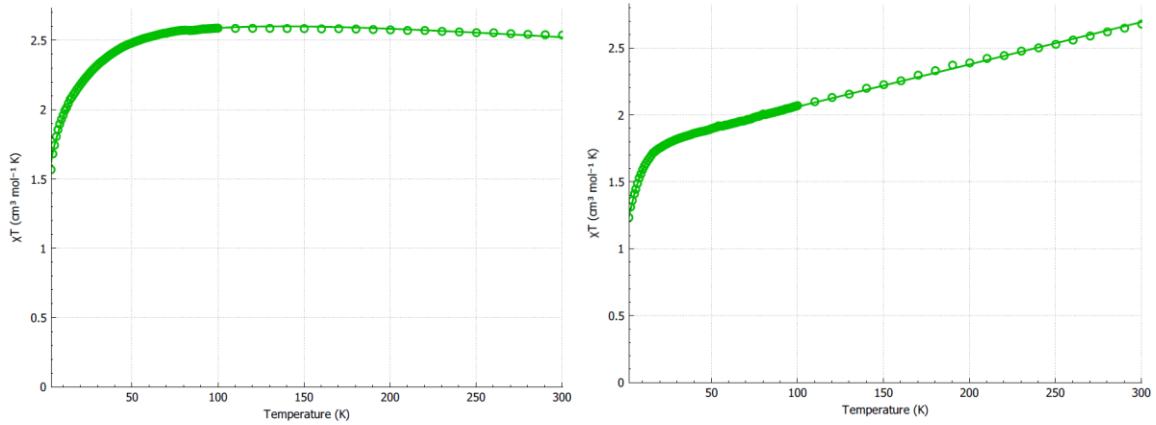

**Figure 4.5**: Variable temperature magnetic susceptibility data for **1** (left) and **3** (right). Best fits of data (solid green lines) acquired through *PHI*.

The room temperature $\chi$T values for both **1** and **3** (2.53 and 2.67 $cm^3$ $mol^{-1}$ K, respectively) are both higher than the spin-only $\chi$T value of 1.875 $cm^3$ $mol^{-1}$ K that is expected for a single molecular spin center with $S = 3/2$ and $g = 2.00$. It should be noted that the previous determination of $\chi$T for $Co(I)_2(PPh_3)_2$ by Dunbar revealed a value of 2.66 $cm^{-1}$. The rapid decrease of $\chi$T at low temperatures (~80 K for **1**, ~30 K for **3**) along with the slow decrease in susceptibility at higher temperatures are evident in both of these complexes. In other Co(II) complexes, both of these phenomena have been connected to significant magnetic anisotropy in the molecule, which was attributed to a greater extent of spin-orbit-coupling at the metal center.[125]

In order to more quantitatively determine the differences in overall spin-orbit-coupling in complexes **1** and **3**, the susceptibility data were fitted and parameterized using the program PHI. In the fitting script, fits were charged to vary the crystal-field-splitting Hamiltonian parameters $B_2^0\theta_2$ and $B_2^2\theta_2$ (which correspond to $D/3$ and $E$, respectively, as detailed in the Introduction of this chapter), as well as the anisotropic $g$ factors ($g_z \neq g_x = g_y$). The $g$-factors were fit in this way, as we suspect a high degree of axial anisotropy in the complex ($g_z$ unique), but due to the symmetry in the complex, we do not expect a large difference between $g_x$ and $g_y$. After attempting to fit the data, PHI will generate a residual value, and best fits were chosen that minimized residual values but also gave logical results for unknown parameters (e.g. $|E/D| < 0.33$). The PHI scripts that were used for complexes **1** and **3** are shown in Figure 4.6.

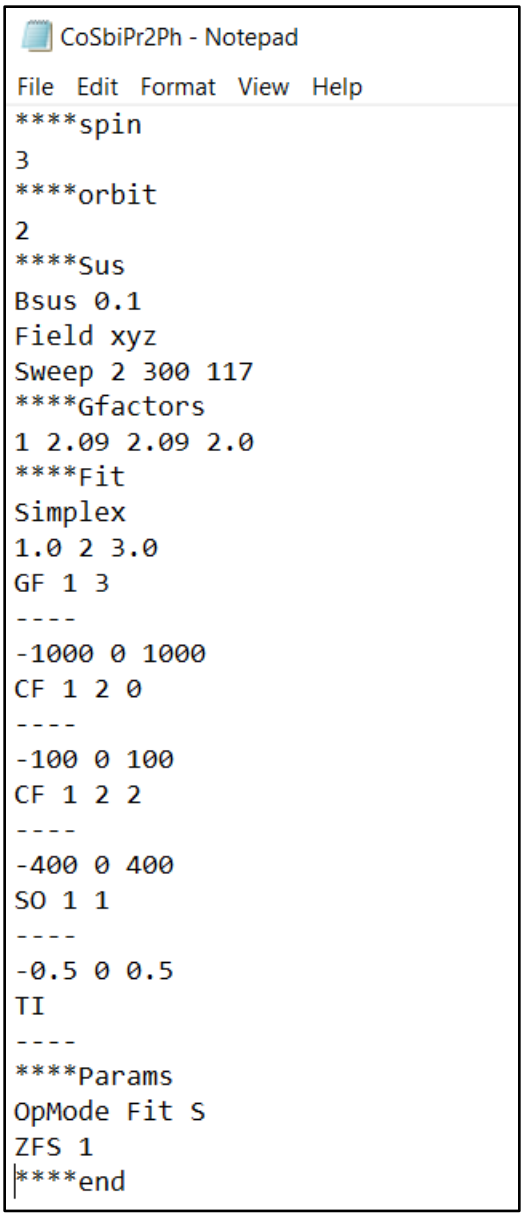


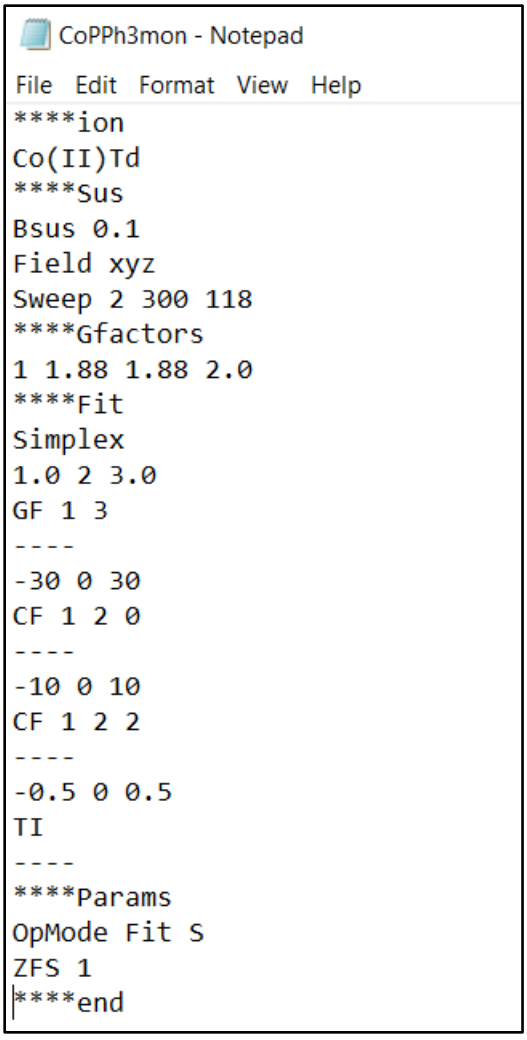


**Figure 4.6** PHI scripts for complex **1** (left) and **3** (right).

These scripts and parameters were chosen in order to minimize the residual value of the fit, while achieving logical values for the *g*-factors, *D*, and *E* parameters. Interestingly, we decided to fit the susceptibility data of **1** by assigning it as a T term

consistent with symmetry lower than $T_d$ rather than as an A term (conventional for Co(II) in $T_d$ and as **3** is assigned). This was due to the substantial improvement in the residual value when the data was treated as a T term versus as an A term. A summary of the parameters and residual values for several fits of complex **1** is shown in Table 4.1 Comparing the results, the residual values from the $^4$T fit were much smaller, giving credence to the accuracy of the $^4$T assignment. Additionally, the $|E/D|$ for tetragonally distorted tetrahedral Co(II) complexes is typically under 0.33. Any result above that cutoff was considered to be a bad fit. Nearly all the $|E/D|$ ratios for the fittings with a $^4$A assignment were ~1. On the other hand, the $|E/D|$ ratios for the $^4$T fits were all very small (~0) and aligned closer to previously reported literature ratios.[125] Finally, the *D* values for the $^4$T fittings were more reasonable than the $^4$A *D* values, both in magnitude and sign. From similar previously reported complexes and *D* values, we expected the *D* value to lie somewhere in the range of -50 to -100 $cm^{-1}$, which was seen for several of the fits using the $^4$T assignment. However, those values were never observed for the $^4$A fit—they did not even come close to reaching the expected magnitudes. From all three reasons, we were confident in assigning complex **1** as a $^4$T term rather than a $^4$A term.

To further rationalize this result and decision, we started by investigating the substantial tetragonal distortion observed in **1**. As the iodide and antimony ligands shift away from the z-axis, the $d_{x^2-y^2}$ and $d_{xy}$ orbitals are destabilized. This destabilization could lead to a triplet degeneracy of the $d_{x^2-y^2}$, $d_{xz}$, and $d_{yz}$ orbitals, affording a T term. Additionally, the weak ligand field afforded by the antimony and iodide ligands could increase the probability of triplet degeneracy through tetragonal distortion. A pictorial description of this destabilization and the possible $^4$A or $^4$T terms can be seen in Figure 4.7.

To note, these orbital splittings are merely hypothetical without thorough theoretical analysis to corroborate.

**Table 4.1** Parameters and Residuals from the PHI fitting of $Co(I)_2(Sb^iPr_2Ph)_2$ as a $^4A$ term and as a $^4T$ term.

| $^4A_2$ | | | | | $^4T_2$ | | | | |
|---|---|---|---|---|---|---|---|---|---|
| $g_x/g_y$ | $g_z$ | $D$ | $E$ | R | $g_x/g_y$ | $g_z$ | $D$ | $E$ | R |
| 1.9 | 2.99 | 1.86 | -5.5 | 0.470 | 1.88 | 3.01 | -1.9 | 15 | 0.016 |
| 1.91 | 2.96 | -14.7 | -15.3 | 0.072 | 1.89 | 3.04 | 4.1 | -22.7 | 0.007 |
| 1.92 | 2.94 | -14.6 | 15.2 | 0.072 | 1.90 | 3.03 | 4.2 | -22.7 | 0.006 |
| 1.93 | 2.94 | -14.6 | -15.1 | 0.072 | 1.92 | 2.99 | 35.3 | 0.0009 | 0.015 |
| 1.94 | 3.00 | 6.45 | -0.002 | 0.294 | 1.93 | 2.94 | -33.9 | -0.0001 | 0.032 |
| 1.95 | 2.91 | -14.5 | -15.0 | 0.071 | 1.94 | 2.97 | 35 | -.19 | 0.013 |
| 1.96 | 2.91 | -14.5 | -14.9 | 0.070 | 1.95 | 2.95 | 34.9 | -0.002 | 0.012 |
| 1.97 | 2.90 | -14.4 | 14.9 | 0.070 | 1.96 | 2.91 | -37.5 | 0.001 | 0.027 |
| 1.98 | 2.89 | -14.4 | 14.8 | 0.069 | 1.97 | 2.88 | -18.2 | 6.23 | 0.041 |
| 1.99 | 2.88 | -14.3 | 14.7 | 0.069 | 1.98 | 2.89 | -40 | 0.001 | 0.023 |
| 2.00 | 2.99 | 8.30 | 0.0001 | 0.212 | 1.99 | 2.93 | 5.3 | 24.4 | 0.004 |
| 2.01 | 2.99 | 8.52 | -0.0003 | 0.206 | 2.00 | 2.87 | -43.05 | -0.002 | 0.021 |
| 2.02 | 2.97 | 8.73 | 0.00009 | 0.199 | 2.01 | 2.86 | -44.73 | -0.0001 | 0.019 |
| 2.03 | 2.83 | -14.2 | -14.5 | 0.068 | 2.02 | 2.85 | -46.53 | 0.0016 | 0.018 |
| 2.04 | 2.82 | -14.2 | 14.4 | 0.067 | 2.03 | 2.87 | 5.59 | 24.6 | 0.003 |
| 2.05 | 2.81 | -14.1 | 14.4 | 0.067 | 2.04 | 2.84 | 33.5 | 0.014 | 0.006 |
| 2.06 | 2.80 | -14.1 | -14.3 | 0.067 | 2.05 | 2.85 | 5.74 | 24.7 | 0.003 |
| 2.07 | 2.79 | -14.0 | -14.2 | 0.066 | 2.06 | 2.82 | -55.5 | 0.0004 | 0.014 |

| | | | | | | | | | |
|---|---|---|---|---|---|---|---|---|---|
| 2.08 | 2.78 | -14.0 | 14.1 | 0.066 | 2.07 | 2.81 | -58.3 | -0.004 | 0.013 |
| 2.09 | 2.76 | -14.0 | -14.0 | 0.065 | 2.08 | 2.81 | -61.48 | 0.001 | 0.012 |
| 2.10 | 2.75 | -13.9 | 13.9 | 0.064 | 2.09 | 2.80 | -64.5 | -0.47 | 0.011 |
| 2.11 | 2.73 | -13.9 | 13.9 | 0.064 | 2.10 | 2.78 | -61.8 | 1.89 | 0.011 |
| 2.12 | 2.73 | -13.9 | 13.8 | 0.064 | 2.11 | 2.76 | 6.3 | 25 | 0.004 |
| 2.13 | 2.84 | 11.5 | -0.0005 | 0.135 | 2.12 | 2.74 | 6.47 | 25.1 | 0.003 |
| 2.14 | 2.83 | 11.9 | 0.0002 | 0.130 | 2.14 | 2.71 | 6.22 | -25 | 0.004 |

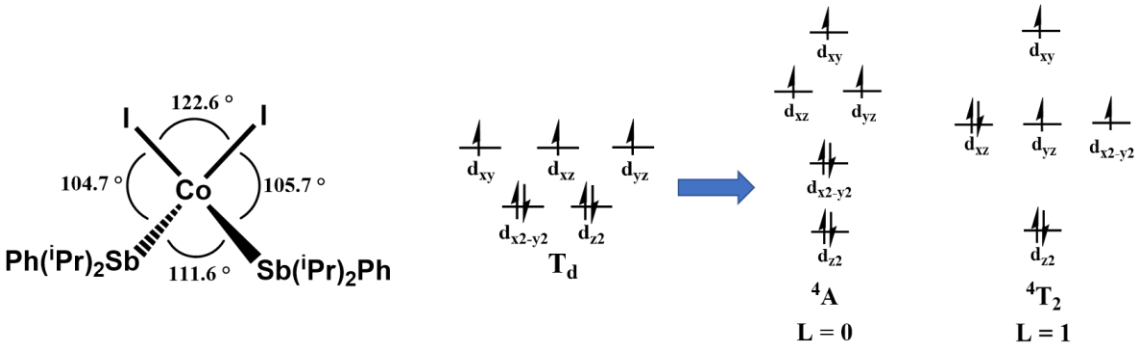


**Figure 4.7:** Possible d-orbital splitting diagrams of complex **1**.

From the best fit of **1**, we determined $g_x = g_y = 2.09$ and $g_z = 2.80$. The *D* value was a remarkable -64.5 $cm^{-1}$ and the *E* value was -0.47 $cm^{-1}$. For **3**, the best fit revealed $g_x = g_y = 1.88$ and $g_z = 2.01$. Complex **3** had a *D* value of only -9.44 $cm^{-1}$ and an *E* value of 0.002 $cm^{-1}$. All relevant parameters from the susceptibility fittings of **1** and **3** are listed in Table 4.2.

**Table 4.2** Summary of anisotropic g-factors, axial (*D*) and transversal (*E*) zero-field-splitting parameters determined through DC magnetic susceptibility fits for complexes **1** and **3**.

| Complex | $g_x/g_y$ | $g_z$ | D ($cm^{-1}$) | E ($cm^{-1}$) |
|---|---|---|---|---|
| **$Co(I)_2(Sb^iPr_2Ph)_2$ (1)** | 2.09 | 2.80 | -64.5 | -0.47 |
| **$Co(I)_2(PPh_3)_2$ (3)** | 1.88 | 2.01 | -9.44 | 0.002 |

The increase in the $g_z$ factor in **1** compared to **3** is possibly (but not necessarily) attributable to increased SOC in the Co-Sb complex versus the Co-P complex.[261] However, accurate values for *g*-factors are classically difficult to determine exclusively through magnetic susceptibility. Historically, *g*-factors are determined through EPR, but $Co^{2+}$ complexes are EPR silent until very low temperatures, which we were unable to access with our current EPR instrumentation. A more accurate indicator of increased SOC in **1** versus **3** is the axial zero-field-splitting, the *D* value. This relationship between *D* and SOC has been expounded upon in Chapter 1 and the Introduction section of this chapter. However, it must be restated that a large *D* value can suggest a large extent of SOC in a complex, especially if it is compared to a complex with similar geometry and composition. The -64.5 $cm^{-1}$ value of *D* for **1** is nearly seven times greater in magnitude than the -9.44 $cm^{-1}$ value for **3**. Although the sign of *D* is negative, as per other tetragonally distorted Co(II) tetrahedral complexes, the sign of *D* is difficult to accurately determine without variable-field magnetization measurements.[262] From previous reports, for tetragonally distorted tetrahedral complexes, the sign of *D* should be negative. [It is noted that Dunbar previously reported on the axial ZFS in $Co(I)_2(PPh_3)_2$ and determined it to be -36.9 $cm^{-1}$.[125] The significant difference in ascertained values could be rationalized by the fact that different fitting software were used (PHI vs. ANISOFIT), or that variable-field magnetization measurements were used in conjunction with susceptibility in the previous

report.] Regardless, the *relative* increase in the magnitude of *D* from our measurement (between 2- and 7-fold, depending on reference point) and fitting of $Co(I)_2(PPh_3)_2$ to $Co(I)_2(Sb^iPr_2Ph)_2$ shows that there is a significant (apparent) increase in SOC on the cobalt center in the antimony-ligated species versus the phosphorus bound species. The percent increase of axial ZFS from P to Sb (~ 7x) is also in line with the percent increase of *D* in going from P to As (~ 2x)[125], given the differences in SOC between As ($\zeta = 2120$ cm$^{-1}$) and Sb ($\zeta = 4800$ cm$^{-1}$).[22] These results strongly indicate the validity of the data and suggest that complexes with even heavier donor atoms (i.e. bismuth) could further increase the axial ZFS and, by extension, the overall spin-orbit-coupling at the paramagnetic metal center.

#### *4.3.2.2 Tetrahedral Dimers: $Co_2(I)_4(Sb^iPr_3)_2$ (2) vs $Co_2(I)_4(PPh_3)_2$ (4)*

SQUID magnetic susceptibility measurements were performed for complex **2**, but unfortunately not for complex **4**. This was due to the difficulty in synthesis of complex **4**, lack of sufficient material for susceptibility studies, and long queues for the SQUID instrument. Thus, no comparative SQUID magnetic susceptibility fittings could be completed for **2** and **4**. However, benchtop magnetic susceptibility measurements were performed for both complexes. For the dimers **2** and **4**, the $\mu_{eff}$ values were determined to be 6.14 B.M. for complex **2** and 5.58 B.M. for complex **4**, which are comparable to previously reported values of other cobalt dimers.[263]

Although the SQUID magnetic susceptibility data could not be collected for complex **4**, the data was collected for complex **2** and the data was fit with two different methods. The first method was through Excel using an equation designed for fitting complexes that have multiple metal centers which are magnetically coupled.[263] Those

fitting data as well as the fitting equation are shown in Figure 4.8. The fitting starts to fail after ~50 K, but this is likely due to the simplicity of the Excel equation. Fitting software, such as PHI, utilize several different Hamiltonians and parameters to fit the data, and it can perform the calculation relatively quickly due to computing power. However, as this fitting was entirely human-based, we cannot utilize massively complex equations and matrices to fit the data by hand. To fit the data using this equation, the fit curve and the susceptibility curve were plotted on the same graph. The values of J and *g* were manually adjusted until the fit curve was determined to adequately align with the susceptibility curve. From the final fit curve that best aligned with the experimental data curve, values for J and *g* were determined. From the data, the isotropic *g*-factor was determined to be 2.48. Also, the fit ascertained a value for J, which is not spin-orbit-coupling, but the exchange coefficient for the two paramagnetic metal centers. The exchange coefficient measures the magnetic interaction between two paramagnetic ions and can originate from a number of physical phenomena, including overlap of magnetic orbitals, interaction through a diamagnetic bridge, or through space. These interactions can lead to isotropic interactions, which dictate ferromagnetism (spins parallel, $J > 0$) or anti-ferromagnetism (spins anti-parallel, $J < 0$) in the complex. For complex **2**, J was determined to be -7.5 K, which means there is anti-ferromagnetic coupling across the two cobalt centers.

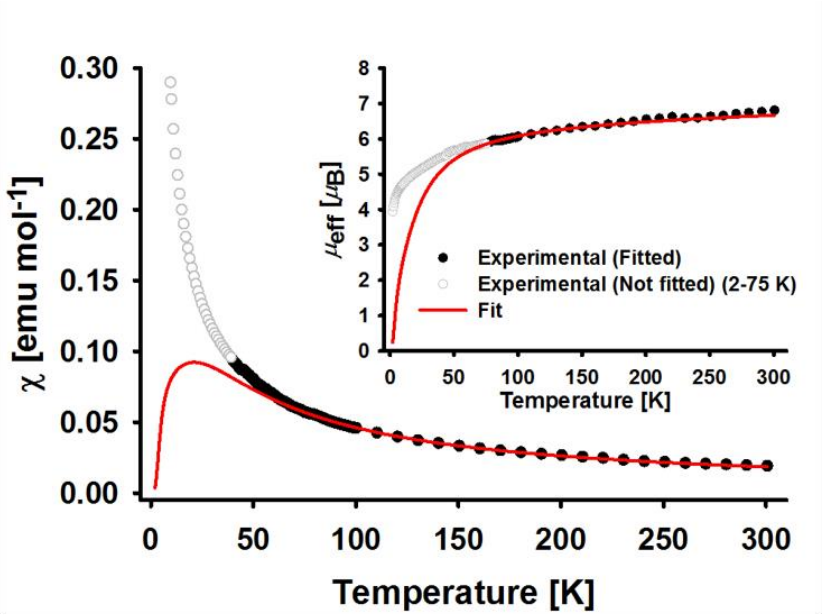


$$\chi = \frac{N_A {\mu_B}^2 g^2}{3kT} \frac{\{82 \exp\left({}^{12J}/_{kT}\right) + 30 \exp\left({}^{6J}/_{kT}\right) + 6 \exp({}^{2J}/_{kT})\}}{\{7 \exp\left({}^{12J}/_{kT}\right) + 5 \exp\left({}^{6J}/_{kT}\right) + 3 \exp\left({}^{2J}/_{kT}\right) + 1\}} + c$$

**Figure 4.8** SQUID magnetic susceptibility data and Excel fitting (top) and fitting equation used (bottom) for complex **2**.

The second method used to fit the susceptibility data for complex **2** was through PHI. The PHI fit can be seen in Figure 4.9, along with the input script used. The input script is very similar to the one used for complex **1**, but both magnetic cobalt centers were accounted for in this fitting and an exchange coefficient variable was added in this script. For the fit, we set $g_x = g_y \neq g_z$ and probed for a $g_z$ value for each cobalt center. For Co1, $g_x = g_y$ =1.91 and $g_z$ = 1.8. For Co2, $g_x = g_y$ = 1.91 and $g_z$ = 3.1. the $|D|$ values for the two spin centers were 39.9 $cm^{-1}$ and 12.4 $cm^{-1}$, but without a strict comparison to $D$ values for an analogous phosphine complex, those numbers are virtually meaningless. Additionally, we determined the exchange coefficient to be -4.4 K from the PHI fitting, which was close to

the J value determined via Excel. A summary of the results and parameters from the Excel and PHI fits of complex **2** are shown in Table 4.3.

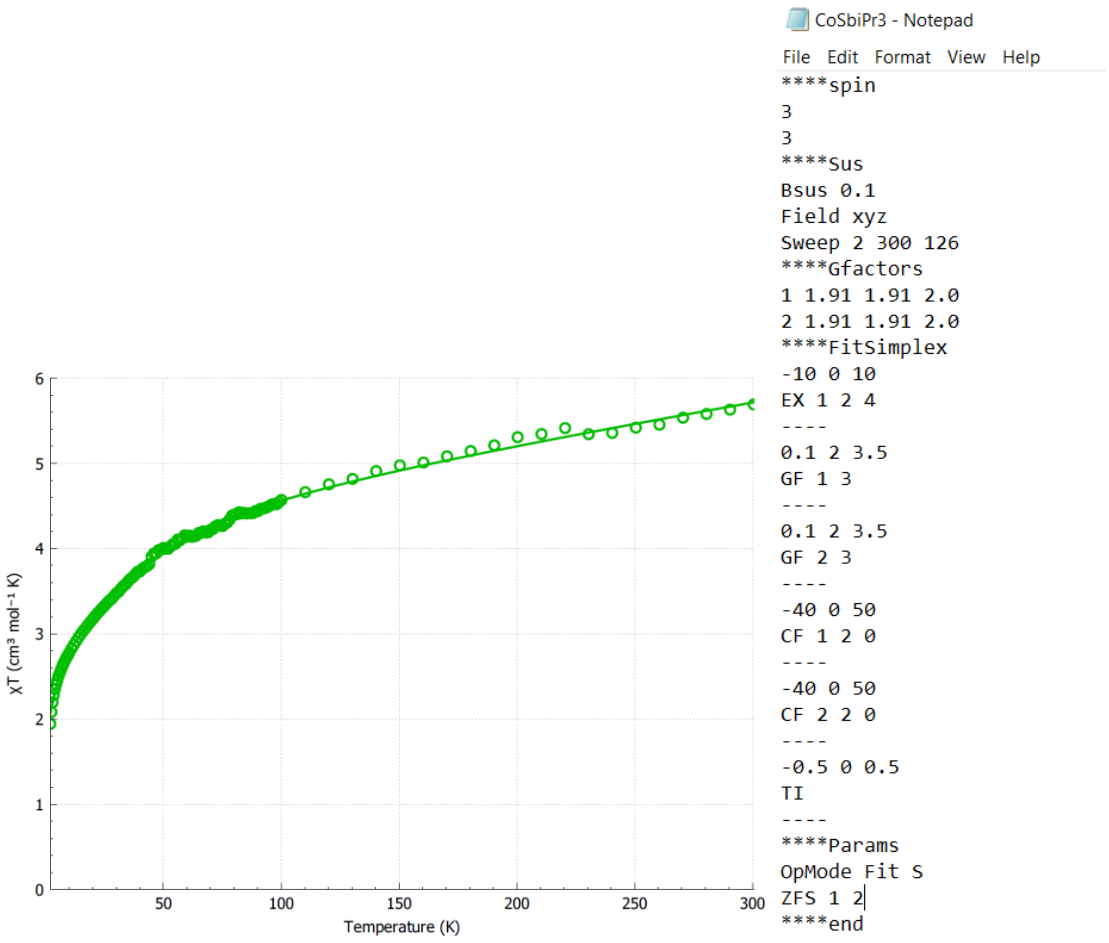


**Figure 4.9:** (Left) Magnetic susceptibility data and PHI best fit for complex **2**. (Right) PHI script used to fit complex **2**.

**Table 4.3** Summary of results and parameters determined from the best fits of **2** using Excel and PHI.

| | $g_{iso}$ | $g_x$ | $g_y$ | $g_z$ | J (K) | $D$ (cm$^{-1}$) | R |
|---|---|---|---|---|---|---|---|
| Excel | 2.48 | - | - | - | -7.5 | - | - |

| | | | | | | | |
|---|---|---|---|---|---|---|---|
| PHI | - | 1.91 | 1.91 | 1.8 & 3.1 | -4.4 | -38.5 & 12.4 | 0.144 |

#### *4.3.2.3 Octahedral complex: $Co(I)_2(SbMe_2Ph)_4$ (5)*

The octahedral complex $Co(I)_2(SbMe_2Ph)_4$ possessed a room temperature magnetic moment of 1.7 B.M. The SQUID susceptibility measurements corroborated this data, revealing a room temperature magnetic moment of 2.00 B.M. It is important to note that, due to the presence of even a very small amount of impurity, gathering an accurate determination of $\mu_{eff}$ from SQUID measurements is difficult. However, those low values of $\mu_{eff}$ from both the benchtop and SQUID susceptibility measurements suggest that $Co(I)_2(SbMe_2Ph)_4$ is a low spin $d^7$ octahedral complex. Although antimony is classically a weak-field ligand, and $SbMe_2Ph$ is one of the weakest ligands synthesized in this work, four soft, neutral-donating ligands were able to generate a low-spin octahedral complex. Low-spin Co(II)-Sb complexes are rare among published structures.

Although the room temperature $\mu_{eff}$ values implied **5** was low-spin, the fitting of the SQUID variable-temperature susceptibility data rendered that distinction ambiguous. When the data was fit as a $S = ½$, $L = 0$ system, no solution could be found that would give an acceptable fit of the data. The residual values were very large, and it was clear this fit was incorrect. However, when an orbital angular momentum component was introduced ($S = ½$, $L = 1$), a good fit was achieved. From that fit, the anisotropic $g$-factor was determined to be 1.85, the $D$ value was -110.5 $cm^{-1}$, and the $E$ value was -1.04 $cm^{-1}$. In particular, the magnitudes of the $D$ value and the $|E/D|$ value were both in line with previously reported Co(II) octahedral compounds.[264,265] Both of those fits from PHI can be

seen in Figure 4.10. A $^2$T term (derived from the $S$ = ½, $L$ = 1 denomination) could be possible if extreme distortions in the structure destabilized the $d_{x^2-y^2}$ and $d_{xy}$ orbitals, while stabilizing all z-component orbitals. A plausible d-orbital splitting for a $^2$T term is given in Figure 4.11, along with the orbital splitting for ideal $D_{4h}$ and the orbital splitting for an axially distorted $D_{4h}$ system. As our system is likely equatorially distorted, the right-most splitting is most plausible.

However, given the large crystal field energy supposed through a low-spin system, this geometric rearrangement is less probabilistic than the $^4$T term label for the tetrahedral complexes above. Clearly, given the ambiguity of the data, a definitive statement on the magnetic properties of complex **5** cannot be provided. Additionally, the lack of an analogous phosphine derivative of complex **5** means we cannot compare the magnetic data to determine the increase in the extent of SOC on the metal center in this octahedral system. More measurements and reactions are necessary to fully investigate and analyze this work.

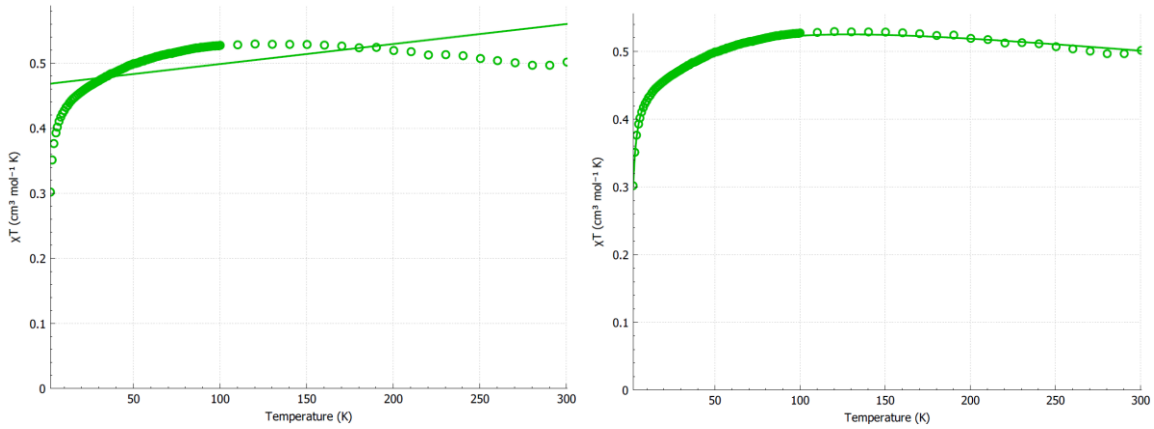


**Figure 4.10** PHI data and fittings for complex **5** using a $^2E_g$ term (left) and a $^2$T term (right) to delineate the system.

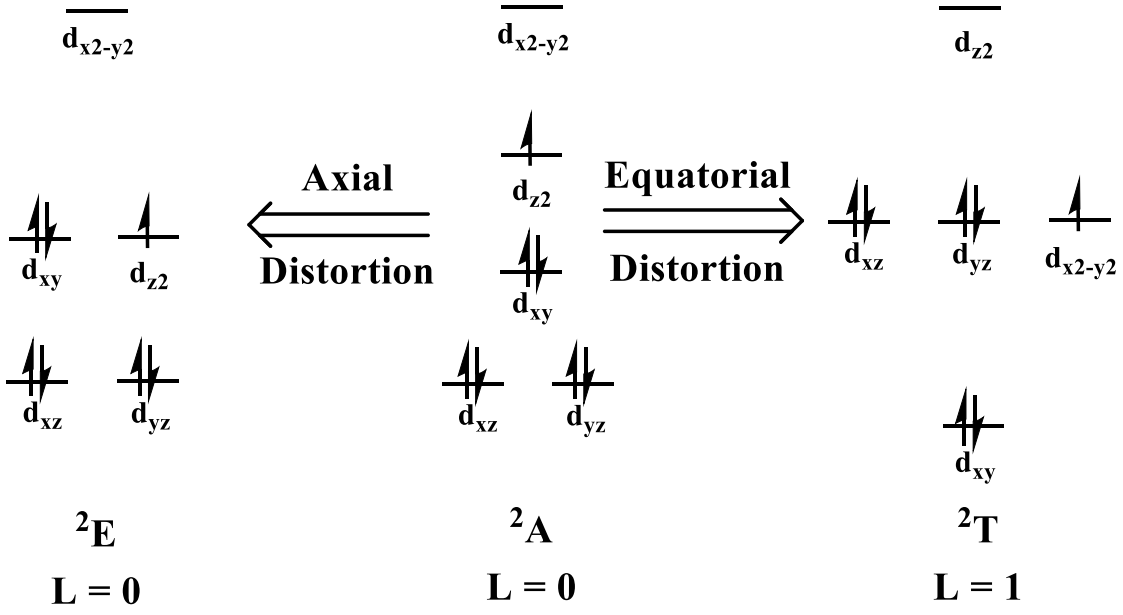


**Figure 4.11** Plausible *d*-orbital splittings for axial and equatorial distortions away from ideal $D_{4h}$ symmetry, relevant for complex **5**.

### 4.3.3 Electronic Absorption Spectroscopy

In an effort to better characterize our complexes and to fully establish a quantitative measure of spin-orbit-coupling in our systems, we performed near-infrared electronic absorption spectroscopy. Spectra were obtained in deuterated benzene up to 3000 $cm^{-1}$ or in $CH_2Cl_2$ up to 4000 $cm^{-1}$. Figure 4.12 shows the NIR electronic absorbance spectra for complexes **1** and **3**. Enhanced $\nu_2$ features for each spectrum are shown in Figure 4.13. For an ideal tetrahedral system, three electronic transitions are expected: $\nu_1$ ($^4T_{2g} \leftarrow {}^4A_2$) at 3000-4000 $cm^{-1}$ (2500-3333 nm), $\nu_2$ ($^4T_{1g}(F) \leftarrow {}^4A_2$) at 5000-8000 $cm^{-1}$ (1250-2000 nm), and $\nu_3$ ($^4T_{1g}(P) \leftarrow {}^4A_2$) at 13000-18000 $cm^{-1}$ (555-770 nm).[185] For $\nu_2$, the feature is often very broad and broadens across thousands of wavenumbers. For both $Co(I)_2(Sb^iPr_2Ph)_2$ (**1**) vs. $Co(I)_2(PPh_3)_2$ (**3**), the $\nu_1$ ($\sim\Delta_{tet}$) was undetectable due to ligand-based C-H stretches. However, the energy of $\nu_1$ was estimated from the $T_d$ Tanabe-Sugano diagram and the

combination of $\nu_2$ and $\nu_3$ transitions. For complex **1**, $\nu_2$ was observed at 6800 $cm^{-1}$ (1470 nm) and $\nu_3$ was at 12880 $cm^{-1}$ (776 nm), leading to calculated $\nu_1$ as 4050 $cm^{-1}$ (2470 nm). For complex **3**, $\nu_2$ was observed at 7810 $cm^{-1}$ (1280 nm), $\nu_3$ at 13770 $cm^{-1}$ (726 nm), and $\nu_1$ was then calculated at 4730 $cm^{-1}$ (2114 nm) from the $T_d$ Tanabe-Sugano diagram. These data are highly consistent with other Co(II) $T_d$ complexes—suggesting synthetic purity—and the red-shifted absorbance features for the Co-Sb complex are typical for complexes with soft, weak-field ligands.[185,266]

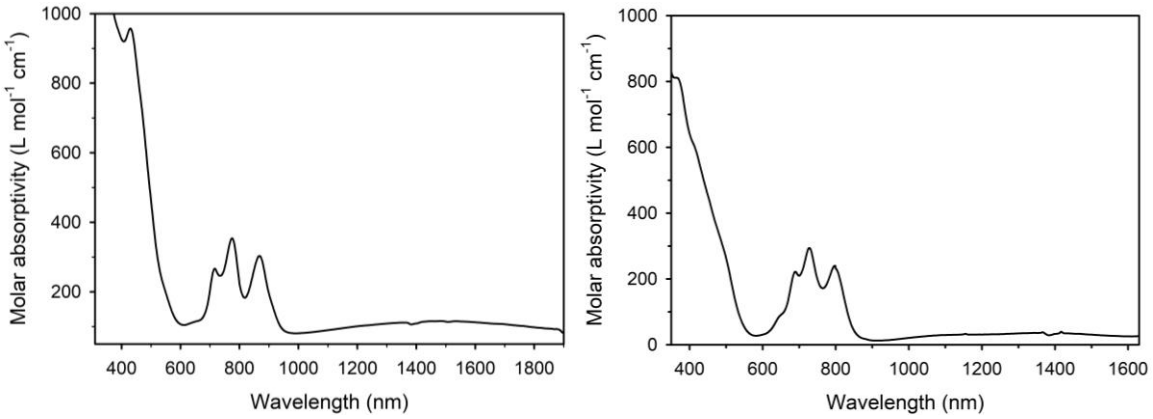


**Figure 4.12:** Near-IR Electronic absorbance spectra for **1** (left) and **3** (right).

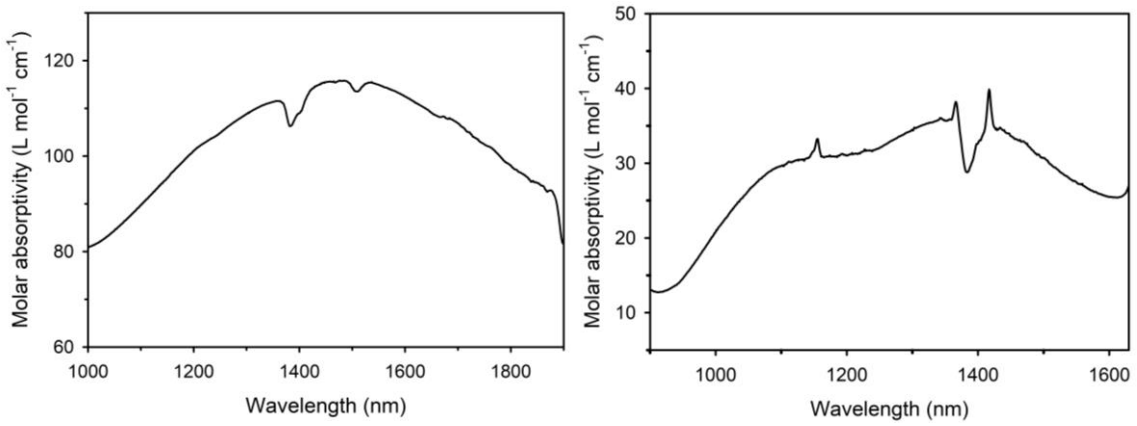

**Figure 4.13:** Enhanced $\nu_2$ features for **1** (left) and **3** (right).

In ideal tetrahedral systems, $\nu_1$ is equal to $10Dq$, and the correlation between $\mu_{eff}$, $10Dq$, and the effective SOC constant ($\lambda$) in complexes with a $^4$A term symbol is given by Equation 4.8:[185]

$$u_{eff} = 3.87 * (1 - \frac{4\lambda}{10Dq}) \qquad \text{(Eq. 4.8)}$$

From this equation, the effective SOC constant in complex **1** was determined to be -206 cm$^{-1}$. However, the effective SOC constant for complex **3** was determined to be -229 cm$^{-1}$. According to the increased axial ZFS found for **1**, it was expected that the antimony-ligated cobalt complex would display a higher effective SOC constant than the phosphorus-ligated. The likely culprit for this discrepancy is the covalency and orbital reduction factor, *k*. In Equation 4.8, the $\lambda$ variable is more precisely described through the equation $\lambda = k\lambda_0$, where $\lambda_0$ is the free-ion spin-orbit-coupling constant, where $\lambda$ then reflects the *effective* SOC constant in the complexed metal ion.[107] In general, *k* is defined as an electron delocalization factor, and substantial electron delocalization will cause a greater decrease in *k*.[267] While *k* can vary from 0 to 1 (1 = no delocalization, 0 = maximum delocalization), tetrahedral systems generally lead to lower k values due to a combination of metal *p* orbitals mixing with ground state molecular orbitals and the ligand orbitals mixing with both *d* and *p* metal orbitals.[267] A deviation away from unity also implies diminished overall covalency within the complex.[107] As the $PPh_3$ ligand can participate is substantial $\pi$-backbonding and likely has more orbital overlap with the Co(II) *d* and *p* orbitals, it may be inferred that **3** has a larger *k* value than **1**. As an estimated guess, we assigned the *k* value for complex **3** as 0.85, while the *k* value for complex **1** was estimated to be 0.5. Consequently, **3** would rationally have a higher effective SOC constant versus **1**, even if the $\lambda_0$ is likely larger in complex **1** versus complex **3**. From our estimates of *k*, the free-ion spin orbit coupling

constant for **1**, $\lambda_0$, would be -412 $cm^{-1}$, while the free-ion SOC constant for **3** would be -269 $cm^{-1}$. However, these are merely estimated values and without an accurate knowledge of the value of *k* for complexes **1** and **3**, the precise extent of SOC at the metal centers cannot be determined. A tabulated summary of the absorbance transitions, *k*, $\lambda$, and $\lambda_0$ values for complexes **1** and **3** is shown in Table 4.4.

**Table 4.4** Summary of absorbance transitions ($\nu_1$, $\nu_2$, $\nu_3$), covalency factor (*k*), effective SOC constant ($\lambda$), and free-ion SOC constant ($\lambda_0$) for complexes **1** and **3**.

| **Complex** | **$\nu_1$ ($^4T_{2g}$ ← $^4A_2$) ($cm^{-1}$)** | **$\nu_2$ ($^4T_{1g}(F)$ ← $^4A_2$) ($cm^{-1}$)** | **$\nu_3$ ($^4T_{1g}(P)$ ← $^4A_2$) ($cm^{-1}$)** | ***k*** | **$\lambda$ ($cm^{-1}$)** | **$\lambda_0$ ($cm^{-1}$)** |
|---|---|---|---|---|---|---|
| **$Co(I)_2(Sb^iPr_2Ph)_2$ (1)** | 4050 | 6800 | 12880 | 0.5 | -206 | -412 |
| **$Co(I)_2(PPh_3)_2$ (3)** | 4730 | 7810 | 13770 | 0.85 | -229 | -269 |

The dimeric tetrahedral complexes **2** and **4** were also examined for their electronic absorbance features out to 2000 $cm^{-1}$. The electronic absorption spectra for complexes **2** and **4** are shown in Figure 4.14 and Figure 4.15, respectively. Spectra showing an enhanced $\nu_2$ transition for each complex are shown along with the full spectrum in each figure.

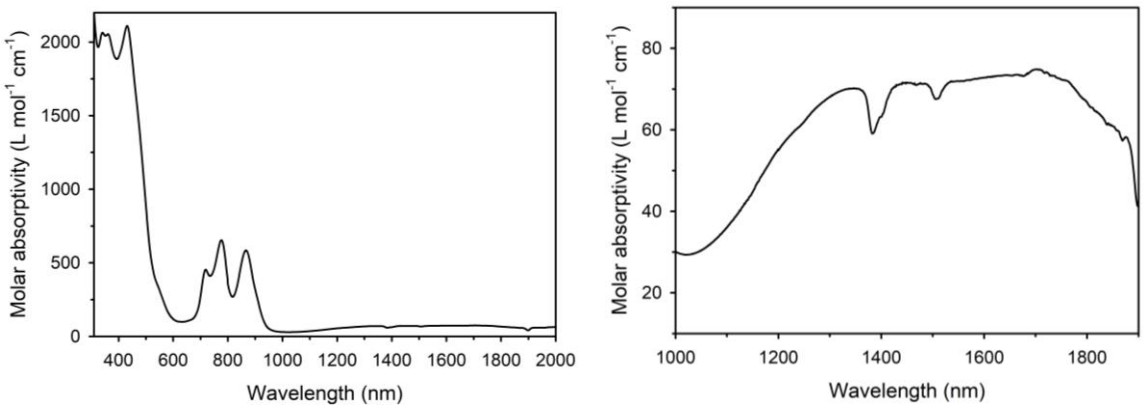


**Figure 4.14:** Electronic absorption spectra of complex **2** (left). Enhanced $\nu_2$ transition (right).

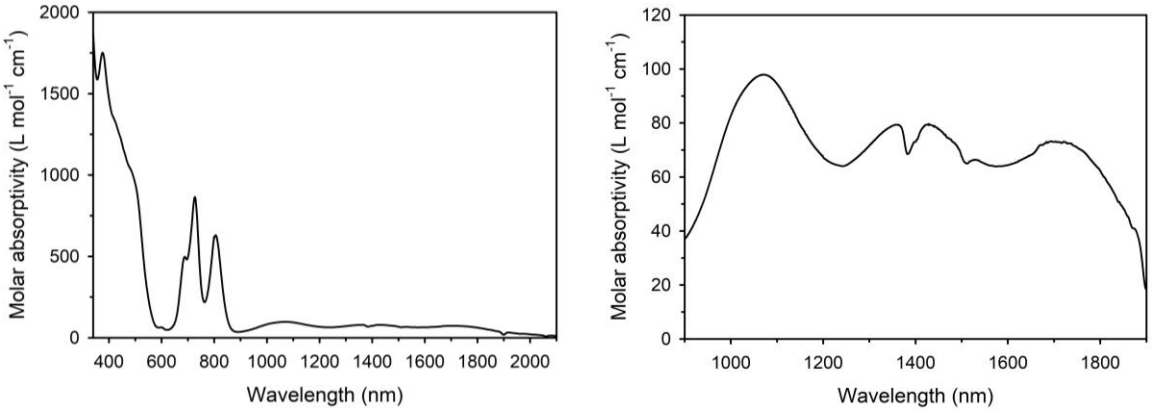


**Figure 4.15:** Electronic absorption spectra of complex **4** (left). Enhanced $\nu_2$ transition (right).

Although dimeric, the cobalt centers are still tetrahedral in geometry, which means they should behave the same as the monomeric species in terms of the number and relative location of the transitions. In preparing the solution, no obvious precipitate or color change occurred that would imply a decomposition of the dimer into the monomeric species. From the NIR electronic absorbance spectrum for complex **2**, $\nu_2$ was observed at 6535 $cm^{-1}$ (1530 nm), while $\nu_3$ was determined to be 12870 $cm^{-1}$ (777 nm). From these data, $\nu_1$ was calculated at 3857 $cm^{-1}$ (2592 nm). For complex **4**, $\nu_2$ was observed at 7352 $cm^{-1}$ (1360

nm), while $\nu_3$ was observed at 13774 $cm^{-1}$ (726 nm). From these data, $\nu_1$ was calculated at 4369 $cm^{-1}$ (2288 nm). As with the comparison between complexes **1** and **3**, the metal complex ligated with the heavier pnictogen ligands displayed a more red-shifted absorption and possessed a narrower $\Delta_{tet}$ energy gap. Unfortunately, the effective spin-orbit-coupling constant of these complexes could not be determined with Equation 4.8, as that equation was designed for mononuclear $^4A$ terms and not multinuclear species. A suitable replacement equation was not found or derived for complexes **2** and **4**. A summary table for the electronic absorbance transitions ($\nu_1$, $\nu_2$, $\nu_3$) is shown in Table 4.5.

**Table 4.5** Summary of absorbance transitions ($\nu_1$, $\nu_2$, $\nu_3$) for complexes **2** and **4**.

| **Complex** | **$\nu_1$ ($^4T_{2g} \leftarrow {}^4A_2$) ($cm^{-1}$)** | **$\nu_2$ ($^4T_{1g}(F) \leftarrow {}^4A_2$) ($cm^{-1}$)** | **$\nu_3$ ($^4T_{1g}(P) \leftarrow {}^4A_2$) ($cm^{-1}$)** |
|---|---|---|---|
| **$Co_2(I)_4(Sb^iPr_3)_2$ (2)** | 3857 | 6535 | 12870 |
| **$Co_2(I)_4(PPh_3)_2$ (4)** | 4369 | 7352 | 13774 |

Complex **5** was also probed for its electronic transitions via NIR electronic absorbance spectroscopy. The electronic absorption spectra of **5**, along with an enhanced NIR region, is seen in Figure 4.16. As complex **5** possesses an octahedral geometry, the expected transitions are $\nu_1$ at 5000-9000 $cm^{-1}$ (1111-2000 nm, $^4T_{2g} \leftarrow {}^4T_{1g}$), $\nu_2$ at 12000-16000 $cm^{-1}$ (625-833 nm, $^4A_{2g} \leftarrow {}^4T_{1g}$), and $\nu_3$ at 17000-26000 $cm^{-1}$ (380-590 nm, $^4T_{1g}(P) \leftarrow {}^4T_{1g}$). The $\nu_2$ transition is often not normally observed as it is formally a two-electron transition.[185]

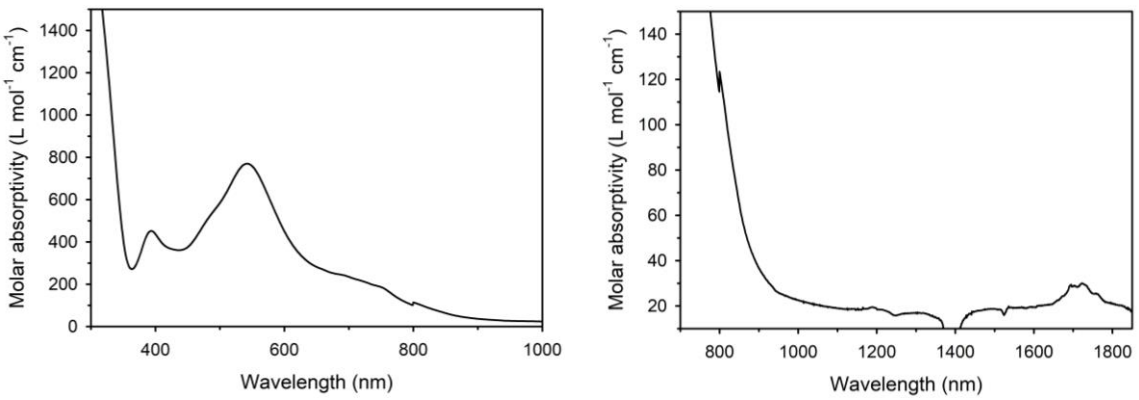


**Figure 4.16:** Electronic absorption spectra of complex 5 (left). Enhanced $\nu_1$ transition (right).

We assign the $\nu_3$ transition at 542 nm (18450 $cm^{-1}$) and the $\nu_1$ transition at 1710 nm (5847 $cm^{-1}$). The $\nu_1$ transition is at the low energy limit for typical $O_h$ compounds of Co(II), but from examination of our other Co-Sb compounds, this appears to be a common theme when using heavy donor ligands (low energy, red-shifted absorption and emission features).

The UV/Vis spectrum gives further evidence for the substantial distortion away from perfect octahedral geometry in the structure. From Lever,[185] the existence of distortion from a regular octahedral structure is often revealed in cobalt(II) complexes by appreciable enhancement in absorption intensity. The peak molar absorptivity in complex **5** reaches 800 L $mol^{-1}$ $cm^{-1}$. Typical octahedral cobalt(II) complexes display molar absorptivity values near 40 L $mol^{-1}$ $cm^{-1}$. Thus, the electronic properties corroborate the structural distortions, and give more credence to the argument of assigning complex **5** as a significantly distorted $^2T$ system.

Similar to the case of the dimeric tetrahedral complexes, determination of the effective SOC constant in complex **5** is not a trivial matter. This is due to the uncertainty

of term symbol labelling for complex **5**. The room temperature magnetic moment and the PHI fitting suggest a $S = ½$ system, however the $L$ value is ambiguous. A typical low-spin octahedral cobalt(II) complex with $S = ½$ would be an $^2E_g$ term, and have $L = 0$. However, the PHI fitting was much more effective when the complex was denoted as a $^2T$ term and setting L = 1. If the complex were an E term, a variation of Equation 4.8 could be used (4λ is swapped to 2λ) to determine the effective SOC constant, once $\mu_{eff}$ and $10Dq$ are known. However, the effective SOC constant cannot be determined through a simple equation such as Equation 4.8 if the complex is a T term. Further theoretical investigation is required to definitively determine the symmetry and *d*-orbital energy splitting of **5**. Additionally, a synthetic analogue with phosphine or other pnictogen ligand is required to draw useful comparisons between **5** and lighter donor atoms. As such, the electronic absorbance spectrum of **5** can serve as an additional characterization method to confirm the distorted octahedral geometry in which the complex occupies. A tabulated summary of all the determined values for complex **5** (isotropic *g*-factor, *D*, and *E* vales for the $^2T$ fit, and absorption transitions) is shown in Table 4.6.

**Table 4.6** Summary of anisotropic *g*-factor, *D*, *E* (from $^2T$ fit), and absorbance transitions ($\nu_1$, $\nu_2$, $\nu_3$), for complex **5**.

| **Complex** | **$\nu_1$ ($^4T_{2g}$ ← $^4T_{1g}$) ($cm^{-1}$)** | **$\nu_2$ ($^4A_{2g}(F)$ ← $^4T_{1g}$) ($cm^{-1}$)** | **$\nu_3$ ($^4T_{1g}(P)$ ← $^4T_{1g}$) ($cm^{-1}$)** | ***g*** | ***D*** **($cm^{-1}$)** | ***E*** **($cm^{-1}$)** |
|---|---|---|---|---|---|---|
| **$Co(I)_2(SbMe_2Ph)_4$ (5)** | 5847 | - | 18450 | 1.85 | -110.5 | -1.04 |

## 4.4 Preliminary C-H Activation Reactivity

As the overall goal of the project was to synthesize new catalysts for C-H activation, the cobalt complexes were tested for their reactivity towards standard C-H activation substrates. The tetrahedral cobalt complexes were chosen as they had shown very rapid reactivity towards oxygen – more specifically, they decomposed in the presence of oxygen in a matter of seconds. The open coordination sites on the cobalt center could facilitate ligand association and oxidative addition. The first simple experiment we performed was to bubble methane through a fluorobenzene solution of each complex (10 mg of each Co-Sb or Co-P complex in 10 mL of solvent), let stir overnight, and observe any color change during the time. After one day stirring at room temperature, the solutions were heated using a pressure vessel inside an argon glovebox (very similar to the metal deposition reaction procedures from Chapter 2). Initially, these reactions were intended as preliminary results for grant purposes. The cobalt-antimony complexes did appear to change color upon initial addition of $CH_{4(g)}$, and they held that color change after one night of stirring. The phosphine compounds, on the other hand, did not show any color change either on addition or after one night of stirring. Some qualitative pictures of these reactions can be seen in Figure 4.17. No heat was applied to any of the reactions shown in Figure 4.17. The readily apparent color changes in the Co-Sb compounds after exposure to methane were promising results. Although several phenomena can cause color changes in reactions, the first assumption of any synthetic chemist is that a reaction (or at least an interaction) occurred between the two substrates.

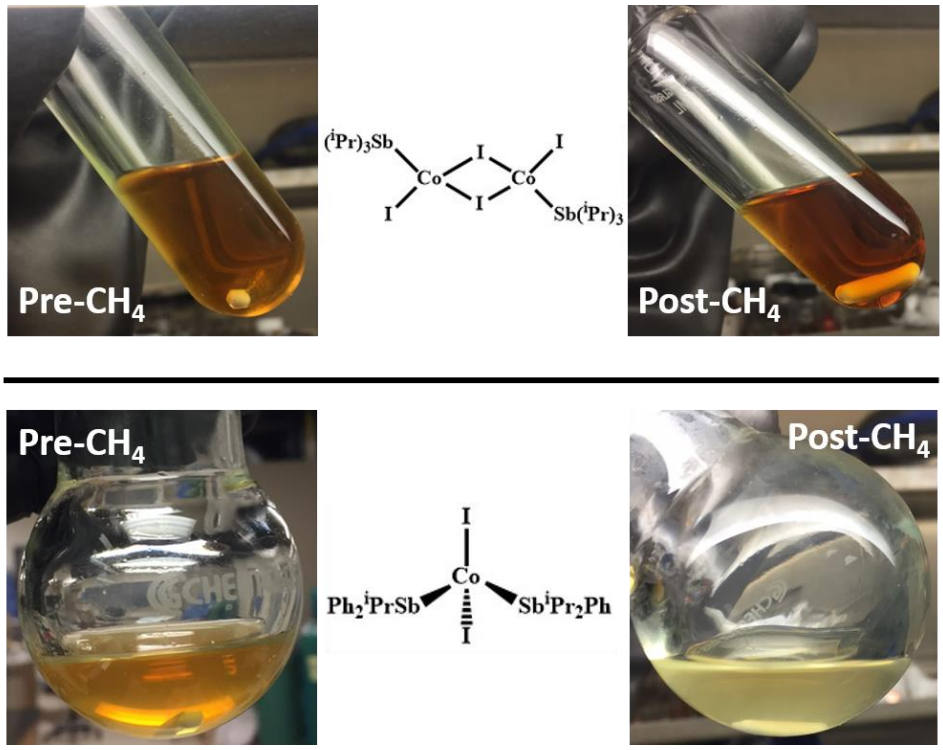


**Figure 4.17:** Qualitative photos showing color change on addition of methane gas to cobalt-antimony tetrahedral complexes.

When these reactions were heated, both solutions lost their color after 4-6 hours. As per the nickel deposition reactions, this loss of color was likely the result of decomposition of the complex, or de-ligation of the antimony ligands. Unlike the nickel reactions, however, there was no obvious precipitate after the heating.

Following these promising results, we moved on to more quantitative experiments. a common C-H activation test substrate is 9,10-dihydroanthracene, as the C-H bond at the 9,10-position is quite labile. Initially, ~10 mg of cobalt complex was stirred with one equivalent of 9,10-dihydroanthracene in fluorobenzene. The reactions were stirred overnight, and then a GC-MS spectrum was obtained to detect the presence of anthracene. If a C-H activation reaction were occurring in these reactions, one hydrogen from both the

9- and 10-positions on DHA would be removed by the cobalt catalyst, affording thermodynamically stable anthracene as the product. Room temperature reactions overnight did not yield any substantial anthracene formation. However, when the reactions were heated overnight, the expected loss of color occurred, and the GC-MS results did show a small presence of anthracene, which increased as the reaction ran longer (up to 48 hours). Using the known amount of 9,10-DHA added to the reaction as an internal standard, we estimated a ~7 % conversion rate of total DHA to anthracene for complex **1**. These modest results were increased to a 20 % yield (5:1 ratio of anthracene: **1**) when excess 9,10-dihydroanthracene was used. The dimeric species, complex **2**, displayed similar results. As a comparison, when the Co-$PPh_3$ complexes were used (both monomer and dimer), no anthracene was ever observed in the GC-MS trace, with or without heating. As a control reaction, 9,10-DHA was heated with solely antimony ligand ($Sb^iPr_2Ph$ or $Sb^iPr_3$) to determine the effect of the cobalt center on the reaction. For both $Sb^iPr_2Ph$ and $Sb^iPr_3$, anthracene was detected in the mass spectrum trace after the reaction, however in lower yields than the cobalt-antimony metal complexes performed ($Sb^iPr_2Ph$ = 4.7 %; $Sb^iPr_3$ = 7.3 %). As another comparison, triphenylphosphine + DHA did not yield any anthracene product. A summary of the reaction conditions and results of the 9,10-dihydroanthracene conversion reaction to anthracene with both tetrahedral metal complexes and ligands can be seen in Figure 4.18.

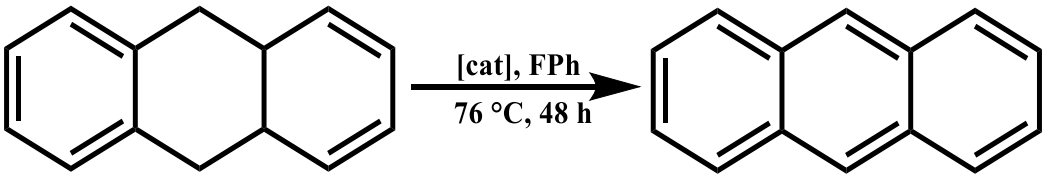


| | DHA : Anth | Percent Yield |
|---|---|---|
| $CoSb^iPr_3$ | 7.1 : 1 | 14.5 % |
| $CoSb^iPr_2Ph$ | 5.1 : 1 | 20 % |
| $Sb^iPr_3$ | 13.7 : 1 | 7.3 % |
| $Sb^iPr_2Ph$ | 21.3 : 1 | 4.7 % |
| $CoPPh_3$ dimer | 154 : 1 | 0.6 % |
| $CoPPh_3$ mon | 199 : 1 | 0.5 % |
| $PPh_3$ | 175 : 1 | 0.5 % |
| No catalyst | 176 : 1 | 0.5 % |

**Figure 4.18:** Summary of reaction conditions and results for the conversion of 9,10-dihydroanthracene to anthracene using cobalt-antimony and cobalt-phosphorus complexes, along with lone ligands and no catalyst.

Another interesting result from these heated reactions was the evidence of alkyl transfer onto the 9- and 10-position of the DHA substrate. In the GC-MS spectra for the reactions of 9,10-DHA heated with complexes **1** and **2**, small traces of ethyl and isopropyl terminated 9-ethyl-10-hydroanthracene (or 9-isopropyl-10-hydroanthracene) were present. These products only were observed after long reaction times (~60 hours) and were a minor product among the main anthracene conversion (3 – 4 % yield). It is not uncommon for antimony (and bismuth) ligands to engage in R-group "shuffling" with other ligands (i.e. com/dis-proportionation). For example, the comproportionation reaction to afford $SbPh_2Cl$

or $SbPhCl_2$ is the result of substituent exchange between $SbPh_3$ and $SbCl_3$. As the alkyl transfer product is only visible after long reaction times and high temperatures, it is possible that the Sb$^i$Pr3 or Sb$^i$Pr$_2$Ph free ligands present in solution may have exchanged an isopropyl substituent with a proton substituent from 9,10-DHA (to afford 9-isopropyl-10-hydroanthracene and Sb$^i$Pr$_2$H, for example). Similar *in situ* rearrangements have been observed before, though these types of reactions are more common with bismuth ligands. For example, the reaction of the triphosphanylbismuthine ligand, (*o*-(Ph$_2$P)C$_6$H$_4$)$_3$Bi), with [AuCl(tht)] (tht = tetrahydrothiophene) resulted in the dissociation of the *o*-(Ph$_2$P)C$_6$H$_4$ substituent from bismuth and the bidentate re-coordination of that substituent to the gold metal center through the phosphine lone pair and the carbon *ortho* to the phosphine.[268] A similar phenomenon could be occurring with these alkyl-transferred dihydroanthracene products. An isopropyl substituent from an Sb ligand may be transferring onto the cobalt center, which may in turn perform alkyl transfer to the 9- or 10-position of dihydroanthracene. No sign of alkyl-transfer was evident with the phosphorus complexes. As antimony is less likely to perform these types of exchange reactions versus bismuth, just so will phosphorus display an even smaller probability for these reactions. It is clear that several additional reactions and experiments are required to deduce the mechanism behind these results, and any plausible conjecturing is still conjecture without tangible data to back up the theory. Still, these are interesting results, as alkyl transfer onto a substrate is classically a sign of C-H activation activity. A graphic of the reaction conditions and an example of an alkyl-transfer product seen from these reactions is shown in Figure 4.19.

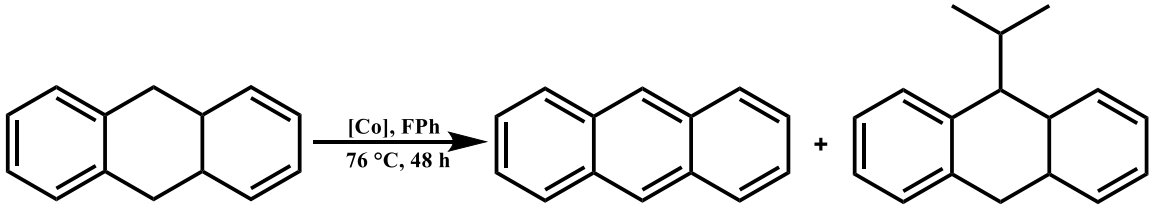

**Figure 4.19:** Alkyl-transfer product, 9-ethyl-10-hydroanthracene, present after the reaction of 9,10-DHA + Co-Sb complex at 60 hours heating.

Overall, these results are interesting but ambiguous and inconclusive. From the data, it appears the anthracene conversion reaction is only successful once the complex begins to decompose – hence why heating the reaction mixture is required for the reaction to proceed. From the nickel deposition and decomposition studies detailed in Chapter 2, the loss of color in these reaction after several hours was an indication that the complex is decomposing, or at least the ligands were disassociating *in situ*. If this same decomposition is happening in the Co-Sb cases, then any C-H activation reactivity happening in the reaction mixture is not the workings of an intact cobalt-antimony complex. Thus, any increase in C-H activation reactivity between Co-Sb and Co-P complexes cannot be attributed to an increased extent of SOC at the cobalt center.

In order to better probe the mechanism of this reactivity, several future studies could be conducted. For one, UV/Vis measurements in conjunction with GC-MS analyses could ascertain if the conversion reaction only begins once the catalyst begins to decompose. As the antimony ligands themselves showed some anthracene conversion, this could be a plausible mechanism. Another important investigation would be to determine what are the other byproducts of the reaction mixture. GC-MS is rather limiting on what products appear in the spectrum, and if anything in the reaction mixture does not ionize (i.e. some Co-Sb product), it will not appear in the final MS result. It would also be beneficial to see if any of those byproducts perform additional C-H activation reactions – that is, can successful conversion of DHA to anthracene occur a second time with the byproducts of the reaction? Or is the reaction merely stoichiometric and once the initial conversion is complete, no future conversion can be observed? Although it appears the reaction is not catalytic in nature, it would be important to determine if the reaction will

proceed backwards – does the reaction of cobalt "catalyst" plus anthracene (plus a proton source) yield dihydroanthracene or some other product? In the same vein, tracking down the 9 and 10 position protons/hydrogens of DHA and determining where they migrate to is a worthwhile experiment to perform. As previously mentioned, all of these reactions and results were preliminary, and additional experiments must be performed before any definitive statements can be made regarding the C-H activation capabilities of these Co-Sb compounds.

## 4.5 CONCLUSION

In conclusion, three new and rare examples of antimony-cobalt(II) complexes of different geometries (approximately $T_d$ and $O_h$) and structural motifs were synthesized and crystallized. Additionally, we synthesized and crystallized two previously reported phosphorus-cobalt(II) complexes that were synthetic analogous to two of our antimony complexes. The magnetic properties of tetrahedral $Co(I)_2(Sb^iPr_2Ph)_2$ (**1**) were studied in detail versus the triphenylphosphine analogue, $Co(I)_2(PPh_3)_2$ (**3**). The best fits of the DC magnetic susceptibility data indicate complex **1** possesses significantly larger axial zero-field-splitting ($D$ = -64.5 $cm^{-1}$) than does complex **3** ($D$ = -9.44 $cm^{-1}$). The most likely attribution to the larger D value in complex **1** is from the greater extent of spin-orbit-coupling on the cobalt center due to the translationally donated SOC from the heavy antimony donor atoms. The magnetic properties of complexes **2**, **4**, and **5** were also probed, but conclusive determinations of the $D$ value or the extent of SOC on those metal centers was not obtained. The electronic absorbance spectra of all five complexes were obtained to better characterize our compounds as well as better quantify the translational spin-orbit-coupling present in the antimony and phosphorus complexes. An investigation of the

electronic absorbance transitions for complexes **1** and **3** reveals the expected red-shift in absorbance features for the Co-Sb complex versus the Co-P complex (a similar expected shift occurs for complexes **2** and **4** as well). However, the effective spin-orbit-coupling constant ($\lambda$) was calculated to be larger in **3** (-221 $cm^{-1}$) than in **1** (-206 $cm^{-1}$), possibly due to the higher extent of covalency and orbital overlap in the phosphine case, which leads to an increase in the covalency constant, *k*. Once the *k* value was estimated and factored in for each complex, the free-ion SOC constant ($\lambda_0$) appears to be larger in complex **1** (-412 $cm^{-1}$) than in complex **3** (-269 $cm^{-1}$). Complexes with more covalent antimony-cobalt bonds could lead to larger effective spin-orbit-coupling constants, as well as could complexes with higher denticity antimony ligands via the chelate effect.

Preliminary C-H activation reactivity studies were performed with complexes **1**-**4** to determine if an increase in the extent of SOC on the cobalt metal center improved C-H activation reactivity towards model substrates. Cobalt-antimony complexes did show some reactivity towards both methane (color change) and in the conversion of 9,10-dihydroanthrance to anthracene (15-20 % conversion yield), while the cobalt-phosphorus analogues showed no signs of activity in either experiment. However, doubts on the stability of the complexes in heated solutions precludes an exact determination of the origin or mechanism responsible for these conversion results. As these were preliminary studies and results, the exact mechanism remains undetermined, and future detailed investigations are required. Still, the moderate activities in both qualitative and quantitative reactions of Co-Sb compounds with C-H activation substrates is an exciting first step towards the synthesis of new catalysts using inexpensive metals and earth-abundant main-group elements.

## 4.6 REFERENCES


(251) Huang, Y.-G.; Jiang, F.-L.; Hong, M.-C. Magnetic Lanthanide–Transition Metal Organic–Inorganic Hybrid Materials: From Discrete Clusters to Extended Frameworks. *Coord. Chem. Rev.* **2009**, *253*, 2814–2834.

(252) Karlin, K. D.; Nanthakumar, A.; Fox, S.; Murthy, N. N.; Ravi, N.; Huynh, B. H.; Orosz, R. D.; Day, E. P. X-Ray Structure and Physical Properties of the Oxo-Bridged Complex $[(F8\text{-}TPP)Fe\text{-}O\text{-}Cu(TMPA)]^{+}$, F8-TPP = Tetrakis(2,6-Difluorophenyl)Porphyrinate($^{2-}$), TMPA = Tris(2-Pyridylmethyl)Amine: Modeling the Cytochrome c Oxidase Fe-Cu Heterodinuclear Active Site. *J. Am. Chem. Soc.* **1994**, *116*, 4753–4763.

(253) Terris, B. D.; Thomson, T. Nanofabricated and Self-Assembled Magnetic Structures as Data Storage Media. *J. Phys. D. Appl. Phys.* **2005**, *38*, R199--R222.

(254) Desrochers, P. J.; Telser, J.; Zvyagin, S. A.; Ozarowski, A.; Krzystek, J.; Vicic, D. A. Electronic Structure of Four-Coordinate $C_{3v}$ Nickel(II) Scorpionate Complexes: Investigation by High-Frequency and -Field Electron Paramagnetic Resonance and Electronic Absorption Spectroscopies. *Inorg. Chem.* **2006**, *45*, 8930–8941.

(255) Gorter, S.; Hinrichs, W.; Reedijk, J.; Rimbault, J.; Pierrard, J. C.; Hugel, R. P. Structure, Spectroscopy and Magnetism of Di-Iodo-Bridged Tetrahedral Cobalt(II) Compounds. The Crystal and Molecular Structures of Di-$\mu$-Iodo-Bis[Iodotriphenylphosphinecobalt(II)] Bis(Benzene) and Di-$\mu$-Iodo-Bis[Iodotriphenylphosphineoxidecobalt(II)] Bis(Benzene). *Inorganica Chim. Acta* **1985**, *105*, 181–186.

(256) Vránová, I.; Alonso, M.; Jambor, R.; Růžička, A.; Erben, M.; Dostál, L. Stibinidene and Bismuthinidene as Two-Electron Donors for Transition Metals (Co and Mn). *Chem. – A Eur. J.* **2016**, *22*, 7376–7380.

(257) Gilli, G.; Sacerdoti, M.; Domiano, P. The Crystal and Molecular Structure of Dicarbonylnitrosyltriphenylstibinecobalt(0). *Acta Crystallogr. Sect. B* **1974**, *30*, 1485–1490.

(258) Suzuki, T.; Fujiiwara, K.; Takagi, H. D.; Kashiwabara, K. Preparation and Characterization of Mixed-Ligand Cobalt(III) Complexes Containing (3-Aminopropyl)Dimethylphosphine (Pdmp). Conformation of the Six-Membered Pdmp Chelate Ring. *Dalt. Trans.* **2007**, 308–319.

(259) Naktode, K.; Kottalanka, R. K.; Adimulam, H.; Panda, T. K. Tetra-Nuclear Copper Complex Having P–N–P Ligand to P–O–P Ligand – Synthesis, Structural, and Mechanistic Studies. *J. Coord. Chem.* **2014**, *67*, 3042–3053.

(260) Bain, G. A.; Berry, J. F. Diamagnetic Corrections and Pascal's Constants. *J. Chem. Educ.* **2008**, *85*, 532–536.

(261) Hota, R. L.; Tripathi, G. S. Theory of Effective G-Factors in Ternary Semiconductors: Application to $Pb_{1-x}Sn_xTe$. *J. Phys. Condens. Matter* **1991**, *3*, 6299–6311.

(262) Vaidya, S.; Tewary, S.; Singh, S. K.; Langley, S. K.; Murray, K. S.; Lan, Y.; Wernsdorfer, W.; Rajaraman, G.; Shanmugam, M. What Controls the Sign and Magnitude of Magnetic Anisotropy in Tetrahedral Cobalt(II) Single-Ion Magnets? *Inorg. Chem.* **2016**, *55*, 9564–9578.

(263) Cho, Y. I.; Ward, M. L.; Rose, M. J. Substituent Effects of $N_4$ Schiff Base Ligands on the Formation of Fluoride-Bridged Dicobalt(II) Complexes via B–F Abstraction: Structures and Magnetism. *Dalt. Trans.* **2016**, *45*, 13466–13476.

(264) Zhou, J.; Song, J.; Yuan, A.; Wang, Z.; Chen, L.; Ouyang, Z. W. Slow Magnetic Relaxation in Two Octahedral Cobalt(II) Complexes with Positive Axial Anisotropy. *Inorganica Chim. Acta.* **2018**, *479*, 113–119.

(265) Wu, Y.; Tian, D.; Ferrando-Soria, J.; Cano, J.; Yin, L.; Ouyang, Z.; Wang, Z.; Luo, S.; Liu, X.; Pardo, E. Modulation of the Magnetic Anisotropy of Octahedral Cobalt(II) Single-Ion Magnets by Fine-Tuning the Axial Coordination Microenvironment. *Inorg. Chem. Front.* **2019**, *6*, 848–856.

(266) Cotton, F. A.; Goodgame, D. M. L.; Goodgame, M. The Electronic Structures of Tetrahedral Cobalt(II) Complexes. *J. Am. Chem. Soc.* **1961**, *83*, 4690–4699.

(267) Cotton, F. A. *Progress in Inorganic Chemistry Volume 10*; Interscience Publishers: New York, 1968.

(268) Lin, T.-P.; Ke, I.-S.; Gabbaï, F. P. Sigma-Accepting Properties of a Chlorobismuthine Ligand. *Angew. Chemie - Int. Ed.* **2012**, *51*, 4986–4988.

# Appendices

## APPENDIX A: MULTIDENTATE LIGANDS

### A.1 Introduction

Multidentate ligands are critical for the improvement of translational spin-orbit-coupling. Following the N.I.C. guidelines outlined in Chapter 1, the extent of spin-orbit-coupling that can be donated to the metal center can be increased through the number of heavy atom donors (N) as well as the degree of covalency in the complex and directly through the donor-metal bond (C). Multidentate ligands can meet both of those requirements, as the successful coordination of the ligand begets multiple donors, and the chelate effect can improve the donor strength of the ligand by an order of magnitude per additional donor atom on the chelating ligand. Thus, a large effort was undertaken to synthesize multidentate antimony ligands, and the results of those efforts are described herein.

Unfortunately, we were not able to successfully synthesize a multidentate antimony ligand that could be reliably re-synthesized. Oftentimes, progress would be made down a synthetic route, only to be halted at varying steps before the final multidentate ligand could be synthesized. This section will provide some detail on those syntheses and hopefully provide advice and caution in the pursuit of these ligands.

### A.2 Tripodal Ligands ($CH_3(CH_2SbR_2)_3$) R = Ph, Me

Two tridentate antimony ligands were synthesized using the tripodal scaffold ($CH_3(CH_2Br_2)_3$), which was synthesized from the hydroxy-terminated starting material, 1,1,1-trishydroxy(methyl)ethane. Both of these antimony ligand syntheses are very

laborious and require multiple steps that must be completed in a 12-hour window. The synthetic experimental procedures for the tris-bromo tripod as well as the $SbR_2$-tripods are given below. For the tris-bromo species, the final product was always a yellow oil, although it should be a solid per literature reports. There was likely residual acetonitrile or toluene solvent with the product, preventing the solid from precipitating. Washing the oil with pentane to remove the solvents and precipitate out the solid is recommended for increased purity.

For the $SbR_2$-tripods, it is important to start the reaction with pure starting materials. That is, solid tris-bromo compound (not oil), dried $SbR_3$ starting material (and distilled, in the case of heteroleptic ligands, namely $SbMe_2Ph$), and an understanding of liquid ammonia/sodium reactions. This last technique requires dexterity, patience, and attentiveness. The reaction must be attended to for upwards of 8-10 hours. Slow additions of sodium are recommended (washed with hexanes to remove mineral oil and cut with a razor blade to expose non-oxidized metal). The reaction must be kept at low temperature (acetone/dry ice bath, -78 °C) to avoid evaporation of ammonia. Similarly, a vent needle and purge line into an ethanol bubbler is required to avoid pressure buildups when condensing liquid ammonia (required during the condensing and evaporating steps). During the condensation of ammonia, it is important to stay attentive to the ethanol bubbler. As the flow and condensation rate is not even throughout the hour-long condensation procedure, the reverse pressure can pull unwanted ethanol into the reaction mixture, thus ruining the reaction. The main impurity of each $SbR_2$-tripod reaction is the dimer, $Sb_2R_4$ (R = Me, Ph). The phenyl dimer is soluble in cold ethanol, while the $SbPh_2$-tripod desired product is not. Thus, a thorough washing of the (air-stable) $SbPh_2$-tripod product with cold ethanol is necessary. For the $Sb_2Me_4$ dimer, the only effective purification method was

Kugelrohr distillation. Slow gentle heating with a Kugelrohr from 40 to 60 °C can eventually distill over the $Sb_2Me_4$ dimer, but there is a high probability of the product decomposing during the process as it is very sensitive to temperature. However, if the distillation is successful, the final $SbMe_2$-tripod will remain in the distillation flask, assuming it wasn't also decomposed during the distillation (it too is very sensitive to heat, vacuum, and oxygen). The final $SbMe_2$-tripod can quickly be transferred to a glovebox and extracted into $CHCl_3$ to obtain the final pure product.

### *A.2.1 Synthesis of tris-bromo, $CH_3(CH_2Br)_3$*

1,1,1-trishydroxy(methyl)ethane (5.25 g, 0.05 mol) was added to a round bottom flask. Phosphorus tribromide, $PBr_3$ (15 mL, 0.15 mol) was added to the flask on ice. The round bottom was heated (without solvent) to ~250 °C (setting 35 on a Variac heating mantle), equipped with a condenser that had a vent line to an ethanol bubbler. The reaction was heated at this temperature for 24 hours, or until a dark black tar was observed and a black solid appeared at the bottom. The black tarry solution was extracted into acetonitrile (150 mL) and refluxed with vigorous stirring for an additional 18 hours. The acetonitrile was quenched slowly with water on ice. The solution was filtered and then extracted with multiple extractions of toluene (~200 mL in total). The toluene solution was washed with sodium bicarbonate, water, and brine. The solution was dried over sodium sulfate, and the solvent was removed by Rotovap. Pentane should be added and removed in vacuo periodically until a solid precipitates from the oil. Yield: 3.5 g, 22 %. $^1$H NMR ($CDCl_3$): 1.3 ppm (s, 3H), 3.5 ppm (s, 6H).

### *A.2.2 Synthesis of $SbPh_2$-tripod, $CH_3(CH_2SbPh_2)_3$*

*Note: all reactions and solutions must be kept air-free and dry.* Liquid ammonia (75 mL) was condensed into a 200 mL Schlenk flask with a dry ice/acetone bath and a purge line to an ethanol bubbler. The triphenylantimony (1.75 g, 5 mmol) was added to the ammonia solution. Solid sodium metal (washed with hexane and cut to expose non-oxidized metal, 0.25 g, 10 mmol) was added to the solution in small pieces. This was continued until the previous blue solution turned bright orange and no more solid SbPh3 was visible. More sodium can be added beyond 2 equivalents to achieve a constant orange color. Tert-butanol (1.1 equivalent, 5 mmol) was added to the solution to neutralize NaPh ions. The tris-bromo (1,1,1-trisbromo(methyl)ethane, 0.5 g, 1.67 mmol) was added to the ammonia solution in 50 mL dry THF. The ammonia was allowed to evaporate by allowing the flask to warm to room temperature. Gaseous ammonia was vented into an ethanol bubbler with positive nitrogen pressure. The THF solution was stirred overnight. The solution was filtered air-free, and the solvent was removed in vacuo. The solution was washed with 5-10 mL of cold ethanol and then filtered (this step can be performed in air). The product was washed with cold ethanol several times to yield the desired product as an air-stable white solid. Yield: 0.55 g, 32 % (more common yields are 10-12 %). $^1$H NMR ($CDCl_3$): 1.2 ppm (s, 3H), 2.3 ppm (s, 6H), 7.1-7.4 ppm (m, 30H).

**Scheme A.1** Synthesis of $SbPh_2$-tripod, $CH_3(CH_2SbPh_2)_3$.

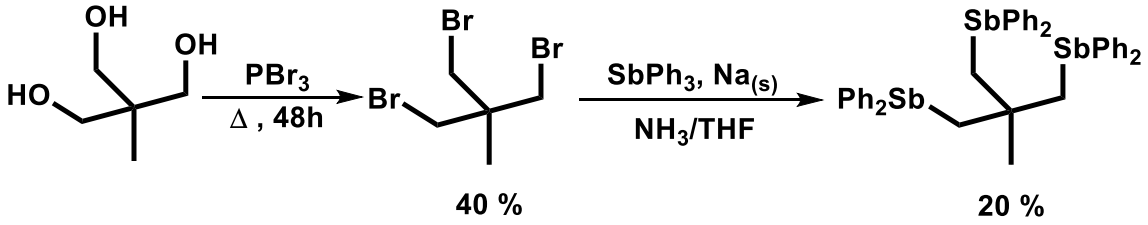

### *A.2.3 Synthesis of $SbMe_2$-tripod, $CH_3(CH_2SbMe_2)_3$*

*Note: all reactions and solutions must be kept air-free and dry.* $SbMe_2Ph$ (2.5 g, 11 mmol) was added to a 3-neck flask in 50 mL toluene. $HCl_{(g)}$ was bubbled through the toluene solution for 10 minutes, excess $HCl_{(g)}$ was removed through a vent line into an ethanol bubbler. Caution should be taken to avoid ethanol backwash into the reaction flask. The reaction was allowed to stir for 20 minutes, then vented for 30 minutes with $N_2$. This reaction forms $SbMe_2Cl$, which can be checked for purity by $^1H$ NMR ($CDCl_3$, 1.44 ppm, s). $SbMe_2Cl$ cannot be isolated and must be used soon after completion of the synthesis. Ammonia (75 mL) was condensed into a Schlenk flask in the same manner as above. Small pieces of (cut and washed) sodium metal (0.62 g, 27 mmol) were added to the flask slowly. The toluene solution holding the $SbMe_2Cl$ was added to the ammonia/Na solution, forming a dark red solution. The solution was stirred for 1 hour, ideally maintaining the dark red color. Additional (or less) sodium metal can be added to achieve red color, but not gross excess. After the red color is achieved, the dark red solution was stirred for 2 more hours. The tris-bromo solution in THF (1.2 g, 4.1 mmol) was added dropwise. The ammonia solution was allowed to evaporate by removing the solution from the dry ice/acetone bath. During the successful iteration of this reaction, the THF/toluene solution was still dark red after removal of ammonia. The solution was quenched with an aqueous solution of $NH_4Cl$ (1 equivalent). The organic layer was separated and dried with $MgSO_4$. The solution was filtered, and the solvent was removed in vacuo. The resulting oil was extracted into THF to yield a yellow solution. The solution was filtered, and the solvent was removed in vacuo to yield an auburn oil. The oil was gently distilled with a Kugelrohr that was slowly ramped from 45 → 55 → 60 °C over 45 minutes. The yellow oil remaining in the distillation flask (the oil that did not distill over) was transferred to the glovebox and extracted into $CHCl_3$.

That solution was filtered through Celite and the solvent removed in vacuo to yield a yellow oil, which was the desired product. Yield: 0.1 g, 1.3 %. $^{1}$H NMR ($CDCl_3$): 1.1 ppm (s, 3 H), 1.79 ppm (s, 6 H), 0.79 ppm (s, 18 H).

**Scheme A.2** Synthetic scheme of the synthesis for the $SbMe_2$-tripod, $CH_3(CH_2SbMe_2)_3$.

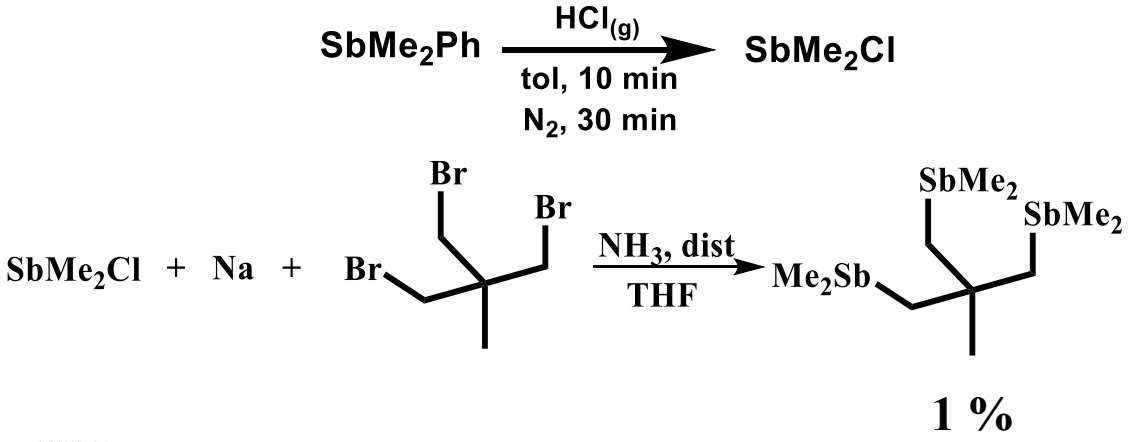


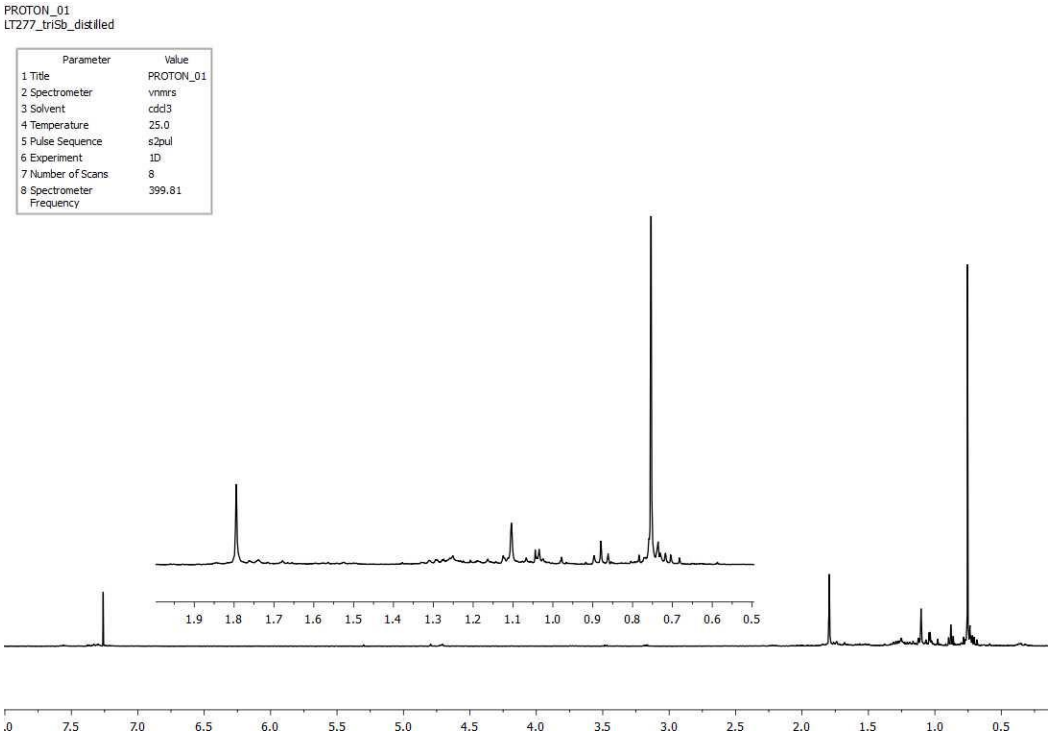


**Figure A.1** $^{1}$H NMR of the $SbMe_2$-tripod, $CH_3(CH_2SbMe_2)_3$.

To confirm the successful synthesis of the methyl-antimony-tripod, a test metalation as attempted with $Mo(CO)_3$(chpt) (chpt = cycloheptatriene). The molybdenum starting metal complex is an excellent test metalation material as the chpt ligand is very labile, allowing for a tridentate ligand to easily take the place. The reaction was performed in pentane, the metal was added to the ligand at -20 °C, and the reaction was stirred overnight. The color changed from red to colorless, and the solvent was removed in vacuo. Crystals of the resulting product were grown from a concentrated solution of pentane, which yielded a crystal structure of $Mo(CO)_3$(L) (L = $SbMe_2$-tripod). That structure is shown in Figure A.2.

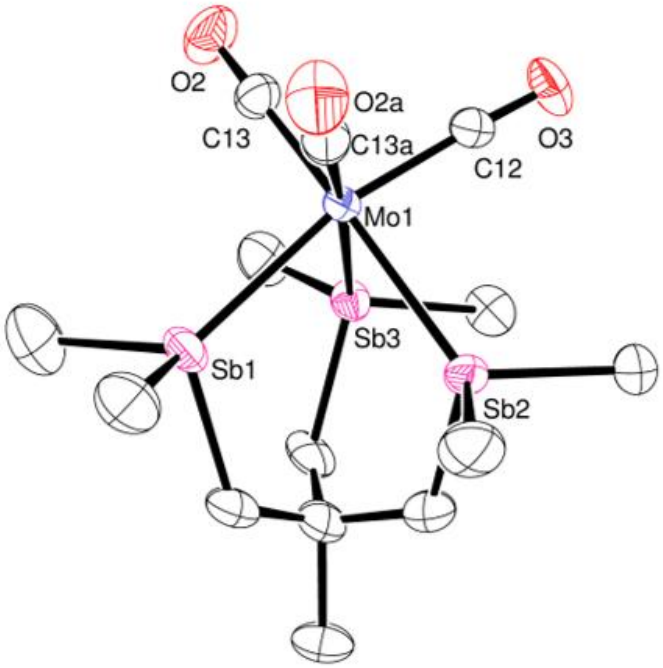


**Figure A.2** ORTEP diagram (30% ellipsoid) of the crystal structure of $Mo(CO)_3$(L) (L = $SbMe_2$-tripod).

## A.3 Towards Sb$^{i}$Pr$_2$-tripod and Simpler Reaction Conditions

From the extreme difficulty in synthesis in the $SbMe_2$-tripod and the notion that the $SbPh_2$-tripod would not coordinate with high valent 3*d* metal centers (and the likelihood of the Sb-Ph bonds to cleave during metal complexation or C-H activation catalysis), we decided to pursue other synthetic routes to generate a tripodal antimony ligand. Several iterations were performed – changing both the scaffold and antimony source – to ease the difficulty of the synthesis. Each synthetic route will be explained, along with the reasoning behind the compound or route.

### *A.3.1 Tris-iodo scaffold, $CH_3(CH_2I)_3$*

A new tripod starting material was synthesized with iodide as the leaving group, instead of bromide. The idea was to increase the electrophilicity of the α-carbon by increasing the rate of elimination of the leaving group by incorporating a weaker halide. The synthesis of an iodo-tripod was successful, but the reaction had difficulty in scaling up, and enough material could not be synthesized to continue on to the sodium/ammonia reaction.

#### *A.3.1.1 Synthesis of tris-iodo tripod, $CH_3(CH_2I)_3$*

1,1,1-trisbromo(methyl)ethane (1.05 g, 3.4 mmol) was added to a solution of sodium iodide (2 g, 13.5 mmol) in butanone and refluxed at 175 C for 2 days. The butanone solvent was removed in vacuo, and the product was extracted into toluene. The toluene solution was washed with water, sodium bisulfite, water again, and brine. The solution was then dried over sodium sulfate, and the toluene was removed in vacuo to yield the product as a beige solid. Yield: 0.45 g, 30 %. $^1$H NMR ($CDCl_3$): 1.37 ppm (s, 3H), 3.37 ppm (s, 6H).

### *A.3.2 Sb(V) compounds, Sb$^i$Pr$_2$X (X = Cl, Br), and Sb-amine compounds*

With the two successful $SbR_2$-tripod ligands detailed above, it was clear that a major issue was the generation and identity of the $SbR_2X$ starting material. For the $SbPh_2$-tripod ligand, the $SbPh_2$ antimony donor was a poor ligand towards M(II) salts, and we were worried about the weak Sb-Ph bonds cleaving during C-H activation reactions. For the $SbMe_2$-tripod ligand, the reaction to generate $SbMe_2Cl$ from $SbMe_2Ph$ and HCl gas is difficult to regulate. The time and vigor of HCl bubbling are inconsistent between reactions, which results in different concentrations and purity of the critical $SbMe_2Cl$ starting reagent. If a $SbR_2X$ starting material could be isolated and purified, perhaps the sodium/ammonia reaction could run more smoothly.

Three different routes to isolate and purify a $SbR_2X$ reagent were attempted: 1) reduction of a Sb(V) species to a useful Sb(III) one; 2) generation of a $NaSb^iPr_2$ nucleophile or $Sb^iPr_2Cl$; 3) through an $SbR_2(NMe_2)$ adduct. For the reduction of a Sb(V) species to a useful Sb(III) one, the idea was to remove R-Br via the distillation of $SbR_3Br_2$ (e.g. $^i$PrBr distills from $Sb^iPr_3Br_2$, leaving behind $Sb^iPr_2Br$). R-Br should distill over, but the distillation is tricky, as the published procedure calls for a partial vacuum (90 mm Hg) rather than the full vacuum strength (0.1 mm Hg) that our vacuum pumps generate. As such, we were never able to separate R-Br from $SbR_2Br$. An additional problem likely arises from R-group scrambling in the high heat and high vacuum environment of the distillation. A third problem that exists is the sublimation of the non-reduced Sb(V) species before reduction if the vacuum pressure is too low. Consequently, this reaction will be difficult to master.

Synthesis of $Sb^iPr_2Br$ from $Sb^iPr_3Br_2$: $Sb^iPr_3Br_2$ was generated by the addition of liquid bromine to $Sb^iPr_3$ in pentane. The desired product immediately crashes out of

pentane and can be washed with additional aliquots of pentane to remove starting material impurities. The white crystalline product is air-stable. ($^1$H NMR ($CDCl_3$): 3.45 (hept, 1H), 1.62 (d, 6H)). For the distillation, Sb$^i$Pr$_3$Br$_2$ was heated to 160 °C without vacuum in a short path distillation vessel. The heating was continued for 2 hours. The residue in the distillation flask can be distilled at 0.01 mm Hg and 27 °C. The product (Sb$^i$Pr$_2$Br) should distill over, but no product was ever obtained.

The next route involves generation of a NaSb$^i$Pr$_2$ nucleophile from Sb$^i$Pr$_3$ or Sb$^i$Pr$_2$Cl, which was synthetically derived from Sb$^i$Pr$_2$Ph and $HCl_{(g)}$. The idea was that a Sb$^i$Pr$_2$-tripod would be a very strong ligand and improve covalency in the final metallated complex. However, the reaction of Sb$^i$Pr$_2$Ph with HCl did not yield Sb$^i$Pr$_2$Cl, but rather gave a mix of starting material, Sb$^i$Pr$_3$Cl$_2$, and Sb$^i$Pr$_2$Cl$_2$Ph. The HCl did not cleave the Sb-Ph bond, but rather oxidized the starting material to an Sb(V) species. The difference between this reaction and the reaction of SbMe$_2$Ph with $HCl_{(g)}$ is likely due to the difference in electron density on the antimony center between the two starting materials. The isopropyl substituent is significantly more electron-donating than the methyl substituent. Consequently, the Sb-Ph bond in the methyl case was more labile, while the Sb center in the Sb$^i$Pr$_2$Ph case is a stronger Lewis acid. As seen in Chapter 2, the antimony ligand with the strongest Tolman electronic parameter was more likely to abstract $I^-$ from solution. The same phenomenon appears to occur in this case, as the ligand with a stronger TEP (Sb$^i$Pr$_2$Ph) would oxidize in the presence of $Cl^-$, while SbMe$_2$Ph (weaker TEP) would react appropriately with $HCl_{(g)}$. For synthetic details, the reaction was performed the same way as SbMe$_2$Ph + $HCl_{(g)}$ reaction, detailed above.

On the Sb$^i$Pr$_3$ + sodium metal reaction, no reaction appeared to occur. The solution did not change to a dark red color, which is the qualitative marker to denote the successful

removal of the carbon substituent and the generation of the nucleophile, $NaSbR_2$. From this result and the fact that the only two successful sodium reaction involved $SbR_2Ph$ ($SbPh_3$ and $SbMe_2Cl$) in this work, it appears the sodium cleavage is only possible when a weak Sb-R bond can be broken. As the Sb-$^i$Pr bond is quite strong, it was not susceptible to cleavage by sodium metal. For synthetic details, the reaction of $Sb^iPr_3$ + Na was performed in the same manner as $SbMe_2Cl$ + Na but was not successful as no red color appeared even after excess addition of sodium metal.

The last route in this series was the generation of antimony-amine compounds. The expectation for this reaction was that the antimony-amine bond would be quite weak and easy to break, leaving behind a $SbR_2$ nucleophile. The first step in the synthetic scheme was to generate $SbCl_2(NMe_2)$ from the reaction of trimethylsilyl-dimethylamine ($Si(Me)_3(NMe_2)$) and $SbCl_3$. This reaction was successful. To synthesize $SbCl_2(NMe_2)$, a solution of ($Si(Me)_3(NMe_2)$) in DCM (1.4 g, 12 mmol in 10 mL DCM) was cooled to Argon freezing point inside the argon glovebox. To that cold solution, a solution of $SbCl_3$ in DCM (2.7 g, 12 mmol in 10 mL DCM) was added dropwise. The resulting solution was warmed to room temperature and stirred for 3 hours. The solvent was decanted, and the colorless crystalline solid was washed with several aliquots of DCM. The product was dried under vacuum to yield the product as a white crystalline solid. ($^1$H NMR ($C_6D_6$): 2.25 ppm (s)) Yield: 2.1 g, 74 %.

The next step in this synthetic scheme was to replace the chlorine sites with carbon substituents via Grignard chemistry. Two separate attempts were made: 1) with isopropyl Grignard (to synthesize $Sb^iPr_2(NMe_2)$) and 2) with a di-Grignard reagent that was generated from the starting material, 1,2-dibromoxylene. The issue in both of these synthetic schemes was this final step, a water wash. Water washes are critical for other Sb-

Grignard reactions as the water quenches unreacted Grignard reagent and dissolves incompletely reacted $SbR_yX_{3-y}$. Because the Sb-amine bond is susceptible to cleavage from water, a water wash could not be performed for either of these reactions. For the di-Grignard reaction, the successful generation of the Grignard reagent must also be questioned, as a one pot-synthesis to put two Grignard sites on one molecule is difficult. Additionally, the di-Grignard reaction appeared to polymerize the THF solvent used. Regardless, this scheme was never successful, and the final reaction to cleave the Sb-amine bond was not attempted. If this intermediate step to replace the chlorines with carbon groups can be achieved, this Sb-amine starting material could be a viable alternative to $SbR_2Cl$ as the antimony nucleophile in these reduction reactions.

Attempted Synthesis of $Sb^iPr_2(NMe_2)$. A Grignard solution of isopropylmagnesiumchloride Grignard was generated in the same manner as detailed in chapter 2 (0.1 g Mg, 0.2 g 2-chloropropane, 10 mL $Et_2O$). Dichlorodimethylaminestibine (0.25 g, 1.1 mmol) in 15 mL THF (Dichlorodimethylaminestibine was insoluble in $Et_2O$) was added to the Grignard solution on ice. A white precipitate was formed on antimony addition. The solution was stirred for 3 hours, and 20 mL DME was added to the flask to help precipitate magnesium salts. The solvent was removed in vacuo to yield a yellow oil. Yield: 0.02 g. $^1H$ NMR in $C_6D_6$ shows only one large peak at 0.2 ppm.

Attempted Synthesis of Sb(*o*-xylene)($NMe_2$). The Grignard reagent was prepared in the same way as the above reaction, but with four equivalents of magnesium turnings (0.7 g, 30 mmol) to 1 equivalent of dichloroxylene (1.3 g, 7.5 mmol). The Grignard turned a dark green color. The dichlorodimethylaminestibine was added to the Grignard solution at -78 °C, but no precipitate was initially observed, and the dark green color remained. After 1.5 days of stirring, still no precipitate was observed. The solution was refluxed for

3 hours, and at that point the color turned to pale yellow and some white precipitate had formed. A portion (50 mL) of the reaction mixture was removed from the main flask and the solvent was removed in vacuo. A large sticky off-white solid was collected. Yield: 0.82 g. From the $^{1}$H NMR spectrum, it looks like THF was polymerized and that was the sticky white solid collected. No signal for the desired product could be seen in the spectrum. The heating of the solution is likely what catalyzed the polymerization reaction.

**A.4 Tetrapod synthesis**

One of the main issues with all of the above reactions, especially the successful $SbR_2$-tripod syntheses, is the use of the antimony reagent as a nucleophile. In those tripod syntheses, an anionic $[SbR_2]^-$ species is generated, which attacks the halide position on the tripodal scaffold. It has been reported by Levason and Reid that in reactions where antimony is used as the electrophile in the synthesis, yields are 4 x greater than when antimony is used as the nucleophile (80 % vs. 20 %).[38,46] As our yields for the successful $SbMe_2$-tripod were so poor (1 %), we designed a ligand synthesis that would utilize antimony as the electrophile, rather than the nucleophile.

The ligand we designed is a tetrapodal ligand, 1,1,1-trisstibinomethyl(*o*-benzyl)stibine ($Sb(CH_2\text{-}2\text{-}C_6H_4SbMe_2)_3$). This ligand is very similar to Reid's hybrid tristibine ligand, $N(CH_2\text{-}2\text{-}C_6H_4SbMe_2)_3$, published in 2013.[36] The main difference in Reid's ligand is the use of a nitrogen anchor. In this project, we are synthesizing antimony ligands to observe the effect of translational SOC from the antimony donors onto paramagnetic metal centers. If other non-antimony donor atoms exist in the ligand (i.e. N), the amount of SOC donated to the metal center from Sb could be ambiguous. Thus, we attempted to synthesize an analogous ligand to Reid's, but we would swap the nitrogen

anchor with another antimony atom. This all-antimony synthetic variation has the added bonus of one additional antimony donor to coordinate to a metal center (improving the *N* parameter in the NIC guidelines). A ChemDraw image of both antimony- and nitrogen-anchored ligands are shown in Figure A.2.

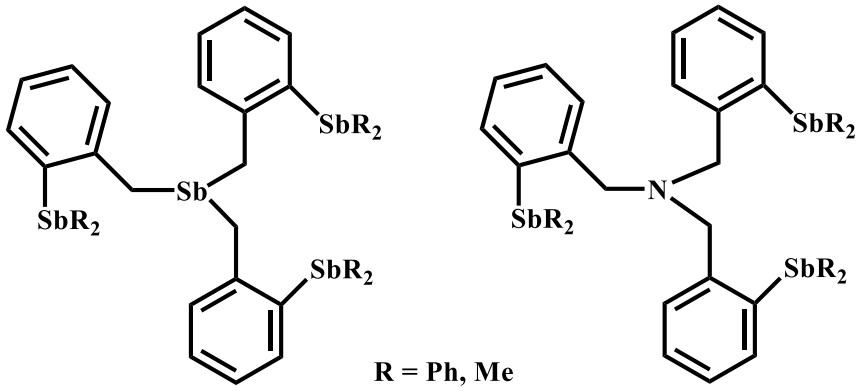


**Figure A.3** Antimony-anchored (left) and nitrogen-anchored (right) variations of a tetrapodal multidentate antimony ligand.

To use antimony as an electrophile, a core scaffold must first be synthesized that has cleverly-positioned nucleophilic sites. The core scaffold for this ligand is a homoleptic antimony compound, $Sb(CH_2\text{-}2\text{-}C_6H_4Br)$. The bromine positions *ortho* to the benzyl arm provide a prime site for lithiation. Once those sites are lithiated, addition of electrophilic $SbR_2Cl$ (R = Ph, Me) should attach an antimony donor atom at each site, providing a multidentate antimony ligand. For this synthesis, the scaffold was a simple reaction. A Grignard reagent was generated from 1-bromo-2-benzylbromide, which formed the Grignard at the benzyl-bromide position. A general rule is Grignard reagents form much easier at an alkyl position than an aryl position. The synthesized Grignard reagent was added to an ethereal solution of $SbCl_3$, which displaced all three chloride positions on the Sb atom. The reaction was very similar to make any other homoleptic antimony ligand previously discussed in Chapters 2-4.

The next step of the process was much more difficult and where the synthesis failed. At the 2-bromo position on the aryl ring, the ligand should be lithiated with n-butyllithium, then reacted with $SbR_2Cl$. However, we never achieved confirmation that the lithiation step was working. Test reactions with methyl-iodide or water as the substrate never resulted in either H-terminated or methyl-terminated ligand. What we believe happened was the harsh $^{n}$BuLi reagent cleaved the weak Sb-$CH_2$ bond, or it lithiated the benzyl arm position instead of the aryl-bromo position. To amend this error, the reaction should be performed at -78 °C and kept at that temperature for the entire reaction. The $^{n}$BuLi reaction should not be left to react for more than 1 hour, and an exact amount of $^{n}$BuLi should be used – the concentration should be exact or in a small excess (1.1 equivalents). As this reaction was performed early in my graduate career, I believe a careful and deliberate synthetic chemist could successfully perform this reaction. The synthetic scheme for the homoleptic antimony ligand and the attempted lithiation of that material is shown in Scheme A.3.

**Scheme A.3** Synthesis of $Sb(CH_2\text{-}2\text{-}C_6H_4Br)_3$ and the attempted lithiation towards a tetrapodal multidentate antimony ligand.

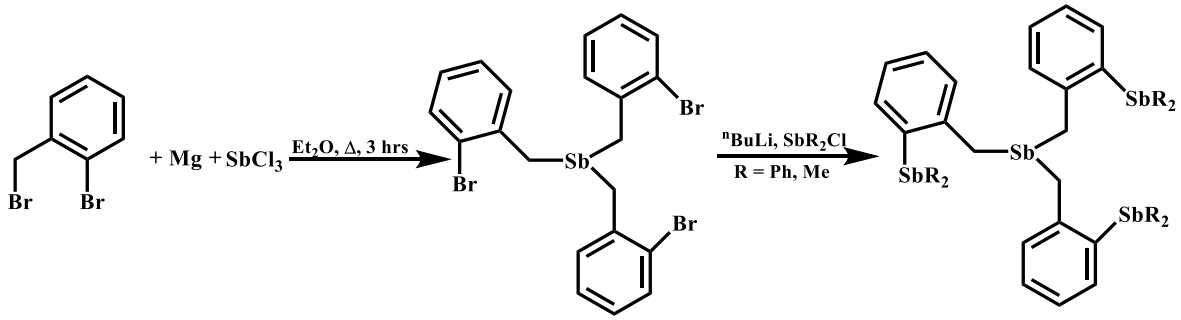


Another route to the tetrapod ligand could be to perform the steps out of order. If the 1-bromo-2-benzylbromide starting material was first lithiated (ideally at the aryl-bromide site), then reacted with $SbR_2Cl$, the final product would be 1-diphenylstibino-2-benzylbromide (in the case of $SbPh_2Cl$). A Grignard reagent of this ligand could be

generated with magnesium turnings in the same manner described in Chapters 2 and 3. That Grignard reagent can react with $SbCl_3$ yielding the final product. This synthesis would avoid exposing weak Sb-C bonds to harsh lithiating reagents and would still utilize antimony as an electrophile. In the quest for a multidentate antimony ligand, electrophilic antimony reactions must be at the forefront, even if moderate success was achieved with nucleophilic antimony reactions. The alternative proposed scheme for the synthesis of $Sb(CH_2\text{-}2\text{-}C_6H_4R_2)_3$ is shown in Scheme A.4.

**Scheme A.4** Proposed scheme for the synthesis of $Sb(CH_2\text{-}2\text{-}C_6H_4SbR_2)_3$ (R = Me, Ph).

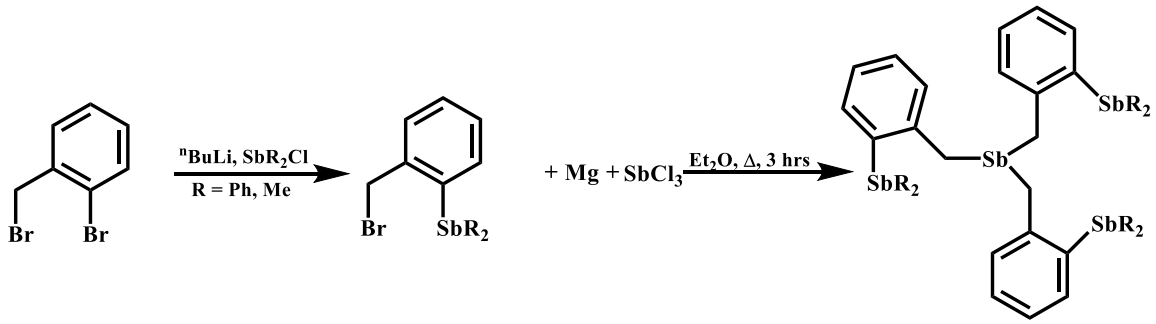


### *A.4.1 Synthesis of $Sb(CH_2\text{-}2\text{-}C_6H_4Br)_3$.*

Magnesium turnings (0.58 g, 24 mmol) were activated with elemental iodine crystals (0.05 g) and heated with a heat gun for 30 minutes to clean the magnesium surface. Diethyl ether (30 mL) was added to the flask, along with 2 drops of 1,2-dibromoethane to activate the magnesium turnings. Ortho-bromobenzylbromide (3 g, 12 mmol) was dissolved in 20 mL of $Et_2O$ and half the solution was added to the magnesium turnings on ice. The *ortho*-bromobenzylbromide solution was diluted with 20 additional mL of $Et_2O$, then the rest of the solution was added dropwise to the magnesium solution on ice. The Grignard solution was refluxed for twenty minutes, then cooled to room temperature. The solution was carefully added to an ethereal solution of $SbCl_3$ (0.9 g, 4 mmol, 10 mL Et2O).

This solution was refluxed for 3 hours, then cooled to room temperature. The solution was quenched with degassed water, then the organic layer was separated and dried with sodium sulfate. The solution was filtered, and the solvent was removed in vacuo to yield the product as a yellow oil. Yield: 0.5 g, 28 %. $^{1}$H NMR ($CDCl_3$): 3.01 ppm (s, 6H), 7.50 ppm (d, 3H), 7.15 ppm (t, 3H), 6.97 (m, 6H).

### *A.4.2 Attempted lithiation of $Sb(CH_2\text{-}2\text{-}C_6H_4Br)_3$.*

$Sb(CH_2\text{-}2\text{-}C_6H_4Br)$ (0.25 g, 0.4 mmol) was dissolved in $Et_2O$ (20 mL) and cooled to -78 °C. $^{n}$BuLi (0.75 mL, 1.6 M in hexane, 1.2 mmol) was added dropwise to the antimony ligand at -78 °C. The solution was stirred for 20 minutes and turned a pink color. The solution was quenched with degassed water slowly, then the organic layer was separated and dried over sodium sulfate. The solution was filtered and then the solvent was removed in vacuo to yield an off-white solid. Proton NMR showed unreacted starting material ($Sb(CH_2\text{-}2\text{-}C_6H_4Br)_3$) as well as several messy peaks around 1 ppm (mix of solvent and butyl groups likely). However, one new singlet appears at 2.40 ppm, as well as new peaks appear in the benzyl region. For reference, the $Sb(benzyl)_3$ singlet appears at 2.78 ppm.

## APPENDIX B: IRON AND MANGANESE METALLATIONS WITH ANTIMONY LIGANDS

### B.1 Introduction

After our initial success of metallating antimony ligands with nickel and copper salts, we wanted to investigate iron and manganese as sources for paramagnetic compounds as well. Mn(II) could form $d^5$ paramagnetic complexes, and the Rose lab has vested interest in Fe chemistry. Any structural or synthetic information that could be gleaned from iron's reactivity towards monodentate antimony ligands could be pertinent to this and other projects in the group. This work was brief as both metal salts posed difficult synthetic problems. The reaction of manganese diiodide with antimony ligands did not produce a coordinated antimony ligand to manganese. In contrast, redox chemistry appeared to happen between the two reagents, resulting in substituent and halide shuffling. In the case of iron, the reaction of $FeI_2$ with $Sb^iPr_3$ did produce crystals, but the structure was unsolvable. The crystals were also very reactive towards oxygen and decomposed almost instantly during the crystal mounting process. Switching to the more user-friendly starting salt $Fe(CO)_4(I)_2$ once again resulted in crystals suitable for x-ray crystallography. The crystal structures did show successful coordination of antimony to iron, but the low-spin octahedral Fe(II) complex was not paramagnetic and of no interest to us to study its magnetic properties. Brief paragraphs detailing the syntheses, crystal structures, and outlooks for the reactions of monodentate antimony ligands with Fe and Mn are given herein.

### B.2 Iron Antimony Reactions and Complexes

The reaction of $FeI_2$ and $Sb^iPr_3$ was successful in either fluorobenzene or diethyl ether. The metal (0.15 g, 0.5 mmol) was added to the $Sb^iPr_3$ ligand (0.25 g, 1.0 mmol) at -

20 °C, then allowed to warm to room temperature and stirred overnight. The yellow solution was filtered through Celite and the solvent was removed in vacuo. The resulting yellow oil was re-dissolved in pentane, filtered through Celite, and then placed in a freezer at -20 °C. Crystals suitable for x-ray diffraction were grown from the concentrated pentane solution after a few days. These crystals were yellow and looked good under a microscope (no cracking). However, they were very air sensitive, and we were never able to obtain a full structure. From the crystal data, it appeared the structure could be two different complexes. One is the simple tetrahedral complex, $Fe(I)_2(Sb^iPr_3)_2$. The other crystal structure option was two charged complexes with an overall neutral charge: $[FeI_4][Fe(Sb^iPr_3)_4]$. This complex may be the more likely result, given the air-sensitivity and difficulty in solving the structure. There is some precedence for this compound too, as a similar structure with diphenylphosphinomethane exists in the CCDC: $[FeI_4][Fe(dppm)_2(MeCN)_2]$. Two acetonitrile solvent molecules helped fill the coordination sphere of the positively charged iron ion, which may be a solution to solving the antimony-based complex. However, given antimony's poor σ-donor capabilities, the MeCN solvent may outcompete antimony and dissociate it from the iron center. The synthesis and ball-and-stick diagram of the unsolved crystal structure can be seen in Figure B.1.

Metallations with $FeI_2$ and our other monodentate antimony ligands were attempted, but no crystal structures were ever obtained from those reactions. The reaction of $FeI_2$ with two equivalents of $SbMe_2Ph$ yielded a purple powder and a yellow solution. The yellow solution was processed, and crystals were grown from a DCM/pentane vapor diffusion. Although a structure was never obtained, preliminary results suggested the charged crystal was $[SbMe_3Ph][I]$. From this result, the purple powder may have been iron

powder (or something similar). From this result and the result with $Sb^iPr_3$, it appears iron will readily perform redox chemistry with antimony ligands as well as facilitate ligand and halide exchange.

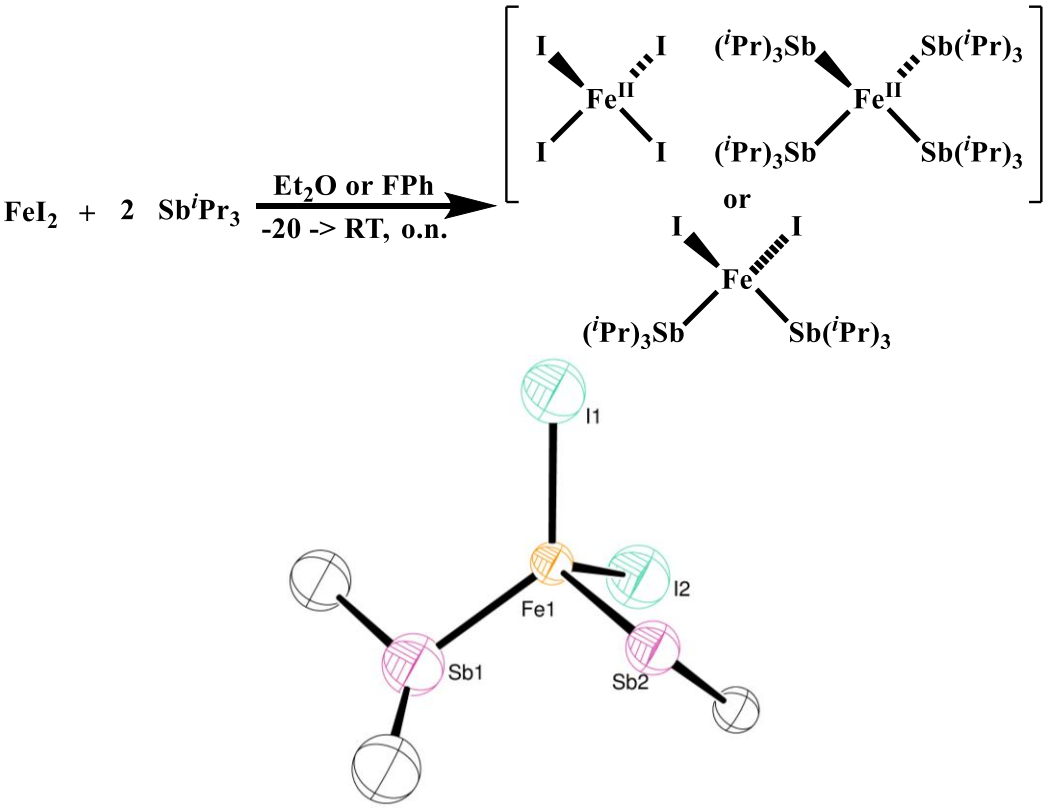


**Figure B.1:** Synthesis and ball-and-stick model of the resulting (truncated) crystal structure from the reaction between $FeI_2$ and $Sb^iPr_3$.

In order to successfully coordinate an antimony ligand onto an iron center, we turned to another iron source: $Fe(CO)_4(I)_2$. The reactions of $Fe(CO)_4(I)_2$ with both $Sb^iPr_3$ and $SbMe_2Ph$ were performed in fluorobenzene. The metal was added to the ligand at -20 °C, then allowed to warm to room temperature and stirred overnight. The red-brown solutions were filtered through Celite and the solvent was removed in vacuo. Both reactions afforded a red-brown oil, which was re-dissolved in pentane, filtered through Celite, and

placed in a freezer at -20 °C. Crystals from each reaction were collected from these concentrated pentane solutions. The crystal structures show that two antimony ligands coordinated to the iron center in each reaction, and that the iron center adopted an octahedral geometry. However, there was difficulty resolving the exact number of iodide and carbonyl ligands completing the octahedral coordination sphere. The IR of the Fe-CO-$Sb^iPr_3$ crystal shows 3 CO peaks, but the crystal structure only showed 2 CO atoms ligated. Regardless, these complexes are low-spin octahedral $d^6$ complexes and are not paramagnetic. We decided not to pursue these reactions or reactions with other Sb ligands and $Fe(CO)_4(I)_2$ further as we were interested in paramagnetic metal complexes. However, these crystal structures demonstrate that antimony will coordinate to iron without redox chemistry.

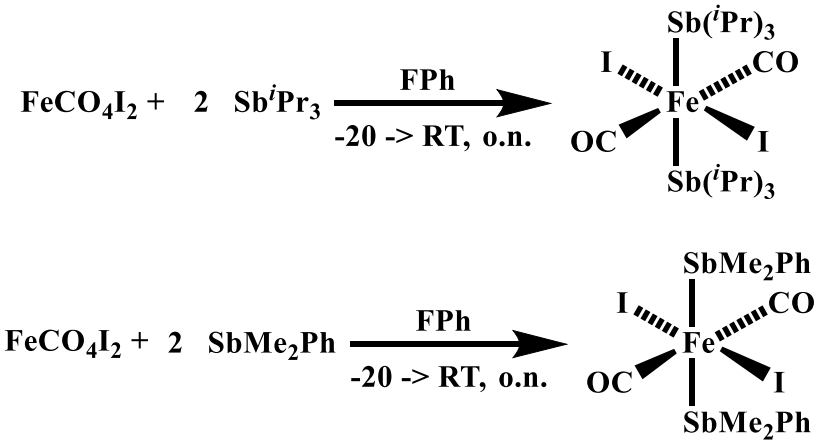

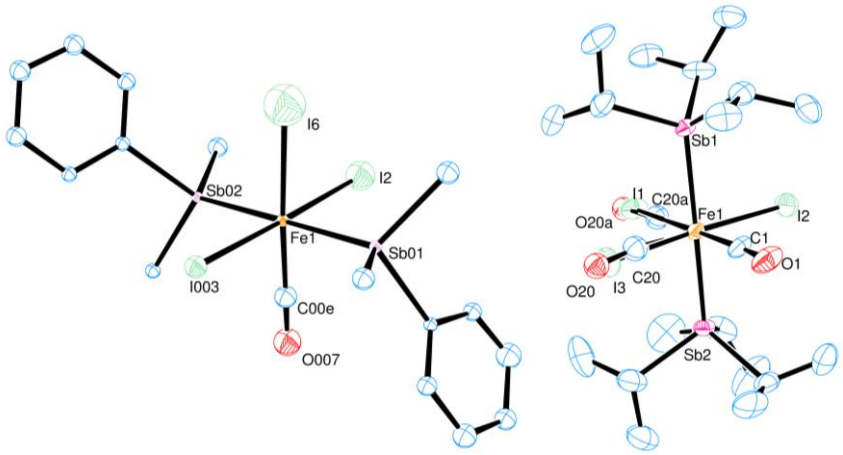


**Figure B.2:** Syntheses and crystal structures from the reactions between $Fe(CO)_4(I)_2$ and $Sb^iPr_3$/$SbMe_2Ph$.

### B.3 Manganese Antimony Reactions and Complexes

Reactions of $MnI_2$ and antimony ligands exclusively performed redox chemistry and R-group exchange between the metals and ligands. The crystal structures were not difficult to acquire but provided no doubt that antimony would not stably coordinate to $MnI_2$. For the reaction of $MnI_2$ and $Sb^iPr_3$, manganese(II) iodide was added to a solution of $Sb^iPr_3$ (0.25 g, 1 mmol) in FPh at -20 °C. The reaction was allowed to warm up to room temperature and then stirred overnight. The beige solution was filtered through Celite and the solvent was removed in vacuo. The colorless crystalline material was re-dissolved in pentane and placed in a freezer at -20 °C. Colorless crystals suitable for x-ray crystallography grew after a few days. The structure was confirmed to be $Sb^iPr_3I_2$. The antimony removed the iodide ions from the manganese center, similar to the nickel deposition reactions. The crystal structure of the result of the reaction between $MnI_2$ and $Sb^iPr_3$ can be seen in Figure B.3.

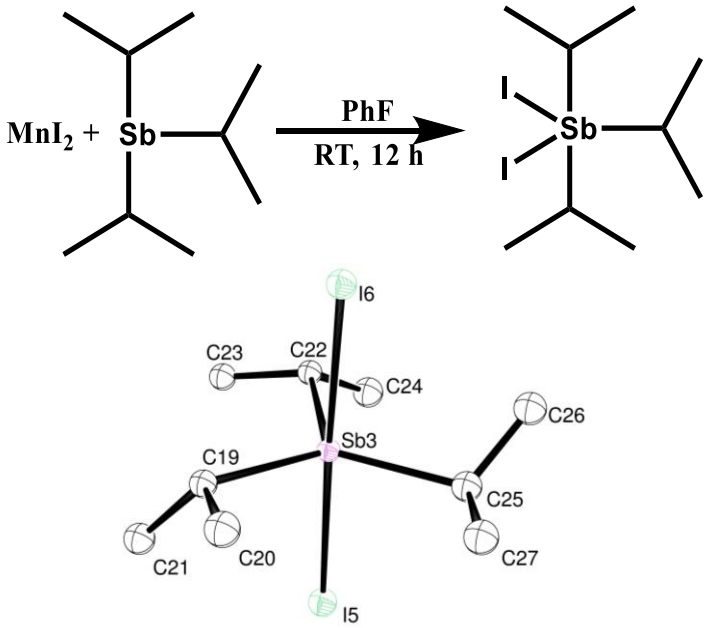


**Figure B.3:** Synthetic scheme and ORTEP diagram (30% ellipsoids) of the crystal structure of $Sb^{i}Pr_3I_2$, the result of the reaction between $MnI_2$ and $Sb^{i}Pr_3$.

A similar result was obtained from the reaction of $MnI_2$ and $SbMe_2Ph$. For synthetic details, the metal was added to the ligand cold at -20 °C in $Et_2O$ (1:2 metal to ligand ratio, 0.5 g scale). White crystalline solid was obtained after filtering and solvent removal. The solid was only partially soluble in pentane, and from the pentane solution crystals suitable for x-ray crystallography were obtained and a crystal structure was solved. The structure obtained from that reaction was another charged complex: $[MnI_4][SbMe_3Ph]_2$. Upon closer inspection, this result is very similar to the result obtained from the reaction of $FeI_2$ and $SbMe_2Ph$, but with an additional $SbMe_3Ph^+$ molecule and a $MnI_4$ counterion. As this structure was obtained from only the partial dissolution of the white solid in pentane, perhaps another complex was formed during the reaction, but only this compound was crystallized and characterized. Regardless, this compound was also not useful, as although there exists a paramagnetic metal center and antimony atoms, the antimony is not

covalently bound to the paramagnetic center and we cannot probe the translational SOC from the Sb to the Mn in this complex. After acquiring both these results from manganese reactions, we halted further investigations into Mn-Sb complexes.

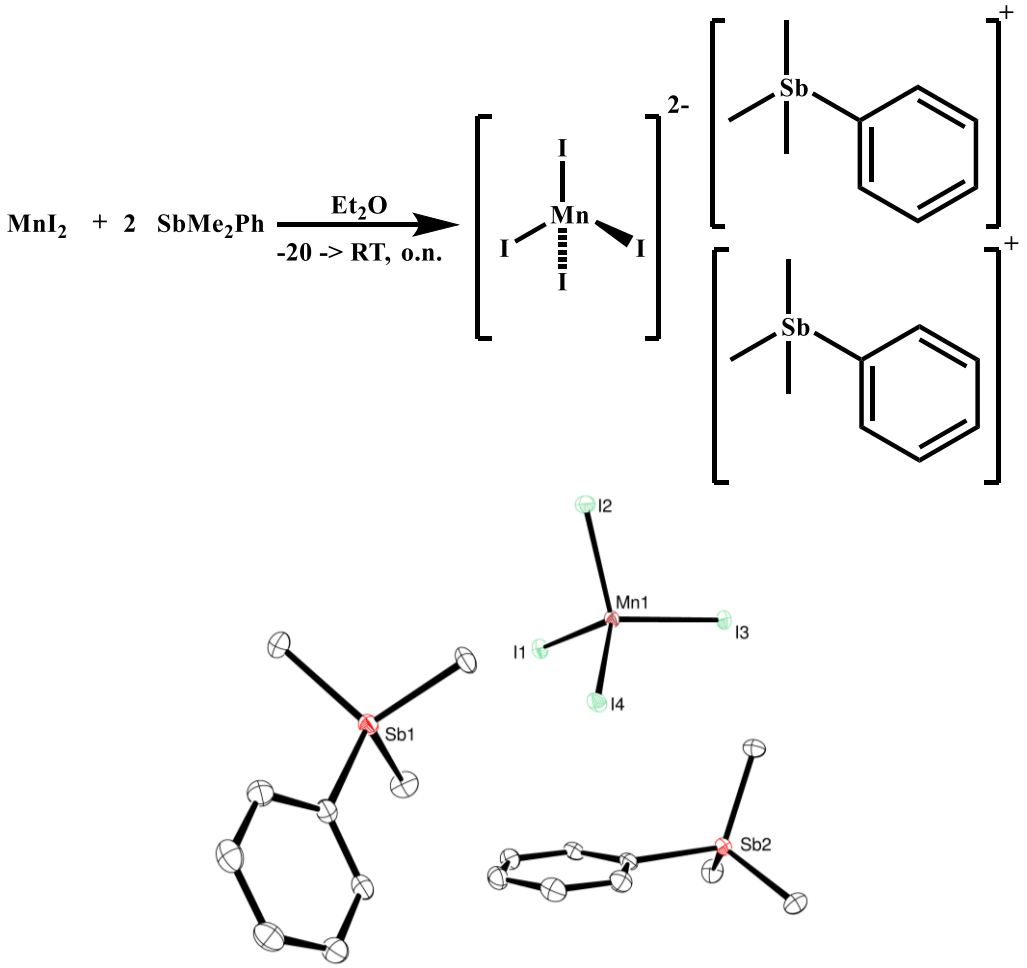


**Figure B.4:** Synthetic scheme and ORTEP diagram (30% ellipsoids) of the charged complex $[MnI_4][SbMe_3Ph]_2$, which was obtained from the reaction of $MnI_2$ and $SbMe_2Ph$.

In conclusion, both the manganese and iron iodide metal salts did not perform the same coordination chemistry as the cobalt, nickel, and copper analogous complexes. The product from the reaction of $FeI_2$ and $Sb^iPr_3$ was ambiguous, and it was unclear if the

antimony ligand successfully coordinated to the iron center or if a redox reaction occurred. Future reactions and crystallizations with other antimony ligands (both larger and smaller) and $FeI_2$ could yield more concrete results. It was clear, however, that reactions with monodentate antimony ligands and $MnI_2$ exclusively performed redox chemistry and R-group exchanges that resulted in difficult-to-crystallographically-solve complexes that were of little practical use. Although these results are not promising for the future of antimony-Mn/Fe complexes synthesized in this lab, we do have a large library of antimony ligands that were synthesized in this work, and we were able to show that antimony ligands will coordinate to Fe(II). Attempting $FeI_2$ metalation reactions with those other ligands, especially the ligands with larger steric bulk and σ-donating ability, could provide paramagnetic complexes that are worth further investigation on SOC effects in Sb-M[3*d*] systems.

## References


(1) Weeks, M. E.; Leicester, H. M. Antimony. In *Discovery of the Elements*; Journal of Chemical Education: Easton, PA, 1968; pp 95–103.

(2) Cheyne, T. K.; Black, J. S. Kerenhappuch. *Encyclopaedia Biblica*; Macmillan Co., 1902; p 2659.

(3) Jagnaux, R. *Histoire de La Chimie*, 2nd ed.; Baudry et Cie: Paris, 1891.

(4) Bostock, J.; Riley, H. T. *The Natural History of Pliny*; Geo. Bell and Sons: London, 1856.

(5) Krebs, R. E. *The History and Use of Our Earth's Chemical Elements*; Greenwood Press: Westport, CT, 1998.

(6) Dufrenoy, M. L.; Dufrenoy, J. The Significance of Antimony in The History of Chemistry. *J. Chem. Educ.* **1950**, *27*, 595–597.

(7) Berthelot, M. Sur Quelques Alliages Connus Au Moyen-Age. *Ann. Chem. Phys.* **1893**, *30*, 286.

(8) Winderlich, R. History of the Chemical Sign Language. *J. Chem. Educ.* **1953**, *30*, 58–62.

(9) Holmyard, E. J. *Alchemy*; Courier Corportation: Chelmsford, MA, 1990.

(10) Agricola, G. *De Re Metallica*; Hoover, H. C., Hoover, L. H., Eds.; Dover Publications: New York, 1950.

(11) Valentine, B.; Tholde, J. *Triumphal Chariot of Antimony*; Kirkringus, T., 1678.

(12) Lemery, N. *Traite de l'antimonie*; Paris, 1707.

(13) de Fontanelle, B. L. B. Eloge de M. Nicolas Lemery. In *Historie de l'Academie Royale des Sciences de Paris*; Paris, 1715; pp 73–81.

(14) Cap, P.-A. *Nicolas Lemery, Chimiste*; Imprimerie et Fonderie de Fain: Paris, 1839.

(15) Butterman, W. C.; Carlin, J. F. *Antimony Commodity Profile*, *U.S. Geological Survey*; 2004.

(16) Carapella, S. .; Hampel, C. Antimony. *The Encyclopedia of the Chemical Elements*; Reinhold Book Corporation, 1968; pp 22–25.

(17) Partheil, A.; Mannheim, E. Mercury Antimonide and Stibonium Compounds. *Arch. Pharm. (Weinheim).* **1900**, *238*, 166–184.

(18) Wieber, M. *Sb Organoantimony Compounds*; Mirbach, M., Ed.; Springer Science and Business Media: Berlin, Germany.

(19) Gruttner, G.; Wiernik, M. Organic Antimony Compounds. II. Preparation of Mixed Alkylarylstibines. *Berichte der Dtsch. Chem. Gesselschaft* **1915**, *48*, 1759–1764.

(20) Breunig, H. J.; Rösler, R. Organoantimony Compounds with Element—element Bonds. *Coord. Chem. Rev.* **1997**, *163*, 33–53.

(21) Breunig, H. J.; Rösler, R. New Developments in the Chemistry of Organoantimony and -Bismuth Rings. *Chem. Soc. Rev.* **2000**, *29*, 403–410.

(22) Dunn, T. M. Spin-Orbit-Coupling in the First and Second Transition Series. *Trans. Faraday Soc.* **1961**, *48*, 1441–1444.

(23) Koziar, J. C.; Cowan, D. O. Photochemical Heavy-Atom Effects. *Acc. Chem. Res.* **1978**, *11*, 334–341.

(24) *IUPAC. Comendium of Chemical Technology, 2nd Ed. (the "Gold Book").*; McNaught, A. D., Wilkinson, A., Eds.; Blackwell Scientific Publications: Oxford, 1997.

(25) Jones, J. S.; Wade, C. R.; Gabbaï, F. P. Guilty on Two Counts: Stepwise Coordination of Two Fluoride Anions to the Antimony Atom of a Noninnocent Stibine Ligand. *Organometallics* **2015**, *34*, 2647–2654.

(26) Dittes, U.; Vogel, E.; Keppler, B. K. Overview on Bismuth(III) and Bismuth(V) Complexes with Activity against Helicobacter Pylori. *Coord. Chem. Rev.* **1997**, *163*, 345–364.

(27) Wilkinson, G.; Stephenson, T. A.; Hallman, P. S. Tetrakis(Triphenylphosphine)Dichlororuthenium(II) and Tris(Triphenylphosphine)Dichlororuthenium(II). In *Inorganic Syntheses*; McGraw-Hill: New York, NY, 1970; pp 237–240.

(28) Champness, N. R.; Levason, W. Coordination Chemistry of Stibine and Bismuthine Ligands. *Coord. Chem. Rev.* **1994**, *133*, 115–217.

(29) Schwab, P.; Mahr, N.; Wolf, J.; Werner, H. Trialkylstibanes as Bridging Ligands: Synthesis and Structure of the Dinuclear Complexes $[Rh_2Cl_2(\mu\text{-}Sb^iPr_3)(\mu\text{-}CR_2)_2]$. *Angew. Chemie Int. Ed. English* **1994**, *33*, 97–99.

(30) Martin, L. R.; Einstein, F. W. B.; Pomeroy, R. K. Axial-Equatorial Isomerism in the Complexes $M(CO)_4(L)$ (M = Fe, Ru, Os; L = Group 15 Ligand). Crystal Structures of Ax-$Ru(CO)_4(AsPh_3)$, Ax-$Ru(CO)_4(SbMe_3)$, and Eq-$Os(CO)_4(SbPh_3)$. *Inorg. Chem.* **1985**, *24*, 2777–2785.

(31) Breunig, H. J.; Kanig, W. Preparation and Spectroscopic Studies of Methyl and Isopropyl Halides. *Phosphorus Sulfur Relat. Elem.* **1982**, *12*, 149–159.

(32) Wieber, M.; Wirth, D.; Fetzer, I. New Synthesis Methods for Organohalostibines. *Z. Anorg. Allg. Chem.* **1983**, *505*, 134–137.

(33) Wieber, M.; Gmelin, L. *Organoantimony Compounds Pt 1*, 8th ed.; Springer-Verlag: New York, 1981.

(34) Balzs, G.; Balzs, L.; Breunig, H. J.; Lork, E. Syntheses and Structures of $Me_3Sb^+CH_2COO^- \cdot H_2O$, the Monohydrate of the Antimony Analogue of Betaine, and Related Compounds. *Appl. Organomet. Chem.* **2002**, *16*, 155–159.

(35) Jura, M.; Levason, W.; Reid, G.; Webster, M. Preparation and Properties of Cyclic and Open-Chain Sb/N-Donor Ligands. *J. Chem. Soc. Dalt. Trans.* **2009**, No. 37, 7811–7819.

(36) Benjamin, S. L.; Levason, W.; Reid, G. Synthesis and Reactions of a Hybrid Tristibine Ligand. *Organometallics* **2013**, *32*, 2760–2767.

(37) Schwarzenbach, G. Der Chelateffekt. *Helv. Chim. Acta* **1952**, *35*, 2344–2359.

(38) Levason, W.; Matthews, M. L.; Reid, G.; Webster, M. Synthesis and Properties of New Ditertiary Stibines Based upon *o*-, *m*- or *p*-Xylyl and *m*- or *p*-Phenylene Backbones and Their Complexes with Tungsten, Iron and Nickel Carbonyls. *J. Chem. Soc. Dalt. Trans.* **2004**, *4*, 51–58.

(39) Shewchuk, E.; Wild, S. B. Organostibines as Ligands. Synthesis of Dimethyl(Alpha-Picolyl)Stibine, Dimethyl(8-Quinolyl)Stibine, and (R;S)-Methylphenyl(8-Quinolyl)Stibine and Some Transition Metal Derivatives. *J. Organomet. Chem.* **1981**, *210*, 181–191.

(40) Champness, N. R.; Levason, W. Coordination Chemistry of Stibine and Bismuthine Ligands. *Coord. Chem. Rev.* **1994**, *133*, 115–217.

(41) Shewchuk, E.; Wild, S. B. Synthesis of *o*-Phenylenebis(Dimethylstibine) and Some Derivatives of Divalent Nickel, Palladium, and Platinum and of Zerovalent Chromium, Molybdenum, and Tungsten. *J. Organomet. Chem.* **1977**, *128*, 115–129.

(42) Levason, W.; McAuliffe, C. A. Coordination Chemistry of Organostibines. *Acc. Chem. Res.* **1978**, *11*, 363–368.

(43) Meinema, H. A.; Martens, H. F.; Noltes, J. G. Investigations on Organoantimony Compounds: XV. The Synthesis of Heterocyclic Antimony Compounds via Thermolysis of α,ω-Bis(Dimethylstibino)Alkanes. A New Route to the Synthesis of 1-Methylstibacycloalkanes. *J. Organomet. Chem.* **1976**, *110*, 183–193.

(44) Levason, W.; McAuliffe, C. A.; Murray, S. G. Bidentate Group VB Chelates: XVI. The Preparation of *o*-Phenylenebis(Diphenylstibine) and Attempts to Prepare Cis- and Trans-1,2-Bis(Diphenylstibino)Ethylene. *J. Organomet. Chem.* **1975**, *88*, 171–174.

(45) Levason, W.; Smith, K. G.; McAuliffe, C. A.; McCullough, F. P.; Sedgwick, R. D.; Murray, S. G. Synthesis and Properties of Group 5B Ligand Analogues of *o*-Phenylenebis(Dimethylarsine), *o*-$C_6H_4(EMe_2)(E'Me_2)$ Where E, E′= P, N, As, or Sb. *J. Chem. Soc. Dalt. Trans.* **1979**, No. 11, 1718–1724.

(46) Jura, M.; Levason, W.; Reid, G.; Webster, M. Preparation and Properties of Sterically Demanding and Chiral Distibine Ligands. *J. Chem. Soc. Dalt. Trans.* **2008**, 5774–5782.

(47) *The Chemistry of Arsenic, Antimony, and Bismuth Compounds*; Patai, S., Ed.; John Wiley & Sons, Ltd: New York, 1994.

(48) Levason, W.; McAuliffe, C. A. *Phosphine, Arsine, and Stibine Complexes of the Transition Elements*; Elsevier: New York, 1979.

(49) Levason, W.; Reid, G. Developments in the Coordination Chemistry of Stibine Ligands. *Coord. Chem. Rev.* **2006**, *250*, 2565–2594.

(50) Levason, W.; Matthews, M. L.; Reid, G.; Webster, M. Synthesis and Characterisation of Transition Metal Halide Complexes of the Xylyl-Distibine, 1, 2-Bis(Dimethylstibanylmethyl) Benzene. *Dalt. Trans.* **2004**, 554–561.

(51) Benjamin, S. L.; Reid, G. Neutral Organoantimony(III) and Organobismuth(III) Ligands as Acceptors in Transition Metal Complexes - Role of Substituents and Co-Ligands. *Coord. Chem. Rev.* **2015**, *297–298*, 168–180.

(52) Benjamin, S. L.; Levason, W.; Reid, G.; Warr, R. P. Halostibines $SbMeX_2$ and $SbMe_2X$: Lewis Acids or Lewis Bases? *Organometallics* **2012**, *31*, 1025–1034.

(53) Benjamin, S. L.; Levason, W.; Reid, G.; Rogers, M. C. Hybrid Dibismuthines and Distibines as Ligands towards Transition Metal Carbonyls. *Dalt. Trans.* **2011**, *40*, 6565–6574.

(54) Brown, M. D.; Levason, W.; Reid, G.; Webster, M. Preparation, Properties and Structures of the First Series of Organometallic Pt(II) and Pt(IV) Complexes with Stibine Co-Ligands. *J. Chem. Soc. Dalt. Trans.* **2006**, *60*, 16671667–16741674.

(55) Orpen, A. G.; Connelly, N. G. Structural Systematics: The Role of P-A σ* Orbitals in Metal-Phosphorus π-Bonding in Redox-Related Pairs of $M\text{-}PA_3$ Complexes (A = R, Ar, OR; R = Alkyl). *Organometallics* **1990**, *9*, 1206–1210.

(56) Holmes, N. J.; Levason, W.; Webster, M. Triphenylstibine Substituted Manganese and Rhenium Carbonyls: Synthesis and Multinuclear NMR Spectroscopic Studies. X-Ray Crystal Structures of Ax-$[Mn_2(CO)_9(SbPh_3)]$, $[Mn(CO)_5(SbPh_3)][CF_3SO_3]$ and Fac-$[Re(CO)_3Cl(SbPh_3)_2]$. *J. Organomet. Chem.* **1998**, *568*, 213–223.

(57) Otto, S.; Roodt, A. Equilibrium, Solid State Behavior and Reactions of Four and Five Co-Ordinate Carbonyl Stibine Complexes of Rhodium. Crystal Structures of Trans-$[Rh(Cl)(CO)(SbPh_3)_2]$, Trans-$[Rh(Cl)(CO)(SbPh_3)_3]$ and Trans-$[Rh(I)_2(CH_3)(CO)(SbPh_3)_2]$. *Inorganica Chim. Acta* **2002**, *331*, 199–207.

(58) Bistoni, G.; Rampino, S.; Scafuri, N.; Ciancaleoni, G.; Zuccaccia, D.; Belpassi, L.; Tarantelli, F. How π Back-Donation Quantitatively Controls the CO Stretching

Response in Classical and Non-Classical Metal Carbonyl Complexes. *Chem. Sci.* **2016**, *7*, 1174–1184.

(59) Ishiguro, A.; Takahashi, M.; Takeda, M. $^{121}$Sb, $^{57}$Fe and $^{127}$I Mössbauer Spectroscopic Study on Antimony-Transition Metal Bond in Metal Carbonyl Derivatives of Tertiary Stibines. *J. Organomet. Chem.* **2000**, *611*, 558–565.

(60) Rheingold, A. L.; Fountain, M. E. Tetracarbonyl(Tri-Tert-Butylstibine)Iron, [$Fe(CO)_4${$Sb(C_4H_9)_3$}]. *Acta Crystallogr. Sect. C* **1985**, *41*, 1162–1164.

(61) Konchenko, S. N.; Virovets, A. V; Apenina, S. A.; Tkachev, S. V. Synthesis and Structure of the Cubane Type [$Fe_2Sb(CO)_5(H_5$-$C_5H_5)]_4$ Cluster. *Inorg. Chem. Commun.* **1999**, *2*, 555–557.

(62) Deng, M.; Leong, W. K. Novel Higher Nuclearity Osmium–antimony Clusters by Alkene- or Diene-Assisted Cluster Condensation. *J. Chem. Soc. Dalt. Trans.* **2002**, No. 6, 1020–1023.

(63) Li, Y.-Z.; Ganguly, R.; Leong, W. K.; Liu, Y. Synthesis and Reactivity of Ruthenium–Antimony Carbonyl Clusters. *Eur. J. Inorg. Chem.* **2015**, *2015*, 3861–3872.

(64) Becker, E.; Rüba, E.; Mereiter, K.; Schmid, R.; Kirchner, K. Facile Rearrangement of Metallacyclopentatrienes to Butadienyl Carbenes by a 1,2-Hydrogen Shift. *Organometallics* **2001**, *20*, 3851–3853.

(65) Jewiss, H. C.; Levason, W.; Spicer, M. D.; Webster, M. Coordination Chemistry of Higher Oxidation States. 25. Synthesis and Properties (Including Cobalt-59 NMR Spectra) of Cobalt(III) Complexes of Ligands Containing Two Tertiary Stibine Groups. Crystal Structure of Trans-[Co{*o*-$C_6H_4(SbMe_2)_2$}$_2Cl_2]_2$[$CoCl_4$]. *Inorg. Chem.* **1987**, *26*, 2102–2106.

(66) Godfrey, S. M.; Lane, H. P.; McAuliffe, C. A.; Pritchard, R. G. Inorganic Grignard Analogues. Reaction of Cobalt Powder with Triorganodiiodophosphorus Compounds to Form [$PR_3I$][$Co(PR_3)I_3$]. Crystal Structure of [$PPh_3I$][$Co(PPh_3)I_3$], and Isolation of the Novel Complexes [$PPh_3I$][$Co(PPh_3)IBr_2$] and [$SbPh_3I$][$Co(SbPh_3)I_3$]. *J. Chem. Soc. Dalt. Trans.* **1993**, No. 10, 1599–1604.

(67) Godfrey, S. M.; McAuliffe, C. A.; Pritchard, R. G. Extreme Symbiosis: The Facile One-Step Synthesis of the Paramagnetic Cobalt(III) Complex of Triphenylantimony, $CoI_3(SbPh_3)_2$, from the Reaction of Triphenylantimonydiiodine with Unactivated Coarse Grain Cobalt Metal Powder. *J. Chem. Soc. Chem. Commun.* **1994**, No. 1, 45–46.

(68) Jiménez-Tenorio, M.; Carmen Puerta, M.; Salcedo, I.; Valerga, P.; De Los Ríos, I.; Mereiter, K. Oligomerization of Styrenes Mediated by Cationic Allyl Nickel Complexes Containing Triphenylstibine or Triphenylarsine. *J. Chem. Soc. Dalt. Trans.* **2009**,10, 1842–1852.

(69) Jones, J. S.; Wade, C. R.; Gabbaï, F. P. Redox and Anion Exchange Chemistry of a Stibine-Nickel Complex: Writing the L-, X-, Z-Ligand Alphabet with a Single Element. *Angew. Chemie - Int. Ed.* **2014**, *53*, 8876–8879.

(70) Tsiatouras, V.; Banti, C. N.; Grześkiewicz, A. M.; Rossos, G.; Kourkoumelis, N.; Kubicki, M.; Hadjikakou, S. K. Structural, Photolysis and Biological Studies of Novel Mixed Metal Cu(I)-Sb(III) Mixed Ligand Complexes. *J. Photochem. Photobiol. B Biol.* **2016**, *163*, 261–268.

(71) Bowmaker, G. A.; Effendy; Hart, R. D.; Kildea, J. D.; White, A. H. Lewis-Base Adducts of Group 11 Metal(I) Compounds. LXXIII Synthesis, Spectroscopy and Structural Systematics of New 1 : 1 "Cubane" Tetramers of Copper(I) and Silver(I) Halides with Triphenylarsine. *Aust. J. Chem.* **1997**, *50*, 653–670.

(72) Thomas, F.; Schulz, S.; Nieger, M. Synthesis of Thermolabile Zinc–Pentel Compounds under Kinetically Controlled Reaction Conditions. *Angew. Chemie Int. Ed.* **2005**, *44*, 5668–5670.

(73) Chiffey, A. F.; Evans, J.; Levason, W.; Webster, M. Synthesis and Properties of the Transition Metal Complexes of a Tritertiary Stibine, 1,1,1-Tris((Diphenylstibino)Methyl)Ethane. Structure of Fac-$[Mo(CO)_3\{MeC(CH_2SbPh_2)_3\}]$. *Organometallics* **1996**, *15*, 1280–1283.

(74) Pope, S. J. A.; Reid, G. Phosphine, Arsine and Stibine Complexes of Manganese(I) Carbonyl Halides: Synthesis, Multinuclear NMR Spectroscopic Studies, Redox Properties and Crystal Structures. *J. Chem. Soc. Dalt. Trans.* **1999**, 1615–1621.

(75) Breunig, H. J.; Jönsson, M.; Rösler, R.; Lork, E. Tetracarbonylchrom-Komplexe Mit $Me_2SbESbMe_2$ (E=O, S) Und $MeSb(SSbMe_2)_2$ Als Liganden. *Zeitschrift für Anorg. und Allg. Chemie* **1999**, *625*, 2120–2124.

(76) Brown, M. D.; Levason, W.; Reid, G.; Webster, M. Preparation and Coordinating Properties of $\{CH_2(o\text{-}C_6H_4CH_2SbMe_2)\}_2$, a Novel Wide-Angle Cis-Chelating Distibine. *Dalt. Trans.* **2006**, No. 47, 5648–5654.

(77) Ke, I.-S.; Gabbaï, F. P. $Cu_3(M_2\text{-}Cl)_3$ and $Ag_3(M_2\text{-}Cl)_3$ Complexes Supported by Tetradentate Trisphosphino-Stibine and -Bismuthine Ligands: Structural Evidence for Triply Bridging Heavy Pnictines. *Aust. J. Chem.* **2013**, *66*, 1281–1287.

(78) Tolman, C. A. Electron Donor-Acceptor Properties of Phosphorus Ligands. Substituent Additivity. *J. Am. Chem. Soc.* **1970**, *92*, 2953–2956.

(79) Chan, K. H.; Leong, W. K.; Mak, K. H. G. Thermolysis of the Osmium−Antimony Clusters $Os_3(CO)_{11}(SbMe_2Ar)$: Higher Nuclearity Clusters and Arrested Ortho Metalation. *Organometallics* **2006**, *25*, 250–259.

(80) Miyamoto, T. K. Synthesis of Water-Soluble Platinum(II) Complexes Stabilized with Trimethylstibane. Stibane Transfer in Aqueous Solution. *Chem. Lett.* **1994**, *23*, 2031–2032.

(81) Hering, C.; Lehmann, M.; Schulz, A.; Villinger, A. Chlorine/Methyl Exchange Reactions in Silylated Aminostibanes: A New Route To Stibinostibonium Cations. *Inorg. Chem.* **2012**, *51*, 8212–8224.

(82) Schulz, S.; Kuczkowski, A.; Nieger, M. First Structural Characterization of Completely Alkyl-Substituted Al–Sb Lewis Acid–base Adducts. *J. Organomet. Chem.* **2000**, *604*, 202–207.

(83) Phadnis, P. P.; Jain, V. K.; Varghese, B. Preparation and Characterization of Tris(Iso-Propyl)Stibine Complexes of Palladium and Platinum. *Appl. Organomet. Chem.* **2002**, *16*, 61–64.

(84) Boddhula, R.; Ghosh, A.; Wölper, C.; Mobin, S. M.; Giri, S.; Chatterjee, S. Synthesis and Structure of Open and Closed Type Iron Telluride – Stibine Cluster Compounds. *J. Organomet. Chem.* **2017**, *851*, 22–29.

(85) Genge, A. R. J.; Holmes, N. J.; Levason, W.; Webster, M. Complexes of Distibinomethane Ligands: 3. Manganese and Rhenium Carbonyl Complexes. *Polyhedron* **1999**, *18*, 2673–2677.

(86) Lorenz, I.-P.; Rudolph, S.; Piotrowski, H.; Polborn, K. Reactions of $K_2[Fe(CO)_3(PPh_3)]$: Reductive Sb−Sb Coupling with $Ph_2SbCl$ To Form Trans-$[Fe(CO)_3(PPh_3)(Sb_2Ph_4)]$ and Salt Metathesis with $Me_3SbCl_2$ To Yield Trans-$[Fe(CO)_3(PPh_3)(SbMe_3)]$. *Eur. J. Inorg. Chem.* **2005**, *2005*, 82–85.

(87) Young, K. J. H.; Oxgaard, J.; Ess, D. H.; Meier, S. K.; Stewart, T.; Goddard William A., I. I. I.; Periana, R. A. Experimental Realization of Catalytic $CH_4$ Hydroxylation Predicted for an Iridium NNC Pincer Complex, Demonstrating Thermal, Protic, and Oxidant Stability. *Chem. Commun.* **2009**, *22*, 3270–3272.

(88) Gross, C. L.; Girolami, G. S. Metal−Alkane Complexes. Rapid Exchange of Hydrogen Atoms between Hydride and Methyl Ligands in $[(C_5Me_5)Os(Dmpm)(CH_3)H^+]$. *J. Am. Chem. Soc.* **1998**, *120*, 6605–6606.

(89) Periana, R. A.; Taube, D. J.; Gamble, S.; Taube, H.; Satoh, T.; Fujii, H. Platinum Catalysts for the High-Yield Oxidation of Methane to a Methanol Derivative. *Science.* **1998**, *280*, 560 LP-564.

(90) https://minerals.usgs.gov/minerals/pubs/commodity/.

(91) https://www.mining-technology.com/features/featuremined-into-extinction-is-the-world-running-out-of-critical-minerals-5776166/.

(92) Than, K.; Brown, G. Critical Minerals Scarcity Could Threaten Renewable Energy Future. *School of Eath, Energy, and Environmental Sciences*. 2018.

(93) Elvidge, C. D.; Ziskin, D.; Baugh, K. E.; Tuttle, B. T.; Ghosh, T.; Pack, D. W.; Erwin, E. H.; Zhizhin, M. A Fifteen Year Record of Global Natural Flaring Derived From Satellite Data. *Energies* **2009**, *2*, 595–622.

(94) Karacan, C. O.; Ruiz, F. A.; Cote, M.; Phipps, S. Coal Mine Methane: A Review of Capture and Utilizaiton Practices with Benefits to Mining Safety and to Greenhouse Gas Emission. *Intl. J. Coal Geol* **2011**, *86*, 121–156.

(95) Labinger, J. A. Platinum-Catalyzed C–H Functionalization. *Chem. Rev.* **2017**, *117*, 8483–8496.

(96) Crabtree, R. H.; Lei, A. Introduction: CH Activation. *Chem. Rev.* **2017**, *117*, 8481–8482.

(97) Bernskoetter, W. H.; Hanson, S. K.; Buzak, S. K.; Davis, Z.; White, P. S.; Swartz, R.; Goldberg, K. I.; Brookhart, M. Investigations of Iridium-Mediated C-H Cleavage: Characterization of a 16-Electron Iridium(III) Methyl Hydride Complex. *J. Am. Chem. Soc.* **2009**, *131*, 8603–8613.

(98) Khudyakov, I. V.; Serebrennikov, Y. A.; Turro, N. J. Spin-Orbit Coupling in Free-Radical Reactions: On the Way to Heavy Elements. *Chem. Rev.* **1993**, *93*, 537–570.

(99) Jones, W. D.; Feher, F. J. Mechanism of Arene Carbon-Hydrogen Bond Activation by $[C_5(CH_3)_5]Rh[P(CH_3)_3](H)(C_6H_5)$. Evidence for Arene Precoordination. *J. Am. Chem. Soc.* **1982**, *104*, 4240–4242.

(100) Janowicz, A. H.; Bergman, R. G. Activation of Carbon-Hydrogen Bonds in Saturated Hydrocarbons on Photolysis of $(\eta_5\text{-}C_5Me_5)(PMe_3)IrH_2$. Relative Rates of Reaction of the Intermediate with Different Types of Carbon-Hydrogen Bonds and Functionalization of the Metal-Bound Alkyl Groups. *J. Am. Chem. Soc.* **1983**, *105*, 3929–3939.

(101) Bengali, A. A.; Bergman, R. G.; Moore, C. B. Evidence for the Formation of Free 16-Electron Species Rather than Solvate Complexes in the Ultraviolet Irradiation of $CpCo(CO)_2$ in Liquefied Noble Gas Solvents. *J. Am. Chem. Soc.* **1995**, *117*, 3879–3880.

(102) Siegbahn, P. E. M. Comparison of the C-H Activation of Methane by $M(C_5H_5)(CO)$ for M = Cobalt, Rhodium, and Iridium. *J. Am. Chem. Soc.* **1996**, *118*, 1487–1496.

(103) Blomberg, M. R. A.; Siegbahn, P. E. M.; Svensson, M. Mechanisms for the Reactions between Methane and the Neutral Transition Metal Atoms from Yttrium to Palladium. *J. Am. Chem. Soc.* **1992**, *114*, 6095–6102.

(104) Siegbahn, P. E. M.; Blomberg, M. R. A. Halide Ligand Effects on the Oxidative Addition Reaction of Methane and Hydrogen to Second Row Transition Metal Complexes. *Organometallics* **1994**, *13*, 354–363.

(105) Siegbahn, P. E. M. Oxidative Addition of Methane to Rhodium(I) and Ruthenium(II) Complexes of Particular Interest. *Organometallics* **1994**, *13*, 2833–2842.

(106) Kahn, O. *Molecular Magnetism*; VCH Publishers, Inc: New York, 1993.

(107) Figgis, B. N. *Introduction to Ligand Fields*; John Wiley & Sons, Ltd: New York, 1966.

(108) Koseki, S.; Matsunaga, N.; Asada, T.; Schmidt, M. W.; Gordon, M. S. Spin–Orbit Coupling Constants in Atoms and Ions of Transition Elements: Comparison of Effective Core Potentials, Model Core Potentials, and All-Electron Methods. *J. Phys. Chem. A* **2019**, *123*, 2325–2339.

(109) He, L.; Bester, G.; Zunger, A. Singlet-Triplet Splitting, Correlation, and Entanglement of Two Electrons in Quantum Dot Molecules. *Phys. Rev. B - Condens. Matter Mater. Phys.* **2005**, *72*, 1–12.

(110) Stepanenko, D.; Rudner, M.; Halperin, B. I.; Loss, D. Singlet-Triplet Splitting in Double Quantum Dots Due to Spin-Orbit and Hyperfine Interactions. *Phys. Rev. B - Condens. Matter Mater. Phys.* **2012**, *85*, 7.

(111) Ishizuka, H.; Balents, L. Magnetism in S=1/2 Double Perovskites with Strong Spin-Orbit Interactions. *Phys. Rev. B* **2014**, *90*, 184422.

(112) Chilton, N. F.; Anderson, R. P.; Turner, L. D.; Soncini, A.; Murray, K. S. PHI: A Powerful New Program for the Analysis of Anisotropic Monomeric and Exchange-Coupled Polynuclear *d*- and *f*-Block Complexes. *J. Comput. Chem.* **2013**, *34*, 1164–1175.

(113) Layfield, R. A. Organometallic Single-Molecule Magnets. *Organometallics* **2014**, *33*, 1084–1099.

(114) Lv, L.; Wang, X.; Zhu, Y.; Liu, X.; Wang, Y. Theoretical Study of Spin-Orbit Coupling and Intersystem Crossing in the Two-State Reaction between $Nb(NH_2)_3$ and $N_2O$. *Sci. China Chem.* **2012**, *55*, 158–166.

(115) Rose, M. J.; Mascharak, P. K. Photosensitization of Ruthenium Nitrosyls to Red Light with an Isoelectronic Series of Heavy-Atom Chromophores: Experimental and Density Functional Theory Studies on the Effects of O-, S- And Se-Substituted Coordinated Dyes. *Inorg. Chem.* **2009**, *48*, 6904–6917.

(116) Dresselhaus, M. *Group Theory: Applications to the Physics of Condensed Matter*; Springer-Verlag: Berlin, 2008.

(117) Landis, C. R.; Morales, C. M.; Stahl, S. S. Insights into the Spin-Forbidden Reaction between $L_2Pd^0$ and Molecular Oxygen. *J. Am. Chem. Soc.* **2004**, *126*, 16302–16303.

(118) Matsunaga, N.; Koseki, S. Modeling of Spin-Forbidden Reactions. *Reviews in Computational Chemistry*. John Wiley and Sons: New York, 2004.

(119) Gorin, D. J.; Toste, F. D. Relativistic Effects in Homogeneous Gold Catalysis. *Nature* **2007**, *446*, 395.

(120) Ye, S.; Neese, F. How Do Heavier Halide Ligands Affect the Signs and Magnitudes of the Zero-Field Splittings in Halogenonickel(II) Scorpionate Complexes? A Theoretical Investigation Coupled to Ligand-Field Analysis. *J. Chem. Theory Comput.* **2012**, *8*, 2344–2351.

(121) Chen, J.-J.; Du, M.-L. Investigation of the Zero-Field Splitting and g-Values of $d^8$ Ions in Trigonal Compounds $CsMgX_3:Ni^{2+}$ (X = Cl, Br, I). *Phys. B Condens. Matter* **1996**, *228*, 409–413.

(122) Mabbs, F. E.; Collison, D. *Electron Paramagnetic Resonance of the d Transition Metal Series*; Elsevier: Amsterdam, 1992.

(123) Holm, R. H.; Cotton, F. A. Magnetic Investigations of Spin-Free Cobaltous Complexes: 1. Tetrahalo Cobalt(II) Ions. *J. Chem. Phys.* **1959**, *31*, 788–792.

(124) Zadrozny, J. M.; Telser, J.; Long, J. R. Slow Magnetic Relaxation in the Tetrahedral Cobalt(II) Complexes $[Co(EPh)_4]^{2-}$ (E = O, S, Se). *Polyhedron* **2013**, *64*, 209–217.

(125) Saber, M. R.; Dunbar, K. R. Ligands Effects on the Magnetic Anisotropy of Tetrahedral Cobalt Complexes. *Chem. Commun.* **2014**, *50*, 12266–12269.

(126) Shores, M. P.; Sokol, J. J.; Long, J. R. Nickel(II)-Molybdenum(III)-Cyanide Clusters: Synthesis and Magnetic Behavior of Species Incorporating $[(Me_3tacn)Mo(CN)_3]$. *J. Am. Chem. Soc.* **2002**, *124*, 2279–2292.

(127) Magnasco, V. *Methods of Molecular Quantum Mechanics*; John Wiley & Sons, Ltd: Chichester, 2009.

(128) Coste, S. C.; Vlaisavljevich, B.; Freedman, D. E. Magnetic Anisotropy from Main-Group Elements: Halides versus Group 14 Elements. *Inorg. Chem.* **2017**, *56*, 8195–8202.

(129) Karunadasa, H. I.; Arquero, K. D.; Berben, L. A.; Long, J. R. Enhancing the Magnetic Anisotropy of Cyano-Ligated Chromium(II) and Chromium(III) Complexes via Heavy Halide Ligand Effects. *Inorg. Chem.* **2010**, *49*, 4738–4740.

(130) Vijayakumar, M.; Gopinathan, M. S. Spin-Orbit Coupling Constants of Transition Metal Atoms and Ions in Density Functional Theory. *J. Mol. Struct. THEOCHEM* **1996**, *361*, 15–19.

(131) Bianchini, C.; Fornasiero, P. A Synthetic Nickel Electrocatalyst with a Turnover Frequency above 100000 $s^{-1}$ for $H_2$ Production. *ChemCatChem* **2012**, *4*, 45–46.

(132) Bini, L.; Müller, C.; Wilting, J.; Von Chrzanowski, L.; Spek, A. L.; Vogt, D. Highly Selective Hydrocyanation of Butadiene toward 3-Pentenenitrile. *J. Am. Chem. Soc.* **2007**, *129*, 12622–12623.

(133) Speiser, F.; Braunstein, P.; Saussine, L. New Nickel Ethylene Oligomerization Catalysts Bearing Bidentate P,N-Phosphinopyridine Ligands with Different Substituents a to Phosphorus. *Organometallics* **2004**, *23*, 2625–2632.

(134) Baber, R. A.; Haddow, M. F.; Middleton, A. J.; Orpen, A. G.; Pringle, P. G.; Haynes, A.; Williams, G. L.; Papp, R. Ligand Stereoelectronic Effects in Complexes of Phospholanes, Phosphinanes, and Phosphepanes and Their Implications for Hydroformylation Catalysis. *Organometallics* **2007**, *26*, 713–725.

(135) Clavier, H.; Nolan, S. P. Percent Buried Volume for Phosphine and N-Heterocyclic Carbene Ligands: Steric Properties in Organometallic Chemistry. *Chem. Commun.* **2010**, *46*, 841–861.

(136) Fukin, G. K.; Guzei, I. A.; Baranov, E. V.; Domrachev, G. A. Analysis of the Supramolecular Structures of Sb(III) and Sb(V) Catecholate Complexes from the Viewpoint of Ligand Solid Angles. *Struct. Chem.* **2009**, *20*, 643–654.

(137) Poddel'Sky, A. I.; Smolyaninov, I. V.; Berberova, N. T.; Fukin, G. K.; Cherkasov, V. K.; Abakumov, G. A. Triaryl/Trialkylantimony(V) Catecholates with Electron-Acceptor Groups. *J. Organomet. Chem.* **2015**, *789–790*, 8–13.

(138) Jones, J. S.; Wade, C. R.; Yang, M.; Gabbaï, F. P. On the Coordination Non-Innocence of Antimony in Nickel(II) Complexes of the Tetradentate (*o*-$(Ph_2P)C_6H_4)_3Sb$ Ligand. *Dalt. Trans.* **2017**, *46*, 5598–5604.

(139) Imyanitov, N. S. Electronic and Steric Effects of Ligands in Square-Planar, Trigonal Bipyramidal, and Octahedral Complexes. *Koord. Khimiia* **1992**, *18*, 1127–1138.

(140) Breunig, H. J.; Ghesner, I. Coordination Compounds with Organoantimony and $Sb_n$ Ligands. *Adv. Organomet. Chem.* **2003**, *49*, 95–131.

(141) Werner, H.; Schwab, P.; Heinemann, A.; Steinert, P. Bis(Triisopropylarsan) - Und Bis(Triisopropylstiban)-Rhodium(I)-Komplexe Mit Isonitrilen, Olefinen, Alkinen Und Diinen Als Liganden. *J. Organomet. Chem.* **1995**, *496*, 207–216.

(142) Grünwald, C.; Laubender, M.; Wolf, J.; Werner, H. Acetato and Acetylacetonato Ruthenium(II) Complexes Containing $Sb^iPr_3$, $P^iPr_3$ and $PCy_3$ as Ligands. *J. Chem. Soc. Dalt. Trans.* **1998**, 833–840.

(143) Yang, J.; Li, P.; Zhang, Y.; Wang, L. A New Library of Arsine, Stibine-Stabilized N-Heterocyclic Carbene Palladium Complexes: Synthesis, Structures and Activities in C-C and C-N Coupling Reactions. *Dalt. Trans.* **2014**, *43*, 14114–14122.

(144) Gomes, C. S. B.; Krishnamoorthy, P.; Silva, L. C.; Costa, S. I.; Gomes, P. T.; Jiménez-Tenorio, M.; Valerga, P.; Puerta, M. C. First Examples of Neutral and Cationic Indenyl Nickel(II) Complexes Bearing Arsine or Stibine Ligands: Highly Active Catalysts for the Oligomerisation of Styrene. *Dalt. Trans.* **2015**, *44*, 17015–17019.

(145) Mlynek, P. D.; Dahl, L. F. New Nickel-Antimony Carbonyl Clusters : Stereochemical Analyses of the $[Ni_{10}(SbR)_2(CO)_{18}]_2$ - Dianions (R) Me, Et, $^{i}$Pr, $^{t}$Bu, *p*-$FC_6H_4$) Containing Empty 1,12-$Ni_{10}Sb_2$ Icosahedral Cages and of the Unprecedented Stibinido-Bridged. *Organometallics* **1997**, *16*, 1641–1654.

(146) Desenfants, R. E.; Gavney, J. A.; Hayashi, R. K.; Rae, A. D.; Dahl, L. F. Reactions of the $[Ni(CO)R_2]^{2-}$ Dianion with Stibine and Bismuthine Reagents : Synthesis and Stereophysical Characterization of the $(Ni_1(SbPh)_2(CO)Is]^*$ - Dianion Containing a Noncentered Icosahedral Ni, Sb, Core and $Ni^*(CO)P_2$, *J. Organomet. Chem.* **1990**, *2033*, 543–572.

(147) Goicoechea, J. M.; Hull, M. W.; Sevov, S. C. Heteroatomic Deltahedral Clusters: Synthesis and Structures of Closo-$[Bi_3Ni_4(CO)_6]^{3-}$, Closo-$[Bi_4Ni_4(CO)_6]^{2-}$, the Open Cluster $[Bi_3Ni_6(CO)_9]^{3-}$, and the Intermetalloid Closo-$[Ni_x@\{Bi_6Ni_6(CO)_8\}]^{4-}$. *J. Am. Chem. Soc.* **2007**, *129*, 7885–7893.

(148) Albano, V. G.; Demartin, F.; Iapalucci, M. C.; Laschi, F.; Longoni, G.; Sironi, A.; Zanello, P. Icosahedral Carbonyl Clusters $[Ni_{10}Sb_2(M_{12}\text{-}Ni)\{Ni(CO)_3\}^{2-}(CO)_{18}]^{n-}$ (n = 2, 3 or 4); Synthesis, Spectroscopic, Electrochemical and Bonding Analysis. Crystal Structures of $[Ni_{10}Sb_2(M_{12}\text{-}Ni)\{Ni(CO)_3\}_2(CO)_{18}]^{n-}$ (n = 2 or 3). *J. Chem. Soc. Dalt. Trans.* **1991**, 739–748.

(149) Charles, S.; Eichhorn, B. W.; Bott, S. G. Synthesis and Structure of $[Sb_7Ni_3(CO)_3]^{3-}$: A New Structural Type for Nido 10-Vertex Polyhedral Clusters. *J. Am. Chem. Soc.* **1993**, *115*, 5837–5838.

(150) Moses, M. J.; Fettinger, J. C.; Eichhorn, B. W. $[Ni_5Sb_{17}]^{4-}$ Transition-Metal Zintl Ion Complex: Crossing the Zintl Border in Molecular Intermetalloid Clusters. *Inorg. Chem.* **2007**, *46*, 1036–1038.

(151) Charton, M. Substituent Effects of Arsenic, Antimony, and Bismuth Groups. In *Organic Arsenic, Antimony, and Bismuth Compounds*; Patai, S., Ed.; John Wiley & Sons, Ltd: West Sussex, 1994; pp 367–439.

(152) Casares, J. A.; Espinet, P.; Martín-Alvarez, J. M.; Martínez-Ilarduya, J. M.; Salas, G. Stable Nickel Catalysts for Fast Norbornene Polymerization: Tuning Reactivity. *Eur. J. Inorg. Chem.* **2005**, *2005*, 3825–3831.

(153) Tolman, C. A. Steric Effects of Phosphorus Ligands in Organometallic Chemistry and Homogeneous Catalysis. *Chem. Rev.* **1976**, *77*, 313–348.

(154) Ferguson, G.; Roberts, P. J.; Alyea, E. C.; Khan, M. Cone Angle and Ligand Profile Calculations for Bulky Phosphine Ligands. *Inorg. Chem.* **1978**, *17*, 2965–2967.

(155) Wu, K.; Doyle, A. G. Parameterization of Phosphine Ligands Demonstrates Enhancement of Nickel Catalysis via Remote Steric Effects. *Nat. Chem.* **2017**, *9*, 779–784.

(156) Mallory, G. O.; Hajdu, J. B. *Electroless Plating: Fundamentals and Applications*; William Andrew, 1990.

(157) Djokie, S. Electroless Deposition Deposition of of Cobalt Cobalt Using Using Hydrazine Hydrazine as an Electroless Reducing Agent. *J. Electrochem. Soc.* **1997**, *144*, 2358–2363.

(158) Paunovic, M.; Schlesinger, M. *Fundamentals of Electrochemical Deposition, 2nd Edition*; Wiley and Sons, 2006.

(159) CrystalClear 1.40. CrystalClear 1.40 (2008). Rigaku Americas Corporation: The Woodlands, TX 2008.

(160) Sheldrick, G. M. SHELXT - Integrated Space-Group and Crystal-Structure Determination. *Acta Crystallogr. Sect. A Found. Crystallogr.* **2015**, *71*, 3–8.

(161) Sheldrick, G. M. Crystal Structure Refinement with SHELXL. *Acta Crystallogr. Sect. C Struct. Chem.* **2015**, *71*, 3–8.

(162) Spek, A. L. Structure Validation in Chemical Crystallography. *Acta Crystallogr. Sect. D Biol. Crystallogr.* **2009**, *65*, 148–155.

(163) Farrugia, L. J. WinGX and ORTEP for Windows: An Update. *J. Appl. Crystallogr.* **2012**, *45*, 849–854.

(164) Saint V8.27 B. SAINT V8.27B Bruker AXS Inc, (2012): Madison, WI.

(165) Granovsky, A. A. Firefly v. 7, www http://classic.chem.msu.su/gran/firefly/index.html.

(166) Andrienko, G. A. Chemcraft, https://www.chemcraftprog.com.

(167) Bode, B. M.; Gordon, M. S. MacMolPlt: A Graphical User Interface for GAMESS. *J. Mol. Graph. Model.* **1998**, *16*, 133–138.

(168) Herber, U.; Weberndörfer, B.; Werner, H. Formation of Novel Dinuclear Mixed-Valence Rhodium Complexes by Intramolecular Migration of a Chelating Ligand. *Angew. Chemie Int. Ed.* **1999**, *38*, 1609–1613.

(169) Chan, K. H.; Leong, W. K.; Hang, K.; Mak, G. Thermolysis of the Osmium - Antimony Clusters $Os_3(CO)_{11}(SbMe_2Ar)$: Higher Nuclearity Clusters and Arrested Ortho Metalation. *Organometallics* **2006**, *25*, 250–259.

(170) Taylor, W. V.; Soto, U. H.; Lynch, V. M.; Rose, M. J. Antimony-Supported $Cu_4I_4$Cuboid with Short Cu-Cu Bonds: Structural Premise for Near-Infrared Thermoluminescence. *Inorg. Chem.* **2016**, *55*, 3206–3208.

(171) Imyanitov, N. S. Cone Angle of Ligands - Group IV and V Compounds. *Koord. Khimiya* **1985**, *11*, 1171–1178.

(172) Scott, M. J.; Christian, W.; Wilisch, A.; Armstrong, W. H. Unprecedented Example of Four Coordination at a Vanadium(II) Center. Synthesis, Structure, and Properties of a Reactive, Nearly Planar V(II) Phenolate Complex, $[V(DIPP)_4\{Li(THF)\}_2]$ (DIPP = 2,6-Diisopropylphenolate). *J. Am. Chem. Soc.* **1990**, *112*, 2429–2430.

(173) Poddel'Sky, A. I.; Cherkasov, V. K.; Bubnov, M. P.; Abakumova, L. G.; Abakumov, G. A. EPR Study of Mono-*o*-Iminobenzosemiquinonato Nickel(II) Complexes with Ni-C σ-Bond. *J. Organomet. Chem.* **2005**, *690*, 145–150.

(174) Falivene, L.; Credendino, R.; Poater, A.; Petta, A.; Serra, L.; Oliva, R.; Scarano, V.; Cavallo, L. SambVca 2. A Web Tool for Analyzing Catalytic Pockets with Topographic Steric Maps. *Organometallics* **2016**, *35*, 2286–2293.

(175) Kendall, A. J.; Zakharov, L. N.; Tyler, D. R. Steric and Electronic Influences of Buchwald-Type Alkyl-JohnPhos Ligands. *Inorg. Chem.* **2016**, *55*, 3079–3090.

(176) Riley, L. E.; Krämer, T.; McMullin, C. L.; Ellis, D.; Rosair, G. M.; Sivaev, I. B.; Welch, A. J. Large, Weakly Basic Bis(Carboranyl)Phosphines: An Experimental and Computational Study. *Dalt. Trans.* **2017**, *46*, 5218–5228.

(177) Poater, A.; Cosenza, B.; Correa, A.; Giudice, S.; Ragone, F.; Scarano, V.; Cavallo, L. SambVca: A Web Application for the Calculation of the Buried Volume of N-Heterocyclic Carbene Ligands. *Eur. J. Inorg. Chem.* **2009**, *13*, 1759–1766.

(178) Garrou, P. E.; Heck, R. F. The Mechanism of Carbonylation of Halo(Bis Ligand)Organoplatinum(II), -Palladium(II), and -Nickel(II) Complexes. *J. Am. Chem. Soc.* **1976**, *98*, 4115–4127.

(179) SaintJoly, C.; Mari, A.; Gleizes, A.; Dartiguenave, M.; Dartiguenave, Y.; Galy, J. Reaction of Monodentate (Tertiary Phosphine)Nickel(II) Complexes $NiX_2(PR_3)_2$, $NiX_2(PMe_3)_3$, and $(NiX(PMe_3)_4)(BF_4)$ with Carbon Monoxide. Crystal and Molecular Structure of $NiI_2(CO)(PMe_3)_2$. *Inorg. Chem.* **1980**, *19*, 2403–2410.

(180) Brock, C. P.; Collman, J. P.; Dolcetti, G.; Farnham, P. H.; Ibers, J. A.; Lester, J. E.; Reed, C. A. A Bent vs. Linear Nitrosyl Paradox. Infrared and X-Ray Photoelectron Spectra of $CoCl_2(NO)L_2$ and Crystal Structure with L = $P(CH_3XC_6H_5)_2$. *Inorg. Chem.* **1973**, *12*, 1304–1313.

(181) Ardizzoia, G. A.; Brenna, S. Interpretation of Tolman Electronic Parameters in the Light of Natural Orbitals for Chemical Valence. *Phys. Chem. Chem. Phys.* **2017**, *19*, 5971–5978.

(182) Bjorsvik, H. R.; Hansen, U. M.; Carlson, R. Principal Properties of Monodentate Phosphorus Ligands. Predictive Model for the Carbonyl Absorption Frequencies in $Ni(CO)_3L$ Complexes. *Acta Chem. Scand.* **1997**, *51*, 733–741.

(183) Flener Lovitt, C.; Frenking, G.; Girolami, G. S. Donor-Acceptor Properties of Bidentate Phosphines. DFT Study of Nickel Carbonyls and Molecular Dihydrogen Complexes. *Organometallics* **2012**, *31*, 4122–4132.

(184) Benner, G. S.; Hatfield, W. E.; Meek, D. W. Five-Coordinate Nickel(II) Complexes with Tris(3-Dimethylarsinopropyl)Phosphine. *Inorg. Chem.* **1964**, *3*, 1544–1549.

(185) Lever, A. B. P. *Inorganic Electronic Spectroscopy*, 1st ed.; Elsevier Publishing Company: Amsterdam, 1984.

(186) Coussmaker, C. R. C.; Hely Hutchinson, M.; Mellor, J. R.; Sutton, L. E.; Venanzi, L. M. Tetrahedral Nickel(II) Complexes and the Factors Determining Their Formation. Part II.* Complexes with Dibutylphenylphosphine and Butyldiphenylphosphine. *J. Chem. Soc.* **1961**, 2705–2713.

(187) Ciampolini, M.; Nardi, N. Five-Coordinated High-Spin Complexes of Bivalent Cobalt, Nickel, and Copper with Tris(2-Dimethylaminoethyl)Amine. *Inorg. Chem.* **1966**, *5*, 41–44.

(188) Gray, H. B. Electronic Structures of Square Planar Metal Complexes. *Transit. Met. Chem. A Ser. Adv.* **1965**, *1*, 239–287.

(189) Dubois, T. D.; Meek, D. W. Five-Coordination. IV. Nickel(II) Complexes Of Diphenyl(o-Diphenylarsinophenyl)Phosphine. *Inorg. Chem.* **1967**, *6*, 1395–1398.

(190) Bröring, M.; Prikhodovski, S.; Brandt, C. D. The First (Tripyrrinato)Nickel(II) Complexes, TrpyNiX with X = Cl, Br, I: Synthesis, Structures and Solvent Coordination. *J. Chem. Soc., Dalt. Trans.* **2002**, 4213–4218.

(191) Marriott, K. E. R.; Bhaskaran, L.; Wilson, C.; Medarde, M.; Ochsenbein, S. T.; Hill, S.; Murrie, M. Pushing the Limits of Magnetic Anisotropy in Trigonal Bipyramidal Ni(II). *Chem. Sci.* **2015**, *6*, 6823–6828.

(192) Ruamps, R.; Maurice, R.; Batchelor, L.; Boggio-Pasqua, M.; Guillot, R.; Barra, A. L.; Liu, J.; Bendeif, E. E.; Pillet, S.; Hill, S.; et al. Giant Ising-Type Magnetic Anisotropy in Trigonal Bipyramidal Ni(II) Complexes: Experiment and Theory. *J. Am. Chem. Soc.* **2013**, *135*, 3017–3026.

(193) Gruden-Pavlovic, M.; Peric, M.; Zlatar, M.; Garcia-Fernandez, P. Theoretical Study of the Magnetic Anisotropy and Magnetic Tunnelling in Mononuclear Ni(II) Complexes with Potential Molecular Magnet Behavior. *Chem. Sci.* **2014**, *5*, 1453–1462.

(194) Yang, H.; Gabbal, F. P. Activation of a Hydroamination Gold Catalyst by Oxidation of a Redox-Noninnocent Chlorostibine Z-Ligand. *J. Am. Chem. Soc.* **2015**, *137*, 13425–13432.

(195) Elie, M.; Renaud, J.-L.; Gaillard, S. N-Heterocyclic Carbene Transition Metal Complexes in Light Emitting Devices. *Polyhedron* **2018**, *140*, 158–168.

(196) Zhang, K. Y.; Yu, Q.; Wei, H.; Liu, S.; Zhao, Q.; Huang, W. Long-Lived Emissive Probes for Time-Resolved Photoluminescence Bioimaging and Biosensing. *Chem. Rev.* **2018**, *118*, 1770–1839.

(197) Shan, X.-C.; Jiang, F.-L.; Chen, L.; Wu, M.-Y.; Pan, J.; Wan, X.-Y.; Hong, M.-C. Using Cuprophilicity as a Multi-Responsive Chromophore Switching Color in Response to Temperature, Mechanical Force and Solvent Vapors. *J. Mater. Chem. C* **2013**, *1*, 4339–4349.

(198) Reineck, P.; Gibson, B. C. Near-Infrared Fluorescent Nanomaterials for Bioimaging and Sensing. *Adv. Opt. Mater.* **2016**, *5*, 1600446.

(199) Wang, W.; Lei, X.; Gao, H.; Mao, Y. Near-Infrared Quantum Cutting Platform in Transparent Oxyfluoride Glass–ceramics for Solar Sells. *Opt. Mater. (Amst).* **2015**, *47*, 270–275.

(200) Liu, Y.; Zhang, P.; Fang, X.; Wu, G.; Chen, S.; Zhang, Z.; Chao, H.; Tan, W.; Xu, L. Near-Infrared Emitting Iridium(III) Complexes for Mitochondrial Imaging in Living Cells. *Dalt. Trans.* **2017**, *46*, 4777–4785.

(201) Otto, S.; Dorn, M.; Förster, C.; Bauer, M.; Seitz, M.; Heinze, K. Understanding and Exploiting Long-Lived near-Infrared Emission of a Molecular Ruby. *Coord. Chem. Rev.* **2018**, *359*, 102–111.

(202) Wagenknecht, P. S.; Ford, P. C. Metal Centered Ligand Field Excited States: Their Roles in the Design and Performance of Transition Metal Based Photochemical Molecular Devices. *Coord. Chem. Rev.* **2011**, *255*, 591–616.

(203) Peng, Y.; Hu, J. X.; Lu, H.; Wilson, R. M.; Motevalli, M.; Hernández, I.; Gillin, W. P.; Wyatt, P. B.; Ye, H. Q. Functionalisation of Ligands through Click Chemistry: Long-Lived NIR Emission from Organic Er(III) Complexes with a Perfluorinated Core and a Hydrogen-Containing Shell. *RSC Adv.* **2017**, *7*, 128–131.

(204) Tan, R. H. C.; Motevalli, M.; Abrahams, I.; Wyatt, P. B.; Gillin, W. P. Quenching of IR Luminescence of Erbium, Neodymium, and Ytterbium β-Diketonate Complexes by Ligand C−H and C−D Bonds. *J. Phys. Chem. B* **2006**, *110*, 24476–24479.

(205) Zampetti, A.; Minotto, A.; Squeo, B. M.; Gregoriou, V. G.; Allard, S.; Scherf, U.; Chochos, C. L.; Cacialli, F. Highly Efficient Solid-State Near-Infrared Organic

Light-Emitting Diodes Incorporating A-D-A Dyes Based on α,β-Unsubstituted "BODIPY" Moieties. *Sci. Rep.* **2017**, *7*, 1611.

(206) Park, S.; Fukuda, K.; Wang, M.; Lee, C.; Yokota, T.; Jin, H.; Jinno, H.; Kimura, H.; Zalar, P.; Matsuhisa, N.; et al. Ultraflexible Near-Infrared Organic Photodetectors for Conformal Photoplethysmogram Sensors. *Adv. Mater.* **2018**, *30*, 1802359.

(207) Skoog, D. A.; Holler, F. J.; Crouch, S. R. *Principles of Instrumental Analysis*, 6th ed.; Thomson Brooks Cole: Belmont, CA, 2007.

(208) Ford, P. C.; Cariati, E.; Bourassa, J. Photoluminescence Properties of Multinuclear Copper(I) Compounds. *Chem. Rev.* **1999**, *99*, 3625–3648.

(209) Bai, S.-Q.; Ke, K. L.; Young, D. J.; Hor, T. S. A. Structure and Photoluminescence of Cubane-like $[Cu_4I_4]$ Cluster-Based 1D Coordination Polymer Assembled with Bis(Triazole)Pyridine Ligand. *J. Organomet. Chem.* **2017**, *849–850*, 137–141.

(210) Hardt, H. D.; Pierre, A. Fluorescence Thermochromism of Pyridine Cu Iodide and Copper Iodide. *Z. Anorg. Allg. Chem.* **1973**, *42*, 107–112.

(211) Perruchas, S.; Goff, X. F. L.; Maron, S.; Maurin, I.; Guillen, F.; Garcia, A.; Gacoin, T.; Boilot, J. P. Mechanochromic and Thermochromic Luminescence of a Copper Iodide Cluster. *J. Am. Chem. Soc.* **2010**, *132*, 10967–10969.

(212) Benito, Q.; Goff, X. F. Le; Nocton, G.; Fargues, A.; Garcia, A.; Berhault, A.; Kahlal, S.; Saillard, J.-Y.; Martineau, C.; Trébosc, J.; et al. Geometry Flexibility of Copper Iodide Clusters: Variability in Luminescence Thermochromism. *Inorg. Chem.* **2015**, *54*, 4483–4494.

(213) Benito, Q.; Maurin, I.; Cheisson, T.; Nocton, G.; Fargues, A.; Garcia, A.; Martineau, C.; Gacoin, T.; Boilot, J. P.; Perruchas, S. Mechanochromic Luminescence of Copper Iodide Clusters. *Chem. - A Eur. J.* **2015**, *21*, 5892–5897.

(214) Tard, C.; Perruchas, S.; Maron, S.; Goff, X. F. Le; Guillen, F.; Garcia, A.; Vigneron, J.; Etcheberry, A.; Gacoin, T.; Boilot, J. Thermochromic Luminescence of Sol-Gel Films Based on Copper Iodide Clusters. **2008**, *5*, 7010–7016.

(215) Lapprand, A.; Dutartre, M.; Khiri, N.; Levert, E.; Fortin, D.; Rousselin, Y.; Soldera, A.; Jug, S.; Harvey, P. D. Luminescent P-Chirogenic Copper Clusters. *Inorg. Chem.* **2013**, *52*, 7958–7967.

(216) Churchill, M. R.; Kalra, K. L. Molecules With an $M_4X_4$ core. III. Comparison of the x-ray crystallographically determined molecular structures of tetrameric triethylphosphinecopper(I) iodide and triethylarsinecopper(I) Iodide. *Inorg. Chem.* **1974**, *13*, 1899–1904.

(217) Churchill, M. R.; Youngs, W. J. (Triphenylarsine)Copper(I). *Inorg. Chem.* **1979**, *18*, 0–5.

(218) Knorr, M.; Bonnot, A.; Lapprand, A.; Khatyr, A.; Strohmann, C.; Kubicki, M. M.; Rousselin, Y.; Harvey, P. D. Reactivity of CuI and CuBr toward dialkyl sulfides RSR: From discrete molecular $Cu_4I_4S_4$ and $Cu_8I_8S_6$ clusters to luminescent copper(I) coordination polymers *Inorg. Chem.* **2015**, *54*, 4076–4093.

(219) Knorr, M.; Khatyr, A.; Aleo, A. D.; Yaagoubi, A. El; Strohmann, C.; Kubicki, M. M.; Rousselin, Y.; Aly, S. M.; Fortin, D.; Lapprand, A.; et al. Copper(I) Halides (X = Br, I) Coordinated to Bis(Arylthio)Methane Ligands: Aryl Substitution and Halide Effects on the Dimensionality, Cluster Size, and Luminescence Properties of the Coordination Polymers. *Cryst. Growth Des.* **2014**, *14*, 5373–5387.

(220) Rose, M. J.; Mascharak, P. K. Photosensitization of Ruthenium Nitrosyls to Red Light with an Isoelectronic Series of Heavy-Atom Chromophores: Experimental and Density Functional Theory Studies on the Effects of O-, S- and Se-Substituted Coordinated Dyes. *Inorg. Chem.* **2009**, *48*, 6904–6917.

(221) Li, P.-F.; Schon, T. B.; Seferos, D. S. Thiophene, Selenophene, and Tellurophene-Based Three-Dimensional Organic Frameworks. *Angew. Chemie Int. Ed.* **2015**, *54*, 9361–9366.

(222) Dobbs, K. D.; Boggs, J. E.; Cowley, A. H. Trends in Structure and Reactivity of Group 15 Alkyls, Alkylidenes, and Alkylidynes. *Chem. Phys. Lett.* **1987**, *141*, 372–375.

(223) Bilbrey, J. A.; Kazez, A. H.; Locklin, J.; Allen, W. D. Exact Ligand Cone Angles. *J. Comput. Chem.* **2013**, *34*, 1189–1197.

(224) Paizanos, K.; Charalampou, D.; Kourkoumelis, N.; Kalpogiannaki, D.; Hadjiarapoglou, L.; Spanopoulou, A.; Lazarou, K.; Manos, M. J.; Tasiopoulos, A. J.; Kubicki, M.; et al. Synthesis and Structural Characterization of New Cu(I) Complexes with the Antithyroid Drug 6-*n*-Propyl-Thiouracil. Study of the Cu(I)-Catalyzed Intermolecular Cycloaddition of Iodonium Ylides toward Benzo[*b*]Furans with Pharmaceutical Implementations. *Inorg. Chem.* **2012**, *51*, 12248–12259.

(225) Kitagawa, H.; Ozawa, Y.; Toriumi, K. Flexibility of Cubane-like $Cu_4I_4$ Framework : Temperature Dependence of Molecular Structure and Luminescence Thermochromism of $[Cu_4I_4(PPh_3)_4]$ in Two Polymorphic Crystalline States W. *Chem. Commun.* **2010**, *4*, 6302–6304.

(226) Sculfort, S.; Braunstein, P. Intramolecular $d^{10}$-$d^{10}$ Interactions in Heterometallic Clusters of the Transition Metals. *Chem. Soc. Rev.* **2011**, *40*, 2741–2760.

(227) Huitorel, B.; El Moll, H.; Utrera-Melero, R.; Cordier, M.; Fargues, A.; Garcia, A.; Massuyeau, F.; Martineau-Corcos, C.; Fayon, F.; Rakhmatullin, A.; et al. Evaluation of Ligands Effect on the Photophysical Properties of Copper Iodide Clusters. *Inorg. Chem.* **2018**, *57*, 4328–4339.

(228) Benito, Q.; Le Goff, X. F.; Nocton, G.; Fargues, A.; Garcia, A.; Berhault, A.; Kahlal, S.; Saillard, J. Y.; Martineau, C.; Trébosc, J.; et al. Geometry Flexibility of Copper Iodide Clusters: Variability in Luminescence Thermochromism. *Inorg. Chem.* **2015**, *54*, 4483–4494.

(229) Perruchas, S.; Tard, C.; Le Goff, X. F.; Fargues, A.; Garcia, A.; Kahlal, S.; Saillard, J.-Y.; Gacoin, T.; Boilot, J.-P. Thermochromic Luminescence of Copper Iodide Clusters: The Case of Phosphine Ligands. *Inorg. Chem.* **2011**, *50*, 10682–10692.

(230) Churchill, M. R.; Kalra, K. L. Molecules with an $M_4X_4$ Core. III. Comparison of the X-Ray Crystallographically Determined Molecular Structures of Tetrameric Triethylphosphinecopper(I) Iodide and Triethylarsinecopper(I) Iodide. *Inorg. Chem.* **1974**, *13*, 1899–1904.

(231) Medina, I.; Mague, J. T.; Fink, M. J. Tetra-$\mu_3$-iodo-tetrakis[(tri-*tert*-butylphosphine)copper(I)]. *Acta Crystallogr. Sect. E* **2005**, *61*, m1550-m1552.

(232) Sculfort, S.; Braunstein, P. Intramolecular $d^{10}$-$d^{10}$ Interactions in Heterometallic Clusters of the Transition Metals. *Chem. Soc. Rev.* **2011**, *40*, 2741–2760.

(233) Shou, R.-E.; Chai, W.-X.; Song, L.; Qin, L.-S.; Shi, H.-S.; Wang, T.-G. Three Luminescent Copper(I) Iodide Clusters with Phosphine Ligands: Synthesis, Structure Characterization, Properties and TD-DFT Calculations. *J. Clust. Sci.* **2017**, *28*, 2185–2203.

(234) Lakowicz, J. R. *Principles of Fluorescence Spectroscopy*, 3rd ed.; Springer: New York, 2006.

(235) Steiner, U. E. Fundamentals of Photophysics, Photochemistry, and Photobiology. In *Photodynamic Therapy*; Abdel-Kader, M. H., Ed.; Springer-Verlag: Berlin, 2014; pp 25–58.

(236) Hardt, H. D.; Pierre, A. Fluorescence Thermochromism and Symmetry of Copper(I) Complexes. *Inorganica Chim. Acta* **1977**, *25*, L59–L60.

(237) Rath, N. P.; Holt, E. M.; Tanimura, K. Fluorescent Copper(I) Complexes: Structural and Spectroscopic Characterization of Bis(*p*-Toluidine)Bis(Acetonitrile)Tetraiodotetracopper and Bis[(*p*-Chloroaniline)(Acetonitrile)Diiododicopper] Tetrameric Complexes of Mixed-Ligand Character. *Inorg. Chem.* **1985**, *24*, 3934–3938.

(238) Hu, G.; Mains, G. J.; Holt, E. M. Correlation of Structure and Emission in Solid State Copper(I) Complexes; $[Cu_4I_4(CH_3CN)_2(L)_2]$, L = Aniline Derivative. *Inorganica Chim. Acta* **1995**, *240*, 559–565.

(239) Vogler, A.; Kunkely, H. Photoluminescence of Tetrameric Copper(I) Iodide Complexes Solutions. *J. Am. Chem. Soc.* **1986**, *108*, 7211–7212.

(240) Yang, K.; Li, S.-L.; Zhang, F.-Q.; Zhang, X.-M. Simultaneous Luminescent Thermochromism, Vapochromism, Solvatochromism, and Mechanochromism in a C3-Symmetric Cubane [$Cu_4I_4P_4$] Cluster without Cu–Cu Interaction. *Inorg. Chem.* **2016**, *55*, 7323–7325.

(241) Vega, A.; Saillard, J. Y. Bonding in Tetrahedral $Cu_4(M^{3-}X)_4L_4$ Copper(I) Clusters: A DFT Investigation. *Inorg. Chem.* **2004**, *43*, 4012–4018.

(242) De Angelis, F.; Fantacci, S.; Sgamellotti, A.; Cariati, E.; Ugo, R.; Ford, P. C. Electronic Transitions Involved in the Absorption Spectrum and Dual Luminescence of Tetranuclear Cubane [$Cu_4I_4$(Pyridine)$_4$] Cluster: A Density Functional Theory/Time-Dependent Density Functional Theory Investigation. *Inorg. Chem.* **2006**, *45*, 10576–10584.

(243) Kitagawa, H.; Ozawa, Y.; Toriumi, K. Flexibility of Cubane-like $Cu_4I_4$ Framework: Temperature Dependence of Molecular Structure and Luminescence Thermochromism of [$Cu_4I_4(PPh_3)_4$] in Two Polymorphic Crystalline States. *Chem. Commun.* **2010**, *46*, 6302–6304.

(244) Kim, T. H.; Shin, Y. W.; Jung, J. H.; Kim, J. S.; Kim, J. Crystal-to-Crystal Transformation between Three CuIcoordination Polymers and Structural Evidence for Luminescence Thermochromism. *Angew. Chemie - Int. Ed.* **2008**, *47*, 685–688.

(245) Ryu, C. K.; Vitale, M.; Ford, P. C. Photoluminescence Properties of the Structurally Analogous Tetranuclear Copper(I) Clusters $Cu_4X_4$(Dpmp)$_4$ (X = I, Br, Cl; Dpmp = 2-(Diphenylmethyl)Pyridine). *Inorg. Chem.* **1993**, *32*, 869–874.

(246) Chen, K.; Shearer, J.; Catalano, V. J. Subtle Modulation of $Cu_4X_4L_2$ Phosphine Cluster Cores Leads to Changes in Luminescence. *Inorg. Chem.* **2015**, *54*, 6245–6256.

(247) Mazzeo, P. P.; Maini, L.; Petrolati, A.; Fattori, V.; Shankland, K.; Braga, D. Phosphorescence Quantum Yield Enhanced by Intermolecular Hydrogen Bonds in $Cu_4I_4$ Clusters in the Solid State. *J. Chem. Soc. Dalt. Trans.* **2014**, *43*, 9448–9455.

(248) Taylor, W. V.; Xie, Z.; Cool, N.; Shubert, S.; Rose, M. J. Syntheses, Structures and Characterization of Nickel(II) Stibines: Steric and Electronic Rationale For Metal Deposition. *Inorg. Chem.* **2018**, *57*, 10364–10374.

(249) Chantzis, A.; Kowalska, J. K.; Maganas, D.; DeBeer, S.; Neese, F. Ab Initio Wave Function-Based Determination of Element Specific Shifts for the Efficient Calculation of X-Ray Absorption Spectra of Main Group Elements and First Row Transition Metals. *J. Chem. Theory Comput.* **2018**, *14*, 3686–3702.

(250) Shou, R. E.; Chai, W. X.; Song, L.; Qin, L. S.; Shi, H. S.; Wang, T. G. Three Luminescent Copper(I) Iodide Clusters with Phosphine Ligands: Synthesis, Structure Characterization, Properties and TD-DFT Calculations. *J. Clust. Sci.* **2017**, *28*, 2185–2203.

(251) Huang, Y.-G.; Jiang, F.-L.; Hong, M.-C. Magnetic Lanthanide–Transition Metal Organic–Inorganic Hybrid Materials: From Discrete Clusters to Extended Frameworks. *Coord. Chem. Rev.* **2009**, *253*, 2814–2834.

(252) Karlin, K. D.; Nanthakumar, A.; Fox, S.; Murthy, N. N.; Ravi, N.; Huynh, B. H.; Orosz, R. D.; Day, E. P. X-Ray Structure and Physical Properties of the Oxo-Bridged Complex [(F8-TPP)Fe-O-Cu(TMPA)]$^{+}$, F8-TPP = Tetrakis(2,6-Difluorophenyl)Porphyrinate($^{2-}$), TMPA = Tris(2-Pyridylmethyl)Amine: Modeling the Cytochrome c Oxidase Fe-Cu Heterodinuclear Active Site. *J. Am. Chem. Soc.* **1994**, *116*, 4753–4763.

(253) Terris, B. D.; Thomson, T. Nanofabricated and Self-Assembled Magnetic Structures as Data Storage Media. *J. Phys. D. Appl. Phys.* **2005**, *38*, R199--R222.

(254) Desrochers, P. J.; Telser, J.; Zvyagin, S. A.; Ozarowski, A.; Krzystek, J.; Vicic, D. A. Electronic Structure of Four-Coordinate $C_{3v}$ Nickel(II) Scorpionate Complexes: Investigation by High-Frequency and -Field Electron Paramagnetic Resonance and Electronic Absorption Spectroscopies. *Inorg. Chem.* **2006**, *45*, 8930–8941.

(255) Gorter, S.; Hinrichs, W.; Reedijk, J.; Rimbault, J.; Pierrard, J. C.; Hugel, R. P. Structure, Spectroscopy and Magnetism of Di-Iodo-Bridged Tetrahedral Cobalt(II) Compounds. The Crystal and Molecular Structures of Di-$\mu$-Iodo-Bis[Iodotriphenylphosphinecobalt(II)] Bis(Benzene) and Di-$\mu$-Iodo-Bis[Iodotriphenylphosphineoxidecobalt(II)] Bis(Benzene). *Inorganica Chim. Acta* **1985**, *105*, 181–186.

(256) Vránová, I.; Alonso, M.; Jambor, R.; Růžička, A.; Erben, M.; Dostál, L. Stibinidene and Bismuthinidene as Two-Electron Donors for Transition Metals (Co and Mn). *Chem. – A Eur. J.* **2016**, *22*, 7376–7380.

(257) Gilli, G.; Sacerdoti, M.; Domiano, P. The Crystal and Molecular Structure of Dicarbonylnitrosyltriphenylstibinecobalt(0). *Acta Crystallogr. Sect. B* **1974**, *30*, 1485–1490.

(258) Suzuki, T.; Fujiiwara, K.; Takagi, H. D.; Kashiwabara, K. Preparation and Characterization of Mixed-Ligand Cobalt(III) Complexes Containing (3-Aminopropyl)Dimethylphosphine (Pdmp). Conformation of the Six-Membered Pdmp Chelate Ring. *Dalt. Trans.* **2007**, 308–319.

(259) Naktode, K.; Kottalanka, R. K.; Adimulam, H.; Panda, T. K. Tetra-Nuclear Copper Complex Having P–N–P Ligand to P–O–P Ligand – Synthesis, Structural, and Mechanistic Studies. *J. Coord. Chem.* **2014**, *67*, 3042–3053.

(260) Bain, G. A.; Berry, J. F. Diamagnetic Corrections and Pascal's Constants. *J. Chem. Educ.* **2008**, *85*, 532–536.

(261) Hota, R. L.; Tripathi, G. S. Theory of Effective G-Factors in Ternary Semiconductors: Application to $Pb_{1-x}Sn_xTe$. *J. Phys. Condens. Matter* **1991**, *3*, 6299–6311.

(262) Vaidya, S.; Tewary, S.; Singh, S. K.; Langley, S. K.; Murray, K. S.; Lan, Y.; Wernsdorfer, W.; Rajaraman, G.; Shanmugam, M. What Controls the Sign and Magnitude of Magnetic Anisotropy in Tetrahedral Cobalt(II) Single-Ion Magnets? *Inorg. Chem.* **2016**, *55*, 9564–9578.

(263) Cho, Y. I.; Ward, M. L.; Rose, M. J. Substituent Effects of $N_4$ Schiff Base Ligands on the Formation of Fluoride-Bridged Dicobalt(II) Complexes via B–F Abstraction: Structures and Magnetism. *Dalt. Trans.* **2016**, *45*, 13466–13476.

(264) Zhou, J.; Song, J.; Yuan, A.; Wang, Z.; Chen, L.; Ouyang, Z. W. Slow Magnetic Relaxation in Two Octahedral Cobalt(II) Complexes with Positive Axial Anisotropy. *Inorganica Chim. Acta.* **2018**, *479*, 113–119.

(265) Wu, Y.; Tian, D.; Ferrando-Soria, J.; Cano, J.; Yin, L.; Ouyang, Z.; Wang, Z.; Luo, S.; Liu, X.; Pardo, E. Modulation of the Magnetic Anisotropy of Octahedral Cobalt(II) Single-Ion Magnets by Fine-Tuning the Axial Coordination Microenvironment. *Inorg. Chem. Front.* **2019**, *6*, 848–856.

(266) Cotton, F. A.; Goodgame, D. M. L.; Goodgame, M. The Electronic Structures of Tetrahedral Cobalt(II) Complexes. *J. Am. Chem. Soc.* **1961**, *83*, 4690–4699.

(267) Cotton, F. A. *Progress in Inorganic Chemistry Volume 10*; Interscience Publishers: New York, 1968.

(268) Lin, T.-P.; Ke, I.-S.; Gabbaï, F. P. Sigma-Accepting Properties of a Chlorobismuthine Ligand. *Angew. Chemie - Int. Ed.* **2012**, *51*, 4986–4988.